Improving Axion Signal Models Through N-Body Simulations

Erik W. Lentz

A dissertation
submitted in partial fulfillment of the
requirements for the degree of

Doctor of Philosophy

University of Washington

2017

Reading Committee:

Leslie J Rosenberg, Chair

Thomas R. Quinn

Ann E. Nelson

Program Authorized to Offer Degree:
Physics

University of Washington

Abstract

Improving Axion Signal Models
Through N-Body Simulations

Erik W. Lentz

Chair of the Supervisory Committee:
Professor of Physics Leslie J Rosenberg
Department of Physics

The QCD axion is a well-motivated candidate for solving both the strong CP and dark matter problems. A great deal may be revealed about physics both on the level of fundamental particles and astronomy if the axion is detected to be the primary component of dark matter. A number of experimental searches for dark matter axions are currently operating under a weakly-motivated signal shape, which degrades the significance of their findings. Modern structure-formation simulations are capable of producing robust estimates of potential axion signals, and further may resolve a standing question in the literature: do axions form unique structures on galactic scales due to their unique state as a highly degenerate Bose fluid, or are they indistinguishable from a classical pressure-less fluid? This dissertation addresses the unique structure problem and provides a robust axion signal shape in the pressure-less fluid limit. Preliminary findings show that axions do contain the potential for unique structure formation on galactic scales. The new signal shape is applied to the most recent data run of the Axion Dark Matter eXperiment, the world's most sensitive axion search. The narrower profile of the updated signal model drastically increases the discovery potential for ADMX and other DM axion cavity searches.

TABLE OF CONTENTS

LIST OF FIGURES

ACKNOWLEDGMENTS

I would like to thank my co-advisors Drs. Leslie Rosenberg and Tom Quinn for their guidance, my parents Don and Karyn and my sister Morgyn for their encouragement and faith, and most of all my wife Meredith for her support through the roller coaster of the past eight(+) years.

I gratefully acknowledge the support of the U.S. Department of Energy offce of High Energy Physics via grant DE-SC0011665.

DEDICATION

To Meredith.

Chapter 1

INTRODUCTION

Physicists have been working for centuries to understand the behavior of the natural world. Starting with objects and phenomena most important in day-to-day life, we have expanded our attention to scales both larger and more microscopic. Today those foci extend to both the state of the visible universe and the inner workings of sub-atomic particles. Both extremes still harbor considerable unsolved problems. This dissertation features two conspicuous problems at either end of the spectrum, a candidate to resolve them, and my contributions to completing the underlying science.

What holds the galaxies together? The most massive bound structures in the visible universe, galaxy clusters, are our first clue to the existence of new physics on the largest scales. Since the 1930s, kinematical and mass observations first by Zwicky (Zwicky, 1937, 1942) and then others (de Vaucouleurs, 1956; Baier, 1978) show that the motions of member galaxies indicate of far more massive systems, up to hundreds of times, than measured by luminosity. More sophisticated mass models for the luminous matter make this disparity even larger (Zwicky, 1953; de Vaucouleurs, 1960) and continued observations have reduced perceptual and physical biases and increased the significance of the observations (Limber, 1959; Holmberg, 1961; de Vaucouleurs, 1974; Komatsu et al., 2011; Anderson et al., 2014; Planck Collaboration et al., 2016b).

The disparity continues into the makeup of individual galaxies. The landmark rotational observations by Rubin and Ford (Rubin & Ford, 1970; Rubin, 1973; Rubin et al., 1973; Rubin & Ford, 1975; Rubin et al., 1980, 1982) over decades show overwhelmingly that stars orbit too quickly to be described by the gravity of observed luminous matter. These results have

increased in significance and robustness with improved modeling and further observation (Rubin et al., 1997; de Blok et al., 2001; McConnachie, 2012; Lelli et al., 2016), Fig. 1.1. Even the oldest light in the visible universe, the Cosmic Microwave Background (CMB), shows early matter to be unusually condensed (Planck Collaboration et al., 2016a,b; Dawson et al., 2013). Altogether, observation of structures on scales above a kiloparsec (kpc) show a profound departure from the physics expected of visible matter.

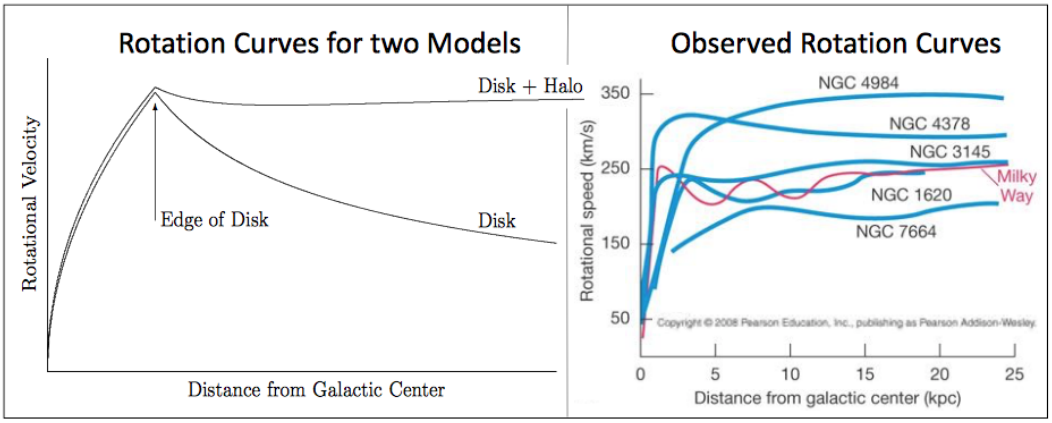

Figure 1.1: Galaxy rotation curves are a prime example of the shortcomings of a luminous matter-only model of structure formation. The left panel outlines the galaxy rotation behavior of one galaxy composed of luminous matter only and another with an additional massive component extending far beyond the galactic disk. The right panel displays smoothed curves from several real galaxies. (Credit: 2012 Pearson Education, Inc., publishing as Addison Wesley)

Even more confounding, cosmological observations on the largest scales also show that galaxies and galaxy clusters are accelerating from each other as if by a uniform pressure and have been for the past seven billion years (Riess et al., 1998; Perlmutter et al., 1999; Huterer & Turner, 1999; Planck Collaboration et al., 2016b). This mutual repulsion is not an expected feature from massive objects, even in unified theories of gravity like Einstein's

General Relativity (Einstein, 1917; Peebles & Ratra, 2003). Such a reversal of gravitational character both in physical scale and time is astounding. Attempts to capture these phenomena using the best-known description of fundamental particle physics, the Standard Model (SM, see Fig. 1.2), have been unsuccessful (Planck Collaboration et al., 2016b; Patrignani & Particle Data Group, 2016; Steigman, 2007). This inability to resolve the discrepancies between observed kinematics and naive gravitational predictions using the known fundamental forces is one of the largest problems in fundamental physics.

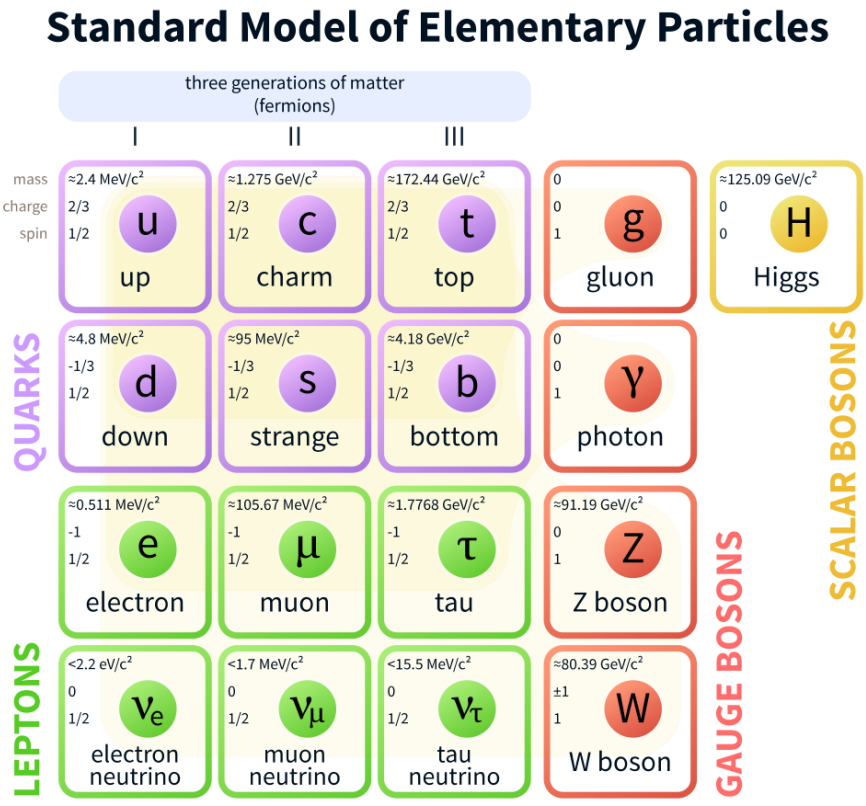

Figure 1.2: The Standard Model of Elementary Particles.

Decades of theorists have produced innumerable models of new physics, seeking to account for these cosmological observations. New models take several forms, ranging from the

new theories of gravitation, to better record keeping of known objects, to introducing unique fundamental particles and fields. Below we give an incomplete list of different approaches. There are several philosophical approaches in overcoming inadequacies of the known fundamental forces. One is to assume that there exists a yet-to-be-discovered fifth or possibly more forces on luminous matter, which appear in the correct proportions to reproduce attraction on galactic and cluster levels and repulsion on larger scales. Such theories have been created and tested since the time of Zwicky (Zwicky, 1942), and while no independent measurements of such forces have been made, the field continues to be a source of much literature (Csáki & Tanedo, 2016).

On the other hand, MOdified Newtonian Dynamics (MOND) is one class of theories that concentrates on the modification of existing fundamental forces (McGaugh & de Blok, 1998; Famaey & McGaugh, 2012). Among the four SM fundamental forces, gravity is observed to dominate on the largest scales and is the primary focus of modification. Early MOND theories matched galactic observations with relatively little difficulty, are simple in form and appear to be well-motivated. Unique and more precise observations in recent years have put great strain on the paradigm, especially outside the galactic scale (McGaugh, 2015). To keep pace with the data, current MOND models have expanded in complexity and decreased in motivation to the point of untenability (Skordis, 2009; Dodelson, 2011). Therefore, the approach explored in this paper is grounded on a different philosophy.

Instead of suspecting the fault to be with the underlying dynamics, the approach we follow assumes an incomplete accounting of matter and energy. Of the set of models that make alterations in the energy content of the universe, ΛCDM is considered to be the most successful to date in predicting cosmological structure formation in our universe and it is often referred to as the standard model of cosmology (see Planck Collaboration et al. (2016b) for a review). To match observations the standard model of cosmology must describe both the collapse of matter and formation of galaxies and clusters on Mpc and smaller scales simultaneously with accelerated expansion on the largest scales (Eisenstein et al., 2005). Collapse into clusters and galaxies and at small scales requires an additional component of

cold matter and the large-scale negative pressure requires an additional component of energy, called Cold Dark Matter (CDM) and dark energy (Λ or DE) respectively. The most precise observations of our visible universe sets the proportions of baryonic (visible) matter to CDM to Λ at $1 : 5.4 : 13.9$ (Planck Collaboration et al., 2016b), implying that CDM outweighs all visible matter by a large factor!, Fig. 1.3.

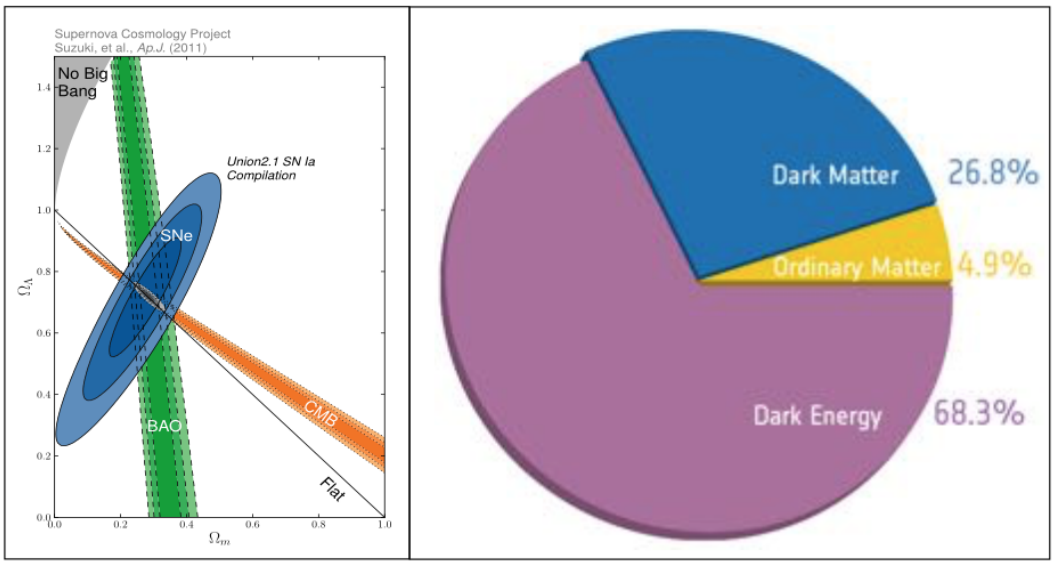

Figure 1.3: Breakup of the observable universe's energy budget (Planck Collaboration et al., 2016b). The left panel shows the intersection of likelihood contours from several data sets. The right panel shows the most likely configuration.

Determining the nature of potential CDM and Λ is challenging. The characterization of DE is particularly fascinating due to its non-intuitive gravitational behavior, but it is beyond the scope of this work. We focus on dark matter, which is responsible for much of the gravitational attraction in galaxies and clusters. Many different theories are capable of fitting within these specifications using a wide range of physics, with the primary differentiator being whether or not new fundamental types of matter are needed. On the negatory side, some speculate that the dark matter comes in the form of black holes, dim stars, and other

known forms of matter condensed into compact objects whose evolution brought them to an essentially invisible state in sufficient quantities to account for the dark matter. Examples include stellar mass black holes, dim dwarf stars, and rogue planets. Many of these MAssive Compact Halo Objects (MACHOs) are accounted for in baryonic mass models of galaxies and clusters, but the models restrict these objects' density. For MACHOs to be the DM, drastically different models of black hole and stellar evolution are needed, but have yet to be borne out by observations (Brown, 2007). Further, modern compact object surveys have produced constraints on the presence of MACHOs in our own galaxy that are indiscernible from expected populations (Alcock et al., 2000; Tisserand et al., 2007; Brown, 2007). It appears as though the DM is not made of baryons.

Many others posit that the dark matter is composed of new fundamental fields and particles, which are designed to satisfy the qualities of DM. We concentrate on this type of DM. Based on the above observations, DM is deduced to have the following qualities

- cold (de Naray et al., 2010; Chau et al., 2017)
- matter-like cosmological scaling
- interact feebly with the strong and weak nuclear forces and electromagnetism
- produced in the radiation dominated epoch
- long-lived

Astronomically, the dark contributions dominate the cosmological and galactic evolution over the last two stretches of the universe's history, which are appropriately dubbed the matter-dominated and dark energy-dominated epochs. Simulations and observations show that effects of these dark components determine the scale of the largest structures, seed the formation of galaxies, and influence all structure in the observed universe down to the kpc level. The presence of these contributions appears to be critical to life as we know it, though we have yet to see anything but a gravitational footprint.

What shapes the atoms? Thought to be the most fundamental constituent of matter at the turn of the twentieth century, atoms have since been divided multiple times, thereby uncovering a more unified description of particle physics. This success with breaking up seemingly fundamental pieces drives many DM models. For instance, in theories of SUper-SymmetrY (SUSY) we find a zoo of new fundamental particles are possible, a number of which could have developed into the DM. Often it suspected that one of the lightest particles left over from the breaking of SUSY early in the universe's history dominates the DM (Jungman et al., 1996; Catena & Covi, 2014). This partner must be electrically neutral and massive to avoid detection in past accelerator experiments. Many other theories also utilize this notion of a consolidating symmetry to introduce more particles whilst unifying the physical description. DM models can be made in a sort of vacuum, but it is these unifying models that are considered to be the best motivated.

The genesis of these models lie in the far past of our universe beyond our current observations and at a time when the ambient temperature was at energy scales far beyond our largest colliders. These scales lie near or beyond energies where we have reason to believe the nuclear and electromagnetic forces become described by a single Grand Unified Theory (GUT), which is suspected to manifest itself at $\sim 10^{15}$ GeV (Patrignani & Particle Data Group, 2016). In cosmological particle physics, once the universe expands and cools below the GUT scale, or whatever scale the prescribed fundamental theory lies, a number of phenomena may occur to collapse the model down to the modern universe with both visible and dark matter.

Spontaneous breaking of a theory's underlying symmetry, phase changes, or other emergent phenomena are common means of regaining both the known low energy physics; they are also a means of creating new particles. After genesis, these DM theories interact with the other dense hot components of matter and energy. These interactions aren't necessarily feeble in the hot dense state of the early universe, and imprints of the DM can be made on the baryonic components (Planck Collaboration et al., 2016b; Dawson et al., 2013; Anderson et al., 2014), Fig. 1.4. As the universe expands and cools in the radiation-dominated epoch,

the DM stabilizes into the above properties and appropriate proportions.

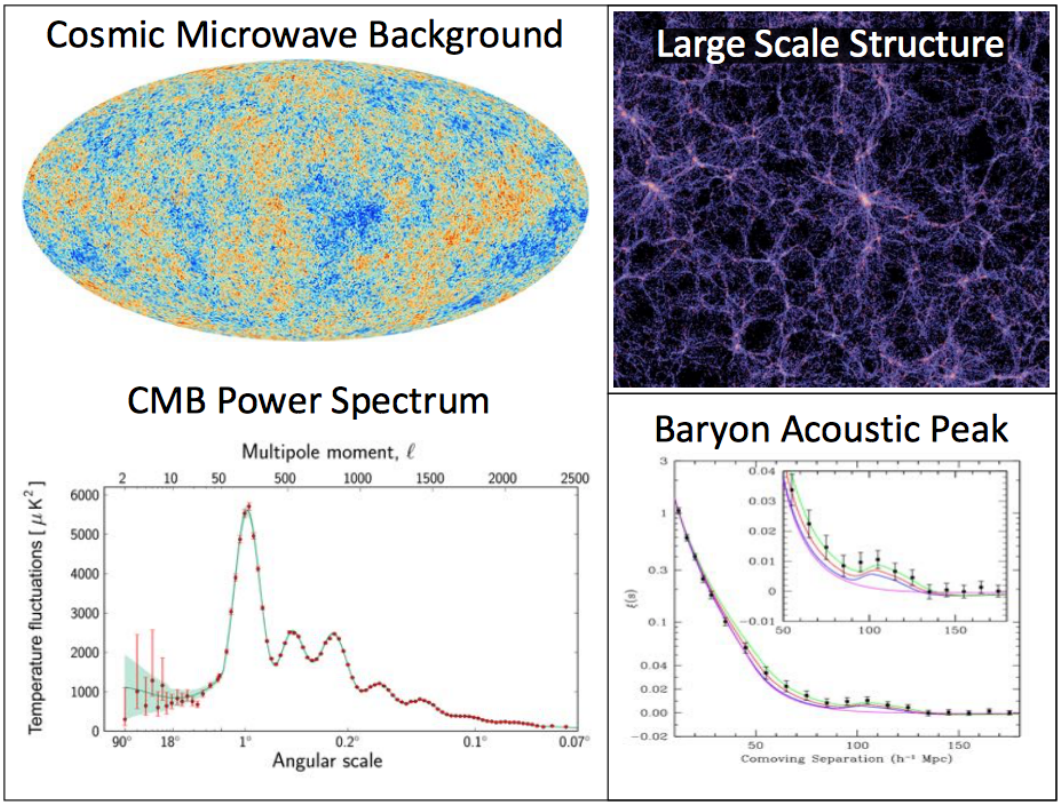

Figure 1.4: Extra structure about natural oscillations of comoving size 100 h^{-1} Mpc in the CMB (Planck Collaboration et al., 2016b) are widely considered as evidence for DM. Current understanding of early cosmology and large scale structure formation puts many DM theories forming structure at this scale at this time, which would amplify the natural structures of baryons at the same scale.

Several categories emerge from the many different models of DM pursued, including Weakly Interacting Massive Particles (WIMPs), Weakly Interacting Slim Particles (WISPs), and sterile neutrinos. WIMPs have been the most popular of these categories over the past several decades, perhaps because they are seen as an extension of accelerator physics, which has had great success in finding ever more massive fundamental particles and uncovering new

physics at high energies (Patrignani & Particle Data Group, 2016; Arcadi et al., 2017; Mitsou, 2015). This category generally concerns candidates of mass energy of a GeV or more. The origins of any particular WIMP theory is usually tied to a more complete candidate theory of physics like SUSY or string theory, but may also be proposed independently. Many WIMP DM searches have been in progress in the last several decades to great effect, pushing sensitivities to near their limit of the noisy neutrino floor (Agnese et al., 2014; Arcadi et al., 2017; Akerib et al., 2017), Fig. 1.5.

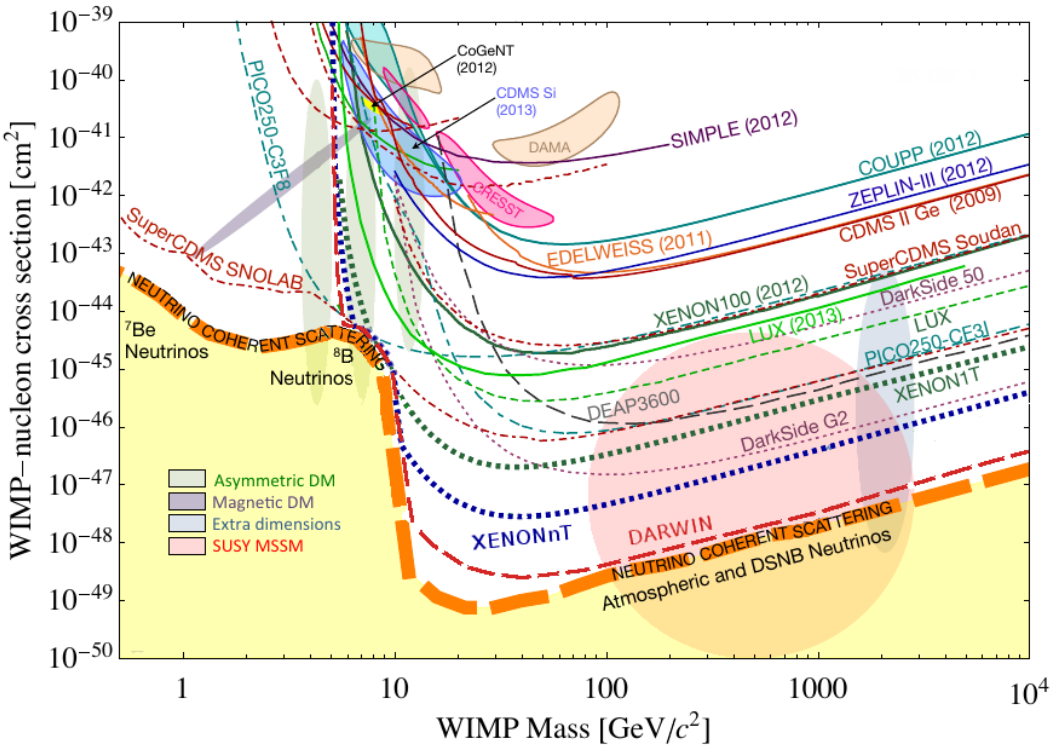

Figure 1.5: WIMP coupling limits over prospective masses (Baudis, 2014). There is an effective lower limit to the sensitivity of current experiments due to the presence of ambient neutrinos, which would eventually overwhelm a detector with false signals.

Sterile neutrinos form a more specific set of DM candidates, which we separate from WIMPs and WISPs as they cross into both mass ranges. Many theories have been pro-

posed that play off of the natural weak interactions of the SM neutrino particles, Fig. 1.2, extending the neutrino family to include new members. These members retain the weak interaction qualities while being imbued with much larger mass to help satisfy the remaining CDM requirements. Careful pains must be taken to ensure that the new neutrinos do not macroscopically mix like their SM siblings, which would have been detectable in numerous neutrino oscillation experiments. The combined searches for these candidates have explored much of the viable space, though the literature is still active (Dodelson & Widrow, 1994; Kopp et al., 2013).

WISPs extend the mass reach of DM candidates into the very thin. Covering a wide range of masses from the eVs to 10^{-30} eV and smaller (Ringwald, 2012), the motivations for WISPs span simple oversights in the quantum nature of SM constituents to grand unified theories of strings. Candidates in this category go by the name of axions, Axion-Like Particles (ALPs), dark photons and others (Redondo, 2008; Ringwald, 2012). Searches for these flavors of dark matter are relatively untrodden, leaving a great deal of space to explore, Fig. 1.6. This dissertation focuses on axions. We specifically focus on a class of axions whose motivation begins by solving a problem on the atomic nuclei scale. Shaping the nucleus is a collection of protons and neutrons held together by the strong nuclear force of the SM 1.2. At the most fundamental level the strong force is described by the theory of Quantum ChromoDynamics (QCD). QCD is a difficult theory with which to make even simple nuclear calculations, containing many barriers to entry and unsolved problems (Patrignani & Particle Data Group, 2016; Lin, 2011; Gupta, 1998). One such problem concerns the unexpected reaction to a classical symmetry. Classical physics predicts that the action of atomic nuclei should be invariant under the flipping of all charges in the universe (C) concurrent with taking the universe's mirror image (P). Implementing this CP transformation onto the quantum world of QCD finds that CP is not a symmetry, but instead should be macroscopically broken, Fig. 1.7. However no such violations of the symmetry have been detected. Research into the impacts to nuclear structure such as a neutron's electric dipole moment measure it to be less than 3×10^{-26} electron-cm, more than 10^{10} times smaller than naively expected from QCD

symmetry breaking (Dar, 2000; Baker et al., 2006; Pendlebury et al., 2015). Such a striking disparity does not lend itself well to coincidence.

The axion is born initially as an attempt to explain the strong CP problem by (Peccei & Quinn, 1977; Weinberg, 1978; Wilczek, 1978), and is only later found to be capable of also solving the DM problem(Kim, 1979; Shifman et al., 1980; Zhitnitsky, 1980; Dine et al., 1981; Dine & Fischler, 1983; Abbott & Sikivie, 1983; Sikivie, 1983; Marsh, 2016). While other axion-like solutions to the DM problem exist, we concentrate only on those multi-tasking models that also solve the strong CP problem, QCD axions. QCD axion DM takes on several interesting characteristics that distinguish it from the popular WIMP candidates: it is much lighter, with masses well below an eV (Preskill et al., 1983; Turner & Wilczek, 1991); it is much colder, with infinitesimal primordial temperature relative to WIMPs (Banik & Sikivie, 2016; Erken et al., 2012); and it is highly degenerate, meaning the axions are highly overlapped (Sikivie, 2008; Sikivie & Yang, 2009; Banik & Sikivie, 2016; Erken et al., 2012), Fig. 1.8. This implies that the axions are a highly degenerate Bose fluid, a unique quantum state capable of inducing highly non-intuitive behavior. Such systems, commonly called Bose-Einstein Condensates (BECs), are fluids known in condensed matter systems to create infinitely deep vortices, to move without friction, and to escape their containers by climbing up the walls (Dalfovo et al., 1999; Anglin & Ketterle, 2002; Yukalov, 2011; Zapf et al., 2014)! Such properties in a DM candidate would imply some very interesting behavior in galactic halos.

The axion is a highly attractive DM candidate as its multi-tasking nature and observational constraints compact its viable parameter space, Fig.1.9. Starting at milli-eV masses, there is a bound above which the axion would have been seen in various astrophysical processes (Raffelt, 2008; Ringwald, 2016; Marsh, 2016). Below the mirco-eV mass, there is a bound below which more axions are produced than there is dark matter. This lower bound is somewhat flexible, as axion creation mechanisms can be suppressed in the details of some axion theories (Shellard & Battye, 1998; Marsh, 2016). The two diagonal lines of Fig. 1.9 represent benchmark axion models. KSVZ represents a theory where the axion couples to

hadrons only (Kim, 1979; Shifman et al., 1980), and DFSZ couples to both hadrons and leptons (Dine et al., 1981; Zhitnitsky, 1980), as consistent with GUTs. The search window is then given by the region between KSVZ and DFSZ, and the lower and upper mass bounds.

Observations and experimental searches are needed to confirm or refute a DM candidate. Constructing an apparatus sensitive enough to detect the unique signature of a candidate is difficult and no known single technique exists to identify the features of the DM. This uncertainty results in a diverse collection of searches with a wide range of range of capabilities. These searches can be split into two groups: direct searches that operate under highly controlled laboratory conditions, and indirect searches that observe the wild processes of nature.

The most successful indirect searches to date involve DM's gravitational coupling to visible matter and its role in the formation of structure in the visible universe. These studies use observations at scales from isolated astrophysical structures to cosmological distances, producing estimates on macroscopic DM densities and energy content (Patrignani & Particle Data Group, 2016; Planck Collaboration et al., 2016b), but have done less to determine its microscopic properties. Most features of DM are too subtle to detect gravitationally on such large scales. Detailed observations and numerical simulations of structure formation are needed to tease out unique DM candidate properties. Other indirect searches take advantage of the conditions not yet present in Earth laboratories, such as the sun, whose proximity, density, size, and relatively high energy make it a prime location to observe interaction with DM candidates. We are also tempted use more removed but also more energetic potential engines for DM-viewing such as the center of the Milky Way (MW), where the baryonic matter and DM densities are very high. Other astrophysical objects such as neutron stars, pulsars, super-novae, and active galactic nuclei are also observed for this reason, and they all suffer from the same flaw: we don't fully understand the baryonic physics involved. Fluid flow, physics at high degeneracy, etc., all have unsolved conceptual problems that complicate our understanding of these objects and our ability to understand their base state. This gap in understanding limits our predictions as to what changes come from an introduction of

new physics. This is why, for the time being, Earth-based experiments are capable of outperforming their astronomical counterparts.

Direct detection of DM occurs when a source of DM produces a unique observable signal in a laboratory setting. The influence that human beings can have over their environment allows for clean manipulation of stimuli and very detailed measurements of signals that are largely impossible with untamed sources. Such environments provide a means to explore fundamental features of a DM model that are currently impossible anywhere else. These searches often choose between detect the DM already present or seek to create a DM candidate. The most famous of the terrestrial experiments looking for DM candidates are the LHC's Atlas and CMS collaborations, which attempt to recreate early universe conditions by colliding protons at ultra-relativistic speeds and observe the resulting cascade of fragments. By piecing together what occurred at the apex of the collision, we can get a glance into how the fundamental constituents of the universe mesh. Since 2008 the LHC has discovered the Higgs boson, which is held to be responsible for imbuing the fundamental fermions (electron, muon, tau, quarks) with mass, but has yet to uncover any indications of particles viable as dark matter candidates (Aaboud et al., 2017). Less renown but more focused experiments present greater viability for detecting DM.

Experiments to detect the ambient DM depend upon its passage through a detector apparatus. Due to the weakness of gravity, current detectors again rely on the DM's weak direct interactions with the SM and have resulted in a very broad range of devices. These devices are often constructed to articulate the shape of the MW halo, including the daily and yearly modulations from relative motion of an Earth-bound apparatuses through the halo. Such details increase the detector's sensitivity to the ambient distribution and the likelihood of a detection, making detailed structure formation simulations over feasible initial conditions and realistic physics very important to the DM search community.

Recoil experiments are a class of sit-and-listen searches looking for signs of relic DM, primarily WIMPs. They operate on the premise that occasionally a WIMP collides with atomic nuclei and/or electrons, providing the detector with an impulse may may be observed

through a variety of emissions. Experiments containing up to hundreds of kilograms of very stable high-density elements such as germanium or xenon are buried deep underground and watched. Even in these isolated conditions the ambient and internal radiation are dominant sources of error. Experimental groups such as the Cryogenic Dark Matter Search (CDMS) and XENON have been operating with single-event sensitivity dating back to the beginning of this century and have yet to find a confirmed signal from a DM source (Agnese et al., 2014; Akerib et al., 2017; Aprile et al., 2017). The sum of these searches have pushed WIMP models to near the the neutrino floor, the extreme where the ambient flow of neutrinos would flood any DM sources.

The axion's low mass leads to unconventional search techniques. One attractive method used by axion DM searches threads a magnetic field through a resonant cavity, stimulating the decay of DM axions into microwaves, which are detected by a receiver sensitive to yacto-watt power (Asztalos et al., 2010). The receiver can also resolve the microwave's energy to a part in 10^9, capable of resolving fine structure in the MW axion distribution. We concentrate on this type of DM search. Despite this sensitivity to energy, many axion cavity searches look for a signal derived from the Standard Halo Model (SHM) (Asztalos et al., 2010; Brubaker et al., 2017), which comes from an assumption that the MW halo is given by a thermalized, pressure-less, self-gravitating sphere of particles. The velocity distribution of the SHM near the earth is given by a Maxwellian distribution

$$f_{\vec{v}} \propto e^{-\vec{v}\cdot\vec{v}/2\sigma_v^2}$$

where $\sigma_v = 160 km/s$ at the solar radius. The SHM is grossly predictive, but incapable of describing fine structure.

All direct DM searches have in common the need to understand the candidate abundance in the vicinity of their experimental apparatus. Astronomical observations are unable to provide these abundances due to difficulties in extracting local DM contributions from ephemeral gaseous and stellar motions, though progress is being made in this area (Valluri et al., 2016; Binney, 2017). In the mean-time we can perform simulations of the MW that

capture the relevant physics. Methods for performing these simulations are already quite sophisticated due to astronomers' efforts to understand the formation of cosmological structure down to the inner workings of galaxies. Often starting from CMB-motivated initial conditions, simulations of structure formation must accurately describe the violent process of collapse, collision, and equilibration of matter into galaxies and other forms.

On galactic scales, gravity is the only pertinent force acting on DM. The model is a straightforward one for WIMPS, neutrinos, and all other non-degenerate DM: move with no resistance to gravity, identically to a pressure-less fluid. Axions are speculated to be different. For example, Pierre Sikivie proposes that quantum effects from the BEC nature of DM axions still influence structures on galactic scales (Banik & Sikivie, 2016; Erken et al., 2012; Sikivie & Yang, 2009). A posited effect of this quantum influence are caustic rings (Sikivie, 1999a,b; Duffy & Sikivie, 2008), high-density flows of axions within the plane of our own galaxy. Such structures would greatly improve the discovery potential of axion DM searches, and their influence may be observable in nearby stars and interstellar gas. The potential for caustic rings and other unique structures is an exciting topic, as it would add a new dimension to axion direct detection and create a new astronomy, should the axion be discovered. However, such structures are highly speculative and rely heavily on the form of relevant dynamics on structure-formation scales; this is a contentious topic (Sanderson & Bertschinger, 2010; Erken et al., 2012; Guth et al., 2015; Banik et al., 2015) with much of the community believing pressure-less fluid dynamics to be sufficient. We call this tension the Unique Structure Problem (USP), and large amounts of this dissertation are dedicated to its resolution.

Regardless of what side of the USP the reader falls, numerical structure formation simulations present an opportunity to provide DM searches with well-motivated models of potential DM sources. There has been significant progress in simulating the formation of galaxies like the MW since these searches have begun. One powerful simulation tool is the N-Body method. Capable of accurately resolving the inner structures of galaxies and their halos, the N-Body simulations are now poised to give accurate models of DM for searches, and is the

principle simulation technique used in this dissertation. N-Body analyses of DM searches already exists for WIMPs, but have not yielded significant differences from the SHM (Sloane et al., 2016). Axion searches require different figures of merit, making an axion-specific analysis of structure-formation simulations worthwhile. Implications of N-Body structure formation simulations on axion DM searches are also a focus of this dissertation.

For the variety of reasons discussed above, the QCD axion dark matter candidate is a well-motivated solution to both the strong CP and dark matter problems. Axion DM also contains some unique properties, which may produce signatures on galactic scales, presenting novel opportunities for astronomers and direct detection searches. I assert that N-body simulations are a crucial tool to DM searches, capable of solving the axion USP and providing DM searches with realistic signal models that can greatly increase their discovery potential. To demonstrate my claim, this dissertation presents the fundamental of modeling relic axions, their structure formation to the current epoch and the impacts on axion searches like ADMX. The form of this dissertation is organized as follows: Chapter 2 introduces the axion formalism in quantum field language during its life in the early universe, including creation, acquisition of mass, and evolution of early structures; Chapter 3 continues the description of axion dynamics through galaxy formation and into the present cosmological time, producing a comprehensive approach to axion structure formation and the preliminary results of the USP research program; Chapter 4 reviews the landscape of axion searches, their techniques and results, paying particular attention to the author's resident collaboration ADMX; Chapter 5 expands on ADMX's results, presenting a robust axion search analysis on their most recent data run; Chapter 6 summarizes the results of this work and prospects for the completion of the USP program.

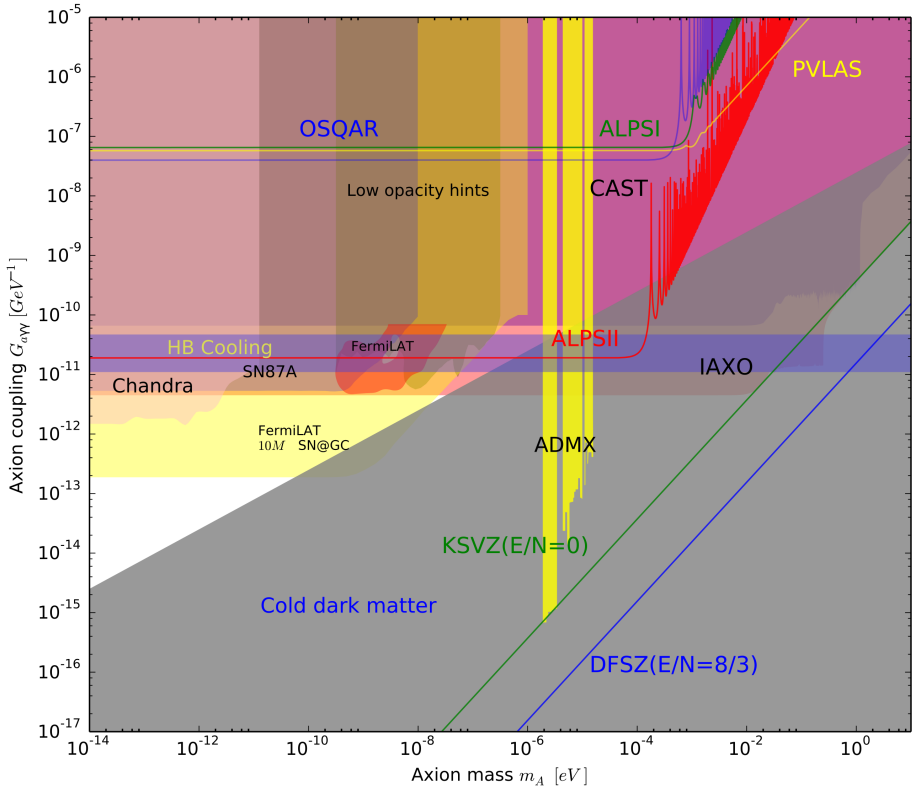

Figure 1.6: WISP coupling limits over prospective masses from current experiments (Collaboration, 2016). The neutrino floor does not impact WISPs until searching at masses higher than the neutrinos, for which there are already many other restrictions.

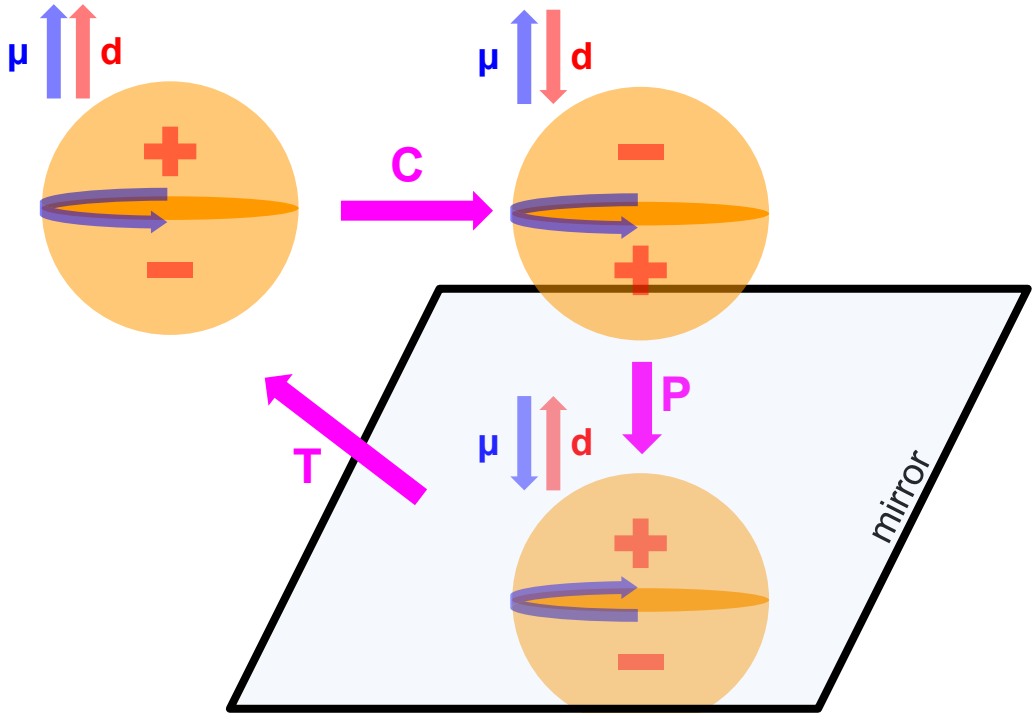

Figure 1.7: The composition of charge conjugation and parity flipping may be violated by some objects or physical processes. The presence of an neutron electric dipole moment is shown to violate CP.

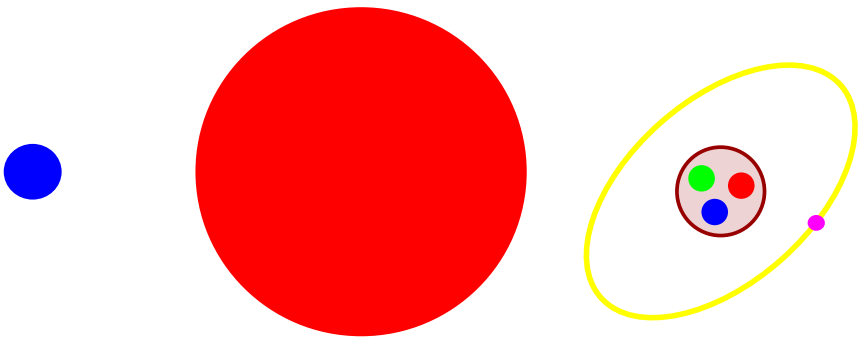

	QCD Axions	WIMPs	Hydrogen
m:	μeV - meV	GeV - TeV	GeV
δv:	~ 10^{-17}c	< 10^{-8}c	--
n:	~ 10^{61}	<< 1	--
$T_{1/2}$:	>> Gyr	>> Gyr	--

Figure 1.8: A comparison of properties between the QCD axion and WIMP DM candidates. Hydrogen atom is shown for scale. Degeneracy and velocity dispersion figures are quoted at the time of DM creation.

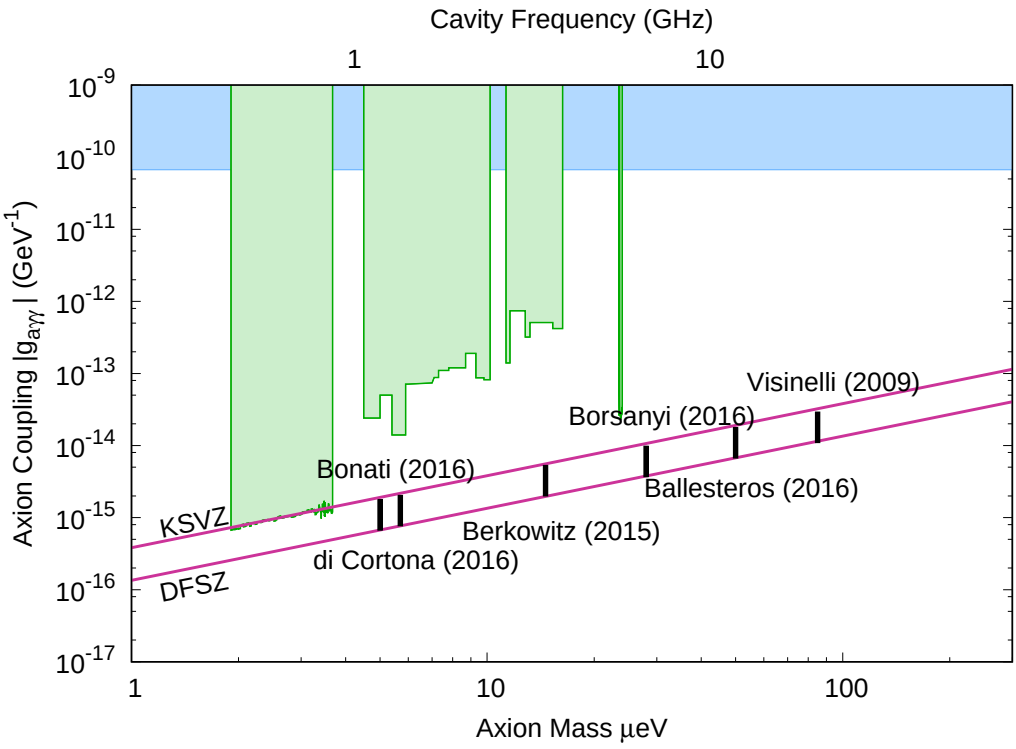

Figure 1.9: Axion DM parameter space populated by experimental bounds, benchmark models, and a collection of theoretical estimates for the QCD axion mass.

Chapter 2

AXIONS IN THE EARLY UNIVERSE

In the standard model of cosmology, a singular Big Bang is assumed to precipitate our universe, Fig. 2.1. For the first hundred thousand years or so the energy density is thought to be dominated by radiation, species whose energy is statistically dominated by kinematic contributions, and briefly interrupted by a period of rapid inflation. This first epoch ended when the radiation cooled and matter contributions gained dominance. With reduced pressure from radiation, matter collapsed to form stars, galaxies, and much of the structure astronomers observe today. The current epoch began as DE gained dominance over matter, sequestering structure formation. We introduce the QCD axion in this chapter according to its historical conception: in the first epoch as a means to solve the strong CP problem of quantum field theory, followed by its coincidental ability to solve the cosmological DM problem. A transition to the formation of galaxies and other structures occurs after matter domination and is largely deferred until Chapter 3.

2.1 Strong CP Problem Origin

As stated in the previous chapter, a problem appears when one compares the theory of the strong force to the observations of nuclei. Introducing QCD as a physical model with gauge-invariant classical action under SU(3)

$$S_{cl}[\Psi_i, A^i_\alpha] = \int dV_g \left(\hat{\Psi}^\dagger_i \left(i \not{\nabla} + i g T^{ij}_k \not{A}^k - m \delta^{ij} \right) \hat{\Psi}_j - \frac{1}{4} G^a_{\alpha\beta} G^{\alpha\beta}_a \right) \tag{2.1}$$

where dV_g is the space-time volume form, ∇ is the space-time covariant derivative operator, $\not{Q} = \gamma^\mu Q_\mu$ and γ^μ are the Dirac matrices which generate local Lorentz invariance of the

fermion and satisfy the commutation relations

$$\left\{\gamma^{\alpha},\gamma^{\beta}\right\} = 4g^{\alpha\beta} \tag{2.2}$$

where $\{\cdot,\cdot\}$ is the anti-commutator operator, $\hat{\Psi}$ is the fundamental fermion (quark) Dirac field operator, T_k^{ij} are the generator matrix elements of the fundamental representation of SU(3), A_μ^i are the SU(3) gauge fields, and $G_{\alpha\beta}^a$ is the gauge field strength

$$G_{\alpha\beta}^a = \partial_\alpha A_\beta^a - \partial_\beta A_\alpha^a + g f^{abc} A_\alpha^b A_\beta^c, \tag{2.3}$$

and we have given the fundamental coupling g to the fermion field. Einstein summation notation is implied for complementary indices unless otherwise noted. To calculate observables and dynamics in the quantum theory, a sampling is taken over all possible configurations contributing to the result, with likelihood weighted by the configuration's deviation from the classical "least action" state. The kernel from which quantities may be calculated is called the path integral, or partition function

$$Z = \int d\Psi d\Psi^\dagger d\tilde{A} e^{\left(iS[\Psi_i, A_\alpha^i]/\hbar\right)} \tag{2.4}$$

where the functional integral $\int d\Psi d\Psi^\dagger d\tilde{A}$ indicates integration over all physical configurations, and whose exact definition is still a source of tension among physicists and mathematicians.

There are some difficulties that arise if this quantum field theory of QCD is taken at face value. The problem on which we first focus is explained by a quirk of the functional integral measure. Acting on the partition function with an axial transformation of the fermion field

$$\Psi_i \rightarrow e^{\left(i\gamma^5\bar{\theta}_{QCD}\right)}\Psi_i \tag{2.5}$$

where $\gamma^5 = i\gamma^0\gamma^1\gamma^2\gamma^3$, the action is found to be invariant save for a violation in the mass term

$$\Delta S_{cl,\theta} = \int dV_g m \left(e^{2i\theta} - 1\right) \hat{\Psi}^\dagger \hat{\Psi} \tag{2.6}$$

Also, if the transformation is propagated to the integral measure, a non-trivial variation is found in the so-called QCD topological term

$$\Delta S = \int dV_g \mathcal{L}_{\theta_{QCD}} = \int dV_g \frac{\bar{\theta}_{QCD}}{32\pi^2} \mathrm{Tr}\left(G_{\mu\nu}\tilde{G}^{\mu\nu}\right) \tag{2.7}$$

where $\tilde{G}$ is the dual to the field strength. Both terms explicitly violate combined Charge-conjugation and Parity (CP) symmetry. It is possible to remove one of these with a judicious U(1) transform, but not both. We choose to retain the topological term. Such variations are referred to as quantum symmetry anomalies, where a respected classical symmetry is violated under quantum consideration.

The Electro-Weak (EW) sector of the SM also has a CP-violating anomaly, which has been observed (Olive et al., 2014). The EW anomaly also contributes to θ_{QCD} via the quark mass matrices

$$\Delta\theta_{QCD} = \arg\det\left(M_u M_d\right) \tag{2.8}$$

where M_u and M_d are the mass matrices over the "up" and "down" families of quarks, the doublets split by the EW symmetry breaking (Patrignani & Particle Data Group, 2016). The full CP-violating angle can now be written

$$\theta_{QCD} = \bar{\theta}_{QCD} + \arg\det\left(M_u M_d\right) \tag{2.9}$$

As these two contributions are, for our intentions, independent and potentially of value O(1), it is extremely unlikely that θ_{QCD} should be observed to be close to 0. Using the prediction of a non-vanishing static neutron Electronic Dipole Moment (nEDM)

$$d_n \approx 3.6 \times 10^{-16}\theta_{QCD}\text{e cm} \tag{2.10}$$

Many experiments have sought to quantify strong CP violation, but it has yet to surface. The current best measurements place the moment at $|d_n| \lesssim 2.9 \times 10^{-26}$ e cm, corresponding to $\theta_{QCD} \lesssim 10^{-10}$. This discrepancy between the expected and measured angle constitutes the strong CP problem.

2.2 Axions in Thermal-Bath Cosmology

Explanations for θ_{QCD}'s size range from anthropic arguments (if θ_{QCD} is larger, the universe would not have been able to produce humans to see it) to additional dynamics driving the parameter towards 0. We concentrate on the class of dynamical solutions, first sampled by Peccei and Quinn (Peccei & Quinn, 1977). We present these theories in the context of cosmology. In early times the universe is considered to be very hot, dense, and nearly uniform, with expansion occurring slowly enough that all concerned field contributions stay in thermodynamic equilibrium. Only after the universe is expanded enough to cool below the GUT scale ($\sim 10^{15}$ GeV), establishing the SM as the governing particle physics, do QCD and the strong CP-solving axion theories become meaningful.

Whether introduced as a complex-valued scalar field complementary to a Higgs or a different sector of particle physics, the uncoupled Lagrangian for the field φ is constructed with a Spontaneous Symmetry-Breaking (SSB) potential

$$\mathscr{L}_\varphi = \frac{1}{2}|\nabla\varphi|^2 - \lambda\left(|\varphi|^2 - \frac{f_a^2}{2}\right)^2 \tag{2.11}$$

The off-axis minimum of the potential is used to spontaneously break the vacuum symmetry by supporting a Vacuum Expectation Value (VEV) once the field temperature drops below f_a, similar to the standard Higgs potential, Fig. 2.2. Interactions with the rest of the SM are motivated in multiple ways. In the original Peccei-Quinn-Weinberg-Wilczek (PQWW) formulation the axion appeares as a second Higgs doublet (Peccei & Quinn, 1977; Weinberg, 1978; Wilczek, 1978). The PQWW breaking scale f_a is tied to the EW scale of $\approx$ 250 GeV. The system contains a PQ axial U(1) symmetry, which acts on φ in the fundamental representation, shifting the angular part by a constant, and acts chiraly on the coupled quark fields such that the action remains invariant. This global chiral invariance sets the PQ charges for the fermions.

$$|\varphi|e^{(i\phi)} \rightarrow \langle\varphi\rangle\, e^{(i\phi/f_a+\theta)} \tag{2.12}$$

$$q \rightarrow e^{\left(i\gamma^5 Q_{PQ}\theta\right)} q \tag{2.13}$$

Yukawa interactions appear between ϕ and the quark sector via the chiral rotations on the kinetic contribution. These interactions have a natural suppression in factors of f_a^{-1}, with the leading-order bare quark coupling of $i\phi m_q/f_a\bar{q}q$. The QCD topological term is likewise found to be modulated, $\propto \phi/f_a \mathrm{Tr}G\tilde{G}$, with further gauge field interactions entering at loop order.

The KSVZ theory of axions introduces φ independently from the Higgs and SM gauge theories, gives φ a charge of two under $\mathrm{U}(1)_{PQ}$. No longer tied to the EW scale, the spontaneous breaking energy may be much higher. The axion interacts only with high-mass-destined quarks, which is introduced as a doublet of right and left-handed type, Q_R and Q_L, each transforming as an SU(3) triplet. The handedness naturally dictates how the quarks rotate under chiral transformations. Invariant Yukawa interactions are then given by

$$\mathscr{L}_{int} = -\left(\lambda_a \varphi \bar{Q}_R Q_L + h.c.\right) \tag{2.14}$$

with λ_a as a free variable, not tied to the axion scale f_a. Again, the topological term comes from chiral rotations in the quark sector, $\propto \phi/f_a \mathrm{Tr}G\tilde{G}$, but its strength is not directly tied to the quark coupling. The heavy quark doublet is eventually integrated out, but the independent topological contribution remains. Interactions with light quarks and other gauge fields can be calculated at loop order.

The last specific axion theory considered here is DFSZ. Like the PQWW theory, φ couples to the SM via the Higgs sector, though the specific structure differs. Containing two Higgs doublets tied to the "up" and "down" families of quarks, the sector also contains the complex φ as a singlet to the SM. Bare interactions occur only with the Higgs

$$\mathscr{L}_{H,\varphi} = \lambda_a \varphi H_u H_d + h.c. \tag{2.15}$$

with φ having PQ charge of 1, forcing the two Higgs to have charge -1 to satisfy global chiral invariance. SM interactions with φ occur via the standard Higgs terms

$$\mathscr{L}_H \supset \lambda_u H_u \bar{q}_L u_R + \lambda_e H_{u,d} \bar{l}_L e_R \tag{2.16}$$

where the Higgs which couples to the lepton sector is a freedom of the theory. The SM reaction to the PQ rotations serve as the origin of fermion-φ interactions, and whose coupling is already set by the Higgs

$$\mathscr{L}_{\varphi} \supset \lambda_u H_u \phi / f_a \bar{q}_L u_R \tag{2.17}$$

Again, the QCD and other gauge topological terms come about just as in PQWW and KSVZ. Due to its unified approach to gaining fermion and gauge couplings, and other reasons which become evident later, DFSZ is often called the GUT axion theory (Dine et al., 1981; Zhitnitsky, 1980).

The behavior of axions during inflation, assuming they are a spectator and not a driver of the process, greatly influences the subsequent cosmological story of the axion field. In brief, if the PQ symmetry is unbroken during inflation, meaning that $f_a < T_I/2\pi$, then φ has a zero VEV and ϕ is randomly distributed over each Hubble patch when the PQ breaking scale is reached, resulting in a large average misalignment angle of $\left\langle \theta_{a,i}^2 \right\rangle = \pi^2/3$. If the PQ symmetry is broken during inflation, a different θ_{PQ} value is given to each Hubble patch. Each patch expands to encompass our current Hubble volume, providing a nearly uniform value of θ_{PQ} everywhere, making it a free parameter of the model. Each possibility has its quirks that must be dealt with.

As the universe cools past the f_a scale the φ temperature becomes unable to sustain configurations close to $\varphi = 0$, settling near the effective minima with VEV $\langle |\varphi| \rangle = f_a/\sqrt{2}$, Fig. 2.2. The VEV creates an anisotropy in the field's degrees of freedom, effectively separating them into the radial component $|\varphi|$ and the angular component ϕ. The radial degree of freedom gets a mass of order f_a, while our axion ϕ remains massless and periodic. The residual shift symmetry in ϕ maintains the Higgs-facilitated fermion interactions of the PQWW and DFSZ theories. The KSVZ interactions are also unimpeded. The ϕ bare Lagrangian becomes that of a free particle once $|\varphi|$ is frozen out

$$\mathscr{L}_{\phi} = \frac{1}{2} |\nabla \phi|^2 \tag{2.18}$$

Now we can discuss the nature of the PQ mechanism in more detail. The nature of the

anomalous contributions, instanton interactions, and the axion potential can be understood in a relatively model-independent way by starting with the PQ rotation

$$x_i \to e^{i\mathcal{Q}_{PQ,i}\phi/f_a} x_i \tag{2.19}$$

where x_i is a field and $\mathcal{Q}_{PQ,i}$ is the PQ charge of x_i. Much like the axial transformations that generate the CP problem, the nature PQ shifts are chiral, meaning that right and left handed components rotate with opposite charge. Again the expected topological contribution appears in the action

$$S \to S + \int d^4x \frac{C\phi}{32\pi^2 f_a} \mathrm{Tr} G_{\mu\nu}\tilde{G}^{\mu\nu} \tag{2.20}$$

where the constant of proportionality is given by the rotation's color anomaly

$$C\delta_{ab} = 2\mathrm{Tr}\mathcal{Q}_{PQ}\mathbf{T}_a\mathbf{T}_b \tag{2.21}$$

and the trace is over all the QCD-charged fermions in the theory and the $\mathbf{T}_a$ are the generators $SU(3)$ in operator notation. Now we can absorb the contributions to θ_{QCD} into ϕ, consolidating the CP-violating terms.

The anomalous contribution is labeled topological as $\mathrm{Tr}G_{\mu\nu}\tilde{G}^{\mu\nu}$ can be written as a boundary term of the action, held to not influence the classical equations of motion. Instead, the form is found to be related to the winding number parameterizing the non-trivial homotopy group between the QCD gauge group SU(3) and the space-time boundary. This group is often evaluated on a flat Euclidean space-time and found to be discrete, meaning the winding number takes on discrete values that may may differ between configurations related by a pure gauge transformation (Gross et al., 1981; Srednicki, 1985; Kim, 1987; Olive et al., 2014). We call these equivalence classes of pure gauge configurations the QCD vacua. The vacuum structure effects are determined by the theory's instantons, solutions to the classical equations of motion with non-extremized action. Without an energy differentiator there are no known means by which a specific vacuum configuration is chosen. Within a vacuum there is an effective potential of θ_{QCD} from the sum of all instanton contributions (Callan et al.,

1978; Gross et al., 1981; Coleman, 1988)

$$E_{vacua} \propto \cos\left(\theta_{QCD}\right) \tag{2.22}$$

The additional contribution from the Peccei-Quinn transform, or in our case $C\phi/f_a$, comes to be

$$E_{vacua} \propto \cos\left(\frac{C\phi}{f_a}\right) \tag{2.23}$$

The axial transformation is periodic under shifts of $\phi/f_a \rightarrow \phi/f_a + 2\pi$. This periodicity constrains the color anomaly to be the integer N_{DW}, which indicates the number of vacua or walls separating vacuum domains contained in a complete axial rotation (Srednicki, 1985). The potential energy from Eqn. 2.23 drives the pseudo-particle ϕ to one of the vacua minima, zeroing the topological contribution. This is the Peccei-Quinn mechanism.

Continuing to cool past the EW scale, both the Higgs and the PQWW axion pass symmetry breaking, picking up their VEVs of $\sim$ 125 GeV (observed (Aad et al., 2012)) and $f_a/\sqrt{2} \approx 180$ GeV respectively. Such a placement constrains the PQWW axion-quark interaction to $\mathrm{O}(10^{-2} - 10^{-4}\ \mathrm{GeV}^{-1})$. Such a highly interacting axion is observable in a multitude of beam-dump and accelerator experiments, and from impacts on astrophysical systems such as white dwarf stars. No such interactions have been observed, ruling out this flavor of axion (Mimasu & Sanz, 2015). Any viable axion theories must be relatively invisible to avoid detection, which the KSVZ and DFSZ models are constructed to be.

The next thermal milestone occurs when the QCD scale is approached at energies of $\Lambda_{QCD} \approx 270$ MeV. Starting at a temperature of $T \approx 1$ GeV, a phase transition occurs, which transforms the hot quark-gluon plasma into confined condensates, such as pions and then nucleons. The interactions between the axion and quarks is

$$\begin{aligned}
\mathscr{L}_\phi \supset\ & m_u \left(\cos\left(N_{DW}\phi/f_a\right)\bar{u}u + i\sin\left(N_{DW}\phi/f_a\right)\bar{u}\gamma^5 u\right) \\
& + m_d \left(\cos\left(N_{DW}\phi/f_a\right)\bar{d}d + i\sin\left(N_{DW}\phi/f_a\right)\bar{d}\gamma^5 d\right) \\
& = \cos\left(N_{DW}\phi/f_a\right)\mu\left(\bar{u}u + \bar{d}d\right) + i\sin\left(N_{DW}\phi/f_a\right)m_o\left(\bar{u}\gamma^5 u + \bar{d}\gamma^5 d\right)
\end{aligned} \tag{2.24}$$

where μ is the reduced mass. The value of these interactions are relatively unhinged prior to the transition due to a near matter-anti-matter symmetry, then converge on the condensate $\langle \bar{q}q \rangle$, giving a renormalized mass to the axion

$$m_a^2 = \frac{m_\pi^2 f_\pi^2 N_{DW}^2}{f_a^2} \frac{m_u m_d}{m_u + m_d} \left\{ 1 + \frac{m_\pi^2}{m_{\eta'}^2} \left[-1 + O\left(1 - \frac{m_\pi}{m_{\eta'}} \right) \right] \right\} \tag{2.25}$$

where $m_\pi = \sqrt{\langle \bar{q}q \rangle (m_u + m_d)}/f_\pi$ is the pion mass, f_π is the pion decay constant, and $m_{\eta'}$ is the η' mass. Note that the mass term breaks ϕ's shift symmetry, centering the axial anomaly about $\langle \phi \rangle = 0$, removing strong CP violation in the static limit. Further presentations such as that by Vafa and Witten add confidence to the result can only be centered about the zero violation phase (Vafa & Witten, 1984).

Now the axion is only symmetric about a discrete subset of shifts ($\phi \rightarrow \phi + 2\pi f_a / N_{DW}$), making it a pseudo Nambu-Goldstone boson. Including the renormalization contribution, the axion potential as generated by QCD come to

$$V(\phi) = m_u \Lambda_{QCD}^4 \left[1 - \cos\left(\frac{N_{DW}\phi}{f_a} \right) \right] \tag{2.26}$$

It is worth noting that the other SM non-Abelian gauge theory, $SU(2)$, also contributes to the axion potential via non-perturbative means, though we will not discuss the specifics here. Otherwise, the axion is protected from quantum-correction shifts in mass due to the remaining shift symmetry. Expanding about a minima, the effective axion potential can be written to lowest order as a mass term

$$V(\phi) \approx \frac{1}{2} m_a^2 \phi^2, \tag{2.27}$$

where the mass m_a contains the symmetry breaking scale f_a and other models specific parameters.

2.3 Axion Interactions with Cosmology

Moving back to times about the f_a breaking scale, there are several critical points in the early universe that impact the state of φ, ϕ, and subsequently DM production. The first point

centers on inflation, the assumed period in the early universe where the cosmos expands rapidly, much faster than the equilibration time of components in contact with the SM. This rapid expansion has the effect of dilating the state of all material components via Hubble drag. Once slower expansion resumes, the universe is given the appearance of thermal equilibration over regions without causal contact.

The state of axions during inflation greatly influences the subsequent cosmological story of the axion field. In brief, if the PQ symmetry is unbroken during inflation, meaning that $f_a < T_I/2\pi$, then φ has a zero VEV and ϕ is randomly distributed over each Hubble patch when the breaking scale is reached, resulting in the large average misalignment angle $\left\langle \theta_{a,i}^2 \right\rangle = \pi^2/3$. If the PQ symmetry is broken during inflation, θ_{PQ} varies on scales above the Hubble volume. This effectively makes θ_{PQ} uniform in the visible universe and a free parameter of the model.

There are issues to be addressed with each inflation possibility. The randomness of θ_{PQ} in the pre-PQ breaking case gives rise to topological defects and seeds other structures that may prove difficult for haloscope experiments (Kolb & Tkachev, 1993; Tinyakov et al., 2016; Fairbairn et al., 2017). Post-PQ breaking inflation, which produces relatively lighter axions, introduces a degree of anthropic reasoning to the state of the visible universe. A narrow range of misalignment angles are allowed to reproduce the observed DM density, severely constraining an otherwise free parameter. Further, the preponderance of evidence for a flat universe and other points of cosmological instability, which depend strongly on the DM density, makes the claim of a random axion phase appear dubious. The second critical point occurs when the post-symmetry-breaking post-inflation misalignment angles leave the freeze-out state. There are several popular models for producing cosmological axions, including decays from parent particles, topological defect decays, thermal populations, and vacuum realignment. We restrict ourselves to the realignment mechanism at this point. The evolution equation for the homogeneous, isotropic, mean-field background axion density in

an Freedmann-Robertson-Walker (FRW) cosmology is

$$\ddot{\phi} + 3H\dot{\phi} - \frac{\delta V(\phi)}{\delta \phi^*} = 0, \tag{2.28}$$

which reduces in the small deflection limit ($|\phi| \ll 1$) to

$$\ddot{\phi} + 3H\dot{\phi} + m_a^2\phi = 0 \tag{2.29}$$

where $H = \dot{a}/a$, and a is the FRW scale factor. Details of general relativity theory and the FRW cosmology are deferred to Chapter 3. The associated background energy density and pressure, from which we can find the axion equation of state ($P_a = \omega_a \rho_a$), are

$$\bar{\rho}_a = \left\langle T^{00} \right\rangle = \frac{1}{2}\left|\dot{\phi}\right|^2 + \frac{1}{2}m_a^2\left|\phi\right|^2 \tag{2.30}$$

$$\bar{P}_a = \left\langle T^{00} \right\rangle = \frac{1}{2}\left|\dot{\phi}\right|^2 - \frac{1}{2}m_a^2\left|\phi\right|^2 \tag{2.31}$$

$$\tag{2.32}$$

The scale factor $a(t)$ runs like a power law during the radiation and matter dominated epochs, $a \propto t^p$, giving ϕ a closed-form exact solution so long as the axion mass changes slowly with respect to the expansion rate $\delta m_a << H$,

$$\phi = a^{-3/2}\left(t/t_i\right)^{1/2}\left(C_1 J_n(m_a t) + C_2 Y_n(m_a t)\right) \tag{2.33}$$

where $n = (3p-1)/2$, C_1 and C_2 are set by initial conditions, and J_n, Y_n are Bessel function of the first and second kind. These solutions are oscillating so long as the mass-time argument continues to grow with time or otherwise changes its value appreciably during the considered period

$$m_a t \neq Const. \tag{2.34}$$

For our purposes, we are satisfied with a growing argument. Note that, prior to the QCD phase transition, ϕ's scaling rate is notably slower than the expected a^{-3} of conserved matter.

Close to the QCD phase transition ($T \sim$ few Λ_{QCD}), the axion begins to acquire its mass, which accumulates until well below $100MeV$. At this point ϕ ceases to be pulled

wholly by Hubble drag and becomes dominated by its mass and topological state. The creation mechanism for these axions depend on whether or not the PQ symmetry breaking occurred before or after inflation. It can be shown that if breaking occurred before ($T_I/2\pi < f_a$), the near homogeneity of the axion field within our horizon causes vacuum realignment (misalignment) to be the primary means of production. If breaking occurred after inflation ($T_I/2\pi > f_a$), the processes of vacuum realignment, axion string decay, and domain wall decay are the primary creation mechanisms.

The relic axion density from misalignment is roughly determined by ϕ's solution once the axion has acquired mass. There is a power-law dependence on the mass at high temperatures, $T \gtrsim 1GeV$,

$$m_a = \alpha_a \frac{\lambda_{QCD}^3 m_u}{f_a^2} \left(\frac{T}{\Lambda_{QCD}} \right)^{-n} \tag{2.35}$$

$$n \sim 4 - 10$$

$$\alpha_a \sim 1.7 \times 10^{-7} \tag{2.36}$$

can be found from calculations of transitioning QCD systems by (Gross et al., 1981).

The radiation temperature of the universe in the radiation-dominated epoch is determined from the first Friedmann equation, producing

$$3H^2 M_{pl}^2 = \frac{\pi^2}{30} g_* T^4 \tag{2.37}$$

where the degrees of freedom are taken to be $g_* = 61.75$ during this period. Substituting the derived values for H and m_a, the axion field ϕ is considered to be oscillating once the solution progresses in phase an appreciable amount

$$t_1 m_a(t_1) = 1 \tag{2.38}$$

where t_1 is the time of the transition start. The temperature at which this is satisfied can be found to be

$$T_1 \sim 1GeV \left(\frac{10^{12} GeV}{f_a} \right)^{1/6} \tag{2.39}$$

if $n = 10$. After this point, the axion is described by an energy density $\bar{\rho}_a$ that can be seen to run as a^{-3} once $m_a \gg H$

$$\bar{\rho}_a \propto a^{-3} \left(t/t_i\right) \left(C_1 J_n(m_a(T)t) + C_2 Y_n(m_a(T)t)\right)^2 \tag{2.40}$$

which asymptotes to

$$\bar{\rho}_a \propto a^{-3} \cos^2 \left(m_a(T)t + \varphi\right) \tag{2.41}$$

Therefore, the axions are behaving as DM. Also note that the oscillating part causes the equation of state to oscillate about $\omega = 0$, making the average equation of state equivalent to CDM on time scales long compared to the axion mass, Fig. 2.3.

The axion relic density may be calculated via the misalignment angle at the start of oscillation, $\theta_{a,i}$,

$$\Omega_a \sim 0.3X \left(\frac{f_a}{10^12 GeV}\right)^{7/6} \left\langle \theta_{a,i}^2 \right\rangle \tag{2.42}$$

where X is a model dependent parameter of value $O(1)$ included to account for other production mechanisms such as domain wall and string decay. This form assumes small initial misalignment, with large angle solutions requiring the inclusion of self-interactions.

Now that we have an idea about the scale at which axions begin behaving as DM, let us calculate a few quantities to help us place them into context as a system of particles. The number density is set at the oscillation time to be

$$n(t_1) = X \left\langle \theta_{a,i}^2 \right\rangle \frac{f_a^2}{t_1} \tag{2.43}$$

and at later times

$$n(t) \sim \frac{4 \times 10^{47}}{cm^3} X \left(\frac{f_a}{10^{12} GeV}\right)^{5/3} \left(\frac{a(t_1)}{a(t)}\right)^3 \tag{2.44}$$

where again t_1 is the time of phase transition.

The misalignment process is a very clean one and axions are very homogeneous at this time, restricting the scale of spatial oscillation to be of order horizon size or larger if few or no DWs are present. An estimate for the momentum dispersion can be formed from the spatial oscillation limit

$$\delta p(t_1) \sim \frac{1}{t_1} \tag{2.45}$$

making the velocity dispersion estimate

$$\delta v(t_1) \sim \frac{1}{m_a(t_1)t_1} \tag{2.46}$$

Given no interactions, the dispersion will evolve as

$$\delta v(t) \sim \frac{1}{m_a(t_1)t_1}\left(\frac{a(t_1)}{a(t)}\right) \tag{2.47}$$

Assuming a proportionality of $O(1)$ the modern dispersion would be of order

$$\delta v(t) \sim 10^{-12}\left(\frac{f_a}{10^{12}GeV}\right)^{5/6} \tag{2.48}$$

though some report a figure closer to $\sim 10^{-17}$ (Erken et al., 2012). The average occupation number can also be found (scale factor independent)

$$\mathcal{N} \sim \frac{n(2\pi)^3}{4\pi/3(m\delta v)^3} \sim 10^{61}X\left(\frac{f_a}{10^{12}GeV}\right)^{8/3} \tag{2.49}$$

as well as the critical temperature for BEC formation

$$T_c(t) = \left(\frac{\pi^2 n(t)}{\xi(3)}\right) \sim 300 \text{ GeV } X^{1/3}\left(\frac{f_a}{10^{12}GeV}\right)^{5/9}\left(\frac{a(t_1)}{a(t)}\right) \tag{2.50}$$

which is far higher than the axion mass. These figures tell us that the axions are very cold and degenerate, qualities that will become relevant when talking about BEC formation and possible corrections to the DM structures.

2.4 Early Axion Structures

Structure in the axion distribution has been more or less ignored to this point. Even though this chapter concerns itself with axions in the first epoch, the seed of today's astrophysical objects are bred from pre-inflation physics and evolve in conjunction with the structure of other components, mostly radiation. These small fluctuations in an otherwise homogeneous isotropic universe aren't allowed to grow significantly during radiation domination due to pressure suspension among the radiative components. In the remainder of this chapter we

briefly study the state of axion structures from the eye of cosmological perturbation theory to the point of setting conditions for the more intense non-linear structure formation to come in the matter-dominated epoch.

Working in the Newtonian gauge and the sub-horizon limit, perturbations in the axion field density evolve to linear order in magnitude ($|\delta\phi|\ |\phi| \ll 1$) under the coupled system

$$\partial_t^2 \delta\phi + 2H\partial_t \delta\phi + \left(-a^{-2}\vec{\nabla}^2 + m_a^2\right)\delta\phi + 2m_a^2 \Phi\phi = 0 \tag{2.51}$$

$$\vec{\nabla}^2 \Phi = 4\pi G \delta\rho \tag{2.52}$$

where Φ is the Newtonian gravitational potential, G is the universal gravitational constant, and $\delta\rho$ is the perturbation in energy density. In Fourier space the system becomes

$$\partial_t^2 \delta\phi_k + 3H\partial_t \delta\phi_k + \left(a^{-2}k^2 + m_a^2\right)\delta\phi_k + 2m_a^2 \Phi_k \phi_0 = 0 \tag{2.53}$$

$$k^2 \Phi_k = -4\pi G \delta\rho_k \tag{2.54}$$

In general, evolving the perturbations in the axion field requires knowledge of the other species involved. Radiation dominates so completely in the first epoch that axion DM traces the radiation structures. Radiation gravitational collapse does occur, though only at super-horizon scales at early times (Thompson, 2008), implying that axion isocurvature perturbations do not grow within the horizon during the radiation-dominated epoch. The super-horizon density fluctuations do grow due to lack of pressure support (Binney & Tremaine, 2008)

$$\delta \propto t \tag{2.55}$$

Primordial perturbations may be propagated through much of the first epoch using raidiation's gravitational stability. If all cosmological perturbations are seeded by single-field inflation, the initial conditions are an adiabatic invariant, meaning the power spectrum is the same before and after inflation. The adiabatic condition allows for a relation between the photon and any other massive fluid component

$$\delta_i = \frac{3}{4}\left(1 + \omega_i\right)\delta_\gamma \tag{2.56}$$

where δ is the dimensionless quotient of the fluctuation energy over the average species energy. At early times, long before the QCD phase transition, the axion field had an equation of state with $\omega_a \approx -1$, indicating that $\delta_a = 0$. The axion field rolls about the $\omega = 0$ state after the phase transition and the acquisition of mass, oscillating near the mass frequency. Axions then begin to fall into the gravity potential wells set up by the photons and eventually satisfy the relation $\delta_{CDM} = 3/4\delta_\gamma$. The cosmological perturbations in the photon spectra are taken to have a random normal power spectra, which is often the starting point for late-time structure formation studies, once properly modulated by horizon level conditions (Binney & Tremaine, 2008).

To gain a rough understanding of structure formation soon after the radiation-matter transition, consider the simplified case of an axion DM-dominated universe. The density in Eqn. 2.54 then becomes the axion density. Substituting the gravitational potential equation into the evolution equation, we find the closed equation

$$\partial_t^2 \delta\phi_k + 3H\partial_t \delta\phi_k + \left(a^{-2}k^2 + m_a^2\right)\delta\phi_k - 2m_a^2\left(4\pi G\delta\rho_{a,k}k^{-2}\right)\phi_0 = 0 \tag{2.57}$$

where we recall that to first order

$$\delta\rho_{a,k} = \frac{1}{2}\left(\phi_0^*\phi_k + \phi_k^*\phi_0\right) \tag{2.58}$$

The solutions to this oscillator equation exhibit two behaviors: equilibrium oscillations and exponential growth/decay. On the smallest scales, the pressure/dispersive terms dominate over gravity and true oscillations occur. On the largest scales, $k^2 \to 0$, the DM has a Jeans Instability (JI) and perturbations grow. The wave-number at which the transition occurs

$$k_J = a\left(6\Omega_a\right)^{1/4}\sqrt{Hm_a} \tag{2.59}$$

is called the Jeans wave-number, implying that axion DM has scale-dependent growth within the horizon, i.e. it has a non-trivial Jeans length ($l_J = 2\pi/k_J$). This is in contrast to CDM, which collapses at all scales. Unfortunately, this length is on the order of an Astronomical Unit (AU), not a promising sign for observing unique galactic structures.

Such a prescription of early DM structures has corrections from horizon physics. In the case of pre-PQ breaking inflation there are regions on the inflation horizon scale which contain local misalignment angle variations that are not small ($\sigma_{\theta^2_{a,i},horizon}/\left\langle\theta^2_{a,i}\right\rangle_{horizon}$). Nonlinear structure formation processes are posited to take hold here once mass is acquired (Kolb & Tkachev, 1993). The behavior of these mini-clusters through the first epoch and the violent collapse into galactic halos in the second is still a topic of study (Sikivie, 2008; Marsh, 2016; Enander et al., 2017). Equilibration with radiative components and continued collapse, even to the point of axion evaporative cooling channels and the formation of compact Bose stars, are particular points of interest. Modern mini-clusters may contain the mass of a cosmologically-averaged $\sim 10(m_a/10^{-3}$ eV) parsec sphere in an kilometer-sized object, condensing DM into effective super-particles. These compact objects would have mean separation of $\sim 0.1(m_a/10^{-3}$ eV) parsec in our solar neighborhood. Mini-clusters are not considered further in this work, but it is worth noting that they would provide an immense hurdle for direct detection experiments designed to observe a constant flow of diffuse axions (Tinyakov et al., 2016; Fairbairn et al., 2017).

2.5 The Radiation-Matter Transition

As the photon energy diminished into the background, matter is left to its own devices. The transition occurs at $T \approx 1$ eV or $z \approx 3000$, about a hundred thousand years after the Big Bang. Relic axions are already cold and dark at this time. In the absence of other forces, DM axions are overtaken by gravitational forces and begin their descent toward halo formation.The SM precipitates are nuclei, electrons, and neutrinos, with all but the neutrinos staying in thermal equilibrium with radiation until the surface of last scattering, $z \approx 1000$. The still-thermalized SM components transition from tracing the photon power spectra and react to the newly-dominant DM spectra. The combination of unstable DM gravitational forces and the pressure response from the 'atomic plasma' oppose each other

with the respective forces

$$\vec{f}_{gravity} = -\vec{\nabla}\Phi \approx -\vec{\nabla}\Phi_D M \tag{2.60}$$

$$\vec{f}_{EOS} = \vec{\nabla}p \tag{2.61}$$

where the plasma pressure p depends on the fluid's Equation Of State (EOS), but is often taken to be that of an adiabatic ideal gas $p = \rho^\gamma$, where $\gamma = 5/3$ is the adiabatic index. These contracting and restorative forces create oscillations in the linear regime about DM over-densities. At the surface of last scattering these Baryonic Acoustic Oscillations (BAO) continue to accumulate, and consequently are on display in the CMB (Dawson et al., 2013). The freeing of baryonic and DM components to move under their mutual gravity marks the beginning of major structure formation.

In the next chapter we continue into the matter-dominated epoch. Here the DM and baryonic components are able to evolve independently of radiation. Thus far we have rested on the assumption that perturbations in density and gravitational potential are small, and that a mean field prescription is sufficient for axion dynamics in the presence of overwhelming radiation; this is not the case in the late universe. Exponential collapse occurs at all astronomical scales for the QCD axion, requiring a non-linear prescription of structure formation capable of capturing the dynamic stages of halo and galaxy formation. The high dynamic range of halo structures also calls into question the adequacy of mean field theory to describe the highly-degenerate axion Bose fluid. We discuss both these topics in great detail.

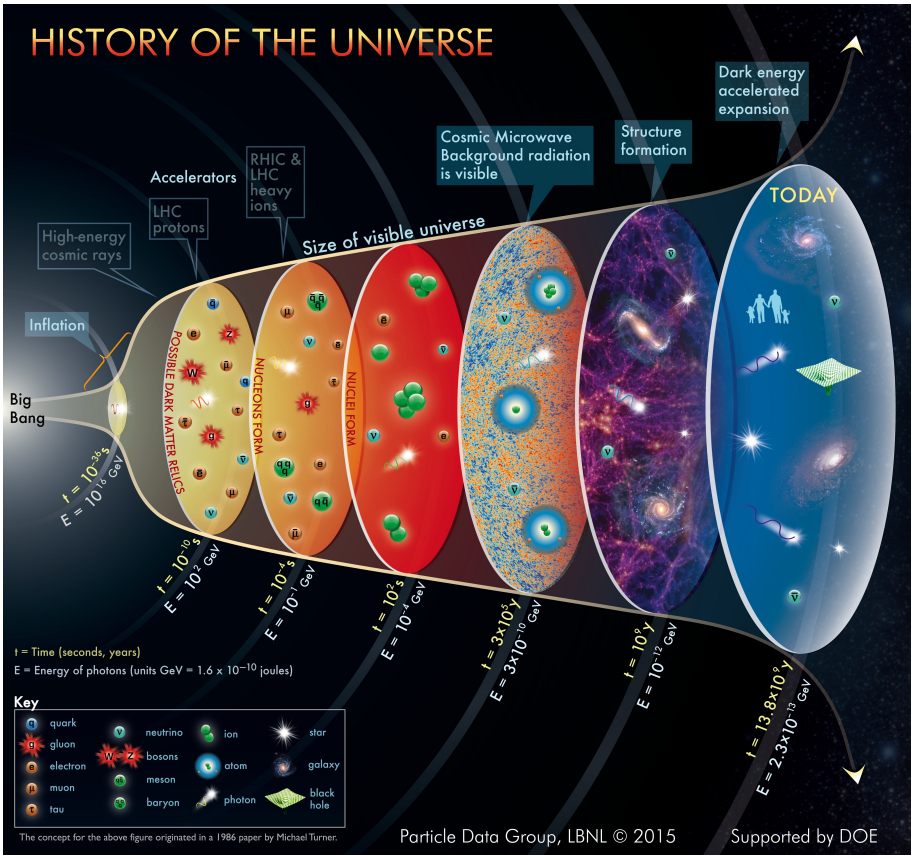

Figure 2.1: The history of the universe with points of particle and cosmological significance (Patrignani & Particle Data Group, 2016). The contents of Chapter 2 refer principally to the first epoch, when radiation dominated the energy density; this occurs before the CMB. Chapter 3 concerns the later two epochs when matter and then DE dominate.

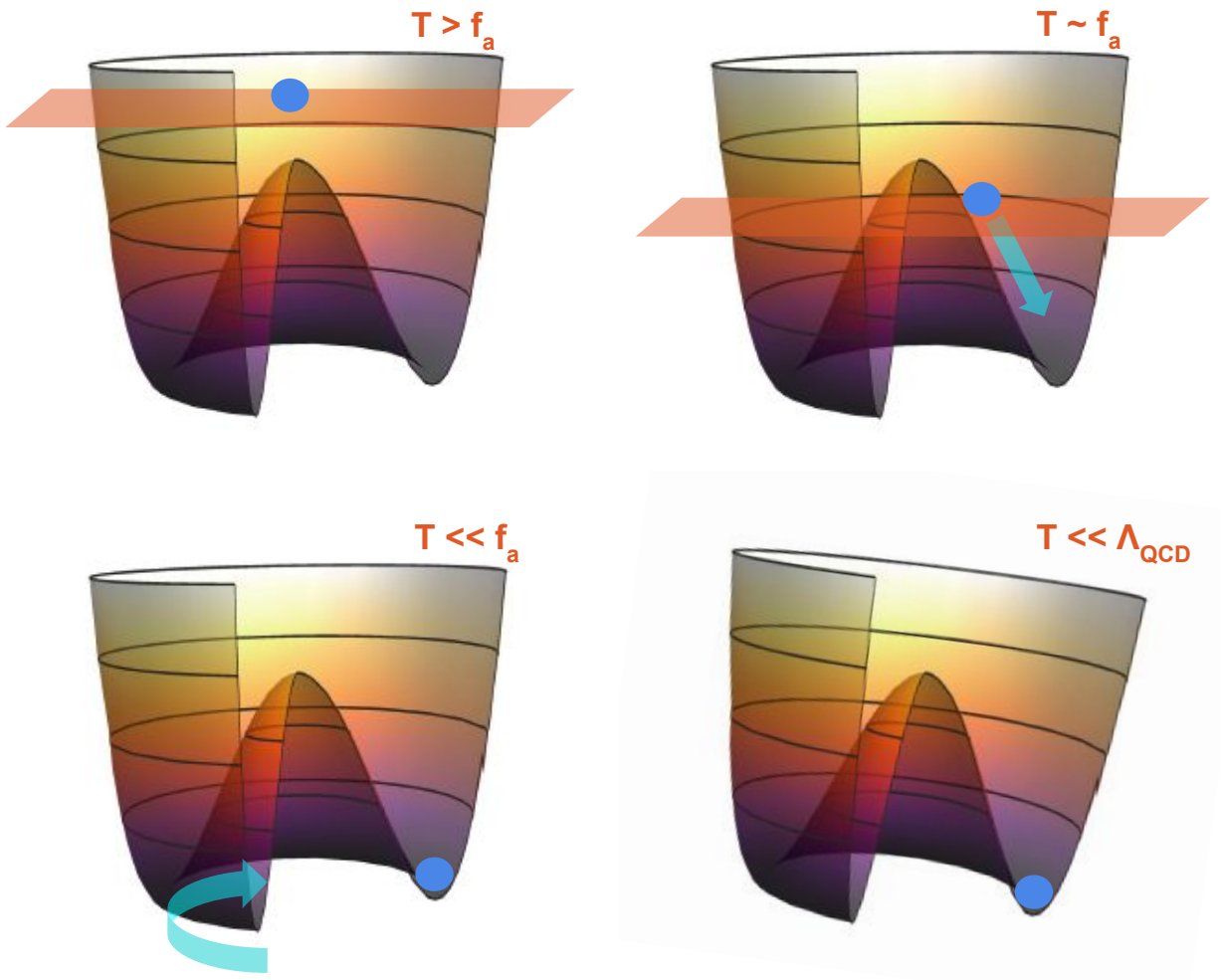

Figure 2.2: The SSB potential assumed of the Higgs, also often the axion (Marsh, 2016). Temperatures are high above the breaking scale at early cosmological times, high enough to support a $< \varphi >= 0$ configuration (upper left). After cooling to below f_a (upper right), φ acquires a non-0 expectation and retains its angular symmetry well past the breaking scale (lower left). The axial symmetry is broken after passing the QCD phase transition at λ_{QCD}, when the quark-axion interactions condense (lower right).

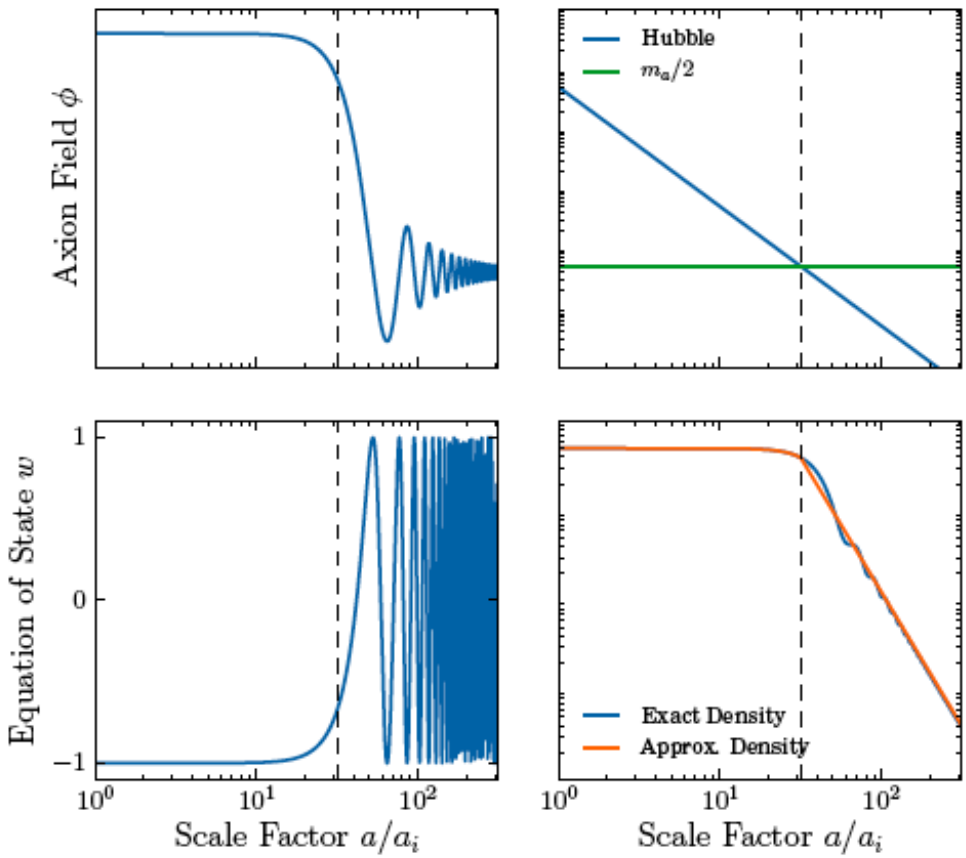

Figure 2.3: Aspects of cosmological axion evolution about the acquisition of mass. Figure from Marsh (2016). Evolution of the axion field is given in the upper right. Relative dynamical strengths are shown in the upper left figure. The equation of state is shown in the lower left figure. Axion density is shown in the lower right figure. The dashed line indicates the point of transition. Axion evolution undergoes a substantial change over the QCD phase transition. Oscillation of the axion field about a potential minima gives an average strong CP violation of 0. The acquisition of mass changes the equation of state and other characteristics of the axion fluid drastically, even in the mean field theory approximation.

Chapter 3

AXIONS IN THE LATE UNIVERSE

This chapter continues the axions' journey into the matter and DE-dominated epochs. Moving largely under its own dynamics, the problem of salient physics for full axion structure formation can no longer be avoided. This chapter begins with cosmology and structure-formation background relevant to this chapter and the previous. Complexity in the axion equations of motion bring about tension in how best to capture the essential physics of axion infall. This chapter also elaborates upon the stances responsible for the current gridlock in the literature. We then construct a novel solution to axion structure formation, as part of an ambitious research program to resolve the USP. The research program has already revealed new features of halo structure and spectra, which are of great utility to current axion DM searches.

3.1 Late-Time Cosmology and Structure Formation Background

To describe axion DM in the era of structure formation we represent the axion as a quantum scalar field (ϕ) defined over a dynamic 3+1 pseudo-Reimannian manifold.

3.1.1 Geometry

The manifold's structure is governed by Einstein's equations

$$R_{\mu\nu} - \frac{1}{2}Rg_{\mu\nu} - \Lambda g_{\mu\nu} = \frac{8\pi G}{c^4}\left\langle T_{\mu\nu}\right\rangle \tag{3.1}$$

where R gives the Ricci curvature, $\langle T\rangle$ is the macroscopic stress-energy, g is the metric, G is Newton's gravity constant, and c is the speed of light. This context is often refined by assuming on the largest scales that the stress-energy is nearly homogeneous and isotropic

and critically dense, which allows the space to evolve under a flat FRW cosmology with small perturbations

$$g = g_{FRW}\,(I + Q) \tag{3.2}$$

An effective linearization ove rQ must be found in order to understand the effective equations governing both space-time and the axion.

In order to emulate the derivation of linearized Einstein's equations, we choose a coordinate system composed of conformal time and space (see Wald (1984) and Weinberg (1972) for a review, including the physical time case). The metric then takes the form

$$g = a(\tau)^2\,(\eta + h)\,. \tag{3.3}$$

and the inverse metric is written as

$$g^{-1} = a(\tau)^{-2}\left(\eta^{-1} + \delta\right). \tag{3.4}$$

The inverse perturbation is then found to be

$$\delta = -h^{-1} + O(h^2), \tag{3.5}$$

where

$$h^{-1} \equiv \eta^{-1} h \eta^{-1}. \tag{3.6}$$

The Christoffel symbol Γ can be expanded likewise

$$\Gamma^{\mu}_{\alpha\beta} = \Gamma^{(0)\,\mu}_{\alpha\beta} + \Gamma^{(1)\,\mu}_{\alpha\beta} + O(h^2) \tag{3.7}$$

$$\begin{aligned} &= H\left(\eta^{-1}\right)^{\mu\nu}\left(-\delta^0_\nu \eta_{\alpha\beta} + \delta^0_\alpha \eta_{\nu\beta} + \delta^0_\beta \eta_{\alpha\nu}\right) \\ &- H\left(\eta^{-1}\right)^{\mu\nu}\left(-h_{\nu\gamma}\left(\eta^{-1}\right)^{\gamma 0}\eta_{\alpha\beta} + \delta^0_\alpha h_{\nu\beta} + \delta^0_\beta h_{\alpha\nu}\right) \\ &+ \frac{1}{2}\left(\eta^{-1}\right)^{\mu\nu}\left(-\partial_\nu h_{\alpha\beta} + \partial_\alpha h_{\nu\beta} + \partial_\beta h_{\alpha\nu}\right) + O(h^2) \end{aligned} \tag{3.8}$$

where $H = \partial_0 a/a$.

Calculating the Ricci tensor is the next step in finding the geometry's governing equations.

$$R_{\mu\rho} = \partial_\nu \Gamma^{\nu}_{\mu\rho} - \partial_\mu \Gamma^{\nu}_{\nu\rho} + \Gamma^{\alpha}_{\mu\rho}\Gamma^{\nu}_{\alpha\mu} - \Gamma^{\alpha}_{\nu\rho}\Gamma^{\nu}_{\alpha\nu} \tag{3.9}$$

The expansion of the Ricci tensor shows multiple terms at each order in h

$$R_{\mu\rho} = R^{(0)}_{\mu\rho} + R^{(1)}_{\mu\rho} + O(h^2) \tag{3.10}$$

$$\begin{aligned} &= \partial_\nu \Gamma^{(0)\nu}_{\mu\rho} - \partial_\mu \Gamma^{(0)\nu}_{\nu\rho} + \Gamma^{(0)\alpha}_{\mu\rho}\Gamma^{(0)\nu}_{\alpha\nu} - \Gamma^{(0)\alpha}_{\nu\rho}\Gamma^{(0)\nu}_{\alpha\mu} \\ &+ \partial_\nu \Gamma^{(1)\nu}_{\mu\rho} - \partial_\mu \Gamma^{(1)\nu}_{\nu\rho} + \Gamma^{(0)\alpha}_{\mu\rho}\Gamma^{(1)\nu}_{\alpha\nu} - \Gamma^{(0)\alpha}_{\nu\rho}\Gamma^{(1)\nu}_{\alpha\mu} \\ &+ \Gamma^{(1)\alpha}_{\mu\rho}\Gamma^{(0)\nu}_{\alpha\nu} - \Gamma^{(1)\alpha}_{\nu\rho}\Gamma^{(0)\nu}_{\alpha\mu} + O(h^2) \end{aligned} \tag{3.11}$$

The lowest order of the tensor coincides with the FRW form, as expected.

$$R^{(0)}_{\mu\rho} = \left(\eta^{-1}\right)^{00} \eta_{\mu\rho} \left(\partial_0 H - 2H^2\right) + \delta^0_\rho \delta^0_\mu \left(-\partial_0 H + 5H^2\right) \tag{3.12}$$

The first order term is a bit more complex to calculate, specifically the two Christoffel commutators. To combat this, we rewrite the perturbation in the form of a subset of terms coming from the Christoffel derivatives (C) plus the remainder (D)

$$R^{(1)}_{\mu\rho} = C_{\mu\rho} + D_{\mu\rho} \tag{3.13}$$

where

$$C_{\mu\rho} = \frac{1}{2}\left(\eta^{-1}\right)^{\nu\gamma} \partial \left(\partial_\rho h_{\mu\gamma} + \partial_\mu h_{\rho\gamma}\right) - \frac{1}{2}\Box h_{\mu\rho} - \frac{1}{2}\partial_\rho \partial_\mu h \tag{3.14}$$

where the introduced terms

$$\Box = \left(\eta^{-1}\right)^{\mu\nu} \partial_\mu \partial_\nu \tag{3.15}$$

$$h = \left(\eta^{-1}\right)^{\mu\nu} h_{\mu\nu}. \tag{3.16}$$

The elements of D can be expressed as a sum of perturbation-dependant terms spanned by $B = \{h, h^{00}, h^0_{()}, h_{()()}, \partial^\gamma h_{\gamma()}, \partial^0 h_{()()}\}$.

The trace term of the Einstein tensor is likewise expanded

$$-\frac{1}{2} g_{\mu\rho} R = -\frac{1}{2}\eta_{\mu\rho} R^{(0)} - \frac{1}{2}\eta_{\mu\rho} R^{(1)} - \frac{1}{2} h_{\mu\rho} R^{(0)} + O(h^2) \tag{3.17}$$

where

$$R^{(0)} = a^{-2}\left(\eta^{-1}\right)^{\alpha\beta} R^{(0)}_{\alpha\beta}, \tag{3.18}$$

$$R^{(1)} = a^{-2}\left(\eta^{-1}\right)^{\alpha\beta} R^{(1)}_{\alpha\beta} - a^{-2} h_{\mu\nu}\left(\eta^{-1}\right)^{\alpha\mu}\left(\eta^{-1}\right)^{\nu\beta} R^{(0)}_{\alpha\beta} \tag{3.19}$$

The first order term is partitioned similarly to the Ricci tensor, with the trace of the C term being separated from the remainder. With all the pieces collected, we may start to construct Einstein's equations.

Expanding the stress-energy about the homogeneous, isotropic conditions of FRW, Einstein's equations may be expressed as

$$G^{(0)}_{\mu\rho} + G^{(1)}_{\mu\rho} + O(h^2) = \frac{8\pi G}{c^4}\left(T^{(0)}_{\mu\rho} + T^{(1)}_{\mu\rho}\right) + O(h^2, A^2, hA) \tag{3.20}$$

where A parameterizes the breaking of the FRW conditions. Matching orders over the equals sign, the lowest order Einstein equation

$$-\left(\eta^{-1}\right)^{00}\eta_{\mu\rho}\left(\partial_0 H - H^2\right) - \frac{1}{2}\eta_{\mu\rho}\left(-\partial_0 H + 5H^2\right) + \delta^0_\rho\delta^0_\mu\left(-\partial_0 H + 5H^2\right) = \frac{8\pi G}{c^4}T^{(0)}_{\mu\rho} \tag{3.21}$$

gives the conformal time flat Friedmann equations

$$-3\partial_0 H + 11H^2 = \frac{16\pi G}{c^4}T^{(0)}_{00} \tag{3.22}$$

$$3\partial_0 H - 9H^2 = \frac{16\pi G}{c^4}T^{(0)}_{**} \tag{3.23}$$

where the $*$ indicates some spatial direction.

The first order Einstein tensor requires more simplification. Keeping with the linearized gravity convention, we introduce the quantity

$$\bar{h}_{\mu\nu} = \eta_{\mu\rho}\left(h_{\mu\nu} - \frac{1}{2}\eta_{\mu\nu}h\right) \tag{3.24}$$

Implementing this consolidation into the first order Einstein tensor, the form can reduce to

$$G^{(1)}_{\mu\rho} = -\frac{1}{2}\Box\bar{h}_{\mu\rho} - \frac{1}{2}\eta_{\mu\rho}\partial^\alpha\partial^\beta\bar{h}_{\alpha\beta} + \left(\eta^{-1}\right)^{\nu\gamma}\partial_\nu\partial_{(\rho}\bar{h}_{\mu)\gamma} + a^2h\left(\eta^{-1}\right)^{00} + D'_{\mu\rho}(B) \tag{3.25}$$

where D' is the remainder term, similar to Eqn. 3.13, and linear in its dependance on perturbations.

We can exploit the theory's diffeomorphism invariance in a calculated way to place these equations in a still more convenient form. Only an infinitesimal diffeomorphism invariance can be guaranteed to relate equivalent physical configurations in a system linearized about

FRW. Such a diffeomorphism can be generated by a vector field ξ, implying that metrics separated by a Lie derivative $\mathcal{L}_\xi$ describe the same physical perturbation. Formulaically,

$$g \to g' = g + \mathcal{L}_\xi g \tag{3.26}$$

describe the same geometry. Therefore, in our scenario, the infinitesimal diffeomorphisms transforming the perturbations

$$\begin{aligned} h_{\alpha\beta} \to h'_{\alpha\beta} &= h_{\alpha\beta} + \partial_\alpha \xi_\beta + \partial_\beta \xi_\alpha + a^{-2}\xi(a^2)\eta_{\alpha\beta} h \\ &\to h' = h + a^{-2}\xi(a^2)\eta^\alpha_\alpha \bar{h}_{\alpha\beta} \\ &\to \bar{h}'_{\alpha\beta} = \bar{h}_{\alpha\beta} + \partial_\alpha \xi_\beta + \partial_\beta \xi_\alpha - a^{-2}\xi(a^2)\eta_{\alpha\beta} \end{aligned} \tag{3.27}$$

are equivalent descriptions. The point of this transform is to simplify $G^{(1)}_{\mu\rho}$ to a desirable form. Consider all terms in $G^{(1)}_{\mu\rho}$ without $h_{\mu\rho}$ index dependence

$$\begin{aligned} &K_{\mu\rho}(h, h^{00}, \partial^\gamma h_{\gamma\alpha}, h^0_\alpha, a, H, \partial_0 H) \\ &= G^{(1)}_{\mu\rho} - \left(-\frac{1}{2}\Box \bar{h}_{\mu\rho} + vH\partial^0 h_{\mu\rho} + x\partial^0 H h_{\mu\rho} + yH^2 h_{\mu\rho} \right) \end{aligned} \tag{3.28}$$

where $\{v, x, y\}$ are rational constants. To eliminate these terms from the Einstein tensor, perform an infinitesimal diffeomorphism via ξ and observe its influence.

$$\begin{aligned} &K_{\mu\rho}(h, h^{00}, \partial^\gamma h_{\gamma\alpha}, h^0_\alpha, a, H, \partial_0 H) \to F_{\mu\rho}(h, h^{00}, \partial^\gamma h_{\gamma\alpha}, h^0_\alpha, a, H, \partial_0 H, \xi, \partial\xi) \\ &= F_{1,\mu\rho}(a, H, \partial_0 H, \xi, \partial\xi) + K_{\mu\rho}(h, h^{00}, \partial^\gamma h_{\gamma\alpha}, h^0_\alpha, a, H, \partial_0 H) \end{aligned} \tag{3.29}$$

where the separation in the last expression is possible due to the linear dependence of K on the B. According to the theory of differential equations, for well-behaved F_1, there exists at least a local solution to $F_1 = 0$ for ξ, implying that there exists a gauge transform such that $K = 0$ in that region.

The governing equation for the perturbation can then be written, in appropriate coordinates, as

$$-\frac{1}{2}\Box \bar{h}_{\alpha\beta} + vH\partial^0 h_{\mu\rho} + x\partial^0 H h_{\mu\rho} + yH^2 h_{\mu\rho} = \frac{8\pi G}{c^4} T^{(1)}_{\alpha\beta}. \tag{3.30}$$

To fully specify the Newtonian limit, we suppose that locally, cosmically speaking, there is a 'global' inertial coordinate system and the stress-energy perturbation is dominated by energy density

$$T^{(1)}_{\alpha\beta} \approx \rho^{(1)} t_\alpha t_\beta \tag{3.31}$$

where t is a time-directed unit vector and $\rho^{(1)}$ is the fluctuation in energy density over the cosmological mean. The lack of time-space components to the stress energy imply that the velocities and time-changing properties in these coordinates are small, causing all but the time-time component and spatial dynamics of Eqn. 3.30 to be sub-leading. Converting to physical time and a Cartesian spatial frame, the remaining first order Einstein equation becomes

$$\Delta \bar{h}_{00} = -\frac{16\pi G}{ac^4}\rho^{(1)} \tag{3.32}$$

where $\Delta = \vec{\nabla}^2$ is the flat spatial Laplacian, and the remaining purely geometric terms cancel as the trace of the perturbation is reduced to the time-time component in this limit. Defining $\Phi = -1/4\bar{h}_{00}$, Poisson's equation for a gravitational potential is recovered. Relating this potential to the standard Newtonian gravitational potential will be accomplished when considering the axions' governing equations.

3.1.2 Axions and Many-Body Formalism

Recall the findings from Ch. 2 that axions are a cold degenerate Bose fluid, with critical temperature $T_{crit} \sim 300GeV$ at the QCD phase transition. By standard thermodynamic measure the fluid should condense and remain so through present day, if thermal equilibrium can be reached. This is a common thread in all axion structure formation efforts to date.

We concentrate on the many-body axion system in the context of a flat environment. The state formalism is used to phrase the many-body system in terms of either a superposition or distribution of configurations. Constructs of field operators mediate the calculation of

observables, configurations, evolution, etc., and obey the basic bosonic commutation rules

$$[\hat{\psi}(x), \hat{\psi}^\dagger(x')] = \delta(x - x') \tag{3.33}$$

$$[\hat{\psi}(x), \hat{\psi}(x')] = 0 \tag{3.34}$$

$$\tag{3.35}$$

To construct equations of motion in the non-relativistic limit we use the Heisenberg picture due to the relative tractability of manipulating field operators as opposed to many-body state vectors. In the presence of a time-independent Hamiltonian, Heisenberg evolution of observables occurs in the familiar way

$$\hat{\psi}(\vec{x}, t) = \hat{U}^\dagger(t)\hat{\psi}(\vec{x}, 0)\hat{U}(t) = e^{i\hat{H}t}\hat{\psi}(\vec{x}, 0)e^{-i\hat{H}t} \tag{3.36}$$

where $\hat{H}$ is a many-body operator. Suppose $\hat{H}$ has the form

$$\hat{H} = \hat{K} + \hat{U} + \hat{V} \tag{3.37}$$

where $\hat{K}$ is the kinetic energy operator $\hat{U}$ is the single body potential energy operator, and $\hat{V}$ is the two body potential energy operator. Expansions to this form will be made as needed. The infinitesimal form of the evolution operator allows for an equation of motion to be derived

$$i\hbar\partial_t\hat{\psi} = [\hat{\psi}, \hat{H}] = [\hat{\psi}, \hat{K}] + [\hat{\psi}, \hat{U}] + [\hat{\psi}, \hat{V}] \tag{3.38}$$

$$= -\frac{\hbar}{2m}\vec{\nabla}^2\hat{\psi} + \int dx' \langle x|u|x'\rangle \hat{\psi} + \int dx_2 dx_1' dx_2' \hat{\psi}^\dagger(x_2) \langle xx_2|v|x_1'x_2'\rangle \hat{\psi}(x_1')\hat{\psi}(x_2') \tag{3.39}$$

Some updates to the quantum forms are necessary in the context of Newtonian gravity over an expanding universe. Beyond the Einstein equations, to which axions contribute their energy density, the axions' governing equations are characterized by a classical Lagrangian of the form

$$\mathcal{L} = \left(\nabla_\mu\phi^\dagger\right) g^{\mu\nu} \left(\nabla_\nu\phi\right) - \phi^\dagger \left(\frac{m}{\hbar}\right)^2 \phi + \frac{\lambda}{4!}|\hat{\phi}|^4 \tag{3.40}$$

where ∇_μ is a covariant derivative over the Christoffel connection. In the semi-classical limit, the field obeys the Klein-Gordon equation over effective fields

$$\nabla^\mu \nabla_\mu \phi + \left(\frac{m}{\hbar}\right)^2 \phi - \frac{\lambda}{3!}|\hat{\phi}|^2 \phi = 0 \tag{3.41}$$

Evaluating the covariant derivatives in the linear approximation, the derivative term in the Klein-Gordon operator becomes

$$\begin{aligned} g^{\mu\nu}\nabla_\mu\nabla_\nu\phi = a^{-2}\Box\phi + 4a^{-2}H\partial^0\phi - a^{-2}\left(h^{-1}\right)^{\mu\nu}\partial_\mu\partial_\nu\phi - 4a^{-2}H\left(h^{-1}\right)^{0\nu}\partial_\nu\phi \\ - a^{-2}h\partial^0\phi + \frac{1}{2}a^{-2}\partial^\nu(h)\partial_\nu\phi + O(h^2) \end{aligned} \tag{3.42}$$

The effective Newtonian limit eliminates the lowest order terms and is consistent with non-relativistic fields in the comoving frame, allowing for the non-relativistic field expansion

$$\phi = \frac{\hbar}{\sqrt{2}m}\left(\psi e^{-imt/\hbar} + \psi^* e^{imt/\hbar}\right) \tag{3.43}$$

Substituting this form of the field operator, and taking the Newtonian limit for gravity, $\bar{h}_{00} = -1/4\Phi$, the Klein-Gordon operator reduces to

$$\begin{aligned} a^{-2}\left(\psi^*\left(\partial_0 + 4H\right)\psi + \psi^*\frac{\hbar^2\vec{\nabla}^2}{2m}\psi + \psi^* m\Phi\psi - \frac{\lambda}{3!}|\hat{\phi}|^2\phi + \{h.c.\}\right) \\ + (\text{quickly oscillating terms}) + O(h^2, m^2/\hbar^2, mh/\hbar) = 0 \end{aligned} \tag{3.44}$$

The quickly oscillating terms are ignored as their actions evaluate to 0 over first order timescales. As the action measure includes a factor of $\sqrt{-g} = a^2 + O(h)$, the terms of the effective axion action can be easily related to the terms of the many body Hamiltonian operator

$$\hat{K} = -\psi^*\frac{\hbar^2\vec{\nabla}^2}{2m}\psi \tag{3.45}$$

$$\hat{U} = \frac{\lambda}{4!}|\psi|^4 \tag{3.46}$$

$$\hat{V} = -\psi^* m\Phi\psi \tag{3.47}$$

which confirms that Φ is indeed the canonical Newtonian gravitational potential.

The many-body axion Schroedinger equation can now be written

$$i\hbar\left(\partial_t + 4H\right)\hat{\psi} = -\frac{\hbar^2\vec{\nabla}^2}{2m}\psi + \frac{\lambda}{4!}|\psi|^2\psi - m\Phi\psi \tag{3.48}$$

or in the real-time parameterization

$$i\hbar\left(\partial_t - \frac{3}{2}H\right)\hat{\psi} = -\frac{\hbar^2\vec{\nabla}^2}{2m}\psi + \frac{\lambda}{4!}|\psi|^2\psi - m\Phi\psi \tag{3.49}$$

This is the operator equation governing the quantum axion field in the presence of classical gravity, which serves as the starting point for all axion structure-formation models considered in this dissertation.

3.2 Controversy in Structure Formation

The state of the art in axion structure formation consists of two viewpoints, which are largely in tension. The first approach assumes that a mean field description of a condensed axions is sufficient for axion dynamics, while the second holds that the full quantum description is needed to describe the axion field.

3.2.1 Axion DM as a Mean Field

The previous chapter 2 shows that relic axions created under the misalignment mechanism fall under the canonical definition of a thermal BEC, falling well over 10^{10} times below the critical condensation temperature at the QCD phase transition. Under that presentation it seems reasonable to assume that every axion is in essentially the same state, with errors appearing as $\mathrm{O}(\exp\left(-\delta E/T_c\right)/N_{axion})$. Proponents of the mean field description use the above error figure to motivate simplification along the single-state constraint.

Coherence Constraint

Mean Field Theory (MFT) at its simplest is a constraint that the state of a many-body Bose system be described by a product of identical single body states.

$$|A\rangle = \frac{1}{\sqrt{N!}}\left(a^\dagger\right)^N|0\rangle \tag{3.50}$$

where $a^\dagger$ is the creation operator for the single particle state of choice. The non-relativistic field operator divided along these lines takes the form

$$\hat{\psi} = \Theta a + \sum_I \omega_I b_I \tag{3.51}$$

where $\{b_I\}$ are the annihilation operators for the other single particle states. This reduction allows the many-body system to be described in terms of an order parameter

$$\theta = \sqrt{N}\Theta \tag{3.52}$$

The evolution of this order parameter may be derived from the many-body equations of motion, or the action

$$S[\theta] = \langle A| \int d^3x \left(\hat{\psi}^\dagger \hat{H} \hat{\psi} - \hat{\psi}^\dagger \left(i\hbar\partial_t - \frac{3}{2}H \right) \hat{\psi} \right) |A\rangle \tag{3.53}$$

$$= \int d^3x \left(\theta^\dagger \hat{H} \theta - \theta^\dagger \left(i\hbar\partial_t - \frac{3}{2}H \right) \theta \right) \tag{3.54}$$

where we keep the lowest axion self-interaction for the moment. Either way the corresponding equation of motion for the system is found to be

$$i\hbar \left(\partial_t - \frac{3}{2}H \right) \theta = -\frac{\hbar^2 \vec{\nabla}^2}{2m}\theta + \frac{\lambda}{4!}|\theta|^2\theta - m\Phi\theta \tag{3.55}$$

and due to the extremal nature of this equation, condensate MFTs are often considered to be semi-classical. For time scales small compared to the expansion rate of the universe, the state evolution and geometry descriptions can be consolidated into the concise Schroedinger-Poisson system of equations

$$i\hbar\partial_t\theta = -\frac{\hbar^2 \vec{\nabla}^2}{2m}\theta + \frac{\lambda}{4!}|\theta|^2\theta - m\Phi\theta \tag{3.56}$$

$$\vec{\nabla}^2\Phi = \frac{4\pi G}{c^2} m|\theta|^2 \tag{3.57}$$

where the axion energy density contribution to Poisson's equation is $\rho_{axion} = mc^2|\theta|^2$. This is often the starting point for MFT approaches to solving axion structure formation.

Hydrodynamic Form

The resulting Schroedinger-Poisson system may be placed into the form of an Euler fluid using the Madelung transformation (Madelung, 1926), where a complex wave-function is written in the form

$$\theta = \sqrt{n}e^{i\vartheta} \text{ for } \theta \neq 0 \tag{3.58}$$

where n is the probability density and ϑ is the 'mean' velocity potential

$$\vec{v} = \frac{\hbar}{m_a}\vec{\nabla}\vartheta \tag{3.59}$$

Inserting the new form of θ into Eqn. 3.55, the Euler-like equation is found.

$$\left(\partial_t - \frac{3}{2}H\right)\vec{v} + (\vec{v}\cdot\vec{\nabla})\vec{v} = -\vec{\nabla}\Phi + \vec{\nabla}Q + \vec{\Pi}_\lambda \tag{3.60}$$

where Q is the pressure induced from the Heisenberg uncertainty

$$Q \equiv -\frac{1}{2m_a^2 a^2}\frac{\nabla^2\sqrt{\rho_a}}{\sqrt{\rho_a}} \tag{3.61}$$

and $\vec{\Pi}_\lambda$ is the contribution from the four-point interaction, which is suppressed by $\mathrm{O}(\hbar\lambda/m_a)$. As mentioned in Ch. 2, the QCD axion is far too massive for the quantum pressure to influence dynamics on galactic scales, and will effectively vanish for our applications. The conservation law embedded in the Schroedinger equation can also be transfered to fluid form

$$\left(\partial_t - \frac{3}{2}H\right)n + \vec{\nabla}\cdot(n\vec{v}) = 0 \tag{3.62}$$

The Madelung form is very popular with those who wish to use high-efficiency hydrodynamics codes to model axion infall, but it does have some shortcomings. The transformation contains a singularity at $\theta = 0$, which prevents vortices or other topologically unique features from appearing in the fluid description. Also the prescription of the phase angle mapping to a velocity field, while sufficient for plane waves, proves somewhat misleading for more complex configurations. The Madelung form implicitly assumes a singularly defined velocity distribution over space, and while consistent with the wave-function expectation value

$$\left\langle\hat{\vec{v}}\right\rangle_{\delta r} \approx \vec{v} \tag{3.63}$$

where $\langle\cdot\rangle_{\delta r}$ is the expectation value in a local region of radius δr, it fails to capture the dispersive nature of the wave-function. Further, a reconstruction of the wave-function is needed when calculating many observables, which can be difficult in this form (Gasser et al., 2000).

Boltzmann Form

The ultimate objective is to construct a simple system of equations capable of describing the quantum dispersive axion media. The Boltzmann equation has the capability of describing dispersion at the cost of expanding the parameter space to the the configuration and momentum $(\vec{x}, \vec{p})$ of phase space. Some creativity is needed to expand the density to a phase-space description. Fortunately, multiple prescriptions of this conversion already exist, only one of which we will touch on. Mapping the MFT wave-function into a distribution can be done via a Wigner function (Wigner, 1932)

$$f(\vec{x}, \vec{p}) = \int d^3x' e^{i\vec{p}\cdot\vec{x}'/\hbar} \theta^*(\vec{x} + \vec{x}'/2)\theta(\vec{x} - \vec{x}'/2), \tag{3.64}$$

where f is the single body pseudo-Distribution Function (pseudo-DF). While not a true DF, in that it can take on negative values,

$$f \geq 0 \text{ (true DF)} \tag{3.65}$$

$$\exists(\vec{x}, \vec{p}) \text{ such that } f < 0 \text{ (pseudo-DF)}, \tag{3.66}$$

it does share a number of properties with true DF, such as being real-valued,

$$\begin{aligned} f^*(\vec{x}, \vec{p}) &= \left(\int d^3x' e^{i\vec{p}\cdot\vec{x}'/\hbar} \theta^*(\vec{x} + \vec{x}'/2)\theta(\vec{x} - \vec{x}'/2) \right)^* \\ &= \int d^3x' e^{-i\vec{p}\cdot\vec{x}'/\hbar} \theta(\vec{x} + \vec{x}'/2)\theta^*(\vec{x} - \vec{x}'/2) \\ &= \int d^3x' e^{i\vec{p}\cdot\vec{x}'/\hbar} \theta^*(\vec{x} + \vec{x}'/2)\theta(\vec{x} - \vec{x}'/2), \ (\vec{x}' \to -\vec{x}') \end{aligned} \tag{3.67}$$

and providing properly-normalized probability densities over 3D projections of phase space

$$\rho(\vec{x}) = \int d^3p f(\vec{x},\vec{p}) \tag{3.68}$$

$$\rho(\vec{p}) = \int d^3x f(\vec{x},\vec{p}), \tag{3.69}$$

The Wigner pseudo-DF can also be expected to provide a reliable DF in certain circumstances (Zurek, 2003; Zachos et al., 2005; Bondar et al., 2013). The differences between a Wigner function and a true DF stem from the uncertainty principles present in the underlying wave-function/quantum-state representation. Complementary parameters such as position and momentum cannot be fully articulated simultaneously when quantum limited, but we see soon that there are classical limits where the two become independent at all effective scales.

The equation of motion for the distribution can be found by straightforward differentiation

$$\partial_t f(\vec{x},\vec{p}) = \int d^3x' e^{i\vec{p}\cdot\vec{x}'/\hbar} \left(\partial_t\theta^*(\vec{x}+\vec{x}'/2)\theta(\vec{x}-\vec{x}'/2) + \theta^*(\vec{x}+\vec{x}'/2)\partial_t\theta(\vec{x}-\vec{x}'/2)\right) \tag{3.70}$$

$$= \frac{1}{i\hbar}\int d^3x' e^{i\vec{p}\cdot\vec{x}'/\hbar} \left(H\left(\theta^*(\vec{x}+\vec{x}'/2)\right)\theta(\vec{x}-\vec{x}'/2) + \theta^*(\vec{x}+\vec{x}'/2)H\left(\theta(\vec{x}-\vec{x}'/2)\right)\right) \tag{3.71}$$

The kinetic contributions to the equation of motion provide a streaming term, plus a sort of quantum pressure of order $\hbar$

$$\frac{1}{i\hbar}\int d^3x' e^{i\vec{p}\cdot\vec{x}'/\hbar} \left(\frac{h^2}{2m}\vec{\nabla}^2_{\vec{x}+\vec{x}'/2}\theta^*(\vec{x}+\vec{x}'/2)\theta(\vec{x}-\vec{x}'/2) - \theta^*(\vec{x}+\vec{x}'/2)\frac{h^2}{2m}\vec{\nabla}^2_{\vec{x}-\vec{x}'/2}\theta(\vec{x}-\vec{x}'/2)\right) \tag{3.72}$$

$$= \vec{p}m\cdot\vec{\nabla}_{\vec{x}} f(\vec{x},\vec{p}) + O(\hbar) \tag{3.73}$$

The gravitational term reduces to a forcing term

$$\frac{1}{i\hbar}\int d^3x' e^{i\vec{p}\cdot\vec{x}'/\hbar}\left(m\Phi(\vec{x}+\vec{x}'/2)\theta^*(\vec{x}+\vec{x}'/2)\theta(\vec{x}-\vec{x}'/2)-\theta^*(\vec{x}+\vec{x}'/2)m\Phi(\vec{x}-\vec{x}'/2)\theta(\vec{x}-\vec{x}'/2)\right) \tag{3.74}$$

$$\begin{aligned}&=-\vec{\nabla}_{\vec{x}}m\Phi(\vec{x})\cdot\vec{\nabla}_{\vec{p}}f(\vec{x},\vec{p})-\frac{m}{i\hbar}\int d^3x' e^{i\vec{p}\cdot\vec{x}'/\hbar}\theta^*(\vec{x}+\vec{x}'/2,t)\theta(\vec{x}-\vec{x}'/2,t)\\&\times\sum_{|\beta|\geq 2}\left(\int_0^1 dl(1-l)\,(x/2)^\beta\,\partial_\beta\left(\Phi(\vec{x}-t\vec{x}'/2)-\Phi(\vec{x}+t\vec{x}'/2)\right)\right)\\&=0-\vec{\nabla}_{\vec{x}}\Phi(\vec{x})\cdot\vec{\nabla}_{\vec{p}}f(\vec{x},\vec{p})+O(\hbar^2)\end{aligned} \tag{3.75}$$

For QCD axions considered far above the deBroglie wavelength, $\hbar$ effectively vanishes, and so vanishes the quantum pressure and potential higher-order gravity impacts. In total, the DF's equation of motion may be put in Boltzmann form

$$\partial_t f+\frac{\vec{p}}{m}\cdot\vec{\nabla}f-\vec{\nabla}m\Phi\cdot\vec{\nabla}_{\vec{p}}f=\Gamma_4 \tag{3.76}$$

where Γ_4 is the four-point interaction encounter term. Aside from the interaction, the above equation looks identical to the classical Boltzmann form.

Expanding the Mean Field: Density of States

Prior to structure formation, the relic axion distribution, thermalized or not, likely spanned some combination of states, with no guarantee of coherence. It is possible that such a mixed state may add effective physics beyond the condensed construction. In this form of MFT we utilize the density matrix operator

$$\hat{\rho}=\sum_J |C\rangle_J\, p_J\, \langle C|_J \tag{3.77}$$

where $\{|C\rangle_J\}$ is an orthonormal basis of the many body space and $\{p_J\}$ are the corresponding probabilities that the system exists in a given state. The expectation value of an operator in the presence of a mixed state is given by

$$\left\langle\hat{O}\right\rangle=Tr\left(\hat{\rho}\hat{O}\right) \tag{3.78}$$

An equation of motion for the operator is given by the Heisenberg form

$$i\hbar\partial_t\hat{\rho} = [\hat{H}, \hat{\rho}] \tag{3.79}$$

though its evaluation is ambiguous without knowledge of each state's evolution.

Expanding the Wigner function to an operator

$$\hat{f}(\vec{x}, \vec{p}) = \int d^3x' e^{i\vec{p}\cdot\vec{x}'} \hat{\psi}^\dagger(\vec{x} + \vec{x}'/2)\hat{\psi}(\vec{x} - \vec{x}'/2), \tag{3.80}$$

the effective distribution function is found to be

$$f(\vec{x}, \vec{p}) = Tr\hat{\rho}\hat{f} \tag{3.81}$$

$\hat{\rho}$ is found to evolve like

$$\partial_t\hat{\rho} = [\hat{\rho}, \hat{H}] \tag{3.82}$$

The density evolution may be broken down into the evolution of individual states, and an equation of motion may be derived for the DF expectation value

$$\partial_t \left\langle \hat{f} \right\rangle = \frac{1}{i\hbar} Tr \left(\hat{\rho}[\hat{f}, \hat{H}] \right) \tag{3.83}$$

Deriving the equation of motion for $\left\langle \hat{f} \right\rangle$ brings us back to the same Boltzmann form

$$\partial_t f + \frac{\vec{p}}{m} \cdot \vec{\nabla} f + \vec{\nabla}\Phi \cdot \vec{\nabla}_{\vec{p}} = \Gamma \tag{3.84}$$

It appears as though standard MFT approaches tell us that relic axions behave like classical CDM.

Implications and Counter-arguments

Implementing an MFT on relic axions is straightforward and attractive. In the limit of Ultra-Light Axions (ULAs), $m_a \leq 10^{-22}$ eV, the physical effect of Heisenberg uncertainty enters the galactic scale. QCD axions are at least sixteen orders of magnitude heavier and, recalling from Ch. 2, will not see outright quantum pressure effects on scales much above an (AU)

$O(10^8 km)$. This reduces the Boltzmann and hydrodynamic representations of the mean field to that of a classical pressure-less fluid, the same used in the ΛCDM model. Such a finding further consolidates the modeling of DM structures to the CDM model, and relegates the detection of axions to to direct (non-gravitational) methods.

There is one comment I would like to add. Purely self-gravitating systems do not fall into the usual categories of thermodynamic systems. Gravity is infinite range, unscreenable, and its highly correlated interactions make separation into single particle states via Fock space unrealistic in a convergent sense. Further the density of the gravitational spectra is such that a single-particle decomposition of a BEC is unfeasible. The system doesn't contain a classical ground state and may not be capable of reaching thermal equilibrium, as exemplified by the gravi-thermal catastrophe (Binney & Tremaine, 2008). Even the quantum ground state to the many-body gravity problem is a non-issue, due to its inaccesibility from cosmic initial conditions. Further, it has been classically shown that virialization is not equivalent to thermalization in its ability to thoroughly mix fluids, possibly leading to further discrepancies between the condensation processes among particle physics forces and those from gravity. The untethered nature this late-time axion system from established material science also requires a more rigorous definition of axion condensation. For these reasons, we conclude that MFT cannot be a robust approach to the statistical behavior of axions.

3.2.2 Axion DM as a Quantum Field

Some believe the situation is not so cut and dry. A small group in the axion community championed by Pierre Sikivie believe that observable axion structures are possible on galactic scales, primarily in the form of a type of caustic ring resulting from a D_{-4} catastrophic event (Sikivie, 1999a,b; Duffy & Sikivie, 2008; Chakrabarty & Sikivie, 2017), unique from those created in CDM collapse. Fueled by the need to coherently conserve quantum numbers such as angular momentum and energy, axions are supposedly drawn to the galactic plane as a series of cold sheets in phase-space, Figs. 3.1 3.2 3.3. It is also claimed that the earth is close to the $n = 4$ caustic in our own MW halo. Cold flows feeding into several of these caustics

would contribute to the local axion energy spectra, significantly influencing the results of terrestrial search experiments.

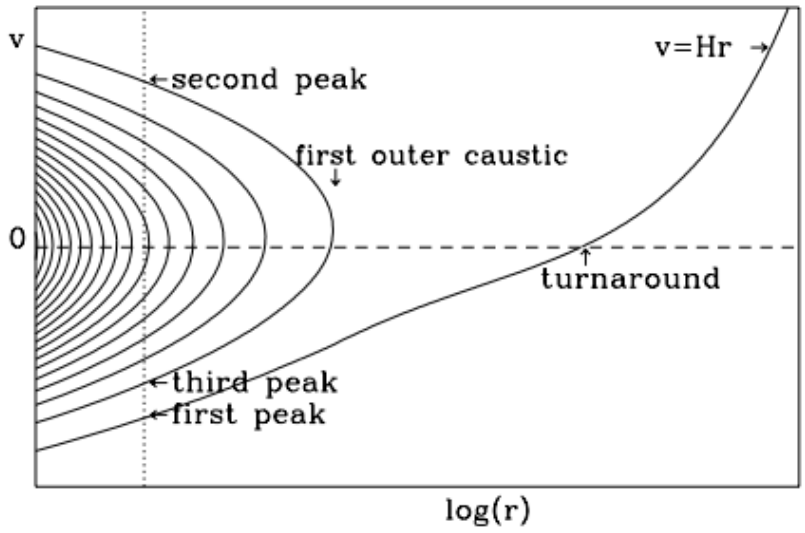

Figure 3.1: Phase-space diagram of a sheet of cold DM undergoing gravitational infall in a cosmology of one spatial dimension (Sikivie, 1999a). Caustics are demonstrated as turn-around points of the matter sheet, where the local density becomes infinite. In general there are many types of caustics, all having the common attribute of singularity of density, with the caustic rings proposed by Sikivie being of the D_{-4} catastrophe type (Sikivie, 1999b).

Prerequisites for the full quantum description of structure formation are the same as those for the MFT, namely that after a misalignment-like creation mechanism, DM axions form a very cold BEC-like state. After misalignment the relics are posited to continue condensation via gravitational mixing, long before non-linear structure formation begins (Erken et al., 2012) and throughout the collapse and virialization process. To accomplish

this the infall model must properly sample the multitude of configurations and accurately capture condensation physics. Sikivie and his collaborators have several models which aim to incorporate various aspects of the quantum fluid into gravitational collapse. We review the most telling here.

Established in (Erken et al., 2012), a small collection of quantum oscillators is exposed to a gravitational field. To make the mathematics tractable we place a bosonic quantum field operator $\hat{theta}$ in a periodic box of side length L. The box allows for a decomposition of the operator into a collection of oscillator-like components, the plane wave orthonormal basis

$$\theta(\vec{x},t) = \sum_{\vec{n}} \sqrt{\frac{\hbar^2}{2L^3 c\epsilon_{\vec{n}}}} \left(a_{\vec{n}}(t) e^{i2\pi\vec{n}\cdot\vec{x}/L} + a^{\dagger}_{\vec{n}}(t) e^{-i2\pi\vec{n}\cdot\vec{x}/L} \right) \tag{3.85}$$

where $\vec{n}$ is a vector of integers, $a^{\dagger}_{\vec{n}}$ and $a_{\vec{n}}$ are the creation and annihilation operators, and $\epsilon_{\vec{n}}$ is the energy of the state. The creation and annihilation operators satisfy the equal-time commutation relations

$$[a_{\vec{n}}(t), a^{\dagger}_{\vec{n'}(t)}] = \delta_{\vec{n},\vec{n'}} \ , \ [a_{\vec{n}}(t), a_{\vec{n'}(t)}] = 0 \tag{3.86}$$

For the case of a highly degenerate system of axions, the Schroedinger equation can be used with Hamiltonian in eqn. 3.56, written in the plane wave expansion as

$$H = \sum_{\vec{n}} \hbar\omega_{\vec{n}} a^{\dagger}_{\vec{n}} a_{\vec{n}} + \sum_{\vec{n_1},\vec{n_2},\vec{n_3},\vec{n_4}} \Lambda^{\vec{n_3},\vec{n_4}}_{\vec{n_1},\vec{n_2}} a^{\dagger}_{\vec{n_1}} a^{\dagger}_{\vec{n_2}} a_{\vec{n_3}} a_{\vec{n_4}} \tag{3.87}$$

where $\Lambda^{\vec{n_3},\vec{n_4}}_{\vec{n_1},\vec{n_2}}$ describes the interactions between plane waves. The interaction term may be expanded into self-interaction and gravity parts

$$\Lambda^{\vec{n_3},\vec{n_4}}_{\vec{n_1},\vec{n_2}} = \Lambda_s \ {}^{\vec{n_3},\vec{n_4}}_{\vec{n_1},\vec{n_2}} + \Lambda_g \ {}^{\vec{n_3},\vec{n_4}}_{\vec{n_1},\vec{n_2}} \tag{3.88}$$

where the self-interaction term takes the form

$$\Lambda_s \ {}^{\vec{n_3},\vec{n_4}}_{\vec{n_1},\vec{n_2}} = \frac{\lambda\hbar^4}{4^2 m^2 c^4 L^3} \delta_{\vec{n_1}+\vec{n_2}=\vec{n_3}+\vec{n_4}} \tag{3.89}$$

and the gravity interaction may be written as

$$\Lambda_g \ {}^{\vec{n_3},\vec{n_4}}_{\vec{n_1},\vec{n_2}} = -\frac{\pi G m^2 \hbar^2}{L^3} \delta_{\vec{n_1}+\vec{n_2}=\vec{n_3}+\vec{n_4}} \left(\frac{1}{|\vec{p}_{\vec{n_1}} - \vec{p}_{\vec{n_3}}|^2} + \frac{1}{|\vec{p}_{\vec{n_2}} - \vec{p}_{\vec{n_4}}|^2} \right) \tag{3.90}$$

where $\vec{p}_{\vec{n}} = 2\pi\vec{n}/L$. The Heisenberg equation of motion for the annihilation operators are derived to be

$$-i\hbar\dot{a}_{\vec{n_1}} = [H, a_{\vec{n_1}}] = -\epsilon_{\vec{n}} - 2\sum_{\vec{n_2},\vec{n_3},\vec{n_4}} \Lambda^{\vec{n_3},\vec{n_4}}_{\vec{n_1},\vec{n_2}} a^{\dagger}_{\vec{n_2}} a_{\vec{n_3}} a_{\vec{n_4}} \tag{3.91}$$

The creation operator's equation of motion may be derived similarly. From here the occupation number operators', $\mathcal{N}_{\vec{n}} = a^{\dagger}_{\vec{n}} a_{\vec{n}}$, equations of motion may be derived. Numerical simulations of small collections of oscillators, O(10), evolution into equilibrium conditions show that the equilibrium state differs significantly from classical or MFT configurations over a range of λ strengths, Fig. 3.4.

Attempts to add many more oscillators to the model are met with some undesirable truths of numerical computation. As more oscillators are added, the size of the computation scales as $\mathrm{O(N^4)}$, at least, which is untenable for systems greater than a few tens. Even if the scaling were somehow brought under control, say O(N), the requirement that each axion be modeled separately as to capture its quantum nature makes galactic simulations impossible with modern computers, at the very least because there are more axions in the MW than there are atoms in the visible universe!

$$N_{\text{axions in MW}} \approx \frac{M_{MW,DM}}{m_a} \frac{10^{12} M_{\odot}}{M_{DM}} \frac{1.99 \times 10^{33} \text{ gram}}{M_{\odot}} \frac{6.02 \times 10^{23+15} \mu \text{ eV}/c^2}{\text{gram}} \approx 10^{84} \tag{3.92}$$

Implications and Counter-arguments

Axions as a highly condensed Bose fluid appear to have unique behavior under gravitational collapse, but a full quantum description of a galaxy's worth of axions is laughable. Simplifications are needed in the degrees of freedom whilst still maintaining the quantum nature of the degenerate bose system. Proponents of caustic rings believe MFT does not satisfy these requirements. The fault with the MFT simplification is reported to lie in the statistical occupation of states after a process that is designed to establish thermodynamic equilibrium. Appx. A recreates the MFT counter-argument, which shows that the resulting statistics from an MFT realization of a quantum field do not represent the underlying Bose system.

Proponents of MFT descriptions disagree. In addition to citing the standard wisdom that a highly condensed Bose system behaves like a classical fluid (Marsh, 2016), they request a sufficient explanation for the fundamental physics responsible for the caustic rings and have been unsatisfied with the results (Erken et al., 2012; Banik et al., 2015).

3.2.3 A Stalemate?

At this point it looks as though both the classical and quantum segments of the axion community are resolute in their own approach to modeling relic axion infall. A lack of rigorous demonstration in the validity of their base claims indicate that neither should be taken at face value. The layers of intermediate physics between the axiomatic quantum description and the salient degrees of freedom to gravitational collapse must be explained.

In both pictures, we can see that the axion field would collapse, virialize and form galaxy-halo structures in conjunction with baryonic species, but we are missing some important pieces. The unique state of relic axions as a highly-degenerate Bose fluid (BEC) causes one to describe the system as a single classical field on length scales far above the deBroglie and Compton lengths. This description is suspiciously similar to that of a WIMP fluid on galactic scales. However this prescription does not properly take into account the impact of long-range eXchange-Correlation (XC) effects propagated by the infinite-range un-screenable gravitational force. In the presence of an external field or weak inter-particle interactions we understand the the XC impacts are small from the application of a dissociative limit, but as gravity is the only interaction of consequence on galactic scales this limit is invalid. Further, this formulation implicitly assumes that the process of reaching gravitational equilibrium is nearly adiabatic, it imparts minimal entropy, due to the superficial connection between gravitational interactions and external potentials. This resulting dissociated and nearly adiabatic classical fluid is at odds with attempts to include effects due to long-range correlations induced by gravity, creating controversy in the literature as to how axion infall should be modeled.

The primary proponents of axion-specific dynamics believe that a full quantum descrip-

tion of the axion is necessary to understand its dynamics, even on galactic scales. Due to the difficulty of performing such complex calculations on and entire galaxy of axions, these groups almost exclusively rely on either numerical models of gravitational infall of disconcertingly few axions or semi-analytic models of BEC structure formation to spur the concept of unique structures in axion DM and baryons. Evidence from these approaches takes several forms. A principal result comes from the comparison of quantum gravitational equilibration timescales to classical collapse models, mainly that they are incompatible over the lifetime of the universe and disqualifying the classical results (Banik et al., 2015; Erken et al., 2012). Another claim is that one should expect entropy increase from quantum axions. Semi-analytic efforts in calculating equilibrium models of axion DM subject to a particular flavor of quantum Bose dynamics also show that structures unique from from classical fluids are present on galactic scales, namely caustic rings. Further assertions are even made that such structure can be viewed within our own MW. A result that is not seen is a computationally feasible model of axion infall that extends beyond linear perturbation theory and with rigorous motivation starting from quantum principles.

To date, neither perspective has motivated their model to the point of fully addressing the other's exceptions. This includes a comprehensive model of structure formation capable of being followed into the nonlinear regime where shell-crossing, halo formation, and equilibration truly occurs. This dissertation addresses this vacancy and aims to resolve this dispute by constructing a model that both camps can agree is sufficient for describing axion structure formation, performing numerical experiments, and observing the resulting structures. The remainder of this chapter concerns my efforts to that end.

3.3 Project Definition

This section reviews some of the vernacular used to execute the research project motivated above. Many very accomplished individuals and research groups have yet to come to a consensus on the complex task of determining the appropriate methods to model axion structure formation, let alone performing the difficult work necessary to resolve the extent

of unique axion structures. To have any hopes of success our plan must be well thought out and organized. To formulate this plan we follow the lead from operations engineering and management and derive requirements by which the progress and success of the project will be measured. A preliminary design flowchart outlining the high-level research plan is presented, and the sub-flows covered by this dissertation are also discussed.

3.3.1 Requirements

The research project is centered on a single requirement, the Project Requirement:

> Determine means to model axion cosmological structure formation and resolve the extent to which axion structures unique from CDM appear.

Further requirements are drawn to serve as a guide through the many levels of detail involved in completing the project, ostensibly all the way down to codifiable tasks. The strictness of these requirements lessens with increasing levels. The next two levels of requirements below the Project Requirement are given here.

1. Project will identify model for QCD axion DM structure formation on galactic scales that captures all appropriate physics.
    - Relic QCD axions will conform to parameters consistent with the most recent observational findings. To date this implies that axions comprise 100% of the DM, and mass and coupling are consistent with the DFSZ theoretical model.
    - The starting point model for axion structure will be of a bosonic many-body quantum field in the non-relativistic limit.
    - The final form of the structure formation model will accurately describe dynamics on galactic scales in few enough degrees of freedom to be conducive to simulation.
2. Project will simulate cosmological structure formation of QCD axion DM at scales sufficient to resolve proposed unique axion structures.

- Test simulations will be run with increasing sophistication up to realistic cosmological environments.
- Cosmological simulations will be run using the ChaNGa N-Body+Smoothed-Particle Hydrodynamics code base, with initial conditions comparable to existing CDM simulations.
- A culminating simulation of a cosmological volume sufficient to simple potential axion structures in MW-like galaxies will be run, which also has a CDM analogue.

3. Project will compare structures from axion simulations to structures from analogous CDM simulations.

   - A search for caustic halo rings unique to axions will be made.
   - A search for alterations to CDM caustics will be made.

4. Project will make conclusion on the existence of unique axion structures on galactic scales.

   - Efficacy to axion DM searches will be made. Success will be measured by projected impact to observations.
   - Efficacy to astrophysical observations will be made. Success will be measured by projected impact to observations.

3.3.2 Roadmap

Next, we develop a roadmap to satisfy the project requirements, though 'roadmap' might not be the best term as the plan largely consists of two paths, Fig. 3.14. The first path involves the development of the axion infall model. The second path develops the tools needed to properly analyze both CDM simulations and those including axion-specific physics.

Path 1: Axion Specific Physics

There are several axion evolution models in the literature, however no single model has been widely accepted as capable of accurately portraying axion behavior. This opening gives us room to develop our own approach. A crucial aspect of our model is that it be capable of providing solutions to structure formation that are unique from normal CDM, respecting the clear-cut differences in their underlying physics. Note that this does not necessarily mean that the solutions will be distinguishable, just that the capacity is there. Such details may not be clear at the onset of a model's development, producing some risk of wasting time on an impotent method. To mitigate that risk we diversify our approach, developing multiple unique models in parallel. Three models are pursued: one builds on the MFT description by including additional classical fields to represent different components of the fluid, namely the BEC and thermal components, which interact according to their thermodynamics properties; another model takes the shape of a density-functional theory, representing axions as non-interacting single field states; the last attempts to distill the solution to the many-body problem to a single degree of freedom using a custom set of techniques. Each of these models are novel in the study of cosmological DM structure-formation, but are commonplace in the condensed matter community. We utilize findings from the gaseous and condensed matter BEC literature to accelerate our cosmological study.

A model is chosen based on its potential to fulfill the needs of the project. Once specified, the continuum model is to be codified for use in the ChaNGa code base. Again there is risk in pursuing only a single algorithm, so we undergo another round of diversification and vetting in order to choose the axions' numerical scheme. The most effective technique is chosen based on the feasibility of implementation into ChaNGa, its accuracy at scale, and potential scalability with respect to simulation size and complexity. These audits are largely conducted by series of small-scale simulation experiments. This is the purpose of the AXP infrastructure.

An intensive round of testing is planned during and after the axion modules are coded

into ChaNGa. This is to ensure the functionality and quality of the model. Simulations from single dimension interactions to isolated halo formation alongside baryonic components are to be run. Here we get our first glimpse into the real-world potential for unique axion structures in a semi-realistic context. The first intensive use of the axion infall model consists of a simulation suite of large cosmological volumes complete with baryonic components. Large here refers both to the ability to model the natural development of MW-like galaxies and sufficiently fine in resolution to describe potential axion structures. Such simulations provide a wide range of natural conditions for axions to display their unique properties and should provide realistic context for addressing the unique structure problem. Tools developed in the second path will be used in the search for unique structures.

Path 2: Developing Tools in CDM

The second path of the project involves developing an understanding of control CDM structures. Tools are to be developed from this understanding to quantify differences in structure generated by axion dynamics. N-Body cosmological simulations generated from ChaNGa provide our baseline CDM structures, as the code is already proven to high accuracy and is to be used in the first path to create the axion-specific simulations.

While accurately modeled, CDM structures are not altogether well understood. Our understanding of the finer points of the gravitational equilibration process (virialization) and CDM's response to baryon potentials contain gaps. The project seeks to shed some light in some of those dark spots, or at least fill them with a heuristic picture. The end goal is to gain quantifiable insight on expected CDM structures and establish points of comparison to axions. Simulations using CDM of many shapes and sizes are available from the smallest of isolated halo formations to cosmological volumes hundreds of Mpcs across. We concentrate on those that we have hopes of reproducing in the early stages of simulating axion-specific dynamics.

One of the tools for comparison is to study the local phase space distribution of a halo much like our MW. Such figures are of great interest to direct detection experiments. The

halo density and energy distribution, both directly calculable from a distribution function, are directly applicable to many direct detection experiments. Such spectra are also capable of displaying caustic type features. Once the tools for analyzing structures with and without Bose physics are cultivated, the two routes converge in the grand analysis stage. Products of this analysis provide axion DM searches with valuable information and a rigorous conclusion on the existence of unique axion structures.

3.3.3 Dissertation Subset

The research presented in this dissertation does not cover the entirety of the project. Initiation through small-scale testing are completed within path one, while path two is in the midst of establishing a CDM baseline. More detailed plans for the remaining stages are covered in future work, Ch. 6.

3.4 A Comprehensive Approach to Axion Structure Formation

This section covers the first two stages of path one, from the starting point of an axion quantum field to the choice of numerical model best suited for large-scale computation. Brief mention of discarded approaches are made for completeness. The contents of this section are preliminary.

3.4.1 Multi-Component Field Theories and their Shortcomings

Many models of many-body quantum systems rely on the ability to retain the notion of an individual particle. The MFT models of Section 3.2.1 accomplished this by assuming the axion system was separable, each axion occupied the same state, and evolved more-or-less independently. Even in the thermal MFT model it is assumed *a priori* that the solution falls into a separable form. Second quantized approaches often share this quality due to the ease of describing system states in Fock space. The condensed matter literature is also rife with this tactic. Following this lead the author pursued several popular BEC models in higher

detail, including multi-fluid and Density-Functional Theory (DFT) techniques, where the more complex BEC physics appears to be commensurate to divvying up states of matter into additional quantum fields with longitudinal transitions packaged as interactions. The two techniques summarized below are candidates for the axion infall model that did not meet project requirements and are documented here for completeness.

Multi-Fluid Model

A favorite for computationally modeling BECs among the condensed matter community is the multi-fluid model (Zaremba et al., 1999; Griffin et al., 2009). Considered here in the two-fluid variety, a system of cold axions is divided into a condensate and a thermalized fluid via a condensate operator

$$\theta(\vec{x},t) = \left\langle \hat{\psi} \right\rangle = \frac{1}{N!} \langle 0| \, (\hat{a})^N \hat{\psi} (\hat{a}^\dagger)^N \, |0\rangle \tag{3.93}$$

and the remainder operator

$$\hat{\tilde{\psi}} = \hat{\psi} - \theta \hat{I} \tag{3.94}$$

Each of these components evolves under its own equation of motion, coupled to the other by the mutual interactions and transitions of objects between components. The bare bones system of equations consists of a Schroedinger-like equation for each component. The condensate:

$$\begin{aligned} i\hbar\partial_t\theta(\vec{x},t) = &-\frac{\hbar^2\vec{\nabla}^2}{2m}\theta(\vec{x},t) + m\Phi(\vec{x})\theta(\vec{x},t) + gn_c(\vec{x},t)\theta(\vec{x},t) \\ &+ 2g\tilde{n}(\vec{x},t)\theta(\vec{x},t) + g\tilde{m}(\vec{x},t)\theta^*(\vec{x},t) + g\left\langle \hat{\tilde{\psi}}^\dagger(\vec{x},t)\hat{\tilde{\psi}}(\vec{x},t)\hat{\tilde{\psi}}(\vec{x},t) \right\rangle \end{aligned} \tag{3.95}$$

The remainder:

$$\begin{aligned} i\hbar\partial_t\hat{\tilde{\psi}} = &-\frac{\hbar^2\vec{\nabla}^2}{2m}\hat{\tilde{\psi}} + m\Phi\hat{\tilde{\psi}} + 2gn_c\hat{\tilde{\psi}} + \theta^2\hat{\tilde{\psi}}^\dagger \\ &+ g\theta^*\left(\hat{\tilde{\psi}}\hat{\tilde{\psi}} - \tilde{m}\right) 2g\theta\left(\hat{\tilde{\psi}}^\dagger\hat{\tilde{\psi}} - n\right) + g\left(\hat{\tilde{\psi}}^\dagger\hat{\tilde{\psi}}\hat{\tilde{\psi}} - \left\langle \hat{\tilde{\psi}}^\dagger\hat{\tilde{\psi}}\hat{\tilde{\psi}} \right\rangle\right) \end{aligned} \tag{3.96}$$

In the limit where the contact interactions vanish the two motive equations simplify greatly, acting only under the influence of the total gravitational potential. As the gravitational potential is considered in an averaged fashion, no transition interactions remain, leaving the condensate and normal component individually conserved. This is little too simple as it does not address the manner by which the system becomes condensed or how it may leave a condensed state. In essence we have divided the system into two MFTs. To see the two-fluid formulation in greater detail, see Appx. B. Additional efforts can be taken to more completely incorporate gravity as an interaction between axions, but such models begin to look more like many-body models, which are covered in Section 3.4.2.

Density-Functional Model

Primarily used by condensed matter theorists to study electronic structures, a fermionic system, the fundamental concept of a DFT is exchange symmetry non-specific (Fiolhais et al., 2003). The basic structure of a DFT, much like the other approaches presented here, rises from the desire to reduce a many-body description of identical particles into a description involving fewer degrees of freedom, specifically one of a collection of nearly independent single-particle systems. The popular Kohn-Sham framework of an electronic DFT provides knowledge of an N electronic system's density ρ_e and its currents using an effective single-body potential V_{eff}, a collection of N orbitals $\{\phi_i\}_{i\in\{1,\dots,N\}}$, and the N lowest single-body energy states $\{\epsilon_i\}_{i\in\{1,\dots,N\}}$

$$\left(-\frac{\hbar^2}{2m}\Delta + V_{eff}\right)\phi_i = \epsilon_i\phi_i \tag{3.97}$$

$$\rho_e = \sum_i^N |\phi_i|^2 \tag{3.98}$$

The form of a system's solution is almost entirely dependent on the form of the effective potential, which is where the challenge lies. Most problematic is finding an accurate description of the effective repulsion between electrons due to their exact exchange anti-symmetry. As a result, many approximations to this effective exchange-correlation energy V_{XC} have

been formed for electronic systems, most only successful to a limited degree and suited for a very limited range of configurations. An analogous potential will have to be formed for the Bosonic DFT (BDFT).

Note that so far we are ignoring time-dependence in the DFT, which is necessary for our eventual model of axion infall. Extensions from the stationary DFT to Time-Dependent DFTs (TDDFTs) are numerous and have seen much development in the last several decades. In this time, a considerable amount of effort and literature has been placed around TDDFT (for an introduction see Marques & Gross (2004)), this would serve as a valuable resource for formulating a Bosonic TDDFT (BTDDFT). One change is immediately apparent for a BDFT that saves it from the scaling pitfall. Fermionic DFTs require the full particle count of free wave-functions due to their required exchange anti-symmetry. The bosonic symmetric exchange condition allows for more than one axion to exist in a single state, allowing a cold collection of axions to be described using only a few orbitals.However this is were the simplification stops. The analogous XC potential for the occupied orbitals is far from forthcoming. The effort expected to construct a promising form is a PhD. thesis unto itself, based on the extent of fermionic literature.

Based on the BDFT work to date and the track record of electronic DFTs, the potential of this model to accurately represent axion DM is high, but the implementability of such a model in an N-body code is uncertain. See Appx. C for a more complete description. Also, to quell concerns about implementability, a disproportionate amount of pen-and-paper development may be required compared to other equally fruitful approaches. This leads the author to look elsewhere for an appropriate model.

3.4.2 Many-Body Quantum Axions as a Many-Body Schroedinger Equation

Our approach to modeling axion Structure Formation (SF) appears to need a more elemental starting point. The condensed matter techniques are too well-suited for electrons, nuclei, and atomic systems to be of immediate us to us. MFT and multi-fluid models have too much gratuitous structure. Creation and annihilation of axions via second quantization formalism,

and a compulsion to separate axions into a product of single particle states are unnecessary as axion number is essentially conserved in the SF era and the correlating effects of gravity cannot be ignored. DFTs bring us closer, but a less than forthcoming description of XC in the context of highly dynamical infall prevents us from pursuing this method further. Even so we do learn a valuable lesson from the DFT literature: only the total distribution is needed to describe the dynamics of a system of identical particles acting in a time-dependent potential. For the precise statement and proof, commonly known as the Runge-Gross theorem (Runge & Gross, 1984), see Appx. D. Based on Runge-Gross, we should expect there should exist a model that adequately describes the dynamics of relic axions using only the total distribution. We aim to find such a model by falling back to first quantization methods, namely the many-body Schroedinger equation.

The very definition of BEC must also come into question before we continue to form our ideal model. Commonly studied thermodynamic systems contain a state of lowest energy, or ground state, which provide a logical location for a condensate to form. For such systems the condensate is defined to be the proportion of the system in the ground state. The use of gravity as the only pertinent force on SF timescales also creates a unique situation, thermodynamically speaking. Self-gravitating systems of axions have a ground state inaccessible to DM initial conditions. The force has unscreenable attraction of infinite range, making it difficult to distinguish the state of individual axions outside of the influence of the rest of the system. Further, studies of pure gravitational collapse show that self-gravitating systems do not come to thermal equilibrium, rather a quasi-equilibrium called virialization where the orbits of individual bodies come to obey the virial theorem, requiring a novel yet consistent definition of what it means to be condensed. This section constructs such as a byproduct of the axion SF model.

Relic axions of the second and third epoch live in the limit of NR motion and conserved particle number, allowing the quantum field equation to be expressed as a many-body

Schroedinger equation

$$i\hbar\left(\partial_t - \frac{3}{2}H\right)\Psi(\vec{x}_1, ..., \vec{x}_m; t) = \hat{H}\Psi(\vec{x}_1, ..., \vec{x}_m; t) \tag{3.99}$$

where Ψ is the many body axion wave-function. As axions are bosons this wave-funciton must also obey an exact exchange symmetry as inherited from the Bose operator. The many-body hamiltonian $\hat{H}$ may be broken down into recognizable kinetic and potential energy parts

$$\hat{H} = \hat{T} + \hat{V} = \sum_i^M \frac{-\hbar^2\nabla^2}{2m_a} + \sum_i \Phi_i + \frac{\lambda}{2\cdot 4!}\sum_{i\neq j}\delta^3\left(\vec{x}_i - \vec{x}_j\right) \tag{3.100}$$

where Φ_i gravitational potential on the i-th axion from other axions and other species. We choose to evaluate the Newtonian gravitational potential in the Coulomb gauge.

Before attempting to solve the full many-body equation of motion, some elaboration is needed on the accepted axion model. For scales of $\sim$ kpc and greater the λ self-interaction term has interaction rate

$$\dot{N} \sim m_a \frac{N_{DW}^2}{f_a^2} \tag{3.101}$$

which at modern cosmological abundances would have a mean free path larger than the visible universe. As the interaction is sub-leading to Newtonian gravity, we remove it from the SF equation of motion.

The gravitational interaction also requires some clarification. Strictly speaking the gravitational potential may come from multiple massive and radiative species. Considering only massive species like stars, atomic gas, Super Massive Black Holes (SMBHs) and axion DM, the potential may be broken up linearly, using the gauge choice where the potential infinitely

far away from all sources goes to zero,

$$\rho = \rho_a + \rho_{stars} + \rho_{gas} + \rho_{SMBH} \tag{3.102}$$

$$\nabla^2\Phi = -4\pi G\rho = -4\pi\left(\rho_a + \rho_{stars} + \rho_{gas} + \rho_{SMBH}\right) \text{ implies} \tag{3.103}$$

$$\Phi = \Phi_a + \Phi_{stars} + \Phi_{gas} + \Phi_{SMBH} \text{ where} \tag{3.104}$$

$$\nabla^2\Phi_a = -4\pi G\rho_a \tag{3.105}$$

$$\nabla^2\Phi_{DM} = -4\pi G\rho_{DM} \tag{3.106}$$

$$\nabla^2\Phi_{gas} = -4\pi G\rho_{gas} \tag{3.107}$$

$$\nabla^2\Phi_{SMBH} = -4\pi G\rho_{SMBH} \tag{3.108}$$

We consolidate all non-axionic density and potential terms into ρ' and Φ'. Now in the Coulomb gauge, the inter-axion gravitational potential may be written simply using the kernel

$$\phi_{ij} = -\frac{4\pi G m_a^2}{|\vec{x}_i - \vec{x}_j|} \tag{3.109}$$

where $\vec{x}_i$ is the position of the i-th axion. The form of the many-body Hamiltonian may now be rewritten

$$\hat{H} = \sum_i^M \frac{-\hbar^2\nabla^2}{2m_a} - \frac{1}{2}\sum_{i\neq j}^M \frac{G m_a^2}{|\vec{x}_i - \vec{x}_j|} + \sum_i^M \Phi'(\vec{x}_i) \tag{3.110}$$

3.4.3 Simplifications of the Many-Body Equations

The next step is to understand the solution space of this operator equation. It is easy to show that the space of solutions is a vector space. From the underlying operator equation we inherit an equal-time norm, $L_2\left(\Re^{3N}\right)$, and inner product naturally extended from this norm

$$\langle g, f\rangle = \int_{\Re^{3N}} d^{3N}x g^\dagger(x) f(x) \tag{3.111}$$

where g is an element of the solution space's dual. Accounting for the desire to be well-defined by these integral measures and the differentiability requirements from the Schroedinger equation itself, the solution space for this PDE is covered by

$$\mathcal{C}\left(\Re^{3N+1}\right) = \left\{f(x,t) : \partial_{x_j}\partial_{x_i} f \text{ exists } \forall i,j; \partial_t f \text{ exists}\right\} \tag{3.112}$$

which has a dense Fock sub-space

$$\mathcal{C}\left(\Re^{3+1}\right) \times ... \times \mathcal{C}\left(\Re^{3+1}\right) \tag{3.113}$$

meaning we may write any solution of the many-body Schroedinger equation as combinations of single-body products to arbitrary accuracy

$$\Psi = \prod_{i\in\{1,...,N\}\alpha\in A} \psi_\alpha\left(\vec{x}_i\right) + ... \tag{3.114}$$

The Bose symmetry condition requires the axion state to occupy only fully symmetric states under particle exchange

$$\Psi\left(\vec{x}_1, ..., \vec{x}_i, ..., \vec{x}_j, ..., \vec{x}_N; t\right) = \Psi\left(\vec{x}_1, ..., \vec{x}_j, ..., \vec{x}_i, ..., \vec{x}_N; t\right) \text{ for some } i, j \tag{3.115}$$

reducing the solution space to

$$\mathcal{C}\left(\Re^{3N+1}\right)/S_N \tag{3.116}$$

where S_N is the totally-symmetric group of permutations among N items. The dense Fock space is also reduced

$$\mathcal{C}\left(\Re^3\right) \times ... \times \mathcal{C}\left(\Re^3\right) \times \mathcal{C}\left(\Re\right)/S_N \tag{3.117}$$

The form of the axion DM Hamiltonian is far from separable across single particle lines, making a Fock space representation and reduction of states untenable. A more concise form to solutions of the symmetric Schroedinger equation exist in the case of no external potentials and central inter-particle potentials, derived in Appx. F. As a result we may display solutions many-body axion solutions as

$$\Psi\left(x, t\right) = perm\left(\prod_{ij\,\alpha} \psi_\alpha\left(\vec{x}_i - \vec{x}_j, t\right)\right) \tag{3.118}$$

where ψ_α is a solution to the single body equation

$$i\hbar\partial_t\psi_\alpha = -\frac{\hbar^2}{2\mu}\nabla^2_{\vec{x}_i-\vec{x}_j}\psi_\alpha - \frac{Gm_a^2}{|\vec{x}_i - \vec{x}_j|} \tag{3.119}$$

where μ is the axion-axion reduced mass. Such a form more efficiently explores the solution space than the single-particle expansion natural to Fock space representations, especially in the case of our highly correlated gravitational Hamiltonian. The elegance of this form is that it also automatically incorporates exact exchange symmetry and its effects on the possible actions and transitions of the system, not possible with the models presented above. The primary shortcoming is that we still must find a way to deal with $\geq 10^{84}$ axions to model the MW!

3.4.4 Distillation to a Condensed Quasi-Distribution Function

To avoid the pitfall of considering too many variables, recall that the Runge-Gross theorem tells us that the only salient degree of freedom for the whole axion system is its density, ρ_a. To focus on distilling down the many-body system from N to a single degree of freedom, let us first phrase the many-bodies into DF form for later use in N-body codes. Our treatment starts by assuming a completely condensed system, meaning the axion state is described by a single ψ_α, followed by a density-of-states derivation.

Many-Body Boltzmann Equation

This derivation of the Boltzmann equation follows a similar route to the MFT derivation. The many-body system can be reduced into Boltzmann form by defining a many-body Wigner function

$$\begin{aligned} &f^{(N)}(\vec{x}_1, \vec{p}_1, ..., \vec{x}_N, \vec{p}_N, t) \\ &= \int d^3x'_1 \cdots d^3x'_N e^{i\sum_j^N \vec{p}_j \cdot \vec{x}'_j/\hbar} \Psi^\dagger(\vec{x}_1 + \vec{x}'_1/2, ..., \vec{x}_N + \vec{x}'_N/2, t)\Psi(\vec{x}_1 - \vec{x}'_1/2, ..., \vec{x}_1 - \vec{x}'_1/2, t) \end{aligned} \tag{3.120}$$

For brevity we understand the arguments of $\Psi^\dagger$ and Ψ are $\vec{x}_i + \vec{x}'_i/2$ and $\vec{x}_i - \vec{x}'_i/2$ respectively from this point on. The equation of motion for the distribution is found by straightforward

differentiation

$$\begin{aligned}&\partial_t f^{(N)}(\vec{x}_1, \vec{p}_1, ..., \vec{x}_N, \vec{p}_N, t) \\ &= \int d^3x'_1 \cdots d^3x'_N e^{i\sum_j^N \vec{p}_j \cdot \vec{x}'_j/\hbar} \left(\partial_t \Psi^\dagger \Psi + \Psi^\dagger \partial_t \Psi\right)\end{aligned} \tag{3.121}$$

Judicious substitution of the Schroedinger equation transitions the expression into an equation of motion

$$\begin{aligned}&\partial_t f^{(N)}(\vec{x}_1, \vec{p}_1, ..., \vec{x}_N, \vec{p}_N, t) \\ &= \frac{1}{i\hbar} \int d^3x'_1 \cdots d^3x'_N e^{i\sum_j^N \vec{p}_j \cdot \vec{x}'_j/\hbar} \left(-\hat{H}\Psi^\dagger \Psi + \Psi^\dagger \hat{H} \Psi\right)\end{aligned} \tag{3.122}$$

where the Hubble flow is absorbed into the time parameterization.

The kinetic contribution can be simplified through successive application of the product

rule of differentiation and consolidation of terms, and expectedly provides transport terms

$$
\begin{aligned}
K &= \frac{1}{i\hbar}\frac{\hbar^2}{2m}\sum_i^N \int d^3x'_1 \cdots d^3x'_N e^{i\sum_j^N \vec{p}_j\cdot\vec{x}'_j/\hbar}\left(\nabla^2_{\vec{x}_i+\vec{x}'_i/2}\Psi^\dagger\Psi - \Psi^\dagger\nabla^2_{\vec{x}_i+\vec{x}'_i/2}\Psi\right)\\
&= \frac{1}{i\hbar}\frac{4\hbar^2}{2m}\sum_i^N \int d^3x'_1 \cdots d^3x'_N e^{i\sum_j^N \vec{p}_j\cdot\vec{x}'_j/\hbar}\left(\nabla^2_{\vec{x}'_i}\Psi^\dagger\Psi - \Psi^\dagger\nabla^2_{\vec{x}'_i}\Psi\right)\\
&= \frac{1}{i\hbar}\frac{4\hbar^2}{2m}\sum_i^N \int d^3x'_1 \cdots d^3x'_N \vec{\nabla}_{\vec{x}'_i}\cdot\left(e^{i\sum_j^N \vec{p}_j\cdot\vec{x}'_j/\hbar}\left(\vec{\nabla}_{\vec{x}'_i}\Psi^\dagger\Psi - \Psi^\dagger\vec{\nabla}_{\vec{x}'_i}\Psi\right)\right)\\
&- \frac{1}{i\hbar}\frac{4\hbar^2}{2m}\sum_i^N \int d^3x'_1 \cdots d^3x'_N \left(\vec{\nabla}_{\vec{x}'_i}\Psi^\dagger\cdot\vec{\nabla}_{\vec{x}'_i}\left(e^{i\sum_j^N \vec{p}_j\cdot\vec{x}'_j/\hbar}\Psi\right) - \vec{\nabla}_{\vec{x}'_i}\left(e^{i\sum_j^N \vec{p}_j\cdot\vec{x}'_j/\hbar}\Psi^\dagger\right)\cdot\vec{\nabla}_{\vec{x}'_i}\Psi\right)\\
&= \frac{1}{i\hbar}\frac{4\hbar^2}{2m}\sum_i^N \int d^3x'_1 \cdots d^3x'_N \vec{\nabla}_{\vec{x}'_i}\cdot\left(e^{i\sum_j^N \vec{p}_j\cdot\vec{x}'_j/\hbar}\left(\vec{\nabla}_{\vec{x}'_i}\Psi^\dagger\Psi - \Psi^\dagger\vec{\nabla}_{\vec{x}'_i}\Psi\right)\right)\\
&+ \frac{1}{i\hbar}\frac{4\hbar^2}{2m}\sum_i^N \int d^3x'_1 \cdots d^3x'_N \left[-e^{i\sum_j^N \vec{p}_j\cdot\vec{x}'_j/\hbar}\frac{i\vec{p}_i}{\hbar}\cdot\vec{\nabla}_{\vec{x}'_i}\Psi^\dagger\cdot\Psi - e^{i\sum_j^N \vec{p}_j\cdot\vec{x}'_j/\hbar}\vec{\nabla}_{\vec{x}'_i}\Psi^\dagger\cdot\vec{\nabla}_{\vec{x}'_i}\Psi\right]\\
&+ \frac{1}{i\hbar}\frac{4\hbar^2}{2m}\sum_i^N \int d^3x'_1 \cdots d^3x'_N \left[e^{i\sum_j^N \vec{p}_j\cdot\vec{x}'_j/\hbar}\frac{i\vec{p}_i}{\hbar}\cdot\vec{\nabla}_{\vec{x}'_i}\Psi^\dagger\cdot\Psi + e^{i\sum_j^N \vec{p}_j\cdot\vec{x}'_j/\hbar}\vec{\nabla}_{\vec{x}'_i}\Psi^\dagger\cdot\vec{\nabla}_{\vec{x}'_i}\Psi\right]\\
&= \sum_i^N S_i + \frac{1}{i\hbar}\frac{4\hbar^2}{2m}\sum_i^N \int d^3x'_1 \cdots d^3x'_N \left[-e^{i\sum_j^N \vec{p}_j\cdot\vec{x}'_j/\hbar}\frac{i\vec{p}_i}{\hbar}\cdot\vec{\nabla}_{\vec{x}'_i}\Psi^\dagger\cdot\Psi + e^{i\sum_j^N \vec{p}_j\cdot\vec{x}'_j/\hbar}\vec{\nabla}_{\vec{x}'_i}\Psi^\dagger\cdot\vec{\nabla}_{\vec{x}'_i}\Psi\right]\\
&= \sum_i^N S_i + \frac{-1}{i\hbar}\frac{2\hbar^2}{2m}\sum_i^N \int d^3x'_1 \cdots d^3x'_N e^{i\sum_j^N \vec{p}_j\cdot\vec{x}'_j/\hbar}\frac{i\vec{p}_i}{\hbar}\cdot\vec{\nabla}_{\vec{x}_i}\left(\Psi^\dagger\Psi\right)\\
&= \sum_i^N S_i - \sum_i^N \frac{\vec{p}_i}{m}\vec{\nabla}_i f_N\\
&= -\sum_i^N \frac{\vec{p}_i}{m}\vec{\nabla}_i f_N + O(\hbar)
\end{aligned}
\tag{3.123}
$$

where $\{S_i\}$ are the surface integrals. The surface terms are supported by long deBroglie wavelength contributions, and again are inconsequential as the QCD axion scale is many orders of magnitude smaller than the desired scale of simulation.

The external potentials again give forcing contributions, found by Taylor expansion of

the potentials about $\vec{x}_i = 0$. Only the odd terms of the expansion survive.

$$\begin{aligned}
F_{ext} &= \frac{1}{i\hbar}\sum_i^N \int d^3x'_1 \cdots d^3x'_N e^{i\sum_j^N \vec{p}_j\cdot\vec{x}'_j/\hbar}\left(\Phi'(\vec{x}_i+\vec{x}'_i/2)\Psi^\dagger\Psi - \Psi^\dagger\Phi'(\vec{x}_i+\vec{x}'_i/2)\Psi\right) \\
&= \frac{1}{i\hbar}\sum_i^N \int d^3x'_1 \cdots d^3x'_N e^{i\sum_j^N \vec{p}_j\cdot\vec{x}'_j/\hbar}\vec{\nabla}_i\Phi'(\vec{x}_i)\cdot\vec{x}'_i\Psi^\dagger\Psi + O(\hbar^2) \\
&= \frac{1}{i\hbar}\frac{\hbar}{i}\sum_i^N \vec{\nabla}_i\Phi'\cdot\int d^3x'_1 \cdots d^3x'_N \vec{\nabla}_{p_i} e^{i\sum_j^N \vec{p}_j\cdot\vec{x}'_j/\hbar}\cdot\vec{x}'_i/2\Psi^\dagger\Psi + O(\hbar^2) \\
&= \sum_i^N \vec{\nabla}_i\Phi'\cdot\vec{\nabla}_{p_i} f_N + O(\hbar^2)
\end{aligned} \tag{3.124}$$

Finally, the two-body interaction potentials also contribute a forcing term

$$\begin{aligned}
F_{int} &= \frac{1}{2i\hbar}\sum_{i\neq j}^N \int d^3x'_1 \cdots d^3x'_N e^{i\sum_j^N \vec{p}_j\cdot\vec{x}'_j/\hbar}\left(\phi_{ij}(\vec{x}_i+\vec{x}'_i/2,\vec{x}_j+\vec{x}'_j/2)\Psi^\dagger\Psi - \Psi^\dagger\phi_{ij}(\vec{x}_i+\vec{x}'_i/2,\vec{x}_j+\vec{x}'_j/2)\Psi\right) \\
&= \frac{1}{2i\hbar}\sum_{i\neq j}^N \int d^3x'_1 \cdots d^3x'_N e^{i\sum_j^N \vec{p}_j\cdot\vec{x}'_j/\hbar}\left(\vec{\nabla}_i\phi_{ij}(\vec{x}_i,\vec{x}_j)\cdot\vec{x}'_i + \vec{\nabla}_j\phi_{ij}(\vec{x}_i,\vec{x}_j)\cdot\vec{x}'_j\right)\Psi^\dagger\Psi + O(\hbar^2) \\
&= \frac{1}{2i\hbar}\frac{\hbar}{i}\sum_{i\neq j}^N \int d^3x'_1 \cdots d^3x'_N \left(\vec{\nabla}_i\phi_{ij}\cdot\vec{\nabla}_{p_i} + \vec{\nabla}_j\phi_{ij}\cdot\vec{\nabla}_{p_j}\right) e^{i\sum_j^N \vec{p}_j\cdot\vec{x}'_j/\hbar}\cdot\vec{x}'_i/2\Psi^\dagger\Psi + O(\hbar^2) \\
&= \sum_{i\neq j}^N \vec{\nabla}_i\phi_{ij}\cdot\vec{\nabla}_{p_i} f_N + O(\hbar^2)
\end{aligned} \tag{3.125}$$

where ϕ_{ij} is the two-body gravitational potential. The result is a Boltzmann equation of motion which looks very similar to the classical form for a collision-less fluid

$$\partial_t f_N = K + F_{ext} + F_{int} \tag{3.126}$$

$$= -\sum_i^N \frac{\vec{p}_i}{m}\vec{\nabla}_i f_N + \sum_i^N \vec{\nabla}_i\Phi'\cdot\vec{\nabla}_{p_i} f_N + \sum_{i\neq j}^N \vec{\nabla}_i\phi_{ij}\cdot\vec{\nabla}_{p_i} f_N + O(\hbar^2) \tag{3.127}$$

We concern ourselves with the Boltzmann equation composed of only lowest order terms. Note that so far we have not enforced any dynamics or even exchange conditions on the state. Such a Boltzmann equation may also by applied to many-body fermionic or mixed systems.

Condensation and the Many-Body Axion Boltzmann Equation

There are a few further simplifications that can be made in the case of axion SF before integrating out superfluous degrees of freedom. The many-body DF expressed as a single coherent state has the form

$$f^{(N)}(\vec{x}_1,\vec{p}_1,...,\vec{x}_N,\vec{p}_N,t)$$
$$=\int d^3x'_1\cdots d^3x'_N e^{i\sum_j^N \vec{p}_j\cdot\vec{x}'_j/\hbar}\prod_{\substack{ij\\ \alpha}}\psi^\dagger_\alpha\left(\vec{x}_i-\vec{x}_j+\vec{x}'_i/2-\vec{x}'_j/2,t\right)\prod_{\substack{ij\\ \alpha}}\psi_\alpha\left(\vec{x}_i-\vec{x}_j-\vec{x}'_i/2+\vec{x}'_j/2,t\right) \tag{3.128}$$

Placing every axion into the same state condenses ever axion state index and the DF collapses to

$$f^{(N)}(\vec{x}_1,\vec{p}_1,...,\vec{x}_N,\vec{p}_N,t)$$
$$=\int d^3x'_1\cdots d^3x'_N e^{i\sum_j^N \vec{p}_j\cdot\vec{x}'_j/\hbar}\prod_{i\neq j}\psi^\dagger_a\left(\vec{x}_i-\vec{x}_j+\vec{x}'_i/2-\vec{x}'_j/2,t\right)\prod_{i\neq j}\psi_a\left(\vec{x}_i-\vec{x}_j-\vec{x}'_i/2+\vec{x}'_j/2,t\right) \tag{3.129}$$

Using a similar projection trick as in Appx. F, the 'wave-functions' may be condensed into 'distribution functions', bringing the total DF to

$$f^{(N)}(\vec{x}_1,\vec{p}_1,...,\vec{x}_N,\vec{p}_N,t)=\prod_{i\neq j}g_a\left(\vec{x}_i-\vec{x}_j,t\right) \tag{3.130}$$

where

$$g\left(\vec{\Delta}_{ij}\right)=\int d^3\Delta'_{ij}e^{i\vec{p}_{ij}\cdot\vec{\Delta}_{ij}/\hbar}\psi^\dagger_a\left(\vec{\Delta}_{ij}+\vec{\Delta}'_{ij}/2,t\right)\psi_a\left(\vec{\Delta}_{ij}-\vec{\Delta}'_{ij}/2,t\right) \tag{3.131}$$

Explicit correlations and exchange symmetries between particles make for a far more straightforward XC contribution to the final motive equation.

Reduction to Single DF

Now to bring the many-body motive equation down to a central single particle description. We follow the approach of projection through integration of the ephemeral degrees of freedom

$$f^{(M)}=\int d^6w_{M+1}\cdots d^6w_N f^{(N)} \tag{3.132}$$

where $w_i = (\vec{x}_i, \vec{p}_i)$ is the i-th six dimensional phase space. Expectations of various operators follow analogously. Performing the single-body projection on the entire Boltzmann equation

$$0 = \int d^6w_2 \cdots d^6w_N \left[\partial_t f^{(N)} + \sum_i^N \frac{\vec{p}_i}{m} \vec{\nabla}_i f^{(N)} - \sum_i^N \vec{\nabla}_i \Phi' \cdot \vec{\nabla}_{p_i} f_N - \sum_{i \neq j}^N \vec{\nabla}_i \phi_{ij} \cdot \vec{\nabla}_{p_i} f^{(N)} \right] \tag{3.133}$$

the explicit time component reduces to

$$\int d^6w_2 \cdots d^6w_N \partial_t f^{(N)} = N \partial_t f^{(1)}, \tag{3.134}$$

where an explanation for the N factor may be found in Appx. E. The kinetic transport term reduces as expected due to the divergence theorem

$$\int d^6w_2 \cdots d^6w_N \sum_i^N \frac{\vec{p}_i}{m} \vec{\nabla}_i f^{(N)} = N \frac{\vec{p}_1}{m} \vec{\nabla}_1 f^{(1)}, \tag{3.135}$$

and the external potential forcing term reduces similarly

$$- \int d^6w_2 \cdots d^6w_N \sum_i^N \vec{\nabla}_i \Phi' \cdot \vec{\nabla}_{p_i} f^{(N)} = -N \vec{\nabla}_1 \Phi' \cdot \vec{\nabla}_{p_1} f^{(1)} \tag{3.136}$$

The primary complication rests in the interactive forcing term, which retains connection to integrated phase spaces via the two-body gravitational interactions

$$- \int d^6w_2 \cdots d^6w_N \sum_{i \neq j}^N \vec{\nabla}_i \phi_{ij} \cdot \vec{\nabla}_{p_i} f^{(N)} = - \int d^6w_j \sum_{j>1}^N \vec{\nabla}_1 \phi_{1j} \cdot \vec{\nabla}_{p_1} f^{(2)} \tag{3.137}$$

Assuming that the axion fluid can attain a solution of the form Eqn. 3.118 even with an external potential, insert our specific f_N into the reduced Boltzmann equation. The usefulness of its convoluted representation comes to light through the interactive forcing term

$$- \int d^6w_j \sum_{j>1}^N \vec{\nabla}_1 \phi_{1j} \cdot \vec{\nabla}_{p_1} f^{(2)} = - \int d^6w_j \sum_{j>1}^N \vec{\nabla}_1 \phi_{1j} \cdot \vec{\nabla}_{p_1} g_a h_a \tag{3.138}$$

where

$$h_a = \int d^6w_3 \cdots d^6w_N \prod_{i \neq j (i,j) \neq (1,2)} g_a \left(\vec{x}_i - \vec{x}_j, t \right) \tag{3.139}$$

and g_a shares the same argument. Let us rewrite $f^{(2)}$ in a form that makes the correlations between single-body DFs more obvious

$$f^{(2)}(w_1, w_2, t) = f^{(1)}(w_1, t)\tilde{g}f^{(1)}(w_2, t) \tag{3.140}$$

where the correlation function $\tilde{g}$ is seen to be symmetric with over both phase spaces. This form has some cute properties. In addition to the standard normalization of the single-body DF

$$\int d^6 w_1 f^{(1)} = 1 \tag{3.141}$$

we also have a normalization condition on the correlation function

$$\int d^6 w_1 \tilde{g} f^{(1)} = 1 \tag{3.142}$$

We do not expect this correlation function to inherently encapsulate the condensate behavior in the same way as the overly-complex $g_a h_a$ expression pools the response of every axion. Instead, we derive the condensed form of $\tilde{g}$ through a combination of mathematical maneuvers and physical conjectures. Assuming $\tilde{g}$ depends only on the local single-body DF and its first derivatives, $\tilde{g}(f^{(1)}, \partial_\nu f^{(1)})$, an invariant functional may be constructed from the normalization properties

$$I = \int d^6 w_1 \left(g_+ f^{(1)} - \lambda f^{(1)} \right) \tag{3.143}$$

where

$$g_+ 2 \left(\tilde{g}(w_1, w_2) + \tilde{g}(w_2, w_1) \right) = \tilde{g} \tag{3.144}$$

The functional is found to be nontrivially invariant under time-translation and transformations of phase space w_2. A variation of Noether's First Theorem (NFT) gives us equations of state for g_+ enough to narrow a solution

$$\text{time: } \lambda \partial_t f_+ + g_+ \partial_t f_+ + f_+ \frac{\partial g_+}{\partial f_+} \partial_t f_+ + f_+ \frac{\partial g_+}{\partial \partial_\mu f_+} \partial_\mu \partial_t f_+ = 0 \tag{3.145}$$

$$w_2\text{: } \frac{\partial g_+}{\partial f_1(w_2, t)} f_1(w_1, t) \partial_\alpha f_1(w_2, t) + f_+ \frac{\partial g_+}{\partial \partial_\mu f_1(w_2, t)} \partial_\mu f_1(w_1, t) \partial_\alpha f_1(w_2, t) = 0 \tag{3.146}$$

where in the time result we have exploited $\tilde{g}$'s exchange symmetry. The above equations are made under the additional assumption that g_+ depends only on $f_+ = 1/2\,(f^1(w_1,t) + f^1(w_2,t))$ and its first derivatives.

We do not expect g_+ to be analytic due to the existence of a *de facto* phase transition at the condensation critical point. Below this point exists the normal/dissociated limit for the Bose system, where both f_+ and $\partial_\mu f_+$ are small. We expand about a state far above the critical point. Constructing a solution as an analytic expansion about some configuration significant to the DF

$$g_+ = \sum_k = 0^\infty A_k \left(\frac{C^\mu \partial_\mu f_+}{f_+} - S \right)^k \tag{3.147}$$

where the C^μ are functions of phase space and S is a quantity central to our configuration, such that

$$S = \int d^6 w_1 f^{(1)}(w_1,t) \frac{C^\mu \partial_\mu f_+}{f_+} \tag{3.148}$$

at any time as f_+ is an integral of motion. Solving a more stringent form of the time equation

$$\lambda f_+ + g_+ \partial_t f_+ + f_+ \frac{\partial g_+}{\partial f_+} f_+ + f_+ \frac{\partial g_+}{\partial \partial_\mu f_+} \partial_\mu f_+ = 0 \tag{3.149}$$

produces the expected infinite tower of equations

$$\left\{ 0 = \lambda \delta_{k,0} + \sum_{l \geq k} A_l (-S)^{l-k-1} \binom{l}{k} \right\}_{l \in \{0,1,\ldots\}} \tag{3.150}$$

The expansion is expected to be convergent in an asymptotic sense, so we shall truncate the solution here at $l = 1$. This truncated form gives

$$A_0 = \epsilon S - \lambda \tag{3.151}$$

$$A_1 = \epsilon \tag{3.152}$$

where ϵ is assumed to be small. The truncated correlation function then takes the form

$$\tilde{g} = (\epsilon S - \lambda) + \epsilon \left(\frac{C^\mu \partial_\mu f_+}{f_+} - S \right) \tag{3.153}$$

The phase space equation allows us to set boundaries on the C^μ

$$\frac{C^\mu \partial_\alpha \partial_\mu f^{(1)}(w_2,t)}{C^\mu \partial_\mu f_+} = \frac{\partial_\alpha f^{(1)}(w_2,t)}{f_+} \tag{3.154}$$

which we take to be the phase-space separation. Normalization of the correlation function can be enforced through Eqn. 3.142

$$\begin{aligned} 1 &= \int f^{(1)}(w_1,t)\left(\epsilon S - \lambda + \epsilon\left(\frac{C^\mu \partial_\mu f_+}{f_+} - S\right)\right) \\ &= \epsilon S - \lambda + 0, \end{aligned} \tag{3.155}$$

setting a balance between λ and ϵ.

Now we may simplify the Boltzmann forcing term.

$$\begin{aligned} &-\int d^6 w_j \sum_{j>1}^{N} \vec{\nabla}_1 \phi_{1j} \cdot \vec{\nabla}_{p_1} f^{(2)} = \\ &-\int d^6 w_j \sum_{j>1}^{N} \vec{\nabla}_1 \phi_{1j} \cdot \vec{\nabla}_{p_1} f^{(1)}(w_1,t) f^{(1)}(w_j,t)\left((\epsilon S - \lambda) + \epsilon\left(\frac{C^\mu \partial_\mu f_+}{f_+} - S\right)\right) \\ &= (N-1)\lambda \vec{\nabla}\Phi \cdot \vec{\nabla}_p f^{(1)}(w_1,t) - (N-1)\int d^6 w_j \sum_{j>1}^{N} \vec{\nabla}_1 \phi_{1j} \cdot \vec{\nabla}_{p_1} f^{(1)}(w_1,t) f^{(1)}(w_j,t)\epsilon \frac{C^\mu \partial_\mu f_+}{f_+} \\ &= -(N-1)(1-\epsilon S)\vec{\nabla}\Phi \cdot \vec{\nabla}_p f^{(1)}(w_1,t) - (N-1)\epsilon \vec{\nabla}\Theta \cdot \vec{\nabla}_p f^{(1)}(w_1,t) \end{aligned} \tag{3.156}$$

where Θ is defined to be the gravitational cross-correlation (XC) potential

$$\Theta = \int d^6 w_2 \phi_{1j} \frac{C^\mu \partial_\mu f_+}{f_+} f^{(1)}(w_2,t) \tag{3.157}$$

Both the averaged Newtonian and XC potentials can be written as sourced by the single-body DF

$$\begin{aligned} \nabla^2 \Phi &= 4\pi G \rho \\ \nabla^2 \Theta &= 4\pi G \int d^6 w_2 \delta^3\left(\vec{x}_1 - \vec{x}_2\right) \frac{C^\mu \partial_\mu f_+}{f_+} f^{(1)}(w_2,t) \end{aligned} \tag{3.158}$$

The final form of the Boltzmann system is

$$\partial_t f^{(1)} + \frac{\vec{p}}{m_a} \cdot \vec{\nabla} f^{(1)} - \frac{N-1}{N}\left[(1-\epsilon S)\,\vec{\nabla}\Phi \cdot \vec{\nabla}_p f^{(1)} - \epsilon \vec{\nabla}\Theta \cdot \vec{\nabla}_p f^{(1)}\right] = 0 \tag{3.159}$$

We shall take $\frac{N-1}{N}$ to be 1 for cosmological situations.

3.4.5 Thermal Generalizations

Let us get back to what it means to be a BEC for a gravitating system. State dispersion should be taken into account in light of the potentially dense Hamiltonian spectra about the axions' initial conditions, and the potential for a mixed state set by the creation mechanism and/or environmental interactions.

Just as in the MFT case, consider the density operator for the many-body system

$$\hat{\rho} = \sum_{\gamma} p_{\gamma} |\chi_{\gamma} >< \chi_{\gamma}| \tag{3.160}$$

which evolves like

$$\partial_t \hat{\rho} = [\hat{\rho}, \hat{H}] \tag{3.161}$$

The density evolution may be broken down into the evolution of individual states, and an equation of motion may be derived for the DF expectation value

$$\partial_t \left\langle \hat{f}^N \right\rangle = \frac{1}{i\hbar} Tr \left(\hat{\rho} [\hat{f}^N, \hat{H}] \right) \tag{3.162}$$

where $\hat{f}^N$ is the operator form of the many-body Wigner transform. The elements composing the right and left hand sides of Eqn. 3.162 can be shown element-wise to be equivalent to Eqn. 3.127 and the thermal Boltzmann equation may be simplified to

$$\partial_t \bar{f}^N + \sum_{i}^{N} \frac{\vec{p_i}}{m} \vec{\nabla}_i \bar{f}^N - \sum_{i}^{N} \vec{\nabla}_i \Phi' \cdot \vec{\nabla}_{p_i} \bar{f}^N - \sum_{i \neq j}^{N} \vec{\nabla}_i \phi_{ij} \cdot \vec{\nabla}_{p_i} \bar{f}^N = 0 \tag{3.163}$$

where $\bar{f}^N = \left\langle \hat{f}^N \right\rangle$.

Reducing to a single body distribution also parallels the single state case, producing

$$\partial_t \bar{f}^1 + \frac{\vec{p}}{m} \cdot \vec{\nabla} \bar{f}^1 - \vec{\nabla} V \cdot \vec{\nabla}_{p_1} \bar{f}^1 - \int d^6 w_j \sum_{j>1}^{N} \vec{\nabla} \phi_{1j} \cdot \vec{\nabla}_p \bar{f}^2 = 0 \tag{3.164}$$

Finding a solution to the interaction forcing term follows the condensed case very closely. The mathematics of defining $\tilde{\bar{g}}$ and implementing NFT on an analogous functional all follow

in lock step, but the physical conjectures differ slightly. The arguments and algebraic form of the correlation $\tilde{\bar{g}}$ are chosen to be the same

$$\tilde{\bar{g}} = \sum_k = 0^{\infty} A_k \left(\frac{\bar{C}^{\mu} \partial_{\mu} \bar{f}_+}{\bar{f}_+} - \bar{S} \right)^k \tag{3.165}$$

The definition of $\bar{f}_+$ and $\bar{S}$ also follow the same prescription

$$\bar{f}_+ = \frac{1}{2} \left(\bar{f}^1(w_1, t) + \bar{f}^1(w_2, t) \right) \tag{3.166}$$

$$\bar{S} = \int d^6 w_1 \bar{f}^{(1)}(w_1, t) \frac{\bar{C}^{\mu} \partial_{\mu} \bar{f}_+}{\bar{f}_+} \tag{3.167}$$

where in progressively dispersed systems $\bar{S}$ is expected to take on value closer to the disassociated fluid limit ($\bar{S}_{diss} = 0$). Taking the same $l = 1$ cutoff in the normalized correlation power series results also in a familiar form

$$\tilde{\bar{g}} = 1 + \bar{\epsilon} \left(\frac{\bar{C}^{\mu} \partial_{\mu} \bar{f}_+}{\bar{f}_+} - \bar{S} \right) \tag{3.168}$$

where the identical mathematics of the power series also show us that that $\bar{\epsilon} = \epsilon$. The primary difference between the condensed and mixed dynamics is most apparent in the final form of the potential and Boltzmann equations

$$\nabla^2 \bar{\Phi} = 4\pi G \bar{\rho} \tag{3.169}$$

$$\nabla^2 \bar{\Theta} = 4\pi G \int d^6 w_2 \delta^3 \left(\vec{x}_1 - \vec{x}_2 \right) \frac{\bar{C}^{\mu} \partial_{\mu} \bar{f}_+}{\bar{f}_+} \bar{f}^{(1)}(w_2, t) \tag{3.170}$$

$$0 = \partial_t \bar{f}^{(1)} + \frac{\vec{p}}{m_a} \cdot \vec{\nabla} \bar{f}^{(1)} - (1 - \epsilon S) \vec{\nabla} \bar{\Phi} \cdot \vec{\nabla}_p \bar{f}^{(1)} - \epsilon \vec{\nabla} \bar{\Theta} \cdot \vec{\nabla}_p f^{(1)} \tag{3.171}$$

We have yet to specify $\bar{C}$. In the condensed case we conjecture that this correlation length be set to the bare axion-separation. Mixed configurations are not expected to have infinite correlation lengths. As the mixed states far outnumber the condensed states, we expect a degradation in the extent of $\bar{C}$. This lays out our new definition of BEC as a correlation condition: a system is condensed if the effective XC length of the system as measured by $\sigma_{|\bar{C}|/|C|}$ exceeds the extent of the system. Further study of the statistics and dynamics involved in motivating and specifying a form for $\bar{C}$ is needed.

3.4.6 Creating N-Body Algorithms

The last steps in forming an algorithm implementable into ChaNGa are to first derive particle equations of motion for a sample of the axion distribution, then develop accurate discretized solvers in the time domain. Our derivations here are restricted to purely condensed axion DM.

Method of Characteristics

The equations of motion for relic axions near coherence are complex, requiring a comprehensive scheme to find solutions through the highly non-linear collapse process. The Boltzmann system falls into the hyperbolic class of PDE's similar to conservation laws and wave equations, which are amenable to many elegant numerical solvers such as Finite Element Methods (FEM) and the Method Of Characteristics (MOC). MOC is decidedly the best suited for discretizing the continuum Boltzmann equation and fulfilling project requirements. A Lagrangian method, MOC propagates integrals of motion to a system of differential equations through parameter space to form an accurate sample of the solution. For an extensive review of the technique, see Courant and Hilbert vol. 2 (Courant & Hilbert, 1953). Conveniently, our system is of first order in derivatives, requiring only a rudimentary level of understanding of the MOC.

The Boltzmann equation of motion falls into the class of Partial Differential Equations (PDEs) of the form

$$F(\{x_i\}, u, \{p_i\}) = 0 \tag{3.172}$$

where $\{x_i\}$ are all n coordinates, u is the solving function, the variables $p_i = \partial_i u$ are the partial derivatives, and F is first-order smooth in its arguments. This implies that F is an integral of motion. If u is any solution to the defining equation, let us construct a curve in $\Re^{2n+1}$ of $(\{x_i(s)\}, u(s), \{p_i(s)\})$ such that $u(s) = u(\{x_i(s)\})$. Differentiating Eqn. 3.172 along the curve gives

$$\sum_i \left(\partial_{x_i} F + \partial_u F p_i\right) \dot{x}_i + \sum_i \partial_{p_i} F \dot{p}_i = 0 \tag{3.173}$$

A constraint equation can also be found in u

$$\dot{u} - \sum_i p_i \dot{x}_i = 0 \tag{3.174}$$

More generally the form $du - \sum_i p_i dx_i = 0$ also holds and a second constraint may be found from taking an exterior derivative

$$\begin{aligned} 0 &= d\left(du - \sum_i p_i dx_i\right) \\ &= \sum_i \left(dp_i \dot{x}_i - \dot{p}_i dx_i\right) \end{aligned} \tag{3.175}$$

Altogether these relations may be organized to provide equations of motion for the solution along the path

$$\dot{u} = \sum_i p_i F_{p_i} \tag{3.176}$$

$$\dot{x}_i = F_{p_i} \tag{3.177}$$

$$\dot{p}_i = -F_{x_i} - F_u p_i \tag{3.178}$$

For our first-order axion Boltzmann equation, we see again that f_1 is an integral of characteristic motion. Further the equation form appears to be much like that from a Hamilton's principle with Hamiltonian F. We choose time to be the suitable parameterization of the characteristic. The characteristic equations are specifically found to be

$$\dot{f}^1 = 0 \tag{3.179}$$

$$\dot{\vec{x}} = \frac{\vec{p}}{\mu} \tag{3.180}$$

$$\dot{\vec{p}} = -\vec{\nabla}\Phi' - (1 - \epsilon S)\vec{\nabla}\Phi - \epsilon\vec{\nabla}\Theta \tag{3.181}$$

where the dot total derivatives are now with respect to time. We can clearly see how the particle physics differs from the standard Newton's second law of WIMP and MFT literature. It is worth noting that the solution to these samples are exact, so long as the Φ', Φ, and Θ are known. The parabolic Poisson PDE for the gravitational potential must also be solved

at each distribution sample to calculate the gravitational force contribution, which is where exactness of modern gravitational MOC N-Body implementations breaks down, though it is still very accurate.

In practice MOC is used to track many sample characteristics from some initial Cauchy surface to a prescribed end time, Fig. 3.6. As the DF is constant along these characteristic curves, choosing sample points according to distribution weight creates an effective distribution sampling from which equal-time observables may be calculated. These sample points are often referred to as particles or bodies, though they do not necessarily map directly to individual axions.

Leap-Frog Symplectic Integration

There is still one dimension left to partition before the axion fluid can be translated to machine language. Due to the invariance of the phase-space DF (i.e. $df_1/dt = 0$), it is wise to choose an integrator which preserves the structure of phase-space.

An integrator of our phase-space samples effectively maps them from an initial time slice to another according to their equations of motion

$$(\vec{x}(t_i), \vec{p}(t_i)) \xmapsto{G_{(t_f - t_i)}} (\vec{x}(t_f), \vec{p}(t_f)) \tag{3.182}$$

A numerical integrator is also such a map, which aims to approximate the exact evolution map. Numerical integrators are often broken up into smaller maps, based on a Courant or other type of convergence condition, and composed many times over to cover the desired span.

$$G_{t_j+\delta_j} \circ \cdots \circ G_{t_1+\delta_1} \circ G_{t_0+\delta_0} (\vec{x}(t_i), \vec{p}(t_i)) = (\vec{x}(t_f), \vec{p}(t_f)) \tag{3.183}$$

where $t_k = t_0 + \sum_{i=0}^{k-1} \delta_i$ and g is the numerical integrator. The numerical integrator chosen for the project is the symplectic leapfrog method.

In short, a symplectic integrator is a one that preserves volumes. A whole class of such integrators may be understood from classical hamiltonian principles. From the MOC

derivations, we can see that the particle equations of motion allow for a classical Poisson-like operator equation

$$\dot{w} = \{w, H\} \tag{3.184}$$

where $w = (\vec{x}, \vec{p})$ and H is the system's Hamiltonian. The axion hamiltonian-like operator is nicely separable along position and momentum lines

$$H = H_p + H_x \tag{3.185}$$

allowing for the definition of Poisson operators

$$T = \{\cdot, H_p\}\, V = \{\cdot, H_x\} \tag{3.186}$$

First order equations of this type have solutions, which can be expressed in operator form

$$w(t) = e^{(T+V)t} w(0) \tag{3.187}$$

with the operator giving the full phase-space integrator of w.

To divide up this difficult operator we appeal to the Baker-Campbell-Hausdorff (BCH) identity

$$e^{Tt} e^{Vt} = exp\left((T+V)t + \frac{1}{2}[T,V]t^2 + \frac{1}{12}[T-V,[T,V]]t^3 + ...\right) \tag{3.188}$$

The operators on the LHS are far easier to compute, but are equivalent to evolving the particle under a Hamiltonian

$$H_p + H_x + H_{error} \tag{3.189}$$

where H_{error} is of order t leading to errors in w of order t^2.

The integrator chosen for the project does one order better. By using an additional term on the RHS of Eqn. 3.188 and taking appropriate operator inverses, we may create an evolution operator with error of order t^3

$$e^{Tt/2} e^{Vt} e^{Tt/2} = exp\left((T+V)t + O(t^3)\right) \tag{3.190}$$

This integrator goes by the name of leapfrog as uses overlapping streaming and forcing operations, Fig. 3.7, and is the native integrator of ChaNGa. The classes of maps which come

from using the BCH identity to approximate the full exponential with integrable operators are area-preserving or symplectic maps.

Applied to our axion system the equations of motion for a sample particle become

$$\vec{x}_1(t/2) = \vec{x}_1(0) + \frac{\vec{p}(0)}{m}\frac{t}{2} \tag{3.191}$$

$$\vec{x}_1(t) = \vec{v}_1(0) - t\left(-\vec{\nabla}_1\Phi' - (1-\epsilon S)\vec{\nabla}_1\Phi - \epsilon\vec{\nabla}_1\Theta\right)|_{\vec{x}_1(t/2)} \tag{3.192}$$

$$\vec{x}_1(t) = \vec{x}_1(t/2) + \frac{\vec{p}(t)}{m}\frac{t}{2} \tag{3.193}$$

We use the usual Courant convergence condition to ensure stability in leapfrog

$$C = \Delta t \sum_{\hat{n}=\hat{x},\hat{y},\hat{z}} \frac{\vec{p}\cdot\hat{n}}{m\Delta\vec{x}\cdot\hat{n}} \leq C_{max} \tag{3.194}$$

where C_{max} is often set to unity and the Δp and Δx are related to the dynamical scales of the system. The next step is to test these algorithms on some simple systems.

3.5 Preliminary Tests: AXP

It is prudent to develop a small-scale test platform to refine our numerical description of axion infall before spending the capital of implementing the algorithms into ChaNGa. This step is performed by a prototype N-Body code Axions in eXternal Potential (AXP) to simulate small systems of interacting degenerate bosons. In short, AXP takes a prescribed sampling axion particles and potential interactions and evolves the MOC equations using the leapfrog integrator to some final time. This section discusses the make-up of AXP and its results on some simple self-gravitating examples. The contents of this section are preliminary.

3.5.1 Parameters and Algorithms

Algorithms for the potentials, the extent of the XC physics, and the numerical convergence constraints still need to be specified. AXP is run in the condensed limit. We prescribe a value of $\epsilon = 0.15$ in the absence of a full understanding of the size of the XC effects. The leapfrog time-steps are set to $10^{-2}t_{dyn}$, corresponding to $C = O(10^{-2})$, where t_{dyn} is the

dynamical crossing time for a typical orbit. The specific Courant value for faster and slower orbits are larger and smaller respectively.

Potentials in large-scale codes like ChaNGa are calculated using sophisticated tree decompositions and multi-pole expansions to improve computational scaling towards $O(N \log N)$. AXP uses a more direct approach in the interest of developmental efficiency and agility. The direct gravity algorithm finds the force on a particle by directly calculating the contribution of every other particle. This algorithm scales as $O(N^2)$, meaning the code is only effective for small numbers of particles. Using the coulomb kernel fro a particle's gravitational potential is not appropriate as each 'particle' represents many axion quanta. Instead we use a softened potential with plumber profile (Binney & Tremaine, 2008). ChaNGa does not use Plumber, instead favoring a spline mass profile with properties adventageous for multi-pole expansion. A softening length commensurate with the particle density is used in our examples

$$d_{soft} \approx \left(\frac{4/3\pi R^3}{N} \right)^{1/3} \tag{3.195}$$

where R is the typical radial length scale.

The XC potenial requires some more attention. We address the integral form of the Θ force term due to our decision to directly calculate forces

$$\vec{\nabla}\Theta = N \int d^6 w_2 \vec{\nabla}\phi_{12} f^{(1)}(w_2, t) \frac{C^\mu \partial_\mu f_+}{f_+} \tag{3.196}$$

We take simplifying steps using basic integral techniques, resulting in a form directly calcuable from the graitatinal kernel.

$$\vec{\nabla}\Theta = -N \int d^6 w_2 f^{(1)}(w_2, t) C \cdot hess\left(\phi_{12}\right) \tag{3.197}$$

where $hess(\cdot)$ is the hessian operator. This expression reduces in the N-body limit to a direct sum of the correlated gravitational hessian over all (other) particles. The plumber potential is used also for the XC direct sum. Note that the XC force is still central and for the infinite range correlations it has an analogous potential, meaning that both angular momentum and energy are conserved quantities of the Bose system.

3.5.2 Spherical Collapse Simulations

The most sophisticated simulations run to date on AXP are of cold spherical collapse in three dimensions. The largest of these simulations consist of 1000 particles arranged in an isotropic gaussian distribution of unite dispersion ($\sigma_r = 1$). Sample particles are chosen over the gaussian through a metropolis-hastings algorithm. Siulations are run over nearly ten dynamical times of a particle displaced σ_r from the center. Stills from sample simulations of classical and Bose collapse may be seen in Fig. 3.8.

3.5.3 Results and Prognosis

Differences in structure are obvious in the post-collapse configurations. The presence of a bar structure at the core of a classical collapse is expected, induced by a well-known radial orbit instability. The observed preservation of the spherical symetry in the Bose case is unexpected. We may begin to understand this unique Bose structure by comparing profiles, Fig. 3.9. Comparable spherical density profiles are surprising given the visible differences in the apatial density, however this may point to a universality of virialization of collisionless fluids in a non-cosmological setting.

The angular analyses are better at displaying the observed structural difference. Enclosed mass shows a distinct difference between the classical and Bose dynamics, with the shifted Bose profile implying a narrower angular momentum distribution, Fig. 3.10. Direct observation of the angular momentum distributions show a far more columnated profile under Bose physics than classical, Fig. 3.11. The calssical case may be understood by considering the formation of the bar. In the beginning no particles have angular momenta. As the bar forms particles on either side oare torqued to varying degrees, giving an extensive angular momentum distribution that gorws with time as the bar grows. The lack of a bar in the Bose case implies that angular momentum changes little from the initial frozen distribution.

This impact is seen more clearly in Fig. 3.12. The initial disruptive collapse interactions impart angular momnetum to particles in both simulations, with lesser impacts in the equili-

bration phase. The accumulation of $|j|$ in the classical case agrees with our understanding of the bar. The near-conservation during Bose equilibration also conforms to our understanding of spherical symmetric structures subject to central forces, though more study is required to understand how the XC potential is better able to preserve the spherical structure.

We achieve a great milestone with the spherical collapse simulations. From an fundamental theory of axion dynamics we derive an inclusive model of Bose infall, develop efficient algorithms to power numerical simulations of cosmological SF froe QCD axion DM, and are currently running the first of these simulations. Further, these simulations show that unique Bose structures are capable of surviving violent collapse! There is still much to learn about the meaning and extent of this new physics, but that is a matter for future work.

3.6 Understanding CDM Halos

The second path to the project involves better understanding the structures formed by CDM. While such simulations are currently the norm, there are still open questions surrounding the gravitational collapse and virialization of collision-less fluids and their interactions with baryonic components. This section presents several efforts to classify and understand these principles, managing also to provide valuable information to axion searches in the form of a best-estimate signal model.

3.6.1 Properties of Basic Gravitational Collapse

The following subsection is based on work first submitted to the Astrophysical Journal (ApJ) in December 2015, later published May 2016. To read the publication in full, see Lentz et al. (2016).

The ΛCDM model is considered by many to be the most successful to date in predicting cosmological structure formation in our universe, and is often referred to as the standard model of cosmology (see Planck Collaboration et al. (2014, 2016b) for a review). ΛCDM matches large-scale structure observations down to a few Mpc (Eisenstein et al., 2005). Even below a Mpc, ΛCDM provides vast insight into the formation of clusters, galactic halos, and

sub-halos; but its limitations also become more evident.

One of these limitations is the so-called core-cusp problem, which can be described as an inconsistency between the inner density profiles of halos found in numerical simulation and those extracted from galactic observations (Moore, 1994; Flores & Primack, 1994), with the density inside a scale radius being much shallower than expected (Walker et al., 2010). Approximating the density ρ scaling as a power law at small radii ($\rho \propto r^{\alpha}$ for $r \to 0$), Cold Dark Matter (CDM) numerical predictions show a nearly universal profile with $\alpha = -1$ or steeper, which closely resembles the curve put forth by Navarro et al. (1996a) (Navarro et al., 1996b; Moore, 1994; Moore et al., 1998, 1999). Current observations, however, provide scaling much closer to $\alpha = -0.5$ or even flat ($\alpha = 0.0$) (Navarro et al., 2010). Further, the central density of a dwarf DM halo is observed to be constant ($\sim 10^8 M_{\odot}\mathrm{kpc}^{-3}$) over multiple orders of magnitude in halo mass (Strigari et al., 2006; Gilmore et al., 2007; Hayashi & Chiba, 2015).

Attempts have been made to understand the nature of the universal profile, which we will approximate using the Navarro-Frenk-White (NFW) profile (Navarro et al., 1996a,b). Statistical techniques applied to this understanding include analysis of approximate integrals of motion during entropy maximization (Pontzen & Governato, 2013), semi-analytic equilibrium phase-space density estimation (Taylor & Navarro, 2001; Barnes et al., 2006), and mass accretion history (Ludlow et al., 2013). Under various constraints, the integral and equilibrium studies produce NFW-like profiles, though there are still gaps in understanding of each technique's motivations, keeping the physical cause of NFW ambiguous. Accretion history studies have also made progress in identifying the limits of NFW, but still fall short in identifying the fundamental mechanisms responsible for the observed similarity. Other semi-analytical approaches include spherical shell collapse models, which produce results that appear to challenge universality (Zukin & Bertschinger, 2010a,b).

The evolution equations governing structure formation are in general non-linear and, as a result, both direct and semi-analytic approaches are used to solve them. To date, semi-analytic methods have probed structure formation before the time of first-crossing,

contributing to topics from angular momentum distribution to the cosmic web (Binney & Quinn, 1991; Quinn & Binney, 1992; Ryden & Gunn, 1987; Casuso & Beckman, 2015; Pichon et al., 2016; Codis et al., 2015). While these methods cannot probe the current epoch, their form and computational efficiency provide agility when surveying classes of models. To reach virialization, a full non-linear approach is needed to retain any sort of accuracy. Thankfully, powerful numerical schemes have been developed which leverage the ever-increasing computational power available. These techniques include both particle, mesh, and hybrid codes, many with sophisticated optimizations that allow them to scale quite efficiently (Jetley et al., 2008; Springel, 2005; Couchman et al., 1995; O'Shea et al., 2004).

We concentrate on how computational methods have been used to study the feature of angular momentum and its role in structure formation (Bellovary et al., 2008; Bullock et al., 2001; van den Bosch, 2002; Barnes & Efstathiou, 1987; Gardner, 2001; Herpich et al., 2015). Most angular momentum studies quantify a structure's spin by the parameter λ (Peebles, 1969)

$$\lambda = \frac{J|E|^{1/2}}{GM^{5/2}} \tag{3.198}$$

where J is the magnitude of the total angular momentum, E is the total energy, and M is the total mass of the halo.

Angular momentum analysis of cosmological structures has a decades-long history, with analyses that span over both the linear and non-linear approaches. Chief among their findings is the log-normal distribution to total halo spins, with semi-analytics producing a mean value of $\lambda \sim 0.09$ (Ryden, 1988) and non-linear means giving $\lambda \sim 0.035$ (Bullock et al., 2001; Barnes & Efstathiou, 1987), both essentially contained well within the small rotational energy limit. Our structure analysis focuses on how halo formation is affected over a range of possible spin values and the subsequent difference of the density profiles from the universal form. We describe the series of N-body isolated collapse simulations used to consistently study spin's contribution to a virialized halo.

Collapse Simulations

To isolate the effects of angular momentum on the structure of halos, isolated spherical perturbations with a range of spin values are evolved in an expanding universe to form halos of a prescribed virialized size at zero redshift.

Initial profiles of the collapse are generated by the Isolated Collapse Initial Conditions Generator (ICInG) package (Tremmel et al., 2015a), made specifically for isolated spherical collapse. The initial condition distributions follow from (Evrard, 1988) and assume an Einstein-de-Sitter cosmology. ICInG uses a glass distribution to avoid numerical artifacts and includes the ability to impart angular momentum as well as random motions.

The generator begins with a density profile at a prescribed initial redshift z_i given by a top-hat over-density of the form

$$\delta(r) = \frac{\delta_0}{2}\left(1 + \cos\left(r\pi/R_s\right)\right). \tag{3.199}$$

where R_s is the radius of the sphere and δ_0 parameterizes the magnitude of the over-density, both of which help specify the mass of the resultant halo.

Given a collection of particles initially distributed in the homogeneous sphere, the radii are shifted to match the perturbed density profile

$$r_0 \rightarrow r_1 = r_0\left(1 - \delta(r_0)/3\right). \tag{3.200}$$

The velocity distribution is comprised of the radial expansion rate of the embedding universe, a peculiar velocity given by linear growing mode theory (Evrard, 1988), a rigid rotor condition parameterized by the spin λ, and a random velocity seed of magnitude equal to the peculiar velocity added to prevent singular collapse

$$\begin{aligned}\mathbf{v} &= \mathbf{v}_{\rm hub} + \mathbf{v}_{\rm pec} + \mathbf{v}_{\rm rot} + \mathbf{v}_{\rm rand} \\ &= H\mathbf{r}_1 - \frac{2}{3}H\delta(r_0)\mathbf{r}_0 + \boldsymbol{\omega}\times\mathbf{r}_1 + \mathbf{v}_{\rm rand},\end{aligned} \tag{3.201}$$

where

$$\boldsymbol{\omega} = \hat{\mathbf{z}}\frac{5\lambda G M^{3/2}}{2|E|^{1/2}R_s^2}. \tag{3.202}$$

The N-body code ChaNGa is then used to evolve the distribution using collisionless dynamics. The code uses a Barnes-Hut tree to calculate gravity, with hexadecapole expansion of nodes. Time-stepping is done with a leapfrog integrator with individual time-steps for each particle. The code base has been thoroughly tested and has contributed to many astronomical topics including DM candidate testing (Kim et al., 2014; Governato et al., 2015; Fry et al., 2015), which is a principle reason behinds its use in path one [1].

Although CDM-only collapse is scale-free, we have chosen a physical scale to simulate the equivalent of a large MW-sized halo ($M_{\rm vir} \approx 1.5 \times 10^{12} M_{\odot}$) starting at $z_i = 6$ with an effective initial over-density $\delta_0 \approx 0.71$ for all halos save $\lambda = 0.00$, where $\delta_0 \approx 0.84$. The progenitor particle number is ∼million with softening length ~ 0.4 kpc, which is more than sufficient to resolve core depletion at the ~ 4 kpc scale. The system is evolved for ~ 10 Gyr with a force accuracy/node opening criterion $\theta = 0.7$ and a time-stepping accuracy such that the time-step $\Delta t < \eta\sqrt{\epsilon/a}$, where ϵ is the gravitational softening, a is the acceleration of a particle, and η is an accuracy criterion; we used $\eta = 0.00013$. Also, note that as these are DM-only simulations, the configuration may be rescaled to a halo size of our choosing because Newtonian gravity is scale-free. Cosmological expansion is turned on, but to model the system as isolated, boundary conditions are not periodic.

To survey the effects of angular momentum, we explore the λ landscape at the points $\lambda \in \{0.00, 0.03, 0.06, 0.08, 0.10, 0.15, 0.25, 0.50\}$, where 0.03 is a typical value for galactic halos (Barnes & Efstathiou, 1987; Bullock et al., 2001; Ryden, 1988), and 0.50 is considered quite unusual. In the next section, we discuss the outcome of these simulations.

Analysis

After the progenitor is evolved to $z \approx 0$, properties such as the radial density profile are calculated, shown for our halos in Fig. 6.1. For the lower λ in our range $\{0.00, 0.03, 0.06, 0.08\}$,

[1] We used the public distribution of ChaNGa available via the UW N-Body Shop GitHub page (https://github.com/N-BodyShop/changa). Literature on its operation can be found on the wiki page (https://github.com/N-BodyShop/changa/wiki/ChaNGa).

the profiles tightly match a universal form as expected. By that we mean they closely follow the NFW (Navarro et al., 1996a) density curve with the slightly faster than r^{-1} growth towards the center that has become expected by some for virialized halos (Fry, 2015; Moore, 1994; Moore et al., 1998, 1999). Surprisingly, the form persists into the higher spin halos until $\lambda = 0.25$, which lies in the 99.9 percentile of halos according to some N-body studies (Barnes & Efstathiou, 1987; Bullock et al., 2001). Deviations in the higher spin profiles, $\lambda \in \{0.25, 0.50\}$, include a divergence from the two power law form, a shrinking virial radius, and a lowered density, the last two of which may be partially attributed to the limitations of ICInG in the high spin regime to set the final virial mass. Our definition of the virial radius and mass are in line with (Bullock et al., 2001), with the virial radius taken to be the distance at which the average interior density equals 200 times the critical density. The particles within the virial radius at this time are called the virialized component, while the remainder comprise the non-virialized component. The relation between the λ values supplied to ICInG and the measured spins of the virialized halos are provided in Table 3.1.

λ (parameter)	λ (measured)
0.00	0.000
0.03	0.035
0.06	0.064
0.08	0.094
0.10	0.109
0.15	0.168
0.25	0.248
0.50	0.381

Table 3.1: Relation between the λ parameter values supplied to ICInG and those measured in the virialized halo.

Cumulative mass profiles of prograde particles within the virial radius versus specific

angular momentum also show a consistency over the lower spin halos, Fig. 3.14, despite their initial differences in rotation rate. (Bullock et al., 2001) (BDK) performed a similar analysis and proposed a universal profile of the form

$$M_{\rm enc}(j) = M_{\rm vir}\frac{j}{j - j_0}, \tag{3.203}$$

where j is the z-component of the specific angular momentum as defined by the imposed spin axis (3.202). This cumulative mass uses only the prograde bodies in the virialized halo, summing the masses of particles with specific angular momentum between 0 and j. For reasonable λ, the inner power law ($M_{\rm enc} \propto j^\alpha$ for $j \approx 0$) of the calculated profiles is noticeably shallower with $\alpha \approx 0.7$. The primary difference between our analysis and BDK's is the presence of some retrograde ($j_z < 0$) constituents due to the differences of their binning process. Due to the consolidated profiles over reasonable λ, we suggest a similar profile shape for the slower halos

$$M_{\rm enc}(j) = M_{\rm vir}\left(\frac{j}{j - j_0}\right)^\alpha \ , \ \alpha \approx 0.7. \tag{3.204}$$

The difference between the profiles (3.203) and (3.204) points at the existence of a retrograde component to the halo, Fig. 3.21, which was not present in the initial configuration. This is curious as the approximate cylindrical symmetry of the initial state should translate to a particle-wise near conservation of the $\hat{\mathbf{z}}$ component of angular momentum. Instead, these halos form a strong bar structure in the rotation plane, Fig. 3.16, reminiscent of the radial orbit instability (ROI) (Bellovary et al., 2008; Polyachenko, 1981; Barnes et al., 1986) in the $\lambda \to 0$ limit. The presence of a strong bar ruins the cylindrical symmetry of the initial conditions, allowing for non-trivial particle-wise angular momentum evolution and the presence of retrograde particles after virialization. The bar is prevalent in all of the generated halos, save for $\lambda = 0.25, 0.50$ where it weakens significantly. The strength of the bar can, in part, be quantified in terms of its triaxial factor (Binney & Tremaine, 2008)

$$T = \frac{\gamma_1 - \gamma_2}{\gamma_1 - \gamma_3}, \tag{3.205}$$

where $\{\gamma_i\}$ are the eigenvalues of the halo's mass quadrupole ordered from largest to smallest, Fig. 3.17. Note that the lack of constraint on the principal axes adds ambiguity to whether

or not this figure measures the strength of axial symmetry breaking. Since we are only interested in elongation in the plane normal to the z-axis, a more relevant measure of bar strength is in the bar parameter (Binney & Tremaine, 2008)

$$B = \frac{\chi_1 - \chi_2}{\chi_1 + \chi_2}, \tag{3.206}$$

where $\{\chi_1, \chi_2\}$ are the eigenvalues of the projected trace-full quadrupole moment sorted in decreasing value, Fig. 3.18.

Despite the breaking of cylindrical symmetry, the transfer of angular momentum between virialized and non-virialized components appears to be minimal over the initial and final configurations, Fig. 3.22. This effective lack of coupling implies that the instability can exist in isolation, similar to the ROI. We can also see that the amount of retrograde material in the halos is significant, and it can be shown that the density profiles for prograde and retrograde components look very similar for barred halos, and only diverge when the bar weakens.

There appears to be a theme here: for our class of initial distributions, the universality of the density and angular momentum profile shapes persist if and only if a strong bar is present.

The NFW and enclosed mass profiles appear to be robust over a wide range of spin values (Fig. 6.1, 3.14). Also present over these spins is a strong in-plane bar, which contains large amounts of prograde and retrograde material (Fig. 3.21). The formation of the bar is analogous to the structure formed by an ROI where a slight breaking of a distribution's spherical or cylindrical symmetry evolves exponentially into a significant asymmetry. (Bellovary et al., 2008) (BDB) showed that for a non-rotating spherical mass, velocity perturbations of the 3D thermal variety disrupted the instability, but purely radial dispersions were ineffective. BDB also made the claim that the ROI is a key physical mechanism contributing to the nearly universal profiles of simulated DM halos.

Binney & Tremaine (2008) also parameterize the instability in the non-rotating small angular momentum limit: by relating a spherical distribution's tangential velocity dispersion

to spherical stability

$$\vartheta^2 \geq L^2/(G\rho r^2 I) \tag{3.207}$$

where L is the typical angular momentum per orbit, ρ is the typical density, r is the radial extent of the halo, and $I = T_r/(\partial_L \Delta\phi)|_{L=0}$. To form a distinct bar, ϑ must be less than 1. Other studies of this instability (Polyachenko, 1981; Barnes et al., 1986) are performed in a similar limit. Our work appears to expand triaxial halo formation conditions to include those with coherent tangential components.

The apparent correlation of bar strength with the consistency of the universal profiles is an important step towards understanding the profiles' limits. Equally important is the point that the geometry forms in isolation, with a lack of angular momentum exchange between the virialized and nonvirialized regions. A commonality between the ROI and the bars formed in this study is the high angular momentum dispersion relative to the averaged values, which tapers off as the spin is increased. The dispersions are also seen to decrease in size as the bars weaken (Fig. 3.17, 3.18). If we are to make the connection between the ROI and the instabilities that we form, this observed trend is in violation of the conclusions of Binney and Tremaine that stability against the ROI is driven by tangential velocity dispersion. As their conclusions were derived under different conditions, namely in a non-rotating small angular momentum limit, tangential dispersion alone may be insufficient to determine a halo's stability.

Cylindrical symmetry in the isolated halo may be restored to some degree by the presence of a strong central mass such as a BH or heavy baryonic bulge. Such objects do not exist for certain classes of dwarf galaxies, making our study particularly pertinent to them. Such dwarfs may still exhibit DM cores, which must overcome this propensity for bar creation.

Based on these findings, we speculate that the NFW and BDK profiles are robust over the range of probable halo spins due to susceptibility to an instability that bears resemblance to the ROI. The breakdown of such an instability is consistent with the departure from a low angular momentum limit. A study of the robustness of axial symmetry and spin provide insight into the nature of this instability and its profile. Also, for galaxies with a strong

central baryonic mass, a study of DM-only collapse with enforced cylindrical symmetry is needed to eliminate spin as a possible solution to the core-cusp problem.

Ultimately, in the larger picture of halo formation, where a cosmological setting leads to hierarchical halo formation, the role of these instabilities becomes less clear. A halo's history consists of periods of gentle minor mergers, interrupted occasionally by more violent major mergers. (Bellovary et al., 2008) performs preliminary simulations of halos subject to controlled minor and major mergers to investigate the realistic role of the ROI, where they speculate that the ROI does not play a significant role in the subsequent relaxation process after a major merger. However, they also state that there are indications of an operational ROI during the minor merger periods, acting on nearly radial tidal streams associated with disrupted subhalos. A similar study with non-radial inflow and torquing may provide insight into the rotational regime.

3.6.2 Extracting Axion Signals from Cosmological CDM SF

This subsection is based on work first submitted to ApJ in December 2016, later published August 2017. To read the publication in full, see Lentz et al. (2017).

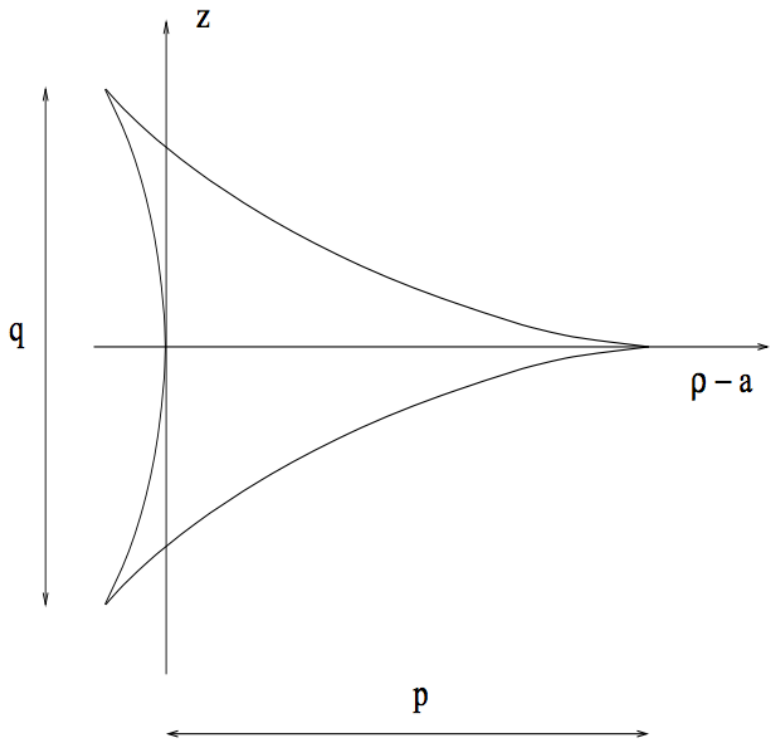

Figure 3.2: Cross-sectional diagram of the caustic ring singularity, with galactic center positioned to the left (Sikivie, 1999a). The edges of the tricusp shape represent turn-around points for axion flows, the regions of infinite density.

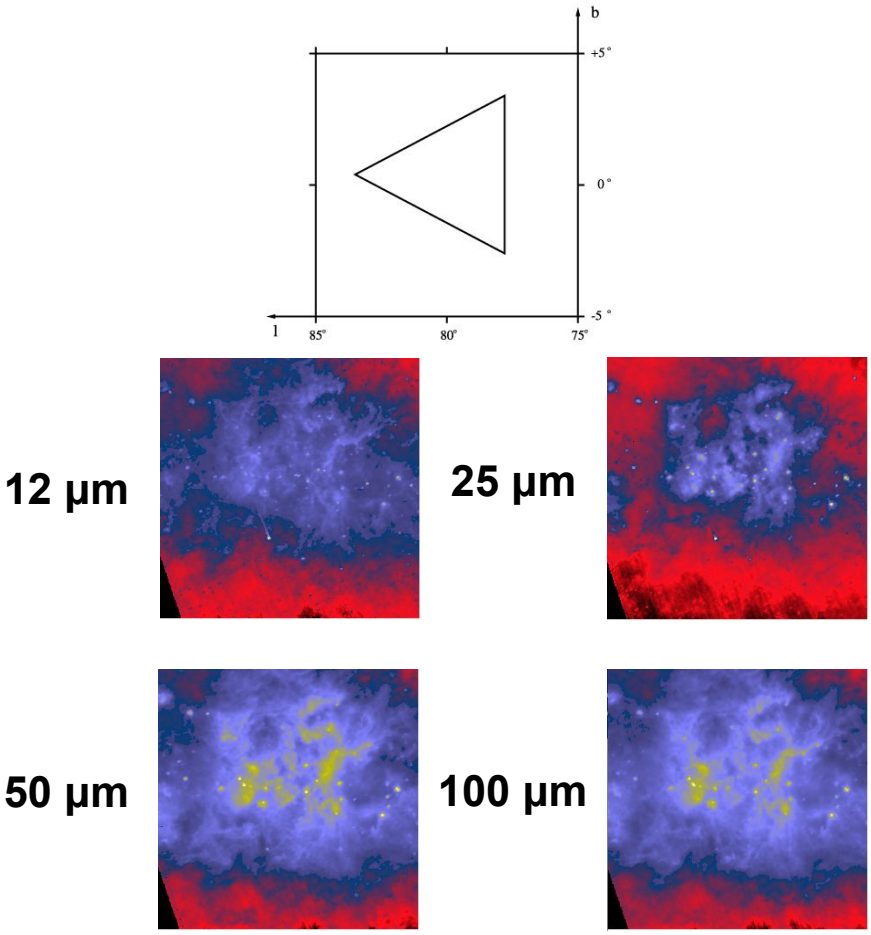

Figure 3.3: IRAS images of a triangular feature at several IR frequencies located 8.3 kpc to the earth's right of galactic center, courtesy of Pierre Sikivie. Phenomena other than axion caustics are also eligible for this feature, including dust rings, though they do not share the constraints of self-similar placement.

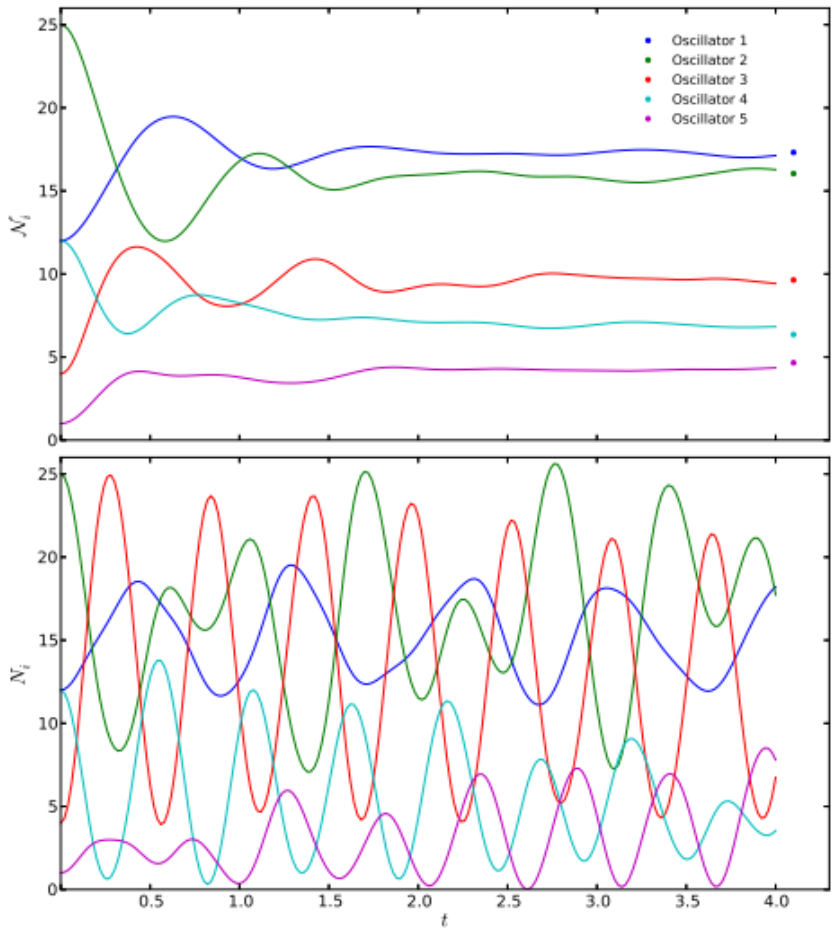

Figure 3.4: Time evolution of a small system of oscillators, with the top panel showing the evolution under classical equations of motion, and the lower evolving under quantum equations of motion (Erken et al., 2012). Both start from the same condition and their evolutions trace for a short time, but quickly diverge and reach different equilibrium states.

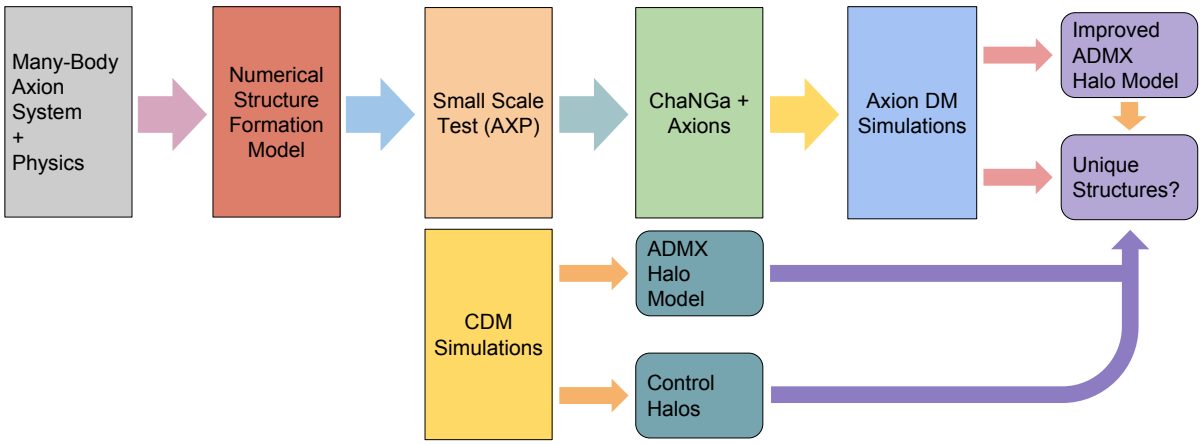

Figure 3.5: Work flowchart of the model development through implementation stages of the project. The top path develops the numerical scheme necessary to model axion structure formation, performs those simulations using the flagship code of the UW N-Body Shop, ChaNGa, and performs the search for unique axion structures. The bottom path seeks to understand the control case of CDM structures, rendering tools for the eventual structure search of the upper path as well as updates halo models for current axion searches.

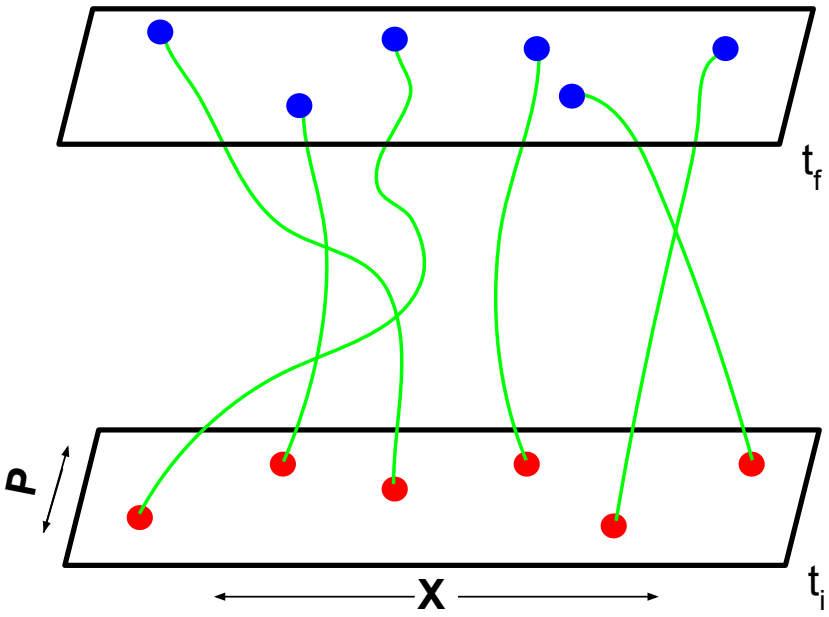

Figure 3.6: Illustration of how the MOC may find the solution to the Boltzmann problem. The Cauchy data provided at the initial time ($f(t_o)$) is evenly sampled according to weight. The equations of motion of the samples are then solved to the final time (t_f), which maintain their weight throughout. A sampling of the final distribution ($f(t_f)$) is then given by the evolved points.

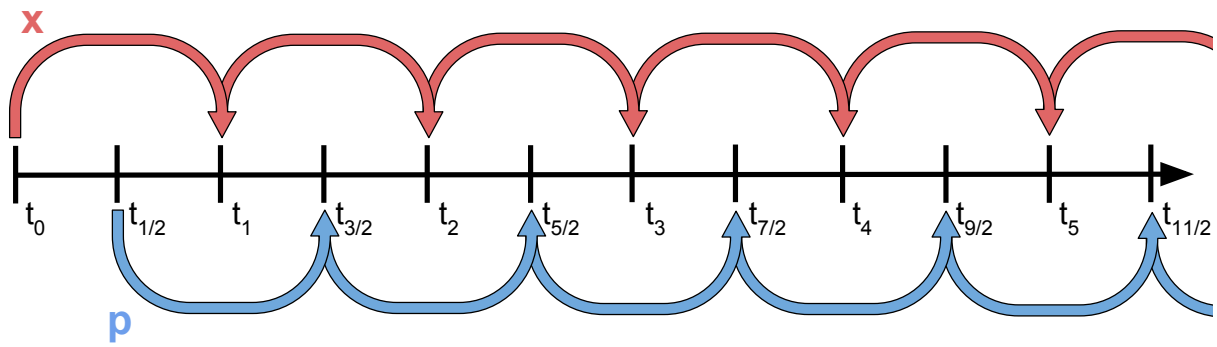

Figure 3.7: Illustration of leap-frog integration showing dependency of a particle's phase space on its previous state.

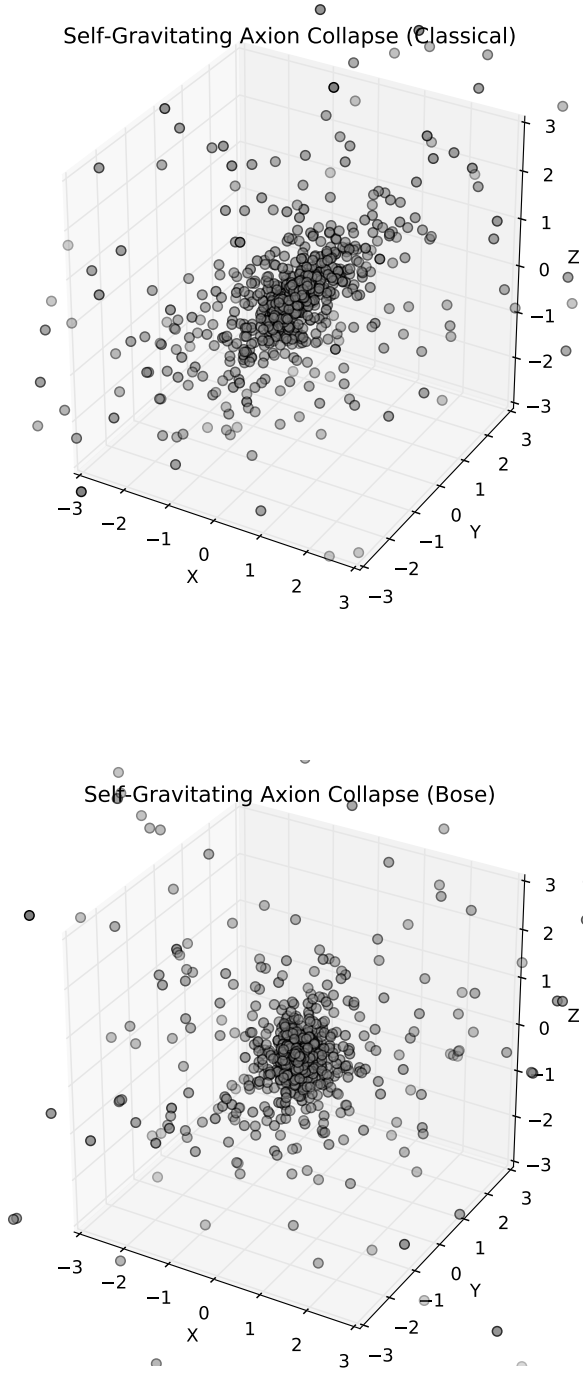

Figure 3.8: Snapshots of 1000-particle normal spherical collapse simulations at $t \approx 5t_{dyn}$. The upper simulation uses classical dynamics and the lower uses Bose dynamics.

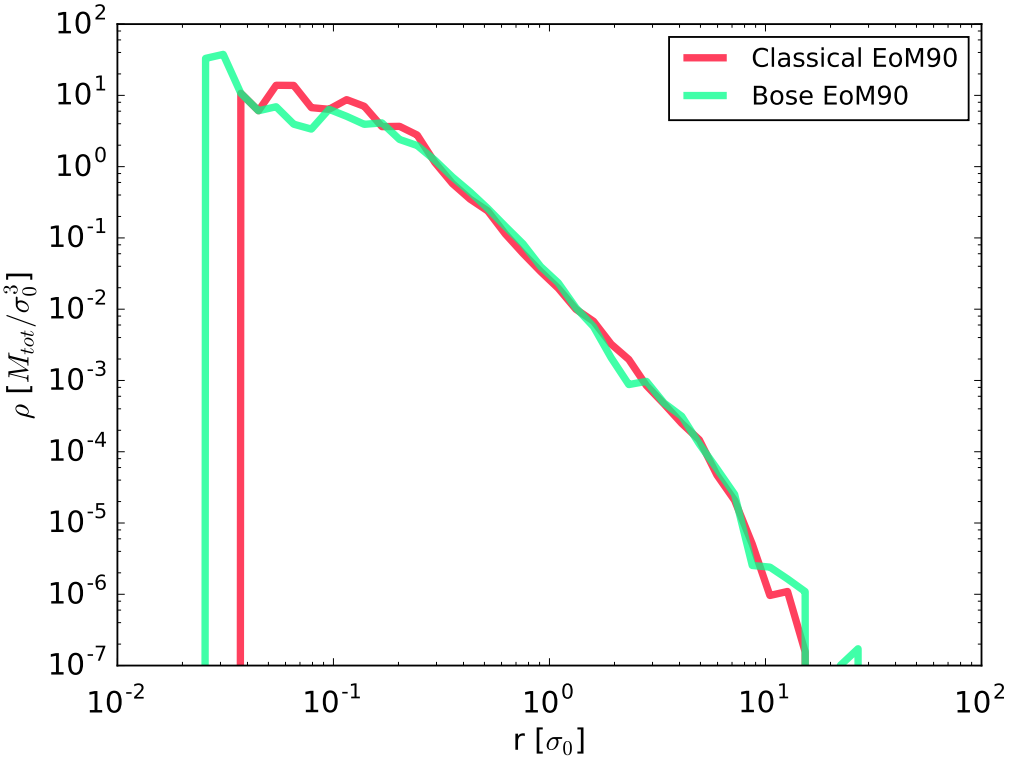

Figure 3.9: Spherical density profiles of 1000-particle simulations of normal spherical collapse under differing infall dynamics, taken at after $9t_{dyn}$. Both profiles appear to conform to a single shape. Several other simulations with these parameters were run with randomly generated initial conditions, with all but one classical simulation producing the conforming profile.

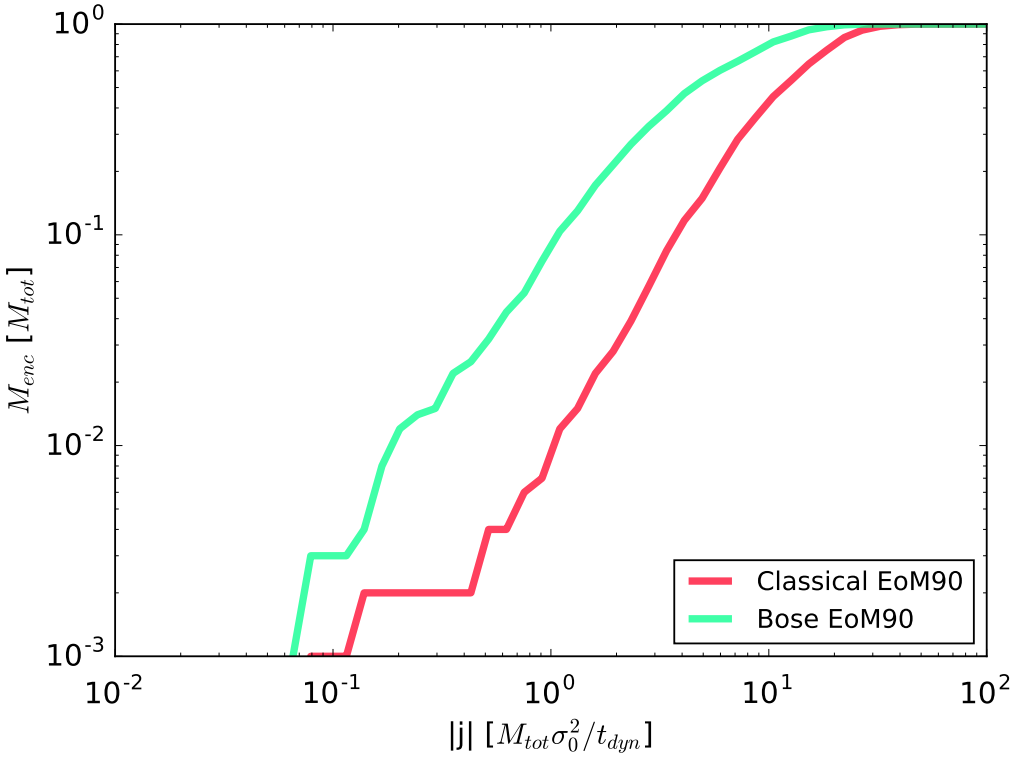

Figure 3.10: Enclosed mass profiles over particle angular momentum magnitude of 1000-particle simulations of normal spherical collapse under differing infall dynamics, taken at after $9t_{dyn}$. The classical profile shows a wide distribution of angular momenta, the Bose profile is far more restricted to low momentum states. These profiles appear to be well-converged on a run-to-run basis.

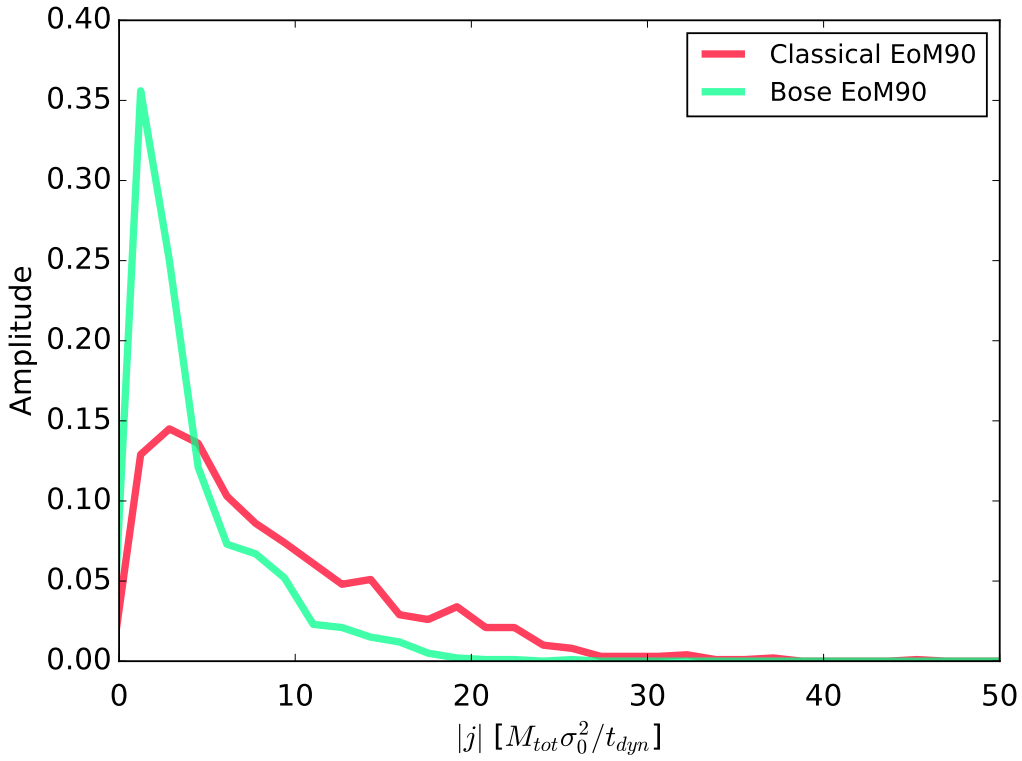

Figure 3.11: Distribution of particle angular momentum magnitude of 1000-particle simulations of normal spherical collapse under differing infall dynamics, taken at after $9t_{dyn}$. Magnitude is chosen instead of j_z, as any particular direction is arbitrary in a sperical collapse. Here we explicitely see the broad distribution of classical rotations, and the relatively condensed Bose distribution.

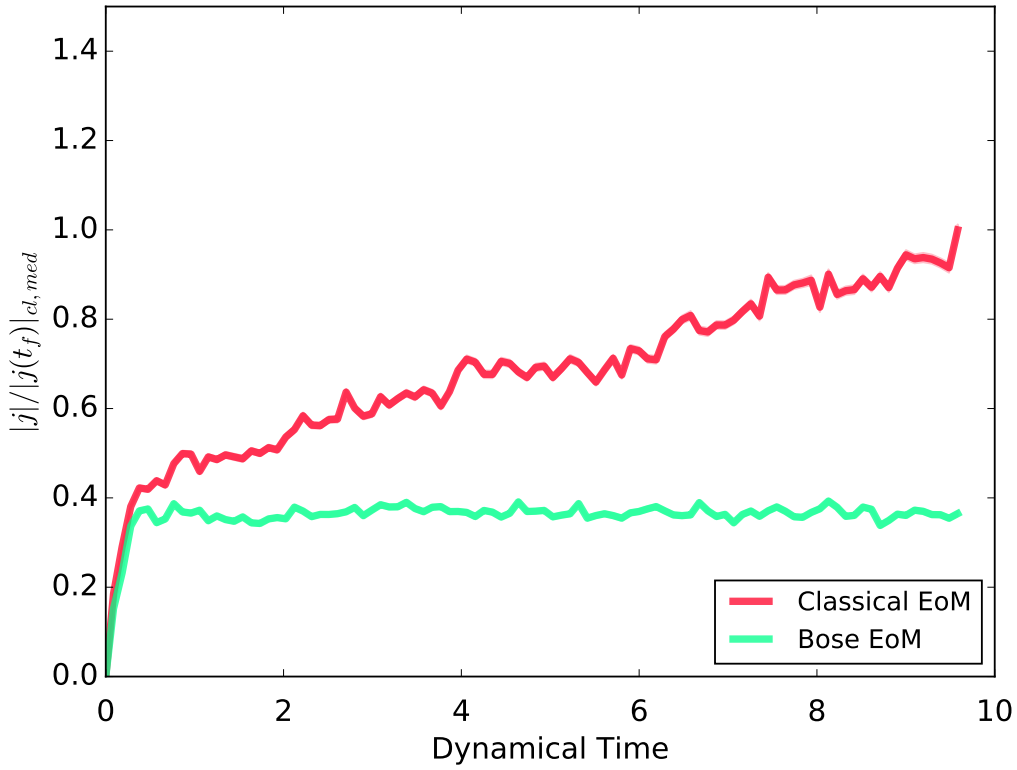

Figure 3.12: Median particle-wise angular momentum conservation over simulation time of 1000-particle simulations of normal spherical collapse under differing infall dynamics. Standard deviation of the mean error bars are also plotted, but their width is of order median line. Conservation for each particle is measured by the comparing its current state within the simulation with the final median particle angular momentum from the classical simulation.

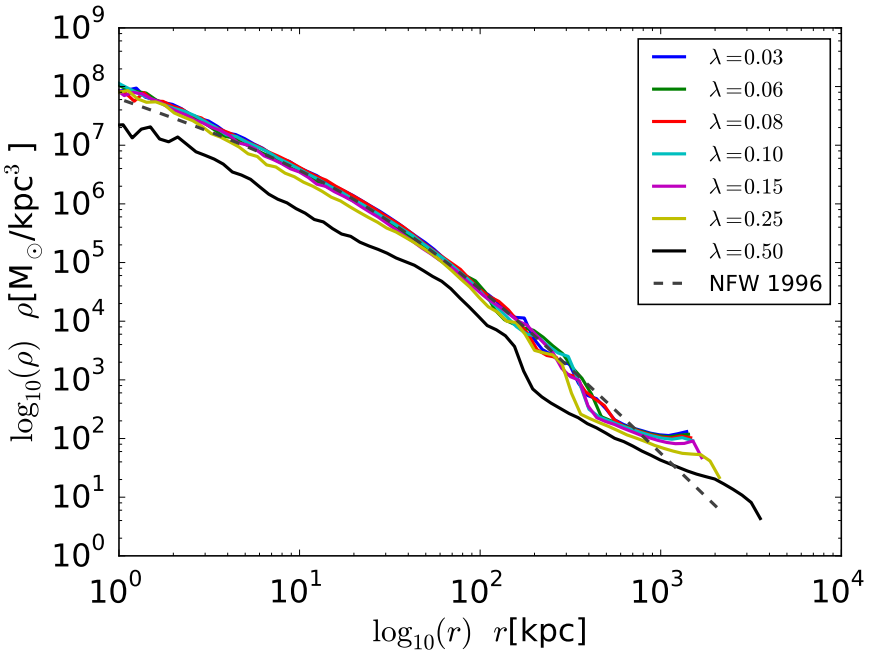

Figure 3.13: Spherically averaged density profile for the various spin values after collapse. The lower spin progenitors form virialized states that match the nearly universal NFW form, save for the notable increase in power law within the scale radius. The reference NFW profile has scale radius 30 kpc and scale density $2.2 \times 10^6 M_\odot/\text{kpc}^3$, which were chosen by eye to match the low spin profiles. The inset plot displays the power law behavior of each profile at 10kpc.

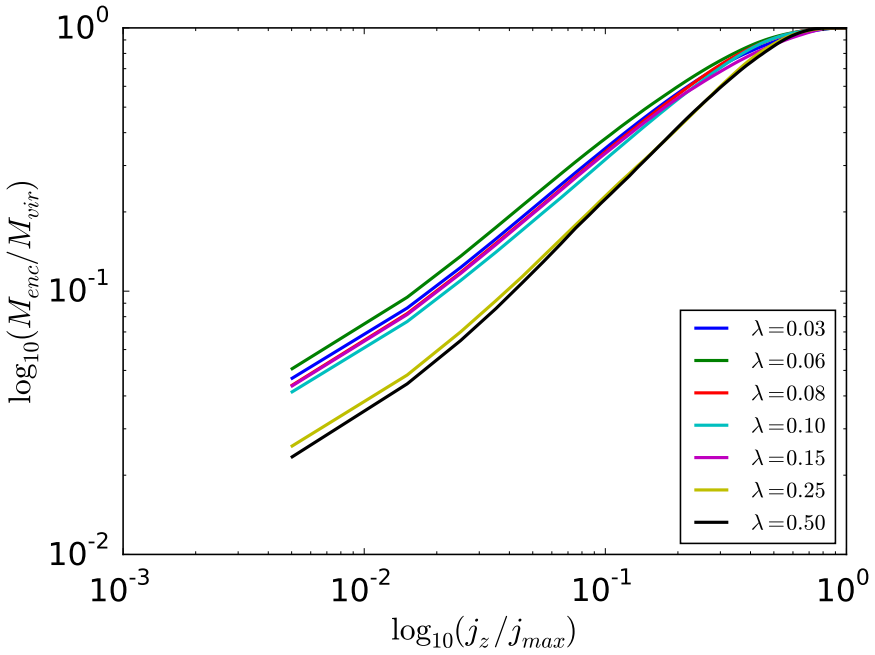

Figure 3.14: Enclosed-mass profile of prograde particles versus the vertical component of specific angular momentum, reminiscent of Figure 4 of (Bullock et al., 2001), showing the lower spin halos take a similar form while the higher spin halos have a steeper inner slope. A difference in technique may be responsible for the discrepancy: Bullock removed large amounts of retrograde ($j_z < 0$) material from the halos before profiling, whereas we have removed every retrograde particle.

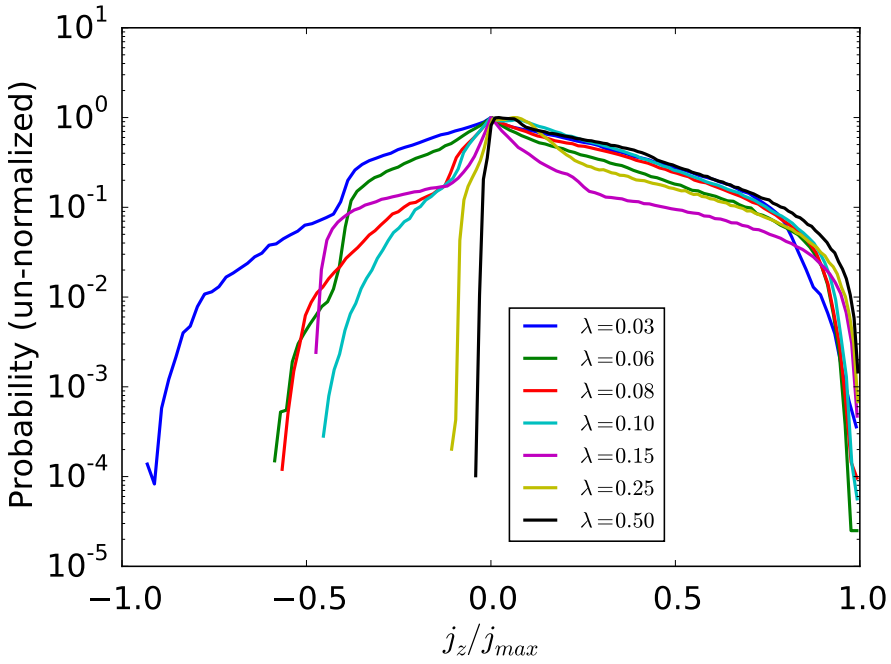

Figure 3.15: Probability density function of the isolated distributions after collapse. The initial configurations for each distribution were well represented by a rotating solid sphere, which would give a distribution with support in positive j. The retrograde component ($j_z < 0$) to the final distributions implies a breaking of the initial axial symmetry.

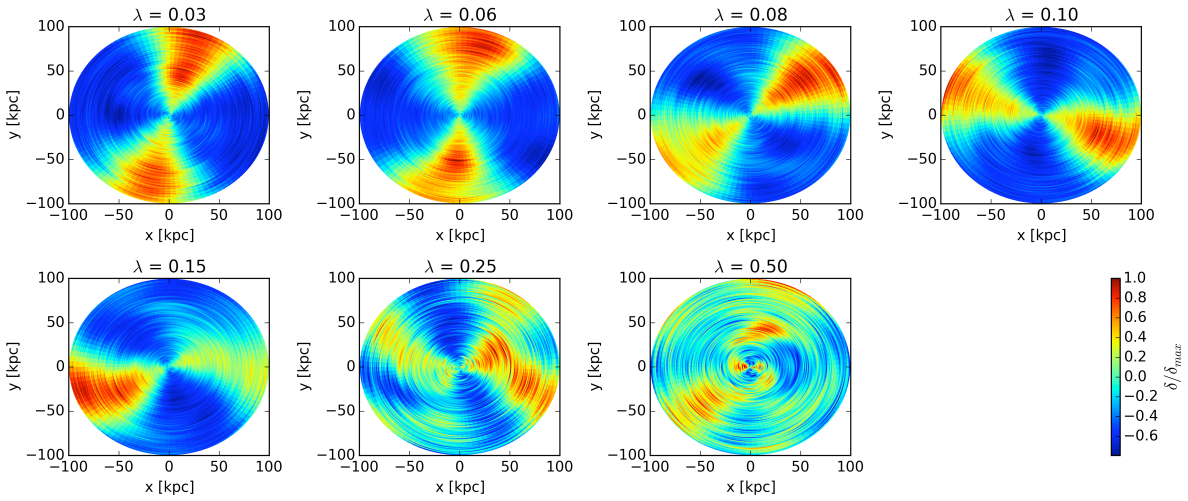

Figure 3.16: Integrated face-on over-density views of all collapsed configurations, obtained via azimuthal inverse Fourier transform over cylindrical bins and normalized bin-wise. The radial bar-like structure forming in the slower halos is visible as the over-dense cones, whereas the faster halos' bar's appear increasingly disrupted.

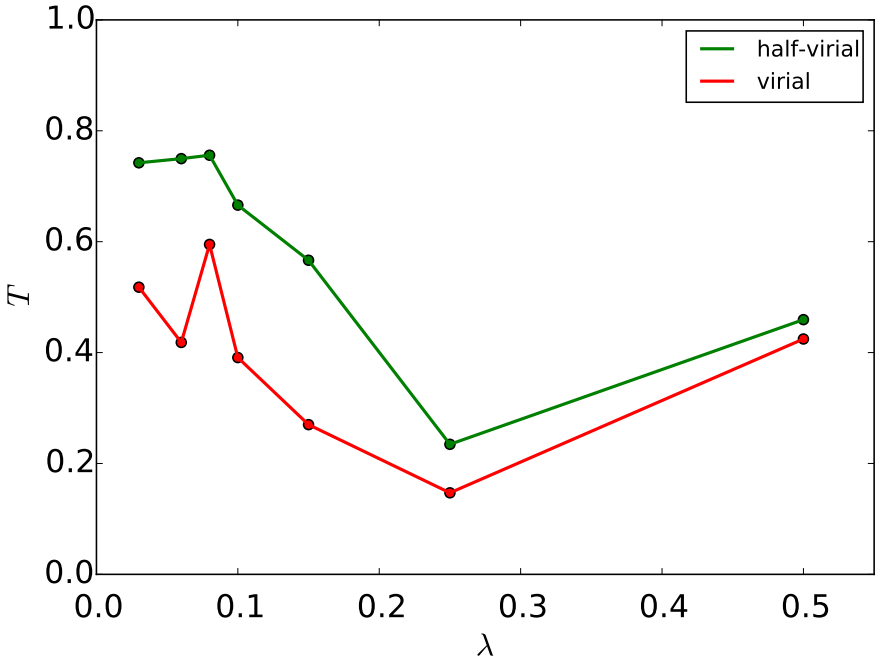

Figure 3.17: Triaxality versus initial spin values for matter within a virial radius and half a virial radius. Note that T values close to 1 are oblate, about 0.5 are triaxial, and close to 0 are prolate. The virialized components appear to shift from a triaxial or partially prolate to oblate shaped over the spin range $[0.00, 0.25]$, with triaxality being resumed for $\lambda = 0.50$. This departure from the trend may due to departure from the small angular momentum energy limit leading to increased extent in-plane.

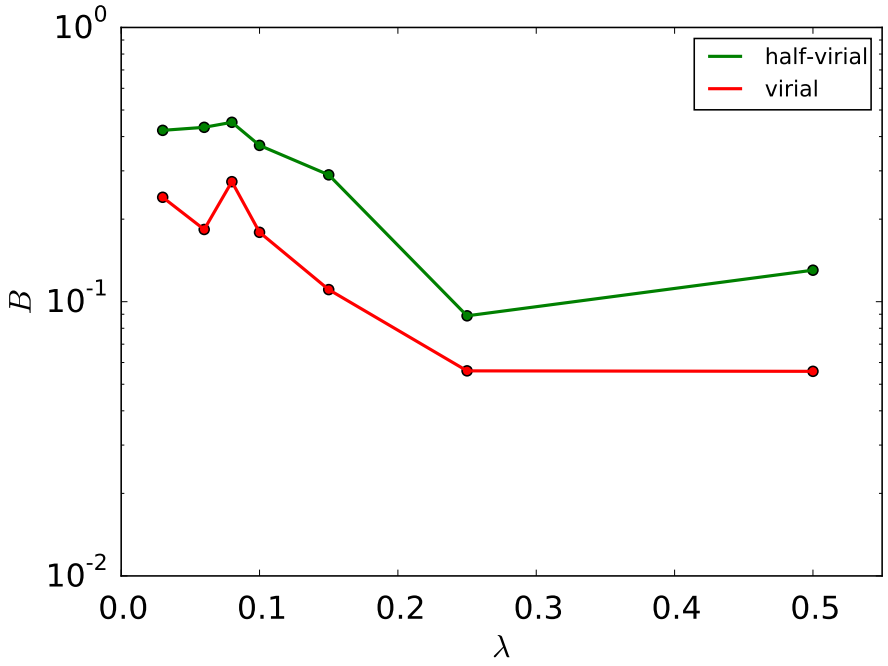

Figure 3.18: Bar parameter versus spin values for particle components within a virial radius and half a virial radius. The bar weakens with increasing spin to $\lambda = 0.25$.

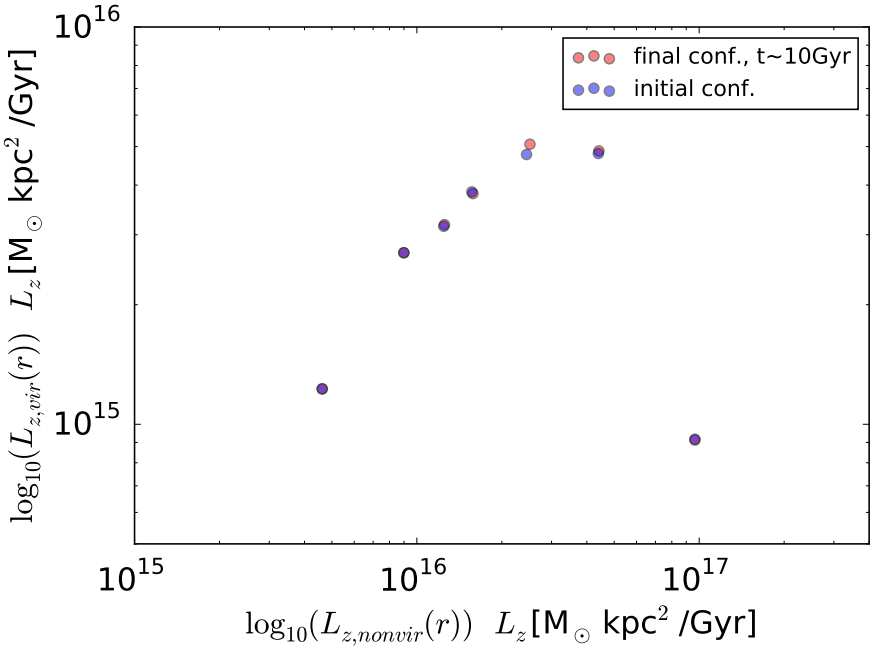

Figure 3.19: Total virialized specific angular momentum versus total nonvirialized specific angular momentum for the initial and final configurations of each spin. The near overlap of the initial and final configurations indicate that angular momentum is almost exactly conserved within the virialized and nonvirialized components *individually*; little to no transfer of angular momentum occurred between the components during the collapse. The spin values of the points increase from left to right. Note that the spin-less simulation's angular momenta are far smaller than the other runs, and therefore do not appear.

The axion's low mass and feeble couplings lead to unconventional search techniques. As will be presented in Chapter 4 in greater detail, one attractive method used by axion DM searches threads a magnetic field through a resonant cavity, stimulating the decay of DM axions into microwaves via the effective CP-violating interaction

$$\mathcal{L}_{int} = \frac{g_{a\gamma\gamma}}{4\pi} a F \tilde{F} \tag{3.208}$$

where a is the axion field, F and $\tilde{F}$ are the electromagnetic field strength and its dual, and $g_{a\gamma\gamma}$ is the coupling strength (Sikivie, 1983). Nearly all the power from axion decays is transferred into microwaves of frequency set by the decayed axion energy

$$E_\gamma = \hbar\nu = m_a c^2 + m_a v^2/2 \tag{3.209}$$

where m_a is the axion mass, v is the axion speed in the lab frame, and ν is the microwave frequency. The energy distribution of axions is sampled by tuning the cavity over large ranges in frequency, making the microwave power spectrum the figure of interest. The resonant microwaves are detected by a receiver sensitive to sub-yocto-watt power. These experiments can have frequency resolution to a part in 10^9 or better (Asztalos et al., 2010), well within the range of resolving fine structure in the axion distribution. A relic axion density of 0.45 GeV c^{-2} cm^{-3} is commonly used by cavity searches, motivated by Milky Way (MW) observations (Gates et al., 1995), making the focus of this letter to update the shape of a potential axion signal.

Despite their good energy resolution, some axion searches use a filter shape derived from the Standard Halo Model (SHM) (Asztalos et al., 2010), which comes from the assumption that the MW halo is given by a thermalized pressure-less self-gravitating sphere of particles. The velocity distribution of the SHM near the earth is given by a Maxwellian distribution below the escape velocity

$$f_{\vec{v}} \propto e^{-\vec{v}\cdot\vec{v}/2\sigma_v^2} \tag{3.210}$$

where $\sigma_v = v_c/\sqrt{2}$ (Binney & Tremaine, 2008) and the v_c is the circular speed. To match the limits from the Axion Dark Matter eXperiment (ADMX) (Asztalos et al., 2010), a value

of $v_c = 226$km/s will be used, though recent observations put the solar orbital speed closer to $v_c = 255$ km/s (Reid et al., 2014). The SHM is broadly predictive, but incapable of describing fine structure.

Since these searches started, there has been significant progress in simulating the formation of galaxies like the MW. One powerful simulation tool is the N-Body+Smoothed-Particle Hydrodynamics (N-Body+SPH) method. Capable of accurately resolving the inner structures of galaxies and their CDM halos and well-calibrated baryonic models, N-Body+SPH simulations are poised to give accurate models of DM structure for direct searches. This has already been done for WIMPs, which have not yielded significant differences from the SHM (Sloane et al., 2016; Kelso et al., 2016; Bozorgnia et al., 2016). As the energy spectra for cavity axion searches are different from the speed spectra relevant to WIMP nuclear recoil searches, an axion-specific analysis of structure-formation simulations is worthwhile.

Romulus25

We utilize the results of the R25 N-Body+SPH simulation produced by the UW N-Body Shop (Tremmel et al., 2017), based on the ChaNGa N-Body+SPH code. R25 was created on the Blue Waters petascale computing facility. To analyze specific galaxies and halos in R25, the Amiga Halo Finder (AHF) (Knollmann & Knebe, 2009) is used to create the catalogue on R25, also at Blue Waters. Finally, the analysis was greatly assisted by the Pynbody N-body analysis software package (Pontzen et al., 2013).

R25 describes a 25 Mpc periodic cosmological box filled with DM particles, evolving gas and star particles, and super-massive black holes (SMBHs). The box is placed in a ΛCDM cosmological setting according to findings from Planck ($\Omega_0 = 0.3086$, $\Lambda = 0.6914$, $h = 0.67$, $\sigma_8 = 0.77$; (Planck Collaboration et al., 2016b)). Particle masses of $3.39 \times 10^5 M_\odot$ and $2.12 \times 10^5 M_\odot$ are used for the DM and gas respectively. DM is over-sampled by a factor of 3.375 relative to the gas, producing more accurate SMBH dynamics (Tremmel et al., 2015b, 2017), and will reduce numerical noise in the analysis.

In addition to gravitational forces, calibrated baryonic physics including star formation

and evolution, cosmic UV background, supernovae feedback, primordial cooling, and SPH are used to govern the gas and stars. The SMBHs in R25 are implemented with realistic formation, dynamical friction-driven evolution, and accretion principles governed by local gas dynamics (Tremmel et al., 2015b, 2017). A Plummer equivalent force-softening length of 250 pc is used, of similar size to (Sloane et al., 2016), which is more than sufficient to resolve the local axion distribution on the kpc scale. The system is evolved to $z = 0$ with a force accuracy/node opening criterion $\theta = 0.65$ until $z = 2$, after which an opening of $\theta = 0.9$ is used. The time-stepping accuracy used is such that the time step $\Delta t < \eta\sqrt{\epsilon/a}$, where ϵ is the gravitational softening, a is the acceleration of a particle, and η is an accuracy criterion; $\eta = 0.185$ is used. ChaNGa is part of the AGORA (Kim et al., 2014) code comparison collaboration.

R25 is large enough that it has O(30) MW-mass halos at z=0. Such a large set allows for a sampling of galaxies where reduction down to a MW-like sample is quantifiable via the use of filters on a halos catalogue.

Halo Catalogue Tools and Filters

The AHF cataloging program is used to identify halos within the simulation. It operates under the principle of identifying halo centers via density-triggered domain refinement, collection of a halo's domain through successive inclusion of particle shells, and removal of particles unbounded to the halo (Knollmann & Knebe, 2009). Beyond finding halos at a single timestep, AHF is capable of tracing individual halos through time and absorption in order to construct a merger tree. Through this tree, quantities like time of last major merger and more detailed merger history can be calculated, which will be important for the selection of halo-galaxy structures that resemble the MW. The TANGOS database package (Pontzen, 2017) is also utilized over the catalogue to aid in the selection process.

The galaxy halos analyzed here are selected using filters in line with the current understanding of MW halo mass, rotational velocity structure, and relatively quiet recent formation history (Bovy et al., 2012; Kafle et al., 2012; Ruchti et al., 2015) without being so

constraining as to limit halo statistics.

$$0.5 \times 10^{12} M_{\odot} \leq M_{vir} \leq 1.6 \times 10^{12} M_{\odot} \tag{3.211}$$

$$R_{vir} \leq 250 \text{ kpc} \tag{3.212}$$

$$z_{major} \geq 0.75 \tag{3.213}$$

$$175 \text{ km/s} \leq v_{circ} \leq 275 \text{ km/s} \tag{3.214}$$

where M_{vir} is the virialized mass, R_{vir} is the enclosing virial radius, and z_{major} is the redshift of last major merger, which is set by the progenitor ratio of 4:1. Several halos experienced no major mergers during the simulation. v_{circ} is the circular velocity in the plane of the galaxy at 8 kpc, which did eliminate several halos from the set satisfying Eqs. 3.211 - 3.213 , though R25 over the mass range does satisfy the virial-stellar mass relation with stellar masses of $2.1 - 8.5 \times 10^{10} M_{\odot}$ (Tremmel et al., 2017). At $z = 0$, R25 contains 16 halos which satisfy the filters; Table 3.2 contains some characteristics of each.

Spectra Analysis

Before presenting the findings of the signal shape analysis, it is prudent to first establish the sensibility of MW-like halos in R25. Fig. 3.21 shows that the speed spectra of solar-radius samples in the galactic frame are consistent with Figures 1 & 2 in (Sloane et al., 2016) and Figure 1 in (Schaller et al., 2016), and are well fit by the SHM. The halos' densities at the solar radius are also seen to match halos from (Sloane et al., 2016) and (Bozorgnia et al., 2016) over their respective mass ranges. The solar sample of particles is given by a 2 kpc by 4 kpc toroid about the solar orbit, which is taken to be in the baryonic disk,

$$-2 \text{ kpc} \leq z \leq 2 \text{ kpc} \ , \ r_l - 1 \text{ kpc} \leq r \leq r_l + 1 \text{ kpc} \tag{3.215}$$

where r_l is chosen to match the MW solar radius of 8 kpc, though the spectral shapes are reasonably robust to the choice of radius. Halo sample spectra are formed by calculating the observable (speed, energy, etc.) for each particle and compiling a normalized histogram

over all sample particles. Sample sizes for these toroids ranged from 15,000 to 28,000 DM particles.

The galactic frame energy spectra of Fig. 3.21 also shows a similar consistency with the SHM, though small speed departures become amplified due to changes in measure from speed to energy.

Terrestrial DM search experiments are moving with respect to the galactic center. The lab is held to be in the galaxy's local standard of rest, approximated as a circular orbit about the center of the galaxy of $r_l = 8$ kpc, coincident with the Sun-MW orbital shape and radius. This seemingly trivial choice of radius for galaxies other than the MW does not affect the structure of the resulting spectra, which are found to be robust over a span of 6 kpc $\leq r_l \leq$ 18 kpc. The orbit speed of the lab is given by setting the acceleration of disk particles at the orbit radius to orbital motion

$$\bar{a}(r_l) = \frac{v_l^2}{r_l} \tag{3.216}$$

where the RHS is the centripetal acceleration of the lab frame and $\bar{a}$ is the average acceleration at the lab radius. In order to approximate the velocity distribution in a point-like lab, this sample region assumes a cylindrically symmetric, homogeneous, equipotential, steady-state system within. To evaluate the particles in the lab frame, a Galilean boost is performed on each sample particle using the solar orbital velocity

$$(v_r, v_t, v_z) \rightarrow (v_r, v_t - v_l, v_z) \tag{3.217}$$

where v_l is taken to be the circular velocity in the presence of DM+baryons at the orbit radius and v_r, v_t, v_z are a particle's radial, tangential, and z-component velocities respectively. The laboratory speed, energy, and other spectra can now be calculated by forming distribution functions over the desired observable.

The laboratory-frame speed spectra of the R25 halos shown in Fig. 3.21 display some deviations from the SHM, particularly in the low-speed region, which suggests bulk motion. Prior WIMP DM studies also observe these deviations, though they find more pronounced

low-speed excesses in DM-only simulations as opposed to when baryons are present. The galactic and solar frame speed distributions, including baryons, are consistent with the count-rate proxy of integrated weighted velocity functions, $g(v_{min})$, of (Sloane et al., 2016).

In contrast, the lab frame energy spectra show a marked difference from the SHM, Fig. 3.21. The deviation towards the lower relative speed becomes much more pronounced due to the change in measure from $dm \sim dv$ to $dm \sim dE \sim vdv$. This apparent narrowing and enhancement of the signal is present over all but one of the 16 halos. The degree of signal intensity enhancement is robust over the halos, with analyses over local DM density and halo mass showing no significant correlations.

Also, recall that filters in Eqs. 3.211 - 3.214 allow galaxies that deviate from the MW. Specifically, the galaxies inside halos h32, h34, h36, h44, and h48 have older stars and larger bulges than is expected for the MW. These galaxies lower the mean deviation as they produce spectra preferentially closer to the SHM than the rest of the halos; such halos are still included, as filters based on morphology are not considered here.

There is a significant difference between galactic and lab frames in the spectra. The lab-frame energy spectra are sensitive to bulk motions, which contribute to the signal narrowing, though there is not yet a full understanding of the mechanisms behind this effect. The characteristic spectral shape over a wide range of galaxies communicates a level of robustness in the line shape and gives confidence in a signal model based on these spectra. The signal shapes expected to be observed by a microwave cavity experiment in each R25 halo are calculated, shown in Fig. 3.22 for a 10^{-6} eV c^{-2} axion. The conversion to frequency is similar to the calculation of the energy spectra, using the relation between the energy of the decayed axion and the resonant microwave's frequency from 3.209. The solid black line of Fig. 3.22 represents the fitted model signal shape. The proposed signal shape keeps a Maxwellian-like form

$$f_\nu \propto \left(\frac{(\nu-\nu_o)h}{m_a T}\right)^\alpha e^{-\left(\frac{(\nu-\nu_o)h}{m_a T}\right)^\beta} \tag{3.218}$$

where the parameters are constrained to be positive. The best-fit parameters are found using a log-normal local M-estimate using parameter data from individually least-squares-fit halos

and are calculated to be $\alpha = 0.36 \pm 0.13$, $\beta = 1.39 \pm 0.28$, and $T = (4.7 \pm 1.9) \times 10^{-7}$, with the errors given by the roots of covariance matrix diagonals.

The narrowing of the observed shapes has implications for axion search experiments. The modeled signal shape has a 90% width—the minimum span which contains 90% of the distribution—that is 1.8 times narrower than the SHM. Such a narrowing of the signal shape would improve a search's SNR by the same factor. For an axion cavity search like ADMX, the increase in sensitivity translates to an improvement in the coupling limit of $\sqrt{1.8}$, suggesting past data runs (Asztalos et al., 2010; Stern & ADMX, 2014) have near-DFSZ sensitivity, Fig. 6.1.

To review, halos from the Romulus25 simulation show major differences from the SHM in observables relevant to axion DM searches. The class of galaxies satisfying Eqs. 3.211 - 3.214, which include the MW, are observed to produce significantly narrower DM energy spectra than the SHM. This narrowing may be caused by bulk rotational motions or other biases toward slow motion relative to the baryonic disk. While beyond the scope of this paper, an explanation for the distribution shape may lie with merger history, the influence of the baryonic disk and the incompleteness of gravitational virialization.

The Romulus25 simulation provides a means to predict realistic axion signals. This high-resolution simulation develops realistic disk galaxies using robust gas dynamics and star formation/feedback models, which reproduce observed galaxy properties (Tremmel et al., 2017; Governato et al., 2007). Further, Romulus25's large size and uniform resolution provide a statistically significant sample of galaxies similar to the MW, and produce a consistent spectral shape in the circularly-orbiting frame. Together, the updated signal model from Eqn. 3.218 provides a marked improvement in the signal shape for axion cavity searches. A conservative estimate of the new shape would serve to improve the signal-to-noise of axion cavity searches by 1.8, increasing the sensitivity of previous analyses and improving future observations through the option of scanning at a higher sensitivity or a higher search rate. Such an optimization would result in faster and more sensitive searches.

3.6.3 Governing Mechanisms of Local Axion Spectra

The narrow signal shape, while advantageous to axion searches, is somewhat unexpected. The virialization process is presumed to reproduce the lowest moments of the local SHM DF up to environmental impacts. To search for the underlying dynamics responsible we pursue those differences from the SHM that attracted us cosmological simulations in the first place: realistic DM infall history and equilibration, and interactions with baryonic components. The results of this subsection are preliminary.

Halo DF Properties

Looking at the local distributions we are confronted with the apparent kinematical causes for the narrowing: bulk rotational motion and velocity anisotropy. The velocity distributions of MW-like halos show these features quite plainly, Fig. 3.23. Transforming to the kinetic energy and angular momentum plane also shows that most R25 MW-like halos depart from the SHM, Fig. 3.24. The anisotropy appears to be biased towards small out-of-plane dispersion, while bulk motion biases also appear to be in the direction of the baryonic disk. To better understand these biases we calculate several of the distribution moments. Means, medians and modes of the velocity distributions bare out that there appears to be not only consistent bias towards co-rotational motion, but also a long but weak counter-rotating tail, Fig. 3.25.

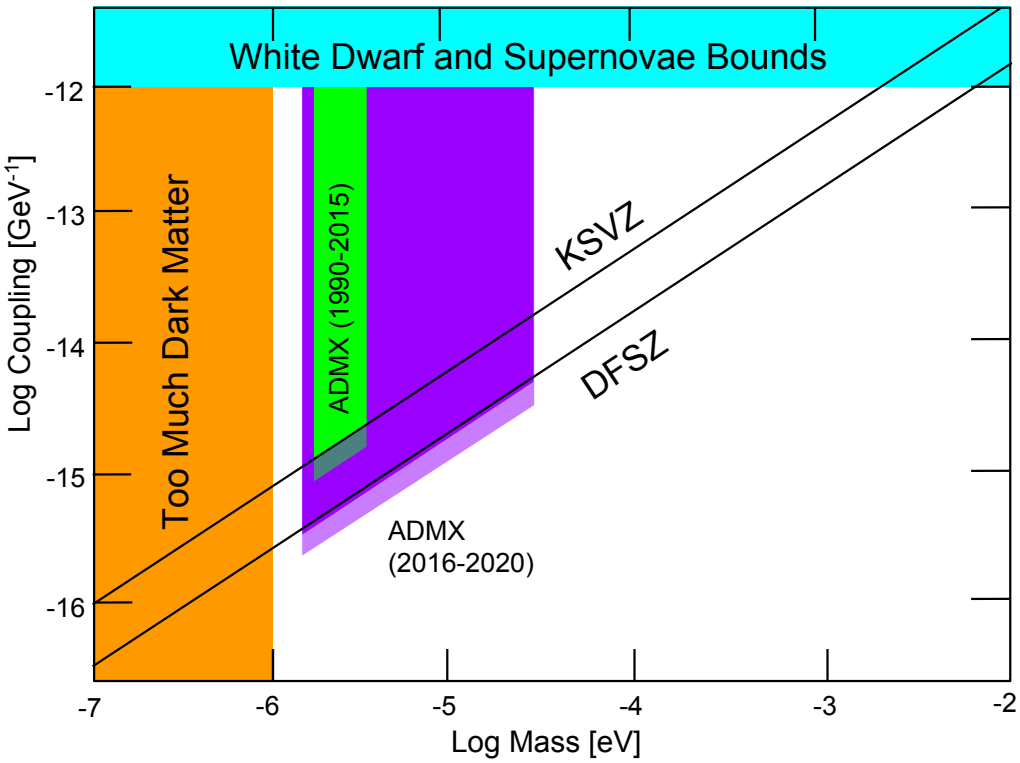

Figure 3.20: Illustration of the QCD axion parameter space over the plausible DM region, with current astronomical and cosmological constraints, plus benchmark theories. The 90 % confidence level coupling bound from the Axion Dark Matter eXperiment's (ADMX's) Phase 1 operations through 2014 (Stern & ADMX, 2014) is included in green, with Generation 2 projections shown in purple (Patrignani & Particle Data Group, 2016). Under the new signal model presented in Section 3.6.2, an increase of the SNR of 1.8 would translate to an improvement in the coupling limit of $\sqrt{1.8}$, illustrated in lighter shades.

Table 3.2: Relevant MW-like Galaxy Properties

halo #	M_{vir} $[10^{12} M_{\odot}]$	v_{circ} [km/s]	z_{major}	$\bar{\rho}$ [GeV c^{-2}/cc]	$n_{90\%}$
32	1.56	202	1.06	0.69	1.3
33	1.42	212	3.00	0.89	1.4
34	1.39	226	2.38	0.90	1.0
36	1.15	209	8.00	0.72	1.3
37	1.03	248	4.59	0.88	1.2
39	1.00	226	1.69	0.62	1.2
42	0.98	178	5.45	0.50	2.0
44	0.92	194	–	0.54	1.9
46	0.77	207	3.41	0.64	1.7
47	0.73	222	5.99	0.66	1.5
48	0.71	195	2.25	0.53	1.7
50	0.66	199	3.09	0.53	1.6
51	0.77	185	–	0.56	2.0
53	0.55	207	2.52	0.69	1.3
55	0.63	195	2.01	0.62	1.6
60	0.55	176	–	0.56	2.2

Note: Selected parameters of the simulated MW-like galaxies analyzed in this paper: M_{vir} is the total virial mass of the halo and galaxy; v_{circ} is the in-disk circular velocity at 8 kpc from the center of the galaxy; z_{major} is the redshift of the last major merger, where one exists; $\bar{\rho}$ is the DM mass density at 8 kpc averaged over the toroidal sample ; $n_{90\%}$ is the factor of narrowing for the axion signal shape.

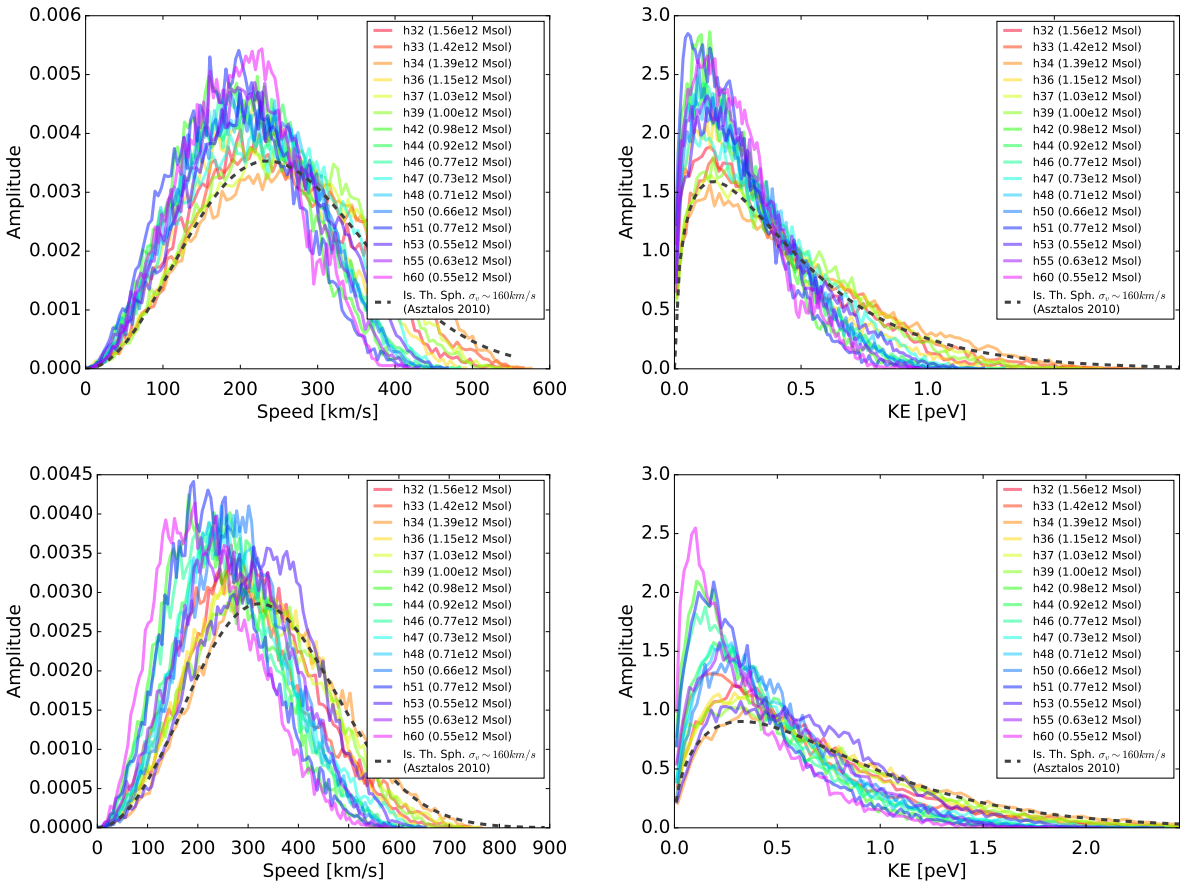

Figure 3.21: Spectra of MW-like halos from Romulus25 at $z = 0$, normalized to unity. The spectra are taken from galaxy-centered in-disk toroidal samples of cylindrical extent $-2kpc \leq z \leq 2kpc$, $r_l - 1kpc \leq r \leq r_l + 1kpc$, where $r_l = 8$ kpc, though the results are fairly robust to changes in the value of r_l. The galaxy center frame speed (upper left) and energy spectra (upper right) show general agreement with the SHM, with small departures in the low-speed spectra amplified in the energy spectra, primarily due to the shift from a measure linear in particle speed to quadratic. The solar frame speed spectra (lower left) shows additional low-speed departures from the SHM, but are still consistent with previous WIMP studies (e.g., (Sloane et al., 2016; Schaller et al., 2016)). The solar frame energy spectra (lower right) displays drastic departure from the SHM, which is expected due to the change in measure when transforming from speed to energy coordinates. The SHM shape in the galactic frame have been boosted tangentially by $\bar{v}_c = 226$ km/s, in line with ADMX analyses (Asztalos et al., 2010).

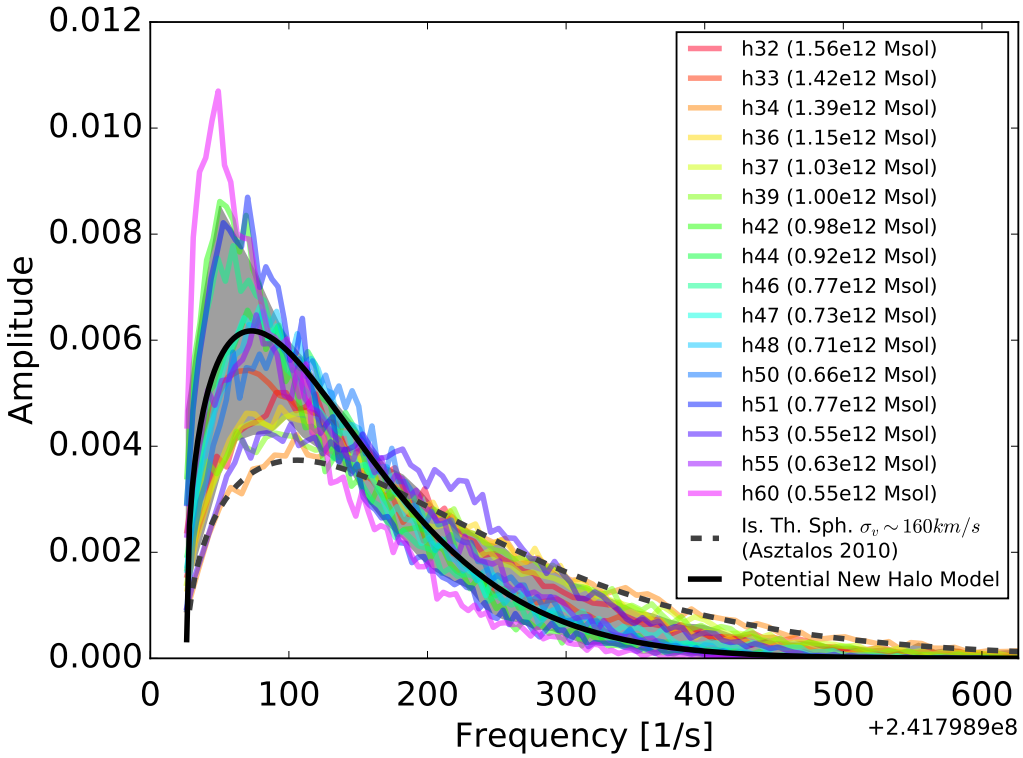

Figure 3.22: Frequency spectra of MW-like halos from Romulus25 at $z = 0$ and the SHM composed of 10^{-6} eV c^{-2} axions, generated from Fig. 3.21 spectra via the energy-to-frequency transform derivable from Eq. 3.209. The solid black line represents the new shape of the form Eq. 3.218 fitted to to the halos, with the gray representing the data-based error estimate using the two-thirds rule.

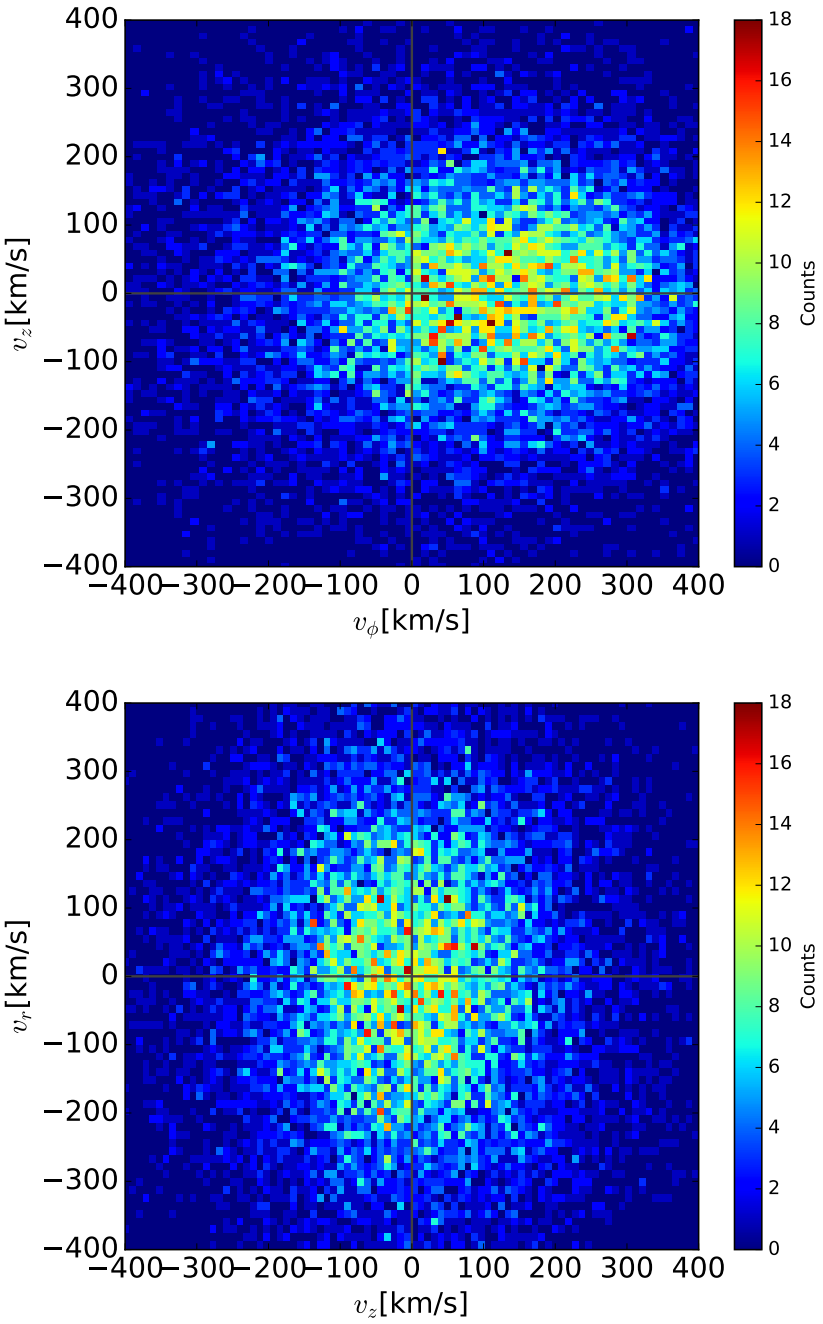

Figure 3.23: R25 halo 44 solar sample velocity distribution, in galactic frame, projected into the circular-vertical plane (upper) and the vertical-radial plane (lower). Plotting ratio is 1:1 for straightforward visualization anisotropy.

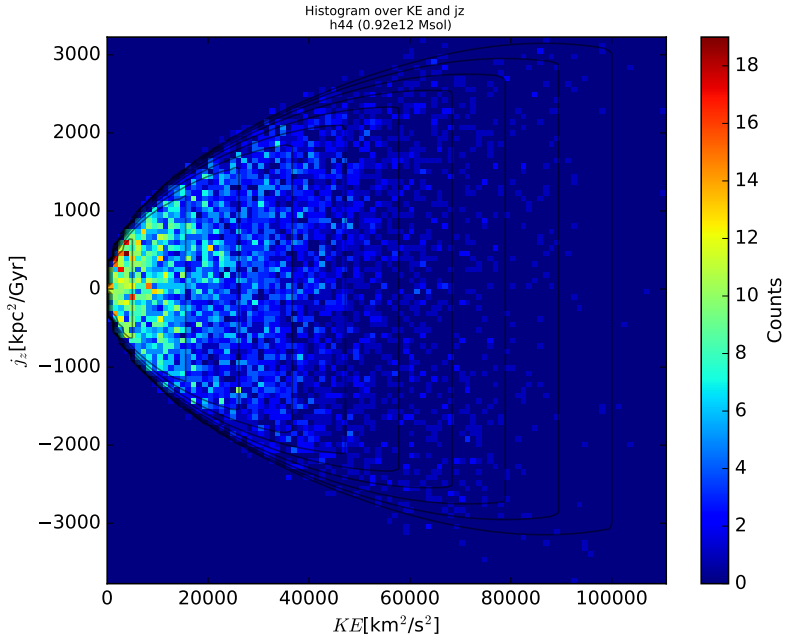

Figure 3.24: R25 halo 44 solar sample kinetic energy and vertical angular momenta distribution, in galactic frame. Several contour lines of the SHM distribution are shown in black.

The next moments also reinforce our intuitive assessment. Correlations among the dispersions showing bias towards co-rotational motion within the galactic plane are obvious, Figs. 3.26 3.27. Moreover, these fractions appear to be robust against halo mass and a number of other halo and galactic quantities, Figs. 3.28 3.29 3.30. There is an existing theory which seems to meet these observations. Primarily fueled by tidally-disrupted accretion of matter toward the galactic plane, Dark Disk theory (DD) speculates an abundance of DM moving in the plane of large galaxies. Is it possible our anisotropy and bulk biases are indications of DDs?

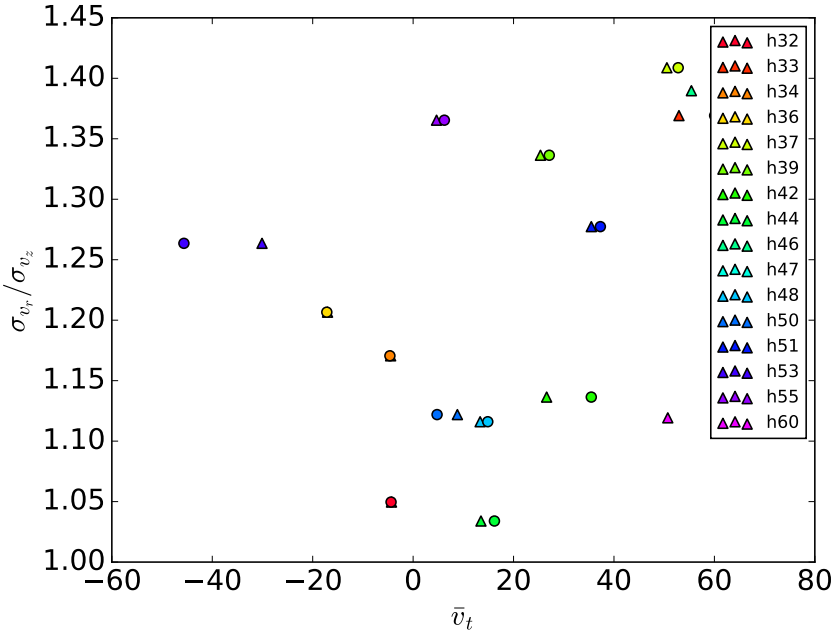

Figure 3.25: Bulk motion statistics of R25 MW-like halos over halo mass. Mean rotational velocity values are triangles and medians are circles.

Effects of Baryons

Untangling the cause of these features from the litany of dynamics at play is a task likely not to be solved in a few months' study. We therefore instead set our goal to better understand the response of CDM halos to different dynamical components. Effects from baryons is our concentration. To test the presence of DDs in our MW proxies, let us see what happens when the galaxy is removed. A DM-only version of R25 (R25D), created before the full SPH run, produces many of the same halos as the full run including our MWs. Analogue halos are pulled to provide insight as to how the baryons contribute to the signal narrowing. One of the R25 halos did not have an analogue.

The local axion spectra for the R25D halos are not wider but narrower! Fig. 3.31. Other statistics confirm that the presence of baryons appears to drastically widen the axion signal,

Figs. 3.32 3.33 3.34. Bulk motions appear to remain stationary in the median but with decreased dispersion, in contradiction with the existence of a DD. Anisotropy ratios do appear to be perturbed, though this is in line with the influence of a highly oblate galactic disk potential. Another important kinematical difference becomes apparent when comparing the two halo types: temperature. The effective speed dispersion increases significantly when baryons are included, by a factor of $\sim 25\%$ on average, which would alone lead to an increase in spectra on the order of $\sim 50\%$. An increase in circular velocity is also observed. Both the heating and velocity increase are likely due to an increase in the interior mass from the presence of the galaxy, which may be the primary reason for spectra widening when adding baryonic species. Baryons don't cause a narrower signal, the signal appears to be narrower in spite of the baryons!

So dark disks do not appear to be the answer. To track down the responsible phenomena and underlying dynamics, we divide up potential influences into two categories: environmental and internal. Within these categories we will concentrate on the process of DM virialization as it pertains to interacting with the baryonic component (internal) and the aspects of a galaxy's merger history (environment).

Drilling down to the complex internal dynamics of a MW-like halo, we revisit our collection of spun-up Isolated Collapse (IC) from 3.6.1. Figure 3.36 shows the axion energy spectra for this collection adhered to a similar spectral shape of the MW-like halos of R25D up through the realistic spin values, making ICs a reasonable comparison to the internal workings of R25 halos (Merritt & Valluri, 1999b,a; Valluri & Merritt, 2000; Valluri et al., 2010; Deibel et al., 2011; Valluri et al., 2012, 2013; Abbott et al., 2017). Focusing on an IC halo with near expectation value $\lambda = 0.03$, let us determine what causes the signal to take shape.

It is well known that DM-only halos are not rotationally symmetric in shape, but triaxial in general. Such a universal shape, perhaps induced by the bar structure tied to the universal NFW and Bullock profiles, implies a type of dynamical locking mechanism. At a particle level a halo is composed of orbits. Understanding halos orbits may reveal shaping mechanisms of

both the halo and its local energy distribution.

Integrating orbits of the $\lambda = 0.03$ halo, after the potential reaches a stable state, gives us another view into the halo state, Fig. 3.37. Considerations of the ITS and equipartition principles dictate that a thermal distribution has symmetric division of action over motions perpendicular to the radial direction. As expected, angular equipartition is not observed by the halo. Further, the columniation of the actions imply that many of the halo orbits occupy resonances of the triaxial structure. Next we identify and analyze these resonances.

Orbits have many types (Binney & Tremaine, 2008). We only concern ourselves with a basis of three: tube, box, and chaotic orbits. Orbit types are defined by the space-filling curve traced out by the particle. Tubes have a hole in their curve and they exist in a finite volume. Boxes have no hole but they do trace out a finite volume, indicating a well-converged frequency spectra. Chaotic orbits are not confined. In our finite simulations of 10 Gyr we classify orbits via a set of simple conditions, intended for orbits intersecting the solar sample.

1. Tube: The curve radius must not fall below 0.5 kpc ($r \geq 0.5$ kpc)

2. Box: If not a tube, the Fourier transform of the curve must not contain significant weight in components far outside the dynamical timescale ($|FFT(\{x\}_i)(1/(10t_{dyn}))|^2 \leq 0.1|FFT(\{x\}_i)(1/(t_{dyn}))|^2$)

3. Chaotic: Not a box or a tube

Decomposing the solar sample orbits shows that $\sim 75\%$ boxes, followed by $\sim 20\%$ tubes, and the remaining $\sim 5\%$ in chaotic orbits. These results are roughly consistent with (Valluri et al., 2012). Action decomposition also shows a division between the types, Fig. 3.38. We may also decompose the axion signal shape along orbit types, Fig. 3.39, showing that the leading contribution to the condensed signal is box orbits. We now understand isolated collapse halos to be a non-thermal resonant structure dominated by low energy tubes at the solar radius.

To determine how the R25 structure may be recovered, we introduce a proxy for the baryonic potential. The baryonic component of a galaxy is expected to condense quickly, especially in the absence of mergers. For our first experiments we drop a point-like particle of prescribed mass into the center of the already-formed $\lambda = 0.03$ halo, let it stabilize, and study its new equilibrium. The particle masses range from the simulation mass resolution to the expected baryonic fraction of the MW. The point-like particle appears to have the desired effect for masses on the order of a MW galaxy, Fig. 3.40. Interior mass and dispersion both seem to match what was seen in R25D, though inspection of the distributions do show some non-adiabatic characteristics, Fig. 3.41. Orbital decomposition of the new equilibrium shows a notable shift in the proportions of orbits, to 55% boxes 25% tubes and 20% chaotic for the $2 \times 10^{10} M_{\odot}$ particle, but with actions still very distinct from a thermal distribution.A promising start.

Dropping in a SMBH is a bit extreme. Subsequent experiments use baryon potentials described by a particle of MW bulge radius softening length, a particle grown over many solar sample dynamical times, and combinations therof. These experiments show the dropped-particle result to be reasonably robust, Figs. 3.42 3.43. Orbit spectra of halos with gentler baryon introduction still show obvious non-thermal characteristics, Fig. 3.44. Orbit decomposition also shows similar proportions to the dropped case, similar division among orbit actions, Fig. 3.45, and similar shifts in axion spectra toward the R25 shape, Fig. 3.46. The primary disparity between the cosmological and IC distributions is the shape of velocity anisotropy, which may made up by merger-induced mixing. A final step is to introduce full MW bulge and disk models to the halo in a realistic way, but this is deferred to future work.

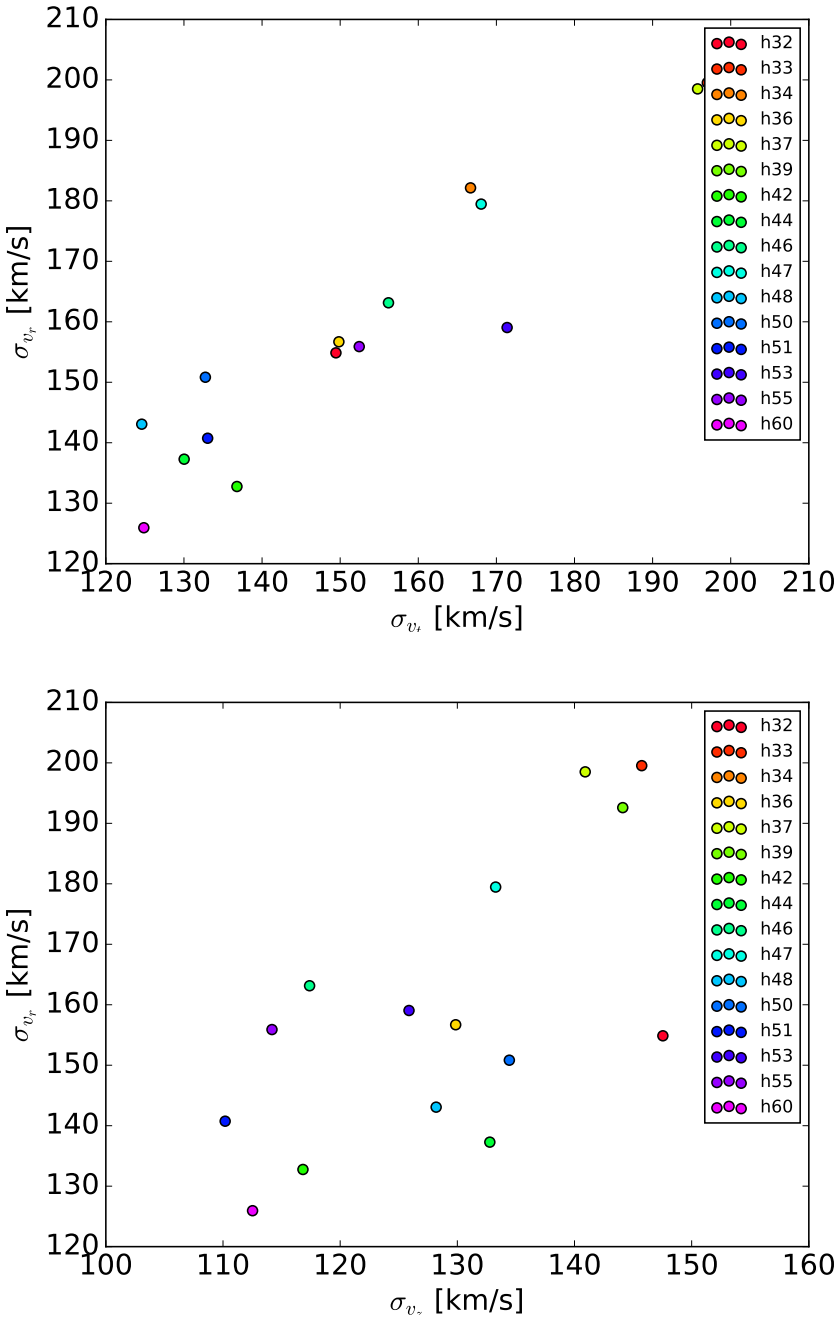

Figure 3.26: Velocity dispersions of R25 MW-like halo solar samples, with the top panel giving circular and radial directions and the bottom panel vertical and radial dispersions.

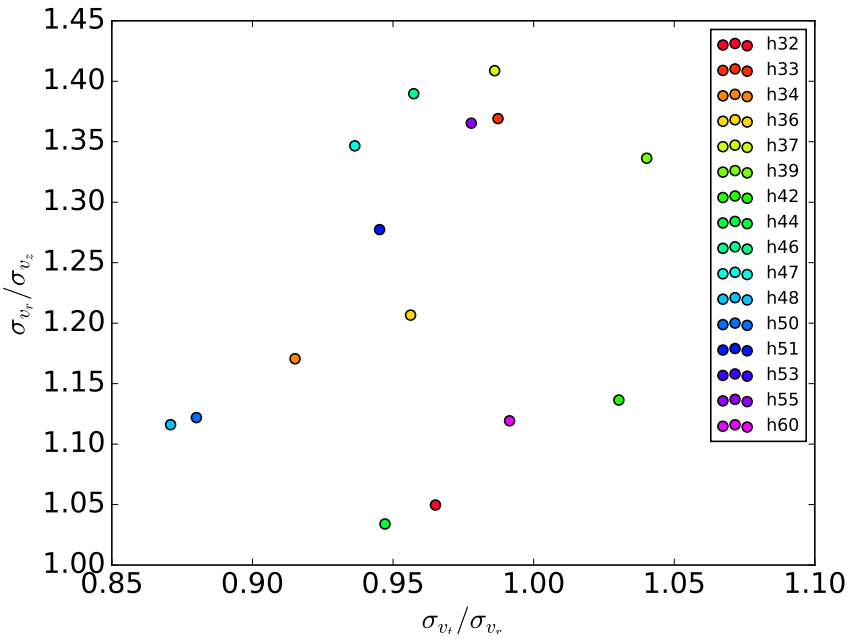

Figure 3.27: Velocity dispersion ratios of R25 MW-like halo solar samples.

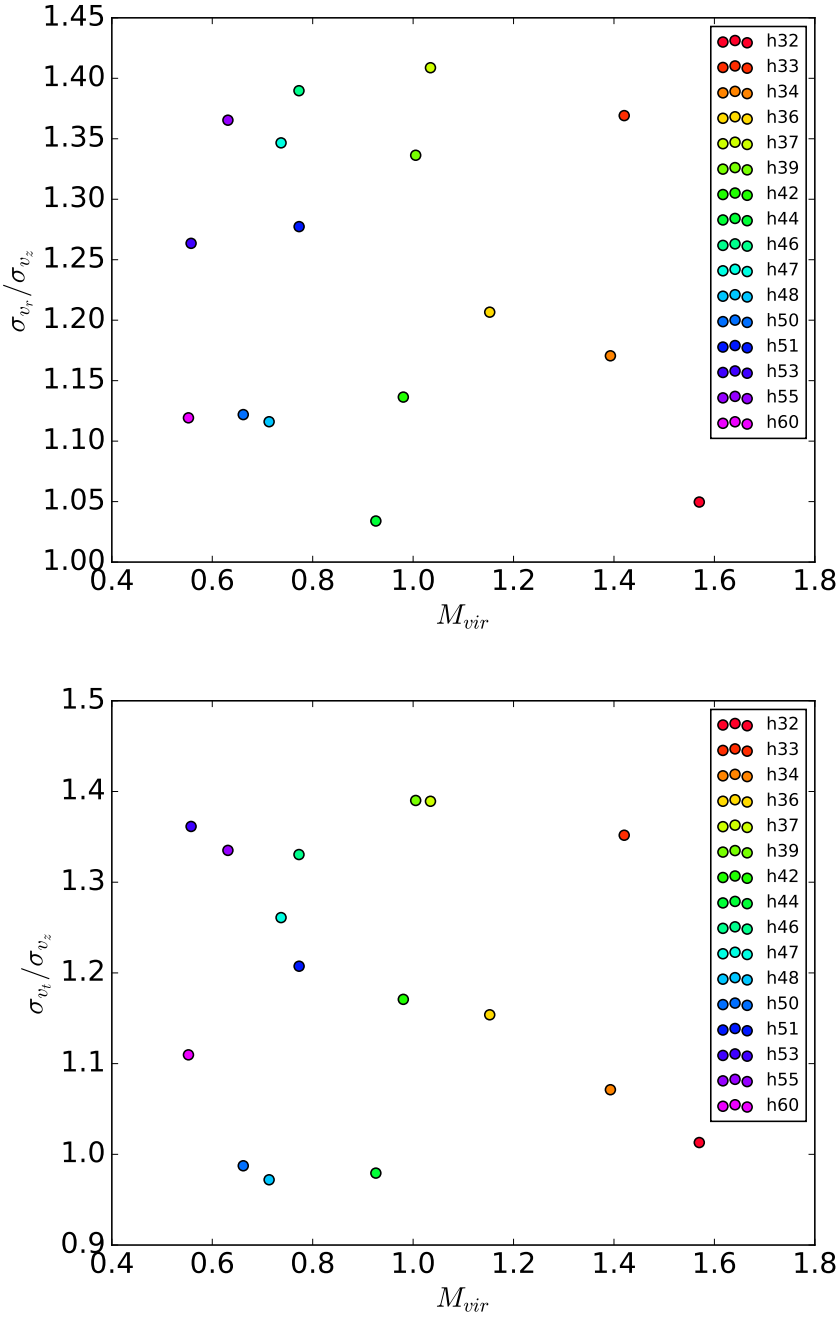

Figure 3.28: Velocity dispersion ratios of R25 MW-like halo solar samples over halo mass, with the top panel giving the radial over vertical ratio and the bottom panel the circular over vertical ratio.

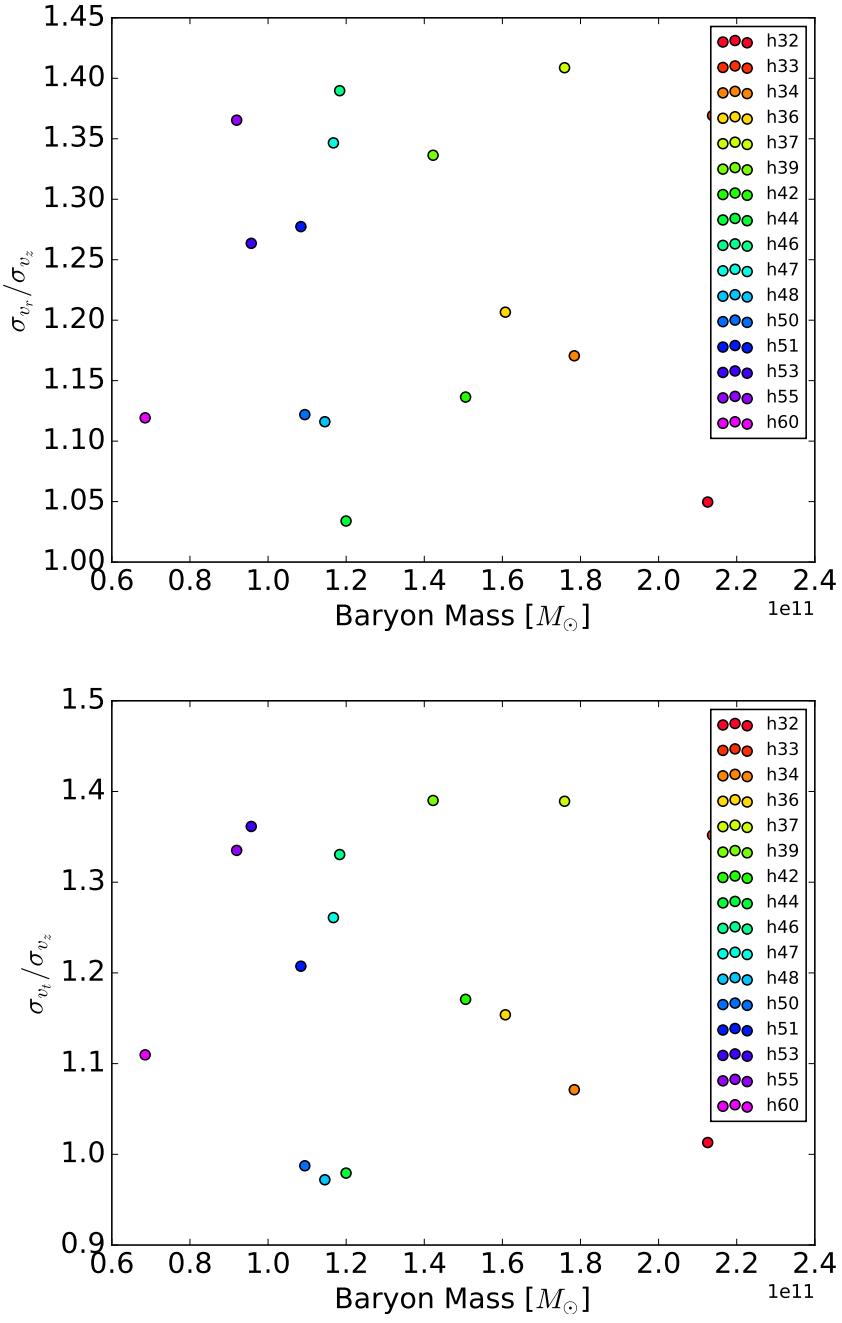

Figure 3.29: Velocity dispersion ratios of R25 MW-like halo solar samples over baryonic mass, with the top panel giving the radial over vertical ratio and the bottom panel the circular over vertical ratio.

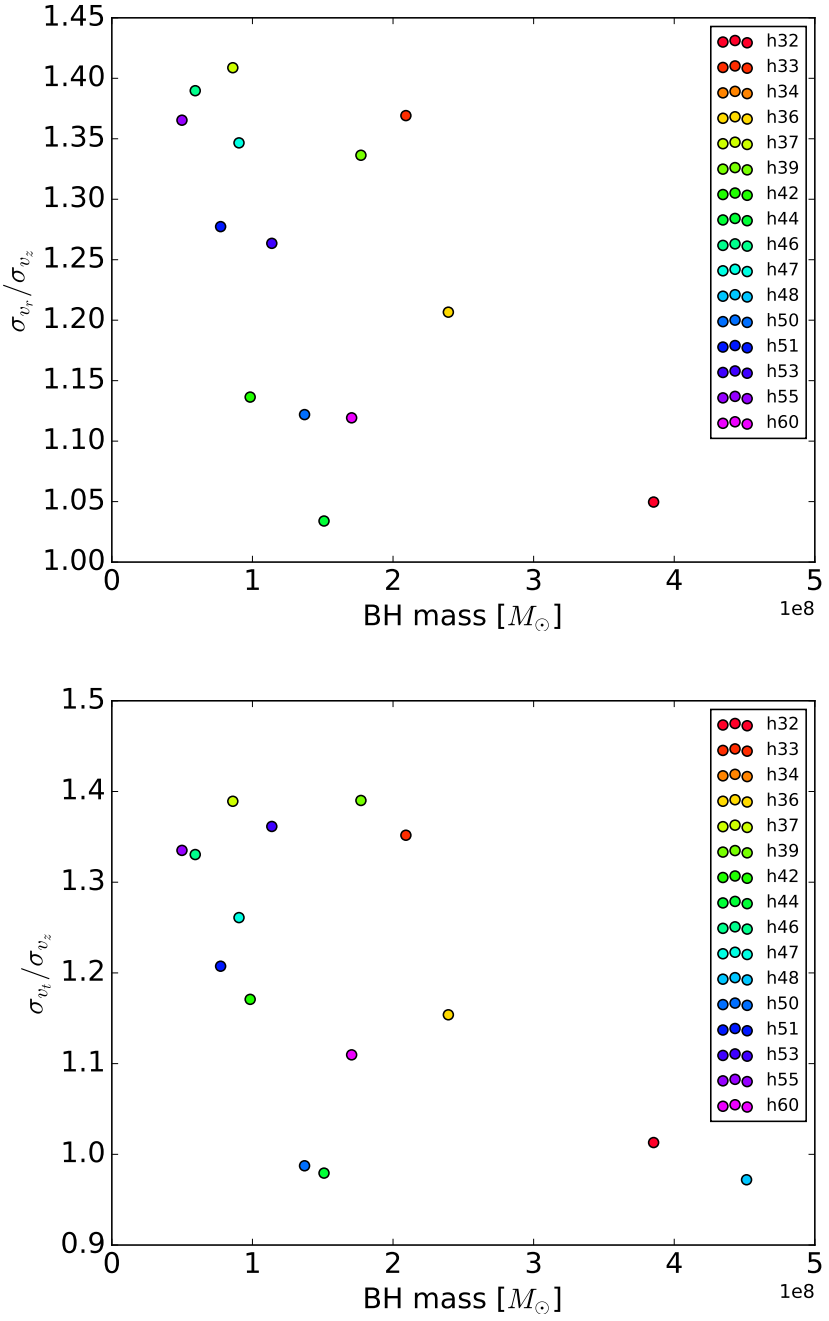

Figure 3.30: Velocity dispersion ratios of R25 MW-like halo solar samples over BH mass, with the top panel giving the radial over vertical ratio and the bottom panel the circular over vertical ratio.

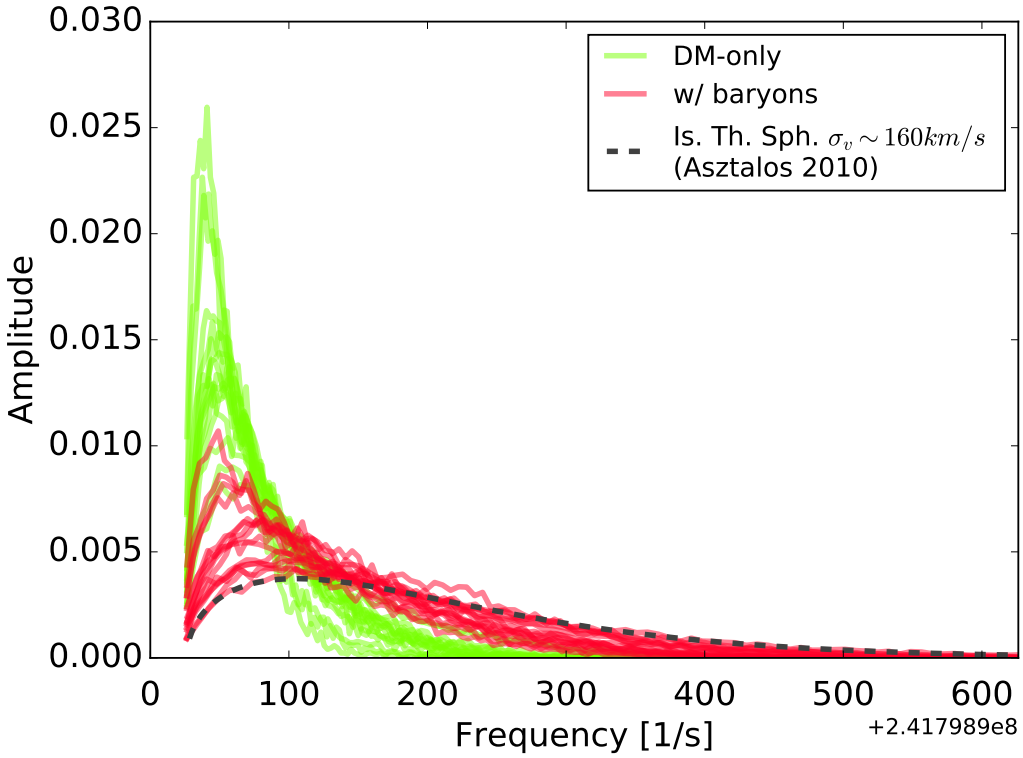

Figure 3.31: Frequency spectra of MW-like halos in R25 and R25D in the solar frame.

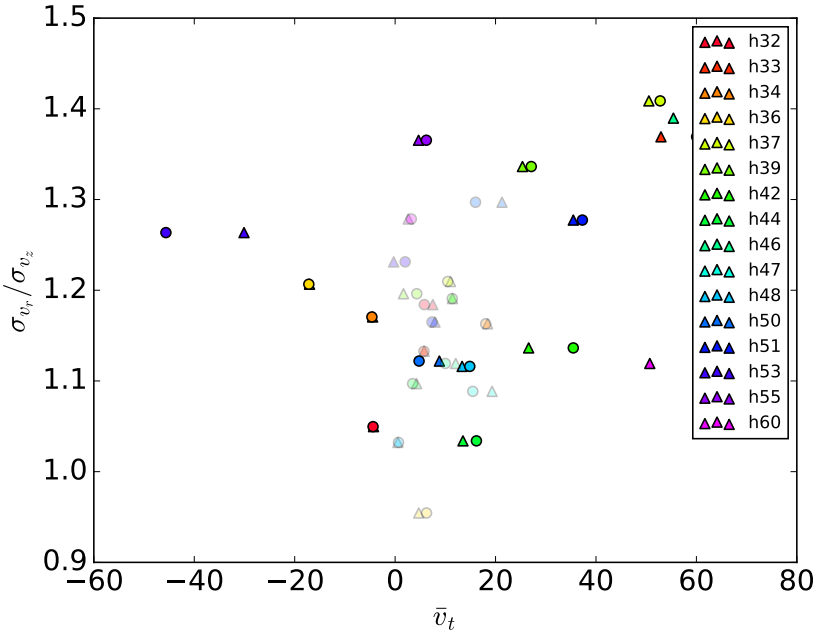

Figure 3.32: Bulk motion statistics over halo mass. R25D points are semi-transparent, with R25 shown for comparison. Mean rotational velocity values are triangles and medians are circles.

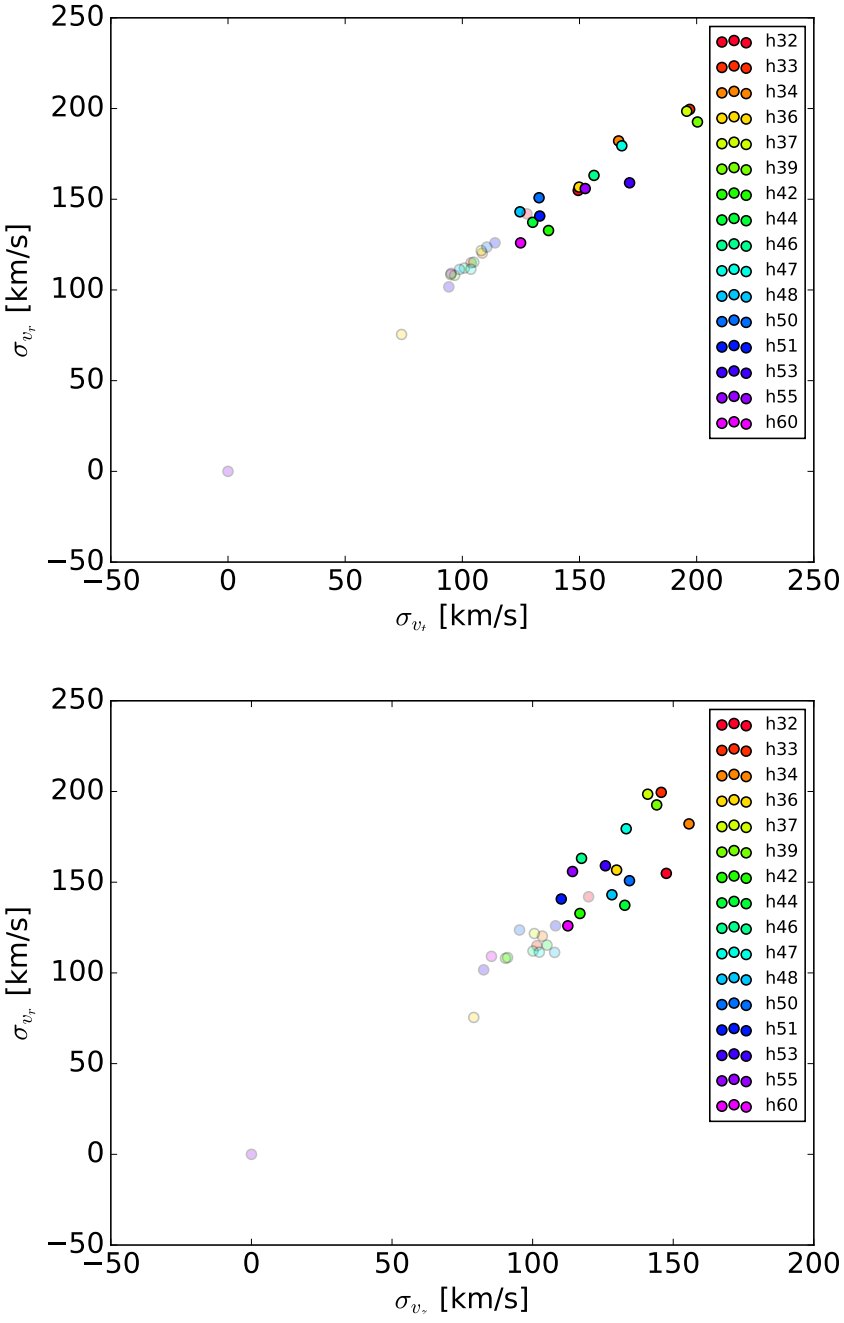

Figure 3.33: Velocity dispersions over MW-like solar samples. R25D points are semi-transparent, with R25 shown for comparison. The top panel gives circular and radial directions and the bottom panel vertical and radial dispersions.

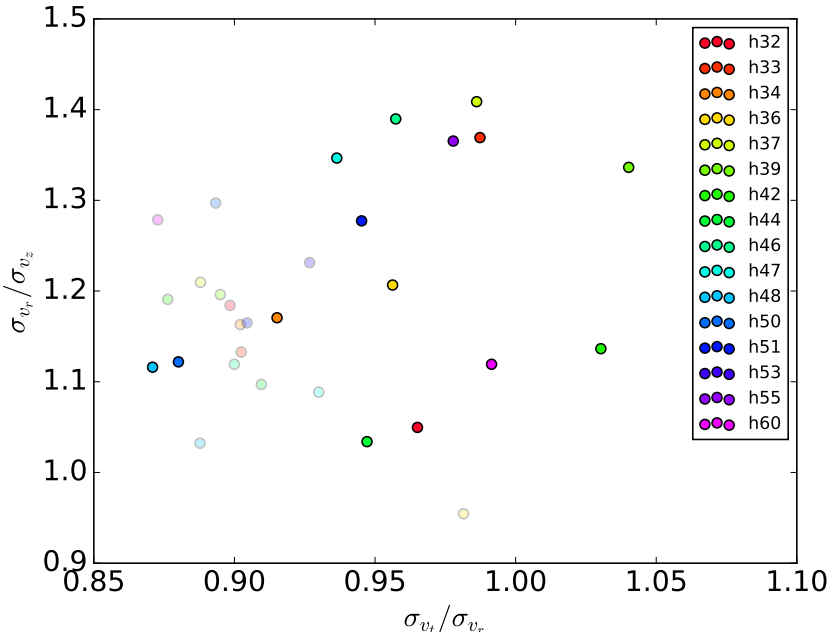

Figure 3.34: Velocity dispersion ratios of MW-like halo solar samples. R25D points are semi-transparent, with R25 shown for comparison.

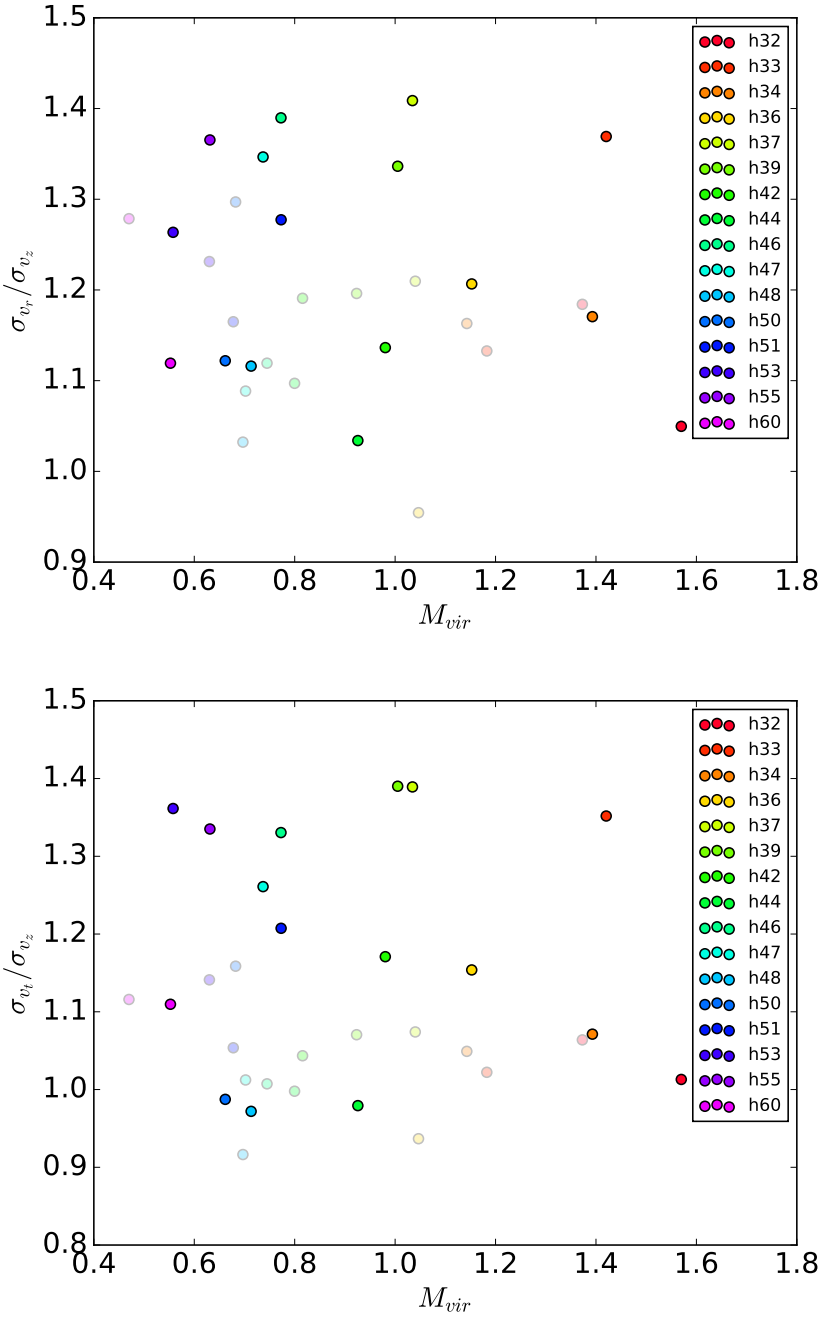

Figure 3.35: Velocity dispersion ratios of MW-like halo solar samples over halo mass. R25D points are semi-transparent, with R25 shown for comparison. The top panel gives the radial over vertical ratio and the bottom panel the circular over vertical ratio.

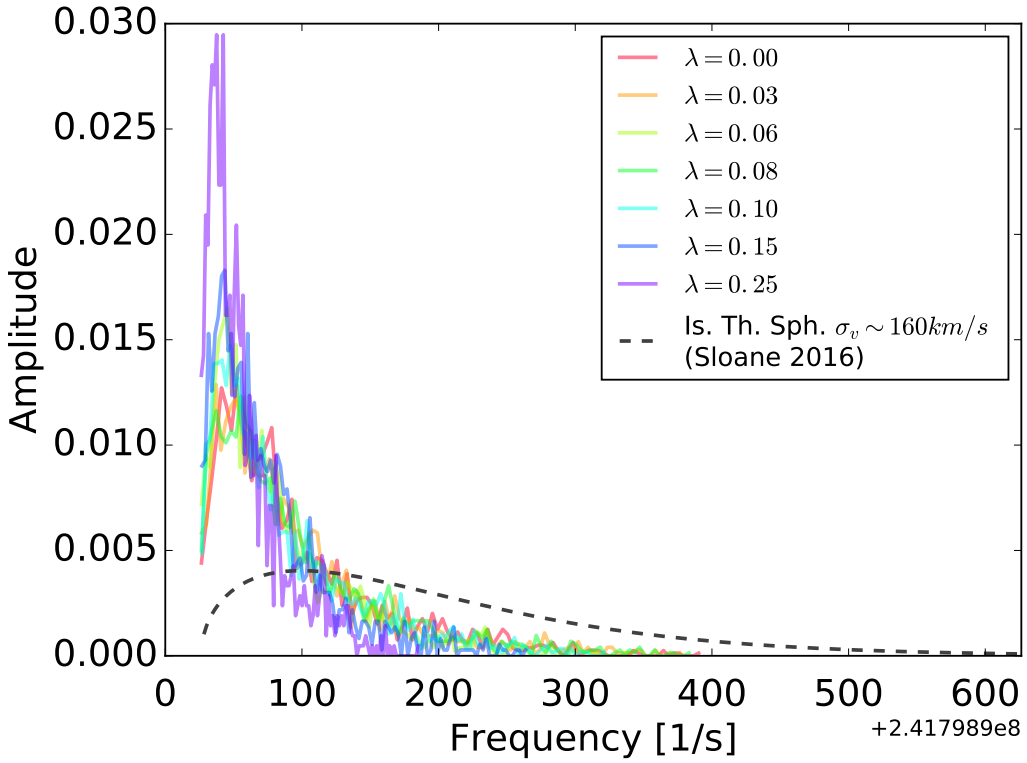

Figure 3.36: Frequency spectra for most isolated collapse halos from 3.6.1, of the solar sample in the solar frame. For moderate spins (< 0.1) the signals roughly align with those of R25D, with increasing co-motion causing an additional unrealized narrowing factor.

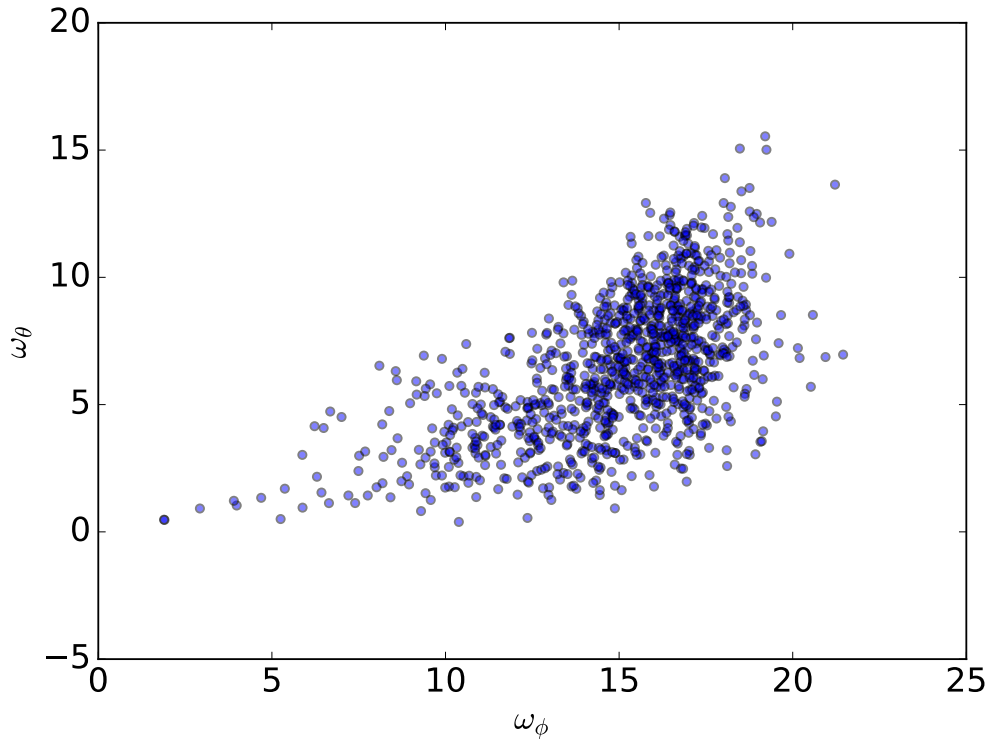

Figure 3.37: Orbital actions in the azimuthal and declination directions for the $\lambda = 0.03$ halo. Integration starts 10 Gyr after formation. Actions are taken of particles in the solar sample. Action units are in orbits over the equilibrium integration time.

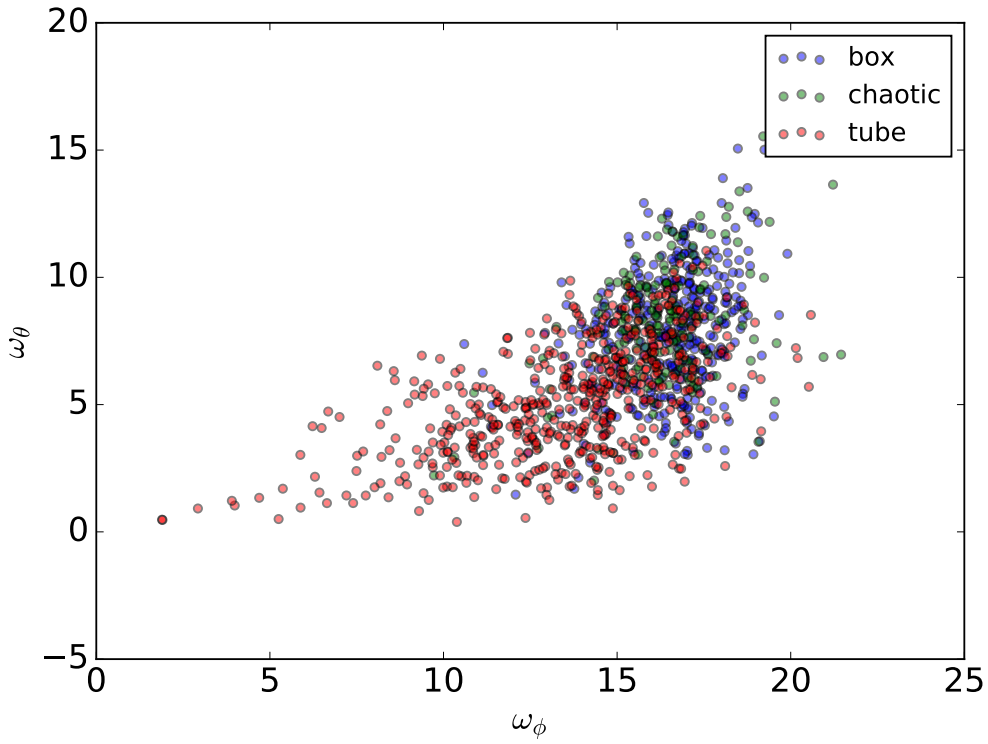

Figure 3.38: Orbital actions in the azimuthal and declination directions for the $\lambda = 0.03$ halo, decomposed by orbit type. Integration starts 10 Gyr after formation. Actions are taken of particles in the solar sample. Action units are in orbits over the equilibrium integration time.

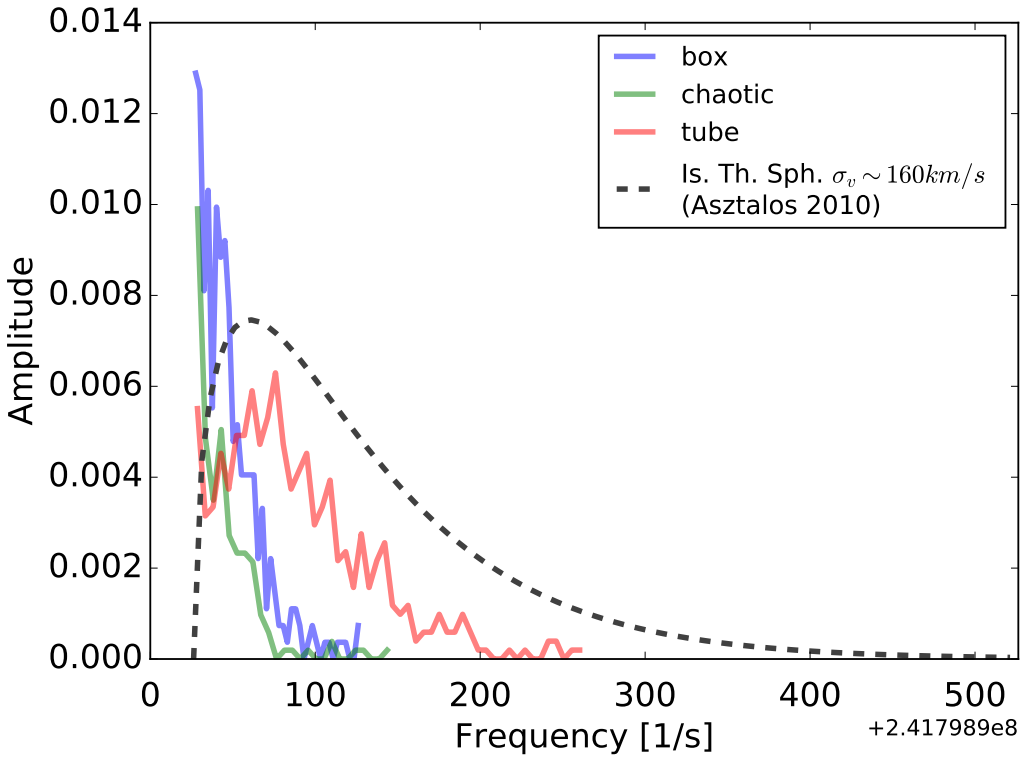

Figure 3.39: Frequency spectra for the $\lambda = 0.03$ halo from, of the solar sample in the galactic frame, decomposed by orbit type.

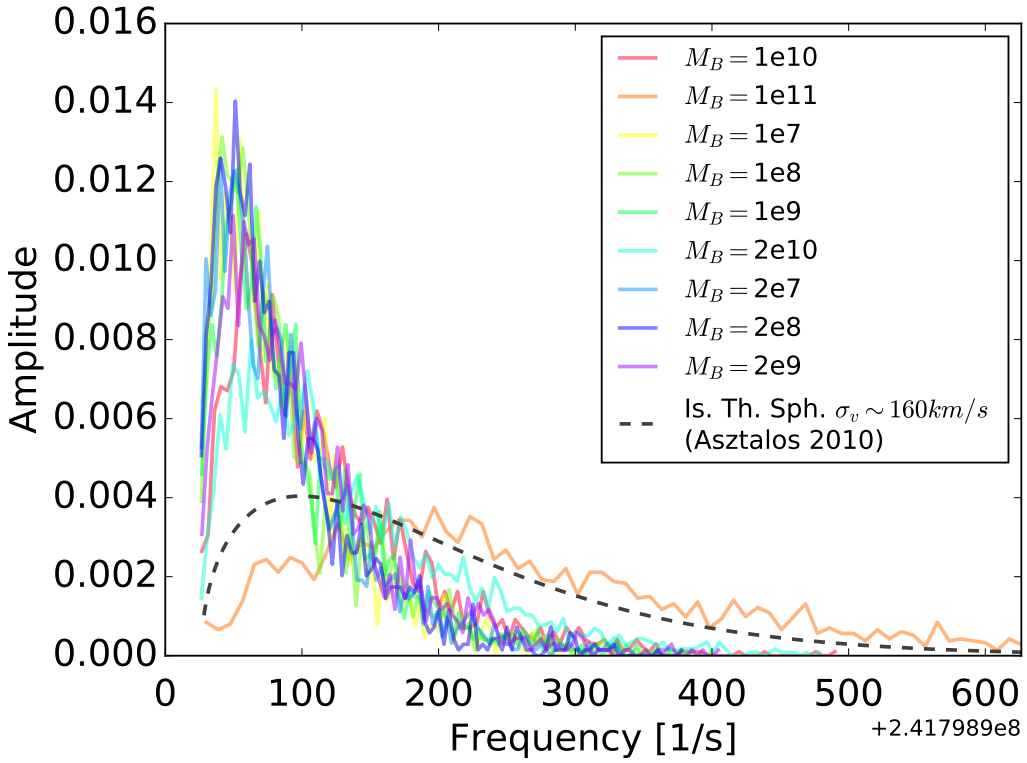

Figure 3.40: Frequency spectra for $\lambda = 0.03$ halo after equilibration from a dropped point particle potential of prescribed mass, of the solar sample in the solar frame.

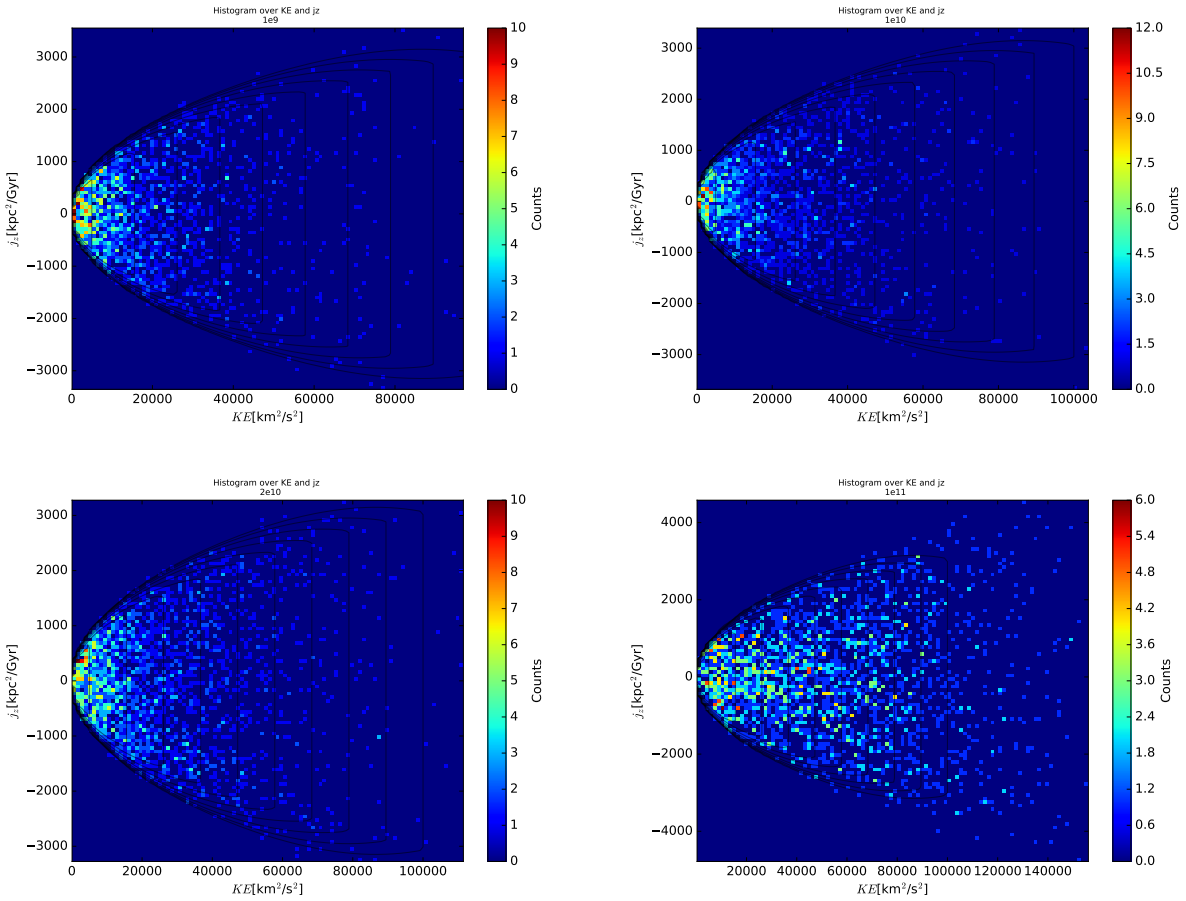

Figure 3.41: Kinetic energy and angular momenta distribution for $\lambda = 0.03$ halo after equilibration from a dropped point particle potential of prescribed mass, introduced at the end point of the 3.6.1 simulation. Distributions are taken from the solar sample in the solar frame. Mass of dropped particle is shown in figure title in units of $M_\odot$.

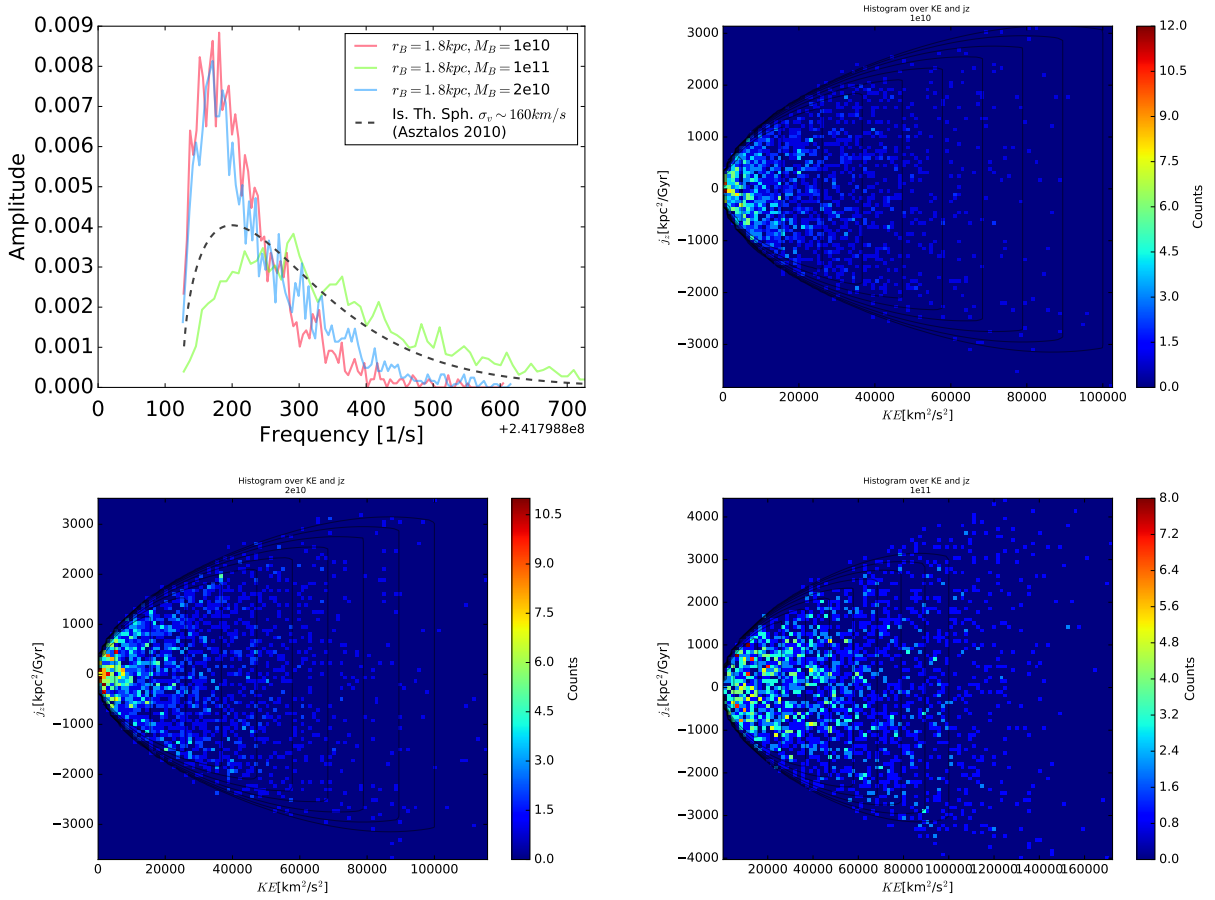

Figure 3.42: Kinetic energy and angular momenta distribution for $\lambda = 0.03$ halo after equilibration from a dynamic particle potential of prescribed mass, introduced at the end point of the 3.6.1 simulation and having a softening radius of 2.0 kpc. Distributions are taken from the solar sample in the solar frame. Mass of particle is shown in figure title in units of $M_\odot$.

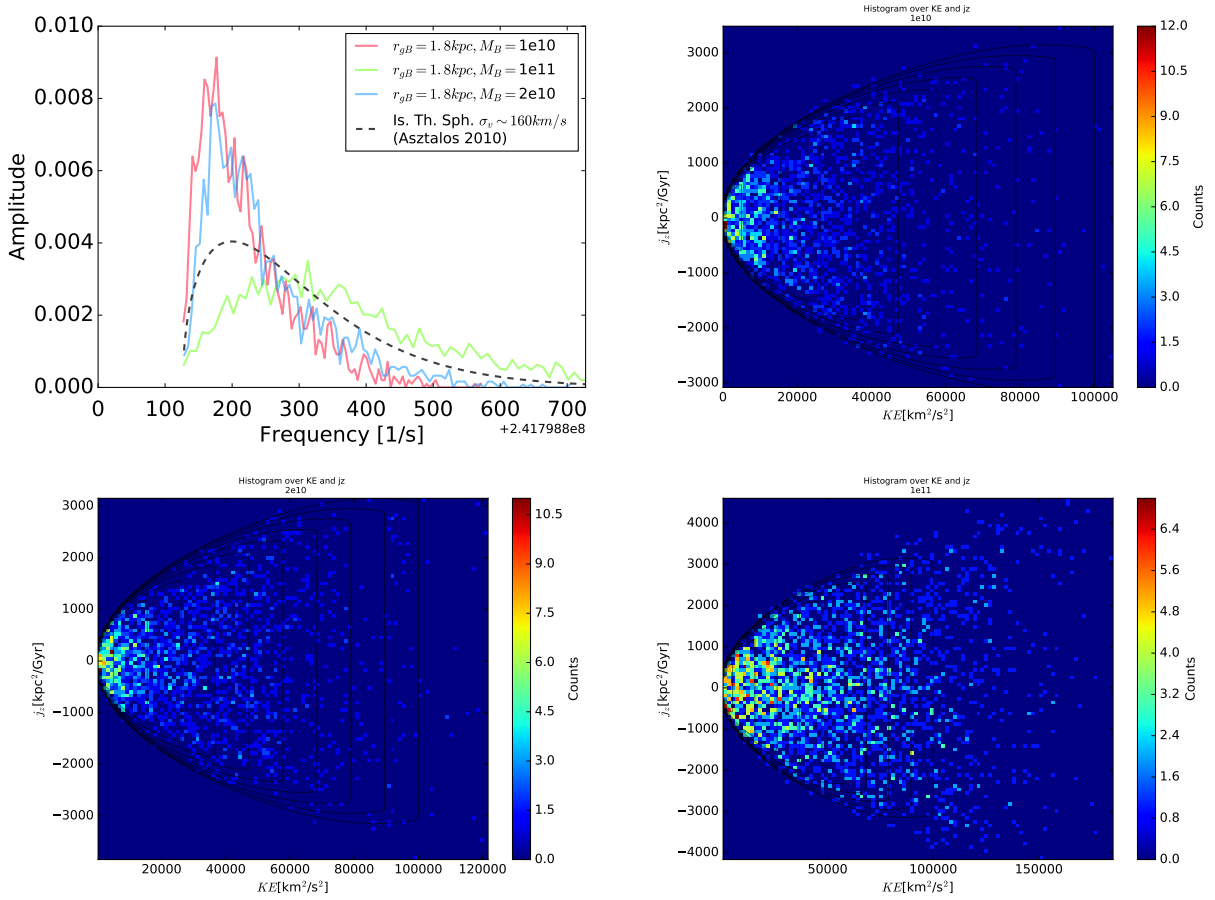

Figure 3.43: Kinetic energy and angular momenta distribution for $\lambda = 0.03$ halo after equilibration from a dynamic particle potential of prescribed mass, grown over a period of 1 Gyr from the end point of the 3.6.1 simulation and having a softening radius of 2.0 kpc. Distributions are taken from the solar sample in the solar frame. Mass of particle is shown in figure title in units of $M_\odot$.

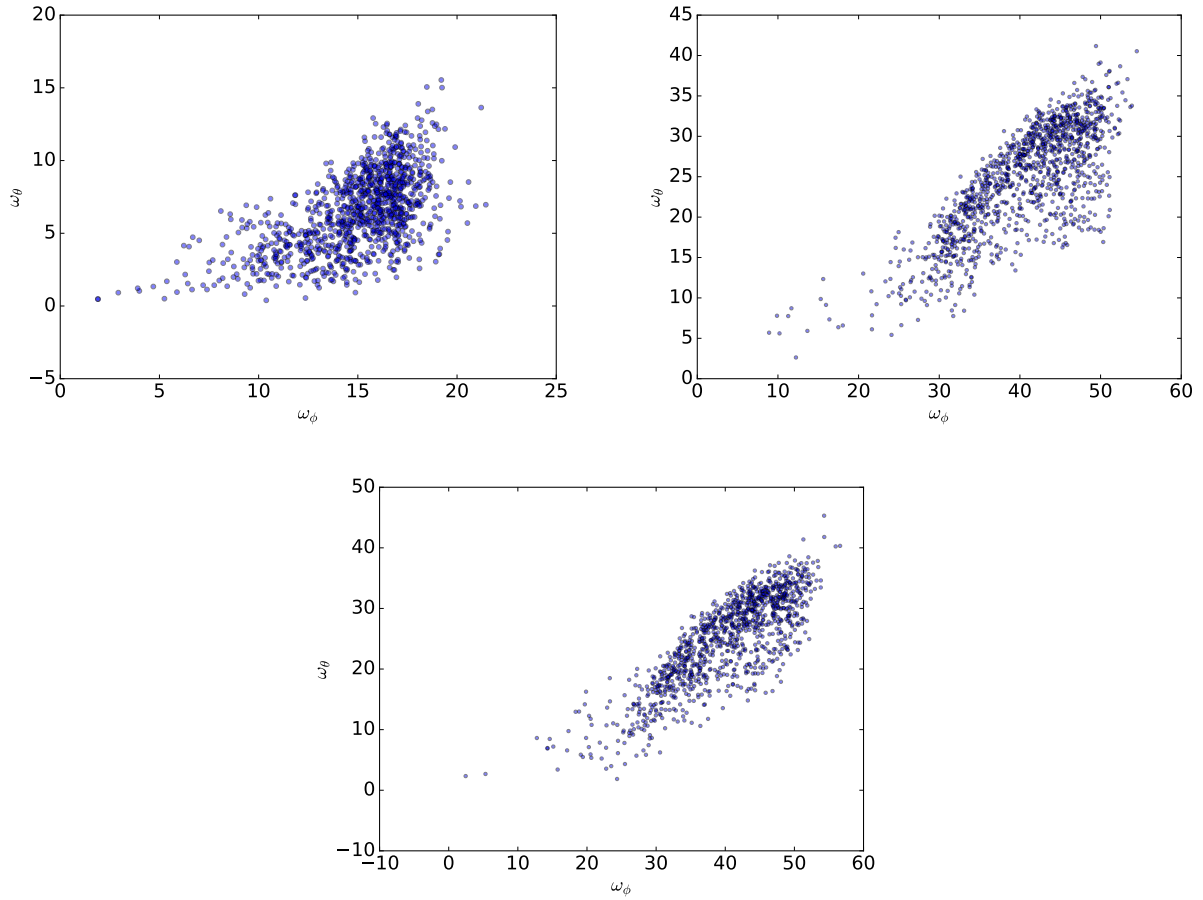

Figure 3.44: Orbital actions in the azimuthal and declination directions for the $\lambda = 0.03$ halos, with the upper left figure being of the control halo, upper right is of the dropped 2 kpc bulge of mass $2 \times 10^{10} M_\odot$, and lower is of a bulge of the same size, but grown over the period of 1 Gyr. Actions are taken of particles in the solar sample. Action units are in orbits over the equilibrium integration time.

We have learned several things about the equilibration process of IC halos from this series of experimentation and analyses:

1. Isolated halos fall into triaxial NFW (spherically averaged) potentials in the absence of baryons, dominated by resonant orbits of the tube and box classes.

2. Introducing a robust simple central potential scatters orbits chaotically and heats their spectra

3. Spectra appear to be robust to the method of introduction, but are sensitive to the mass

4. Orbit class' contributions to the axion spectra broaden with baryon mass

5. Nature of widening is non-thermal

Based on the ability of a crude baryonic potential to reproduce the the halo spectral width measured in R25 and our other analysis, we posit that heating and scattering is the primary cause of spectral widening. Further we have learned a great deal about the highly resonant structure of CDM halos, much of which may be applied to analyzing the results of future Bose simulations.

3.7 Summary

To review, we started the chapter by laying out an adventurous project for determining whether or not relic axions form unique structures on galactic scales. Guided by project requirements we identified and derived an ideal means of modeling axion structure-formation dynamics, which show the potential to produce unique structures. Small-scale simulations of axion infall performed using the AXP platform result in the identification of unique Bose structures capable of surviving the rigors of gravitational collapse. Efforts to better understand the structure of halos formed under the control physics of CDM were also presented.

Insight to the forming dynamics of DM halos and a better-motivated axion signal shape were found. In the next chapters we migrate into the impetus for this theoretical effort: axion search experiments. While we have yet to compute a signal for axion DM searches using full Bose physics, the model proposed from R25 is still a vast improvement over the SHM in terms of motivating physics. Focusing on the resident Axion Dark Matter eXperiment (ADMX), we see how the new model impacts the axion coupling sensitivity, $g_{a\gamma\gamma}$.

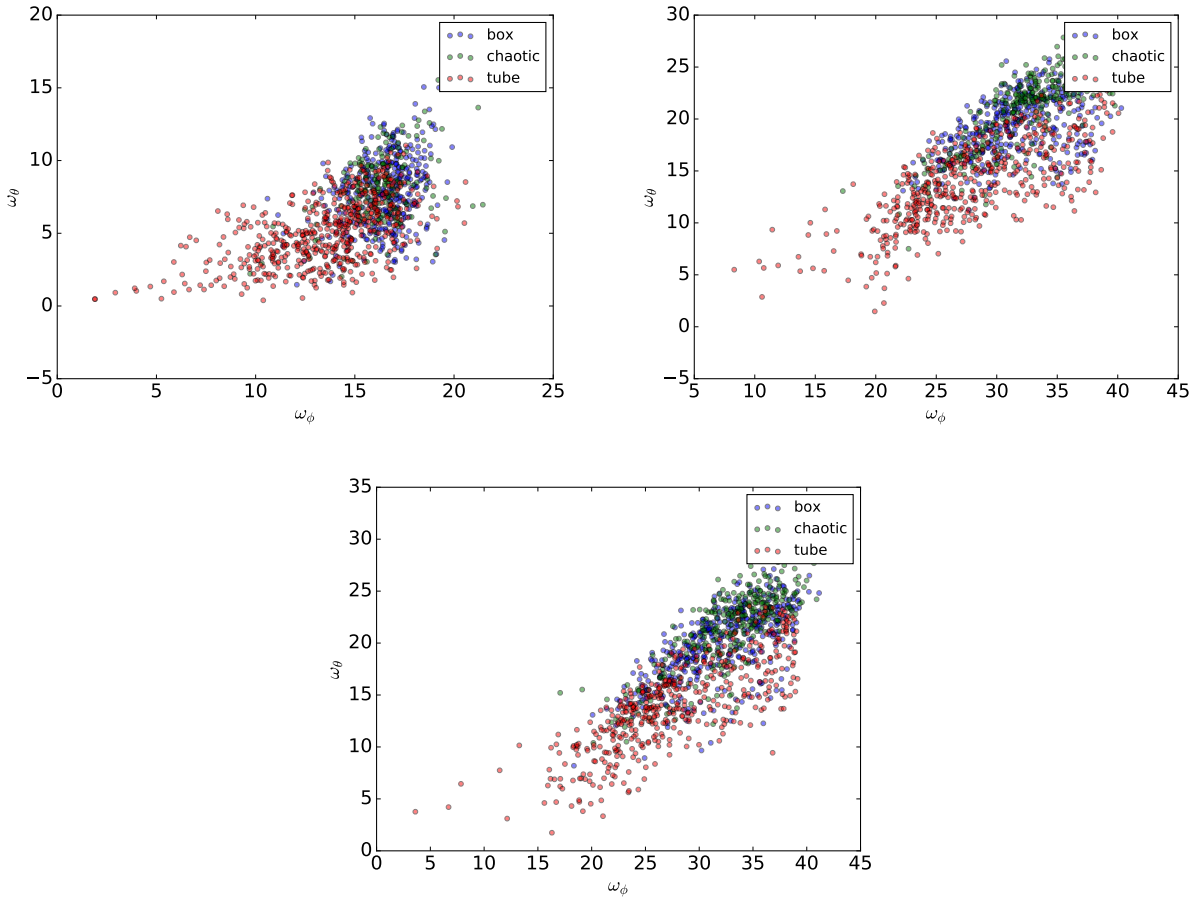

Figure 3.45: Orbital actions in the azimuthal and declination directions for the $\lambda = 0.03$ halos, decomposed based on orbit type. The upper left figure is of the control halo, the upper right is of the dropped 2 kpc bulge of mass $1 \times 10^{10} M_\odot$, and the lower is of a bulge of the same size but grown over the period of 1 Gyr. Actions are taken of particles in the solar sample. Action units are in orbits over the equilibrium integration time.

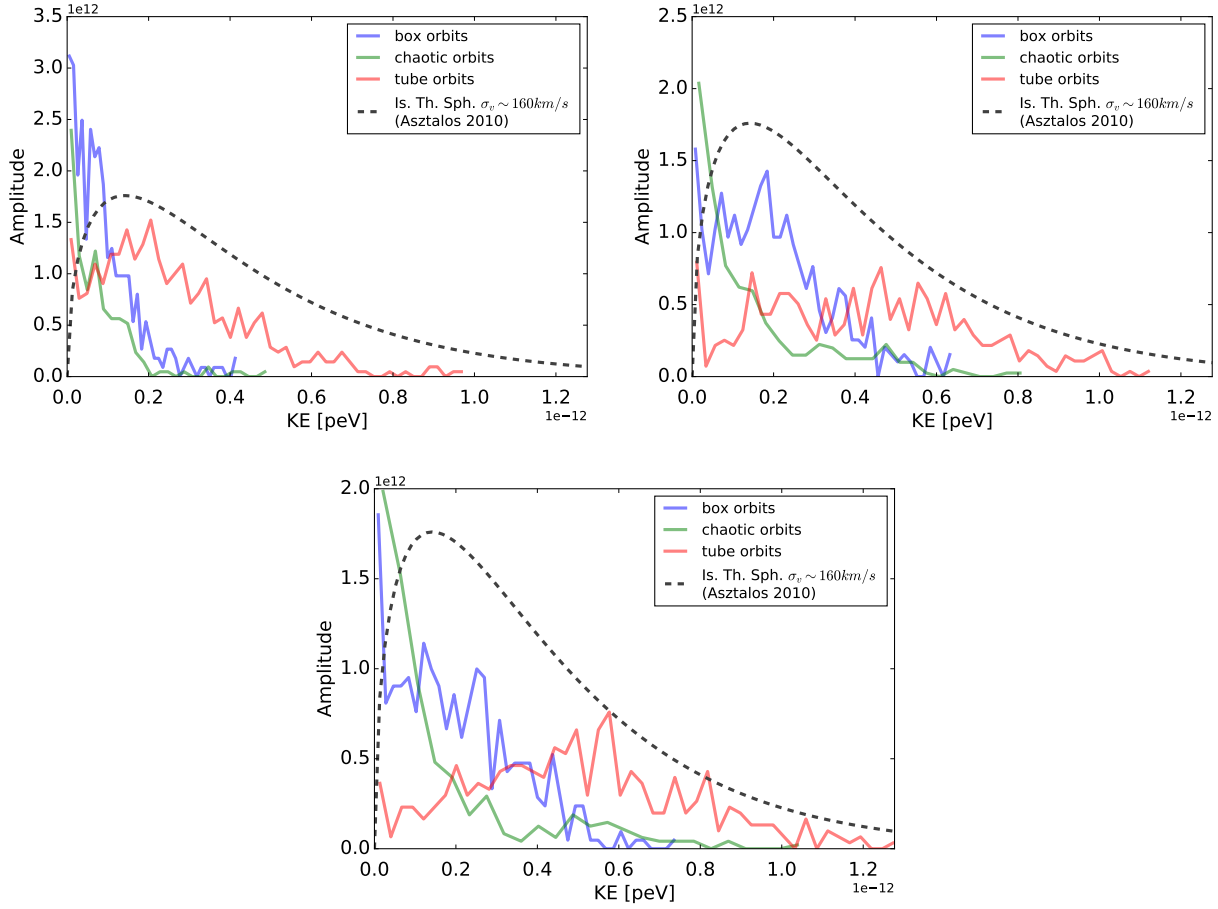

Figure 3.46: Energy spectra of $\lambda = 0.03$ halos, decomposed based on orbit type. The upper left figure is of the control halo, the upper right is of the dropped 2 kpc bulge of mass $2 \times 10^{10} M_{\odot}$, and the lower is of a bulge of the same size but grown over the period of 1 Gyr. Spectra are taken from the solar sample, in the galactic frame to best show differentiation.

Chapter 4
AXION SEARCHES

Searches for the axion over the past several decades are numerous, both as a product of axial symmetry breaking and as a DM candidate. The stress on WIMP DM parameter space is increasing the focus on axions, driving new developments in technologies and techniques. This chapter provides an overview of past, present, and some future means by which axions are searched. These searches span both direct and indirect detections, and both remote and terrestrial types. Special attention will be paid to the ADMX relic axion search, with a detailed analysis of their most recent data run deferred to Ch. 5.

4.1 Unique Particle, Unique Techniques

The axion's unique properties make it difficult to search for via standard WIMP approaches. For example, WIMP DM nuclear recoil has a the signal strength which scales like

$$\frac{dN}{dt} \propto \int_{v_{min}}^{\inf} \frac{f(v)}{v} dv \tag{4.1}$$

where $v_{min} = \sqrt{E_R m_T/(2\mu_{T\chi}^2)}$ and m_T is the target mass, $\mu_{T\chi}^2$ is the reduced target-DM mass, and E_R is the minimum nucleon recoil energy a detector can measure. The cutoff recoil energy currently lies in the keV range (Agnese et al., 2014; Akerib et al., 2017; Aprile et al., 2017), making DM axions far too light to register. Even for electronic recoil, the phonon strength function is similar in form to nuclear recoil, though the result would be highly model dependent (DFSZ only) and the cutoff would at best reach to meVs, far from the neV energies of the typical DM axion. In fact, axion interactions with any fundamental SM fermions are model dependent, but all of these theories are forced to interact with electromagnetism, leading many dedicated axion searches to utilize purely electromagnetic detection schemes.

4.2 Late-time Creation and Detection

Axions can be produced where the available energy exceeds the axion rest mass. Among astrophysical sources this happens most readily in regions of high energy density such as stellar cores, neutron stars (NS), supernovae (SN), and accreted matter on massive objects. Without the need to create significant relic axions, the low mass isocurvature and high mass warm DM constraints essentially disappear. With creation mechanisms suppressed, the mass constraints for axial symmetry breaking axions are reduced to those made by astrophysical and terrestrial sources.

4.2.1 Astrophysical Production

The sun is the most promising source of axions within our solar system. Multiple projects are centered around the detection of solar axions (Armengaud et al., 2014; CAST collaboration et al., 2017). Each operate under the principle that sufficiently light axions are created by both nuclear and electromagnetic channels within the sun's core, Fig. 4.1. These processes produce axions roughly isotropically in a spherical stellar core, with incident radiated power on a displaced detector

$$F_{\text{solar axions}} = \frac{\int_{\odot} \sum_i (\sigma_i f_i)\, d^6 w}{4\pi r^2} \tag{4.2}$$

where σ_i is the interaction cross-section, f_i is the distribution function of the reactants, and the integral is over the active solar region. The Primakov mechanism is expected to dominate stellar axion production, but searches for other mechanisms are also performed (CAST collaboration et al., 2017). To convert the stream of stellar axions into electromagnetic radiation, a strong transverse magnetic field is placed just upstream of batteries of electromagnetic signal detectors, which convert the miniscule power from Primakov converted axions

$$P_{signal} \sim g_{a\gamma\gamma}^2 A (BL)^2 F_{\text{solar axions}} \tag{4.3}$$

into an electric current, Fig. 4.2. Detectors operate under a wide band of energies simultaneously, allowing for broad observations of axion mass. While the electrical power of the axion

signal is small, the number of axions contributing to the signal is large over the coarse of an observation, allowing the detectors to fill out a spectra, Fig. 4.3.

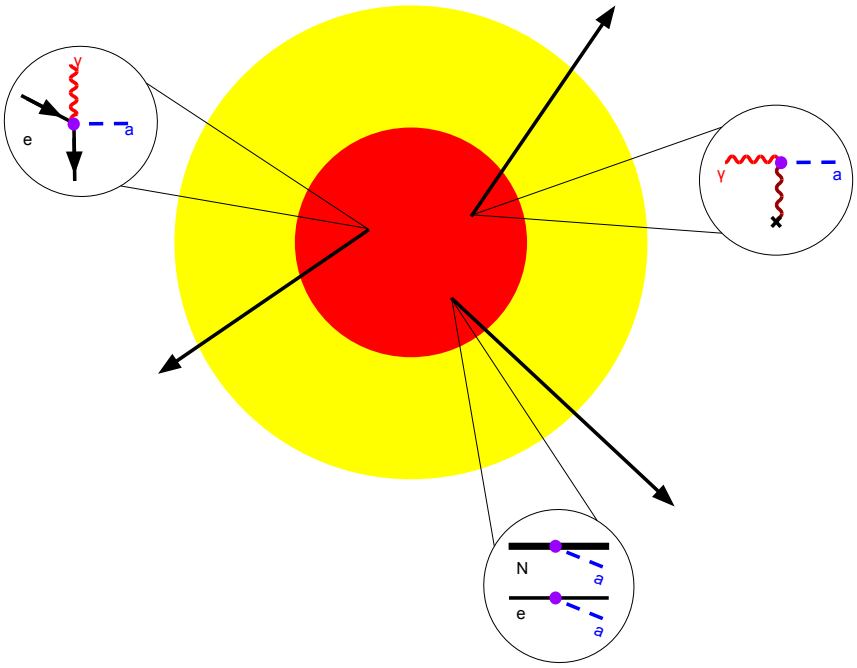

Figure 4.1: A selection of processes for axion-creation in stellar environments.

Understanding background events is key to the success of such experiments. Baseline event counting and modulation of the axion signal via magnetic field amplitude are all tools to improve the identification of stellar axions (Irastorza et al., 2011). Long timeline observation also improves signal identification, with coupling response

$$g_{a\gamma\gamma}^4 \propto t^{-1/2} \tag{4.4}$$

in the limit of well-understood backgrounds. Axion helioscopes have managed to place very broad bounds on the axion coupling, Fig. 4.4, though their depth is limited by the coupling-integration time relation.

Next we look outside the solar system. Main sequence stars are quite numerous within

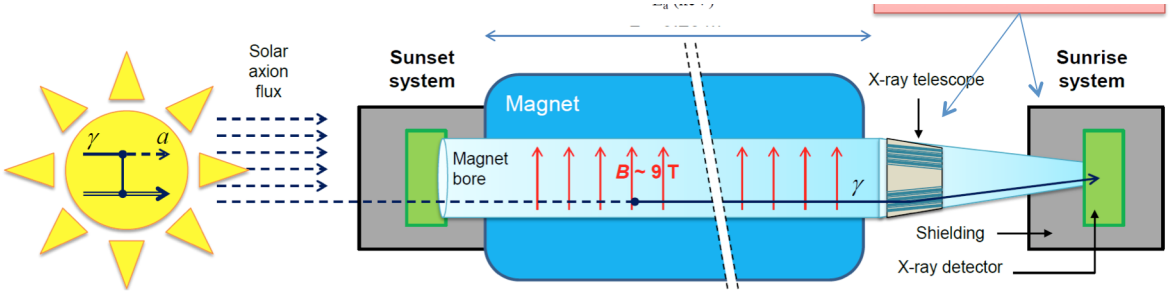

Figure 4.2: Illustration of example axion helioscope apparatus (Armengaud et al., 2014).

our galaxy, but their large displacement makes more remote helioscopes impractical. In the environments of more extreme stars, however, new processes for axion influence are available. Hotter, denser stars such as O and B types, white dwarfs (WDs), and NSs, have high degeneracy among the electronic or nuclear matter, which enhances the fermion-to-axion and axion-to-fermion channels in addition to Primakov channels. These enhancements allow for greater radiation out of the star and appreciable energy transport within the star (Raffelt & Dearborn, 1987; Raffelt, 1996, 1999), Figs. 4.5. Faster energy transport alters the thermodynamics and hydrodynamics of the star, and may change the evolutionary course of its host. The primary change to stellar evolution is suspected to be a shortening in the lifespan and increase in brightness compared to the null result.

Among these star types a change in the star's birthing rate is not expected, implying that a shortening in lifetime leads to a decrease in abundance (Raffelt, 1996). Direct observations of abundances show no significant depressions of high-energy stars relative to complementary populations, producing an exclusion limit, Fig. 4.6.

$$m_a \leq 10meV \tag{4.5}$$

Stepping up in energy, SN produce some of the strictest astrophysical bounds on symmetry-breaking axions. Operating through the same channels as stars, axions supplement neutrino transport in conducting and radiating energy from the collapsing core. Observations of no-

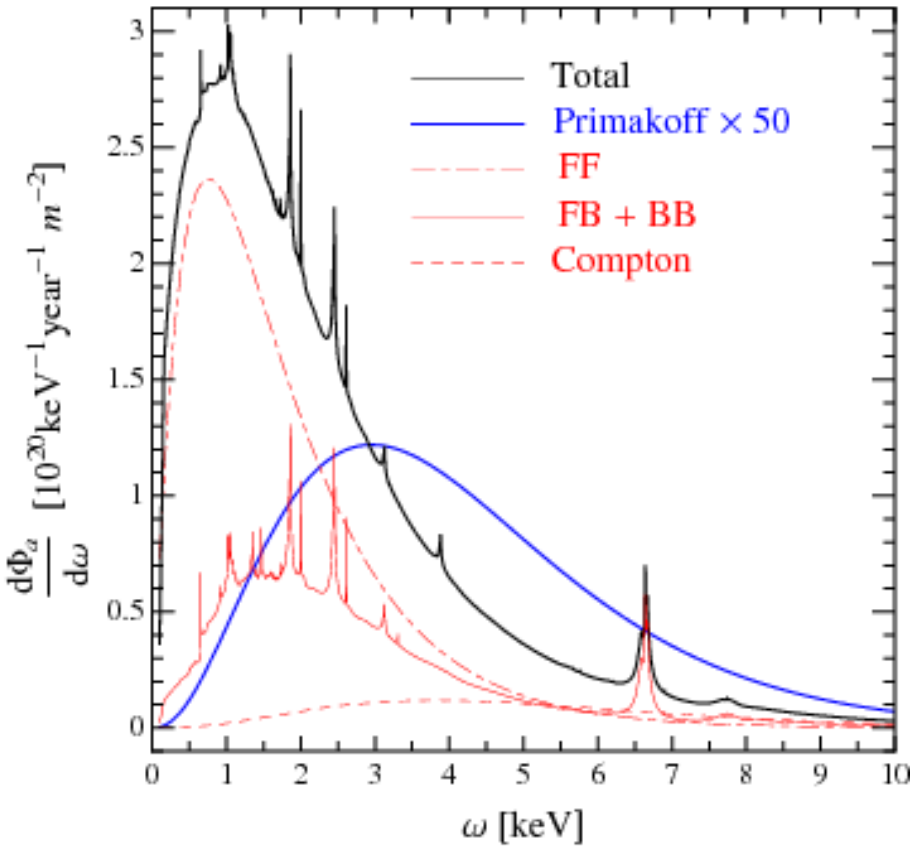

Figure 4.3: Potential energy spectra observed by axion helioscope (Redondo, 2013).

vae profiles, including neutrinos and light from recent SN1987A, show no deviations from the null axion hypothesis, producing limits in axion coupling, Fig. 4.7. It should be noted that the physics involved, even without axion contributions, is very complicated. As of the completion of this dissertation there are several aspects of SN and high-density stellar structure which are still poorly understood (Hillebrandt & Niemeyer, 2000; Sumiyoshi, 2013), and whose resolution may influence axion bounds.

Reaching the largest scales and high energy the cosmological symmetry-breaking axions can produce signatures in TeV (10^{12} eV) photons and primordial gravitational waves. Observations of the InterGalactic Media (IGM) show an enhancement of high energy photon

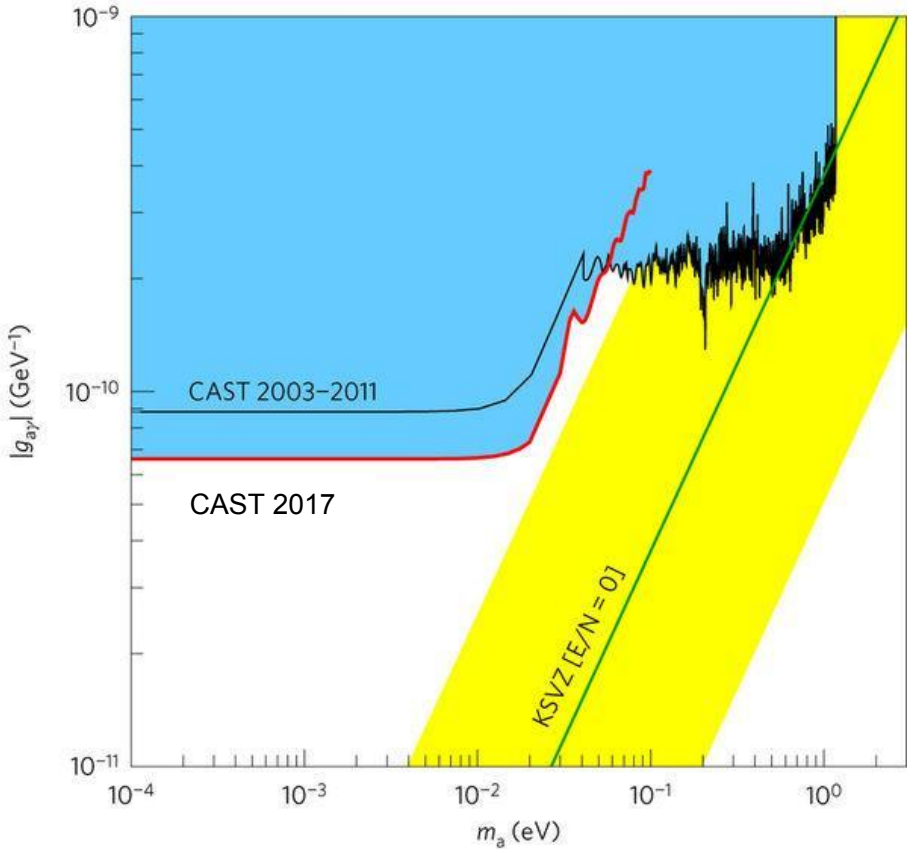

Figure 4.4: Axion parameter space with current helioscope limits (Armengaud et al., 2014).

abundance relative to expected opacities (Montanino et al., 2017). Opaqueness of cosmological media at these energies is still far from well understood, but a possible explanation is due to Primakov conversion in the presence of intergalactic magnetic fields, Fig. 4.8. Using common figures of magnetic field distribution and otherwise unimpeded cosmological photons, the observed abundances are reproduced for a wide range of axions, ruling out ALPs of $m_a \leq 10^{-8}$ and $g_{a\gamma\gamma} \geq 4 \times 10^{-12}$ GeV^{-1} (Montanino et al., 2017). Unfortunately this does little to isolate potential symmetry-breaking or DM theories of axions.

Primordial Gravitational Waves (PGWs) are an excellent probe of early cosmological physics. Currently the only available observations of such PGWs are the imprints of these

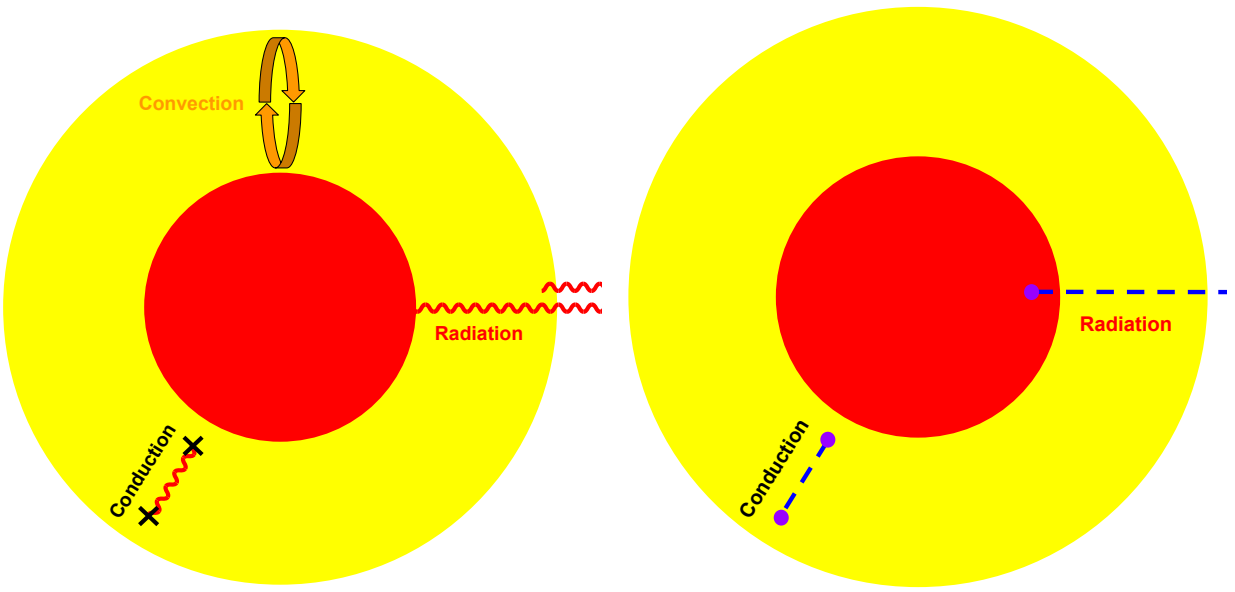

Figure 4.5: Illustrations of common processes of stellar energy transport (left) and axion-driven energy transport processes (right). See (Raffelt, 1999) for a review.

waves on the CMB and pulsar timing observations, which have placed some limits on ultra-light axion influence, Fig. 4.9. Future PGW observing projects like the Laser Interferometer Space Antenna (LISA) will have the ability to directly measure the strain produced by this early physics on space-time (Arvanitaki et al., 2015; Brito et al., 2017).

4.2.2 Terrestrial Searches

The coupling of axions to light in the presence of electric or magnetic fields lends it to a unique set of terrestrial searches. An excellent example are a class of tabletop experiments that operate on the theme of shining light through a wall (Redondo & Ringwald, 2011), Fig. 4.10. In Light-Through-Wall (LTW) experiments, a coherent laser serves as a source of axions when the beam passes through a transverse magnetic field, creating a coherent parallel beam of axions. The beams encounter a barrier many skin-depths thick to the laser,

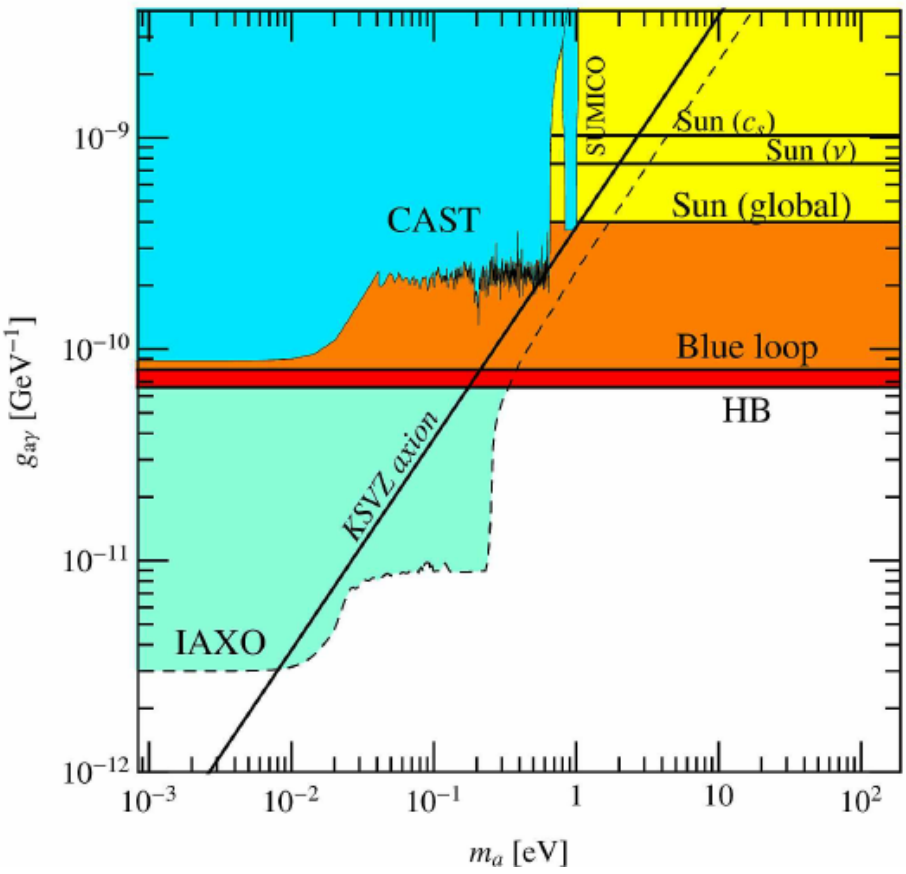

Figure 4.6: Limits on axion parameter space from low-energy stellar evolution (Vinyoles et al., 2015).

but do not impede the axions. Once through of the barrier the axions enter another magnetic field, allowing a portion of the beam to be converted back into a near-coherent light beam. There are multiple means by which the post-barrier light may be measured, its power and phase information encoding the coupling and mass of the produced axions

$$P_{signal} \propto g_{a\gamma\gamma}^4 B^4 L^4 \tag{4.6}$$

$$\delta\omega \propto m_a \left(\delta\omega_o^{1/2} L'\right)^2 \tag{4.7}$$

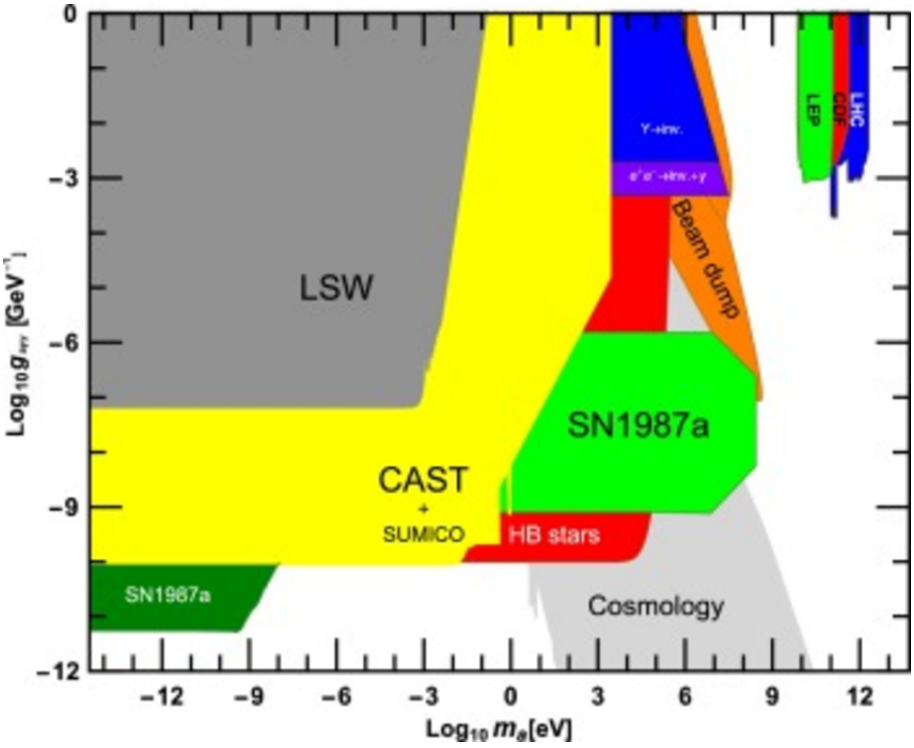

Figure 4.7: Limits on axion parameter space from SN (Jaeckel & Spannowsky, 2015).

where P_{signal} is the signal power, B is the magnitude of the transverse magnetic field, L is the length of the magnetic field region, $\delta\omega$ is the measured frequency dispersion, $\delta omega_o$ is the laser frequency dispersion, and L' is the inter-magnet distance. Such 'tabletop' experiments of light mixing in magnetic fields also extend to Earth orbit. Proposals to study potential axion rotations, using the Earth's magnetic field and GPS satellites as transceivers are being fielded, though they suffer from unconstrained magnetic fields and unpredictable barrier materials much like the cosmological observations. If such systematics are managed, low-earth-orbit experiments would test axions in the lower end of the DM range.

Material responses may also reveal properties of the axion. Many ALP theories create a time-dependent nEDM on the scale of the axion mass

$$\vec{d}(t) \propto \cos m_a t \hat{s}. \tag{4.8}$$

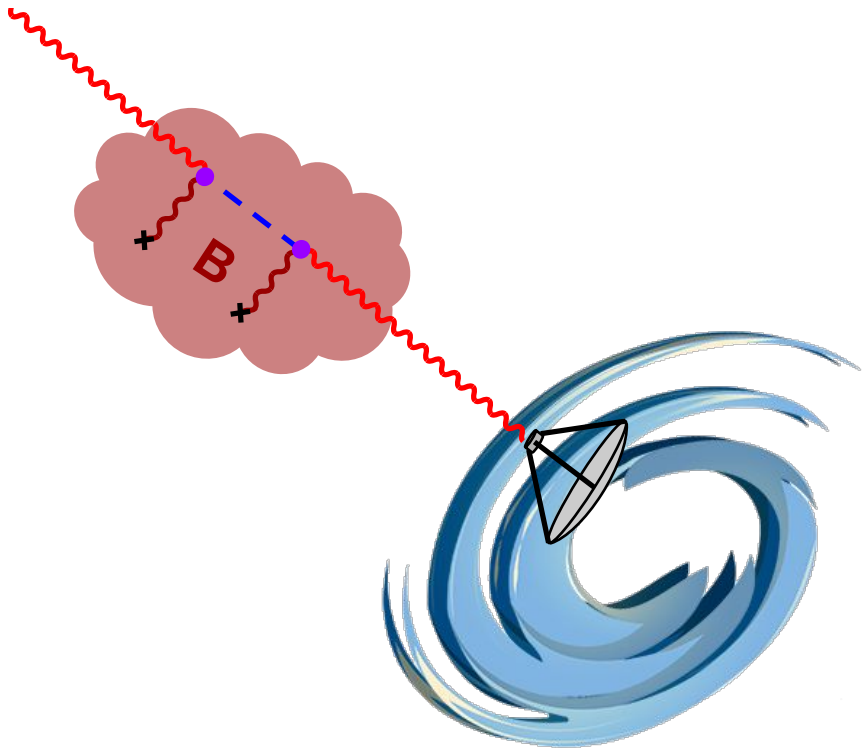

Figure 4.8: Illustration of TeV photon IGM transmission enhancement from axions (Montanino et al., 2017).

Such a driving nEDM has impacts on dynamical properties of nuclei, including an influence on their resonant properties. Multiple experiments of axionic effects on Nuclear Magnetic Resonance (NMR) are currently in development, both as measures of pure symmetry breaking and as DM tests (Budker et al., 2014; Garcon et al., 2017), and have produced limits on axion masses below the typical DM region, Fig. 4.11.

4.3 Relic Detection

Symmetry breaking detections of axions are inherently difficult as the axions must be both created and destroyed by rare processes. DM detection alleviates half of this burden as the axion is taken to already exist in abundance. This section reviews several ongoing and

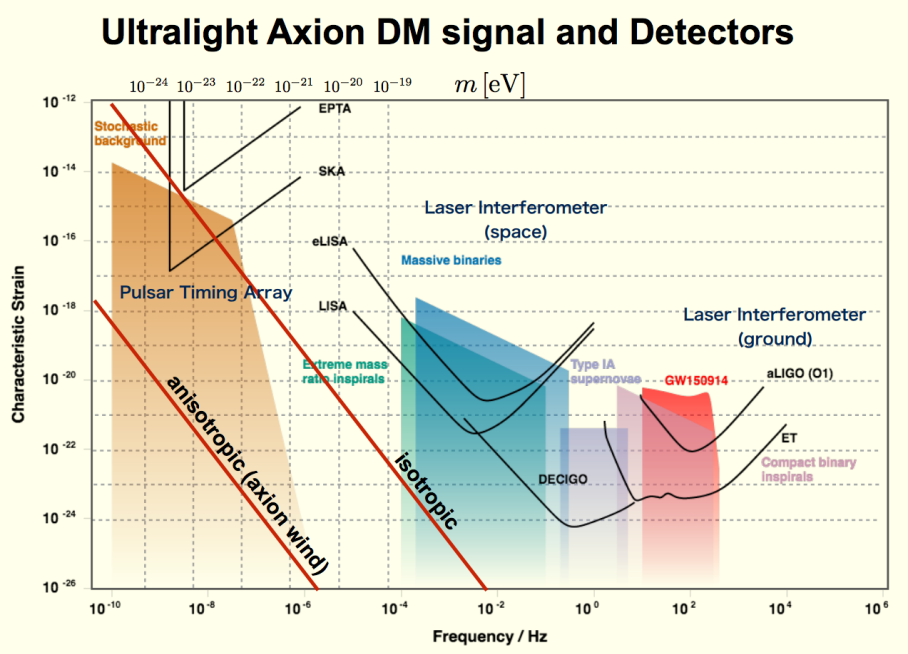

Figure 4.9: Expected axion limits from primordial GW experiments (Brito et al., 2017).

planned axions DM searches, with an emphasis on ADMX.

4.3.1 Astrophysical Searches

Looking to remote detection first, galactic observations can reveal conversions of DM axions in the presence of a magnetic field into microwaves. Condensed objects like pulsars have very strong magnetic fields, up to 10^{10} tesla (Morris et al., 2002), and are easy to locate, with huge conversion power

$$P_{signal} \propto \int_V f_a \left(g_{a\gamma\gamma} \vec{B} \cdot \hat{r} \right)^2 dV \tag{4.9}$$

where f_a is the axion flux. Their displacement adds a factor of $\frac{1}{4\pi r^2}$ to the incident flux on a detector, and large backgrounds in the wavelengths of interest diminish the significance of these singular emitters. For remote sources the incident power figure of merit is governed by

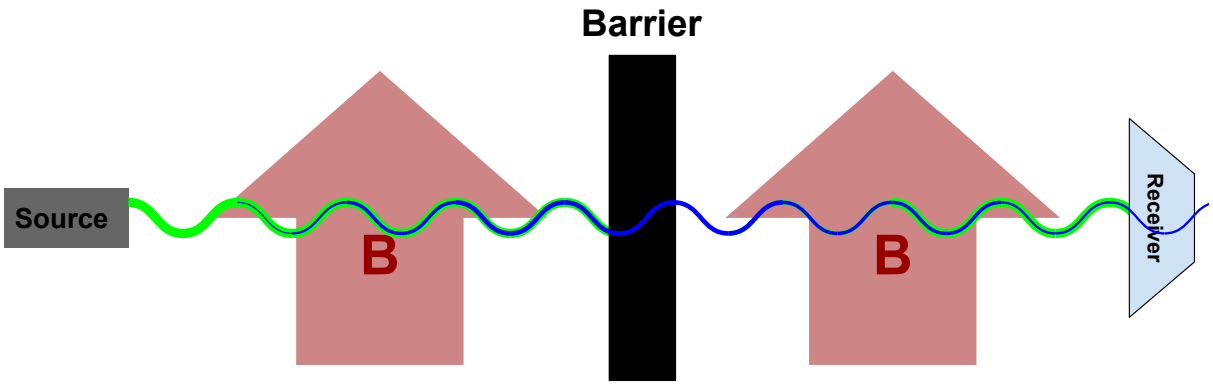

Figure 4.10: Illustration of light-through-wall apparatus.

the 'power kernel'

$$P_{inc} \propto K = \rho_D M V \frac{B^2 m_a^2 c^2}{\hbar^2 4\pi r^2} \tag{4.10}$$

which scales with distance as $\frac{L^3}{r^2}$, giving very high weight to extensive regions of magnetic field even if they are far off, Fig. 4.12. The non-relativistic motions of axions and magnetic fields in these regions imply that the signal spectral shape is still quite narrow, with $\Delta\nu/\nu_o \sim 10^{-6}$.

A number of Earth-based detectors are capable of reading such a signal, most notably radio telescopes, Fig. 4.13. Over the DM mass range of sub-μeV-meV (100s MHz - 100s GHz), modern radio telescopes commonly have bandwidths of GHz and resolution to the sub-Hz level (Kelley & Quinn, 2017), making individual arrays capable of scanning wide swaths of the DM axion mass range in great detail. A very effective approach if meaningful sensitivity can be reached in a reasonable time.

To determine the feasibility of this attractive project, let us calculate the time needed to reach DFSZ sensitivity. Primakov emissions over an astronomical object such as the MW core or other nearby galaxies are incoherent as the deBroglie wavelength of a DM axion is much smaller than the extent of the emitter, though any single axion decay is coherent over the whole telescope array. Intimate knowledge of magnetic fields in our own galaxy and

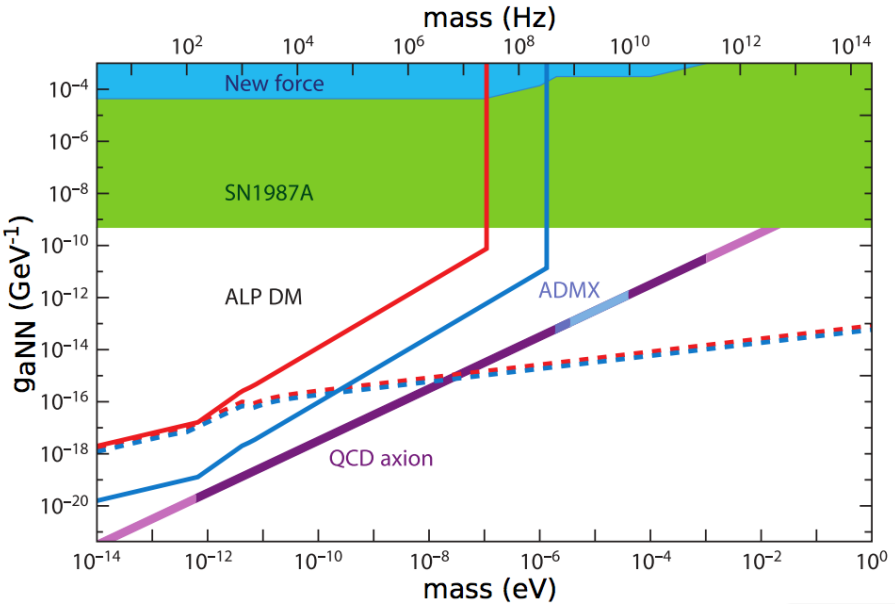

Figure 4.11: Expected axion limits from NMR searches, courtesy of (Garcon et al., 2017)

beyond is necessary to effectively model the signal from decayed axions.

The continuous stream of axion decay signals places the bulk of source error on the uncertainty in the magnetic field state. Full 3D magnetic field measurements of these structures are limited, and realistic models/simulations are still developing. Realistic models of magnetic fields and backgrounds are also needed to converge on an experiment's sensitivity, making current telescope searches highly speculative. To be conservative, a figure of micro-Gauss (10^{-10} tesla) is commonly used (Kelley & Quinn, 2017). For this example backgrounds are taken to be perfectly subtracted, which is difficult to do without sophisticated models.

For a well-calibrated telescope the error over a potential signal is dominated by thermal noise. The noise power emitted is governed by the Dickie radiometer equation parameterized by the physical temperature of the receiver

$$P_n = BkT + N(1) \times BkT/\sqrt{tB} \tag{4.11}$$

where k is the Boltzmann constant, B is the observation bandwidth, T is the temperature, t

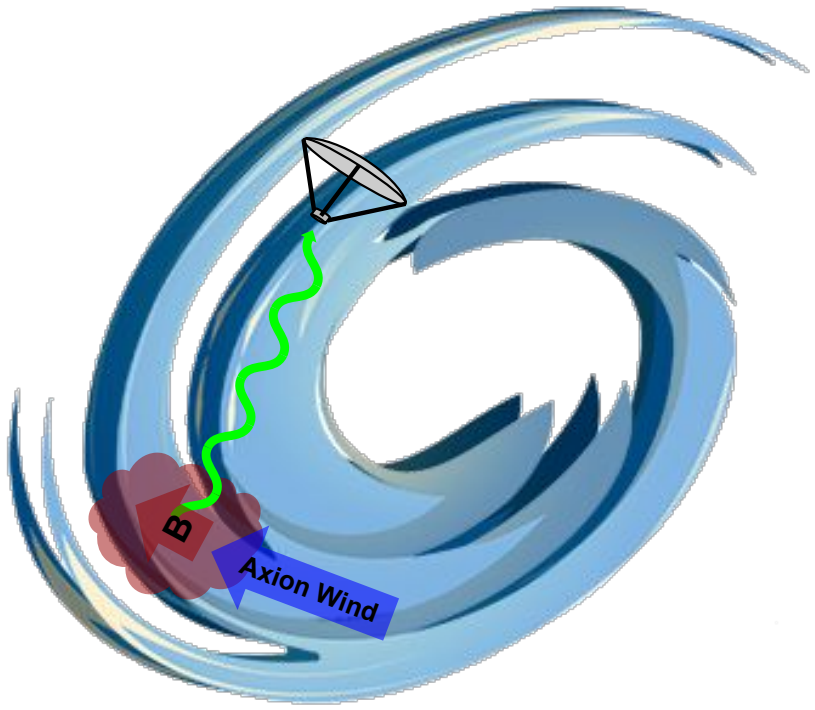

Figure 4.12: Illustration of remote axion Primakov conversion and detection in the MW disk. The magnetized intra-galactic cloud converts incident halo axions into microwaves in perpendicular directions to the cloud's field.

is the scan time, and N(1) is a normal random number with unit dispersion (Kelley & Quinn, 2017). Contributions are also made downstream by both passive and active electronics, and are largely taken to be thermal in profile, adding to the radiometer spectrum

$$P_{total} = \prod_i G_i \left(P_{i-1} + P_{i,n} \right) \tag{4.12}$$

where P_i is the total power at the i-th stage, assuming the elements to contribute by gain. Note that the early portion of the transmission line is most important to the noise, with the next element contributing as $1/G_1$. The noise power fluctuations are given by a Johnson

Figure 4.13: Artist rendering of a segment of the Square Kilometer Array (SKA), operating in 0.4-13.8 GHz, a potential instrument for remote axion DM search (Huynh & Lazio, 2013).

spectra

$$P_{j,n} = N(1) \times BkT_j/\sqrt{tB} \tag{4.13}$$

and are the primary source of uncertainty in our example. An effective system temperature may be given at the point of signal power injection by inverting the receiver's gain

$$T_{sys} = T_0 + T_1 + \sum_{i=2} T_i \prod_{j<i} \frac{1}{G_j} \tag{4.14}$$

Now we may compare the modeled signal power to an effective noise level at the same point. As we shall see in Chapter 5, the Signal to Noise Ratio (SNR) is a central figure to estimating sensitivity. In crude terms, SNR is purely the ratio of cumulative signal power to cumulative noise power

$$SNR = \frac{P_s}{P_n} = \frac{P_s}{\sigma_n}\sqrt{Bt} \tag{4.15}$$

where σ_n is the fundamental power dispersion of the scan. Fortunately the noise power can be degraded with increased integration time due to the uncorrelated nature of Johnson spectra, which means such experiments can improve their sensitivity just by observing longer. The

normal nature of thermal noise also allows for the direct mapping of the ratio to confidence level in units of standard deviation.

Based on the calculations of (Kelley & Quinn, 2017), for a single telescope of collecting area 10 m^2, 12 K system temperature, centuries are needed to reach DFSZ when observing the galactic center with 90% confidence over the axion DM range. Such a search is untenable. Fortunately SNR scales like collecting surface if collected coherently. The Square Kilometer Array (SKA) is the largest planned terrestrial astronomical observation project for these wavelengths, and is hoped to be complete by 2030 (Kelley & Quinn, 2017), boasting a collection area of 1 $km^2 = 10^6$ m^2.Such a boost in surface area cuts down the DFSZ integration time to months! Wide-band projected limits are shown in Fig. 4.14. If these figures hold, projects like the SKA bring such searches from speculative to an experiment worth serious consideration, though the issues of backgrounds and proper modeling of galactic scale magnetic fields have the potential to severely impact its efficacy.

4.4 Terrestrial Searches

Laboratory DM detectors are able to avoid many of the systematic errors inherent in astrophysical observations. By converting DM axions into a visible signal near the point of detection, impacts to the sensitivity of the search are restricted to the material properties of the detector, which lend themselves to detailed scrutiny more easily than galactic structures.

Several DM searches use axial current interactions as their primary source. Coherent decays of DM axions into the creation of electric dipole moments of nucleons and other fermions are capable of being seen in NMR, convolved with the DM spectra. Detectors made from systems of cold inert gas, crystals, and neutron sources are in the works to observe this this induced dipole (Budker et al., 2014; Garcon et al., 2017).

A more macroscopic tactic is to utilize the axion halo to induce microwave signals at dielectric transitions, Fig. 4.15. MADMAX aims exploit this feature by amplifying the signal induced by halo axions decaying in an external magnetic field to readable levels via the use of a dielectric train, Fig. 4.16, and aims to search for axions of masses 40-400 μeV

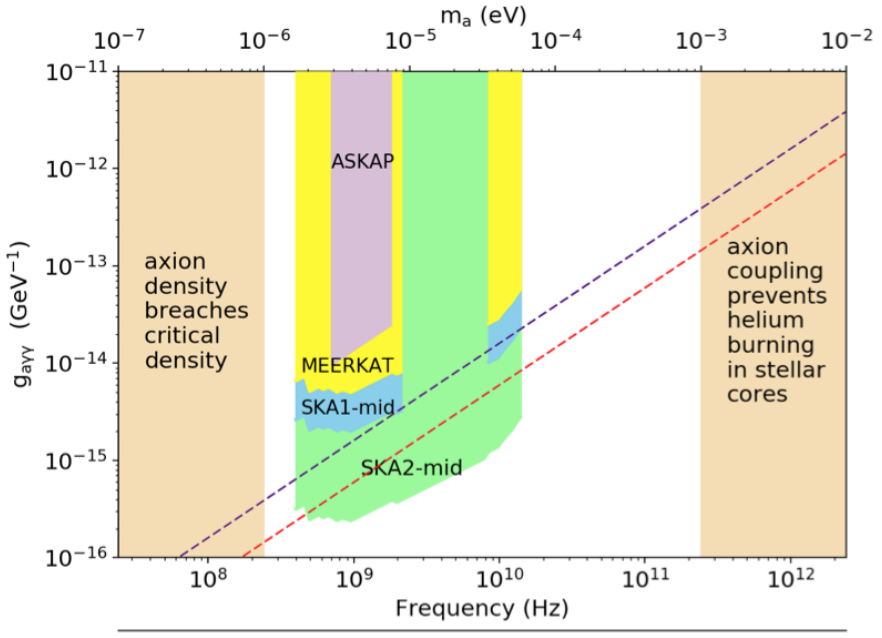

Figure 4.14: Projected axion DM sensitivity from radio telescope searches after 24 hours of observation per bin (Kelley & Quinn, 2017).

at sensitivities approaching DFSZ, Fig. 4.17.

Stimulated axion decay through use of a resonant cavity is the last technique covered in this chapter, and is arguably the closest to detecting an axion. Resonant cavity searches utilize the universality of the Primakov interaction, the clarity of a point-like sample of the MW halo, the stability of man-made high-capacity magnets, and the plethora of sensitive microwave technology, bringing together many of the best features from the other axion searches presented above.

The basic layout of the resonant decay detector uses a high-quality microwave cavity threaded by a strong magnetic field, creating the potential for Primakov conversion, Fig. 4.18. Axion conversion is coherent over the cavity as the axion deBroglie wavelength is much larger

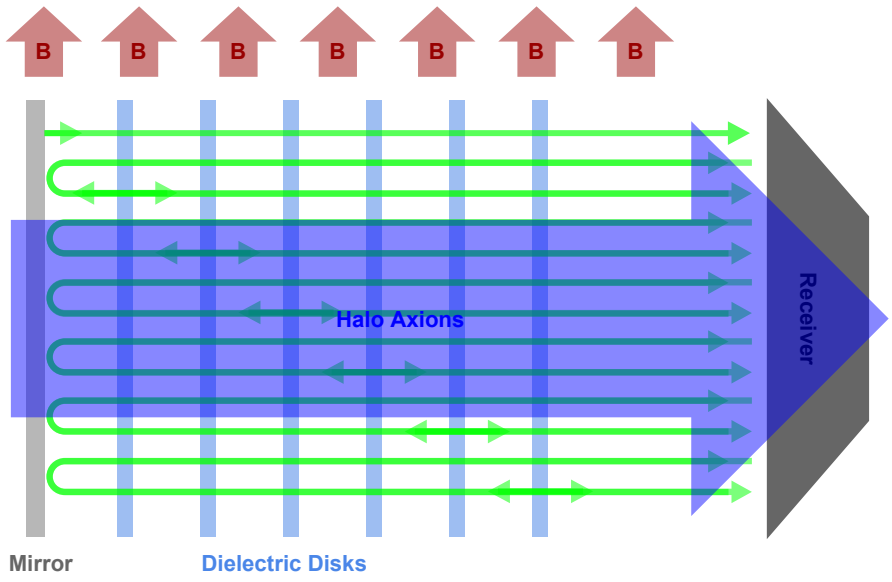

Figure 4.15: Illustration of dielectric-induced axion conversion to microwaves (Majorovits & Javier Redondo for the MADMAX Working Group, 2016).

than the size of the cavity, allowing resonances to form according to the cavity's properties. Many of the cavities used by these experiments are enclosed by highly conductive materials such as copper or superconducting materials, and contain an infinite tower of resonant modes (Lyapustin, 2015; Boutan, 2015). For a review of cavity dynamics, see (Jackson & Zia, 1977).

Let us consider the cavity dynamics to observe how resonant modes may improve the detectability of halo axions. The presence of a magnetic field allows axions to induce electric fields via the Primakov interaction

$$\mathscr{L}_{g_{a\gamma\gamma}} = -\frac{g_{a\gamma\gamma}a}{8\pi}F_{\mu\nu}\tilde{F}^{\mu\nu} = -\frac{a}{4\pi}\vec{E}\cdot\vec{B} \tag{4.16}$$

where F and $\tilde{F}$ are the electromagnetic field strength and its dual respectively, a is the axion field. $g_{a\gamma\gamma}$ is the coupling strength, calculated from fermion loops and their PW couplings,

$$g_{a\gamma\gamma} = \frac{\alpha g_\gamma}{\pi f_a/N} \tag{4.17}$$

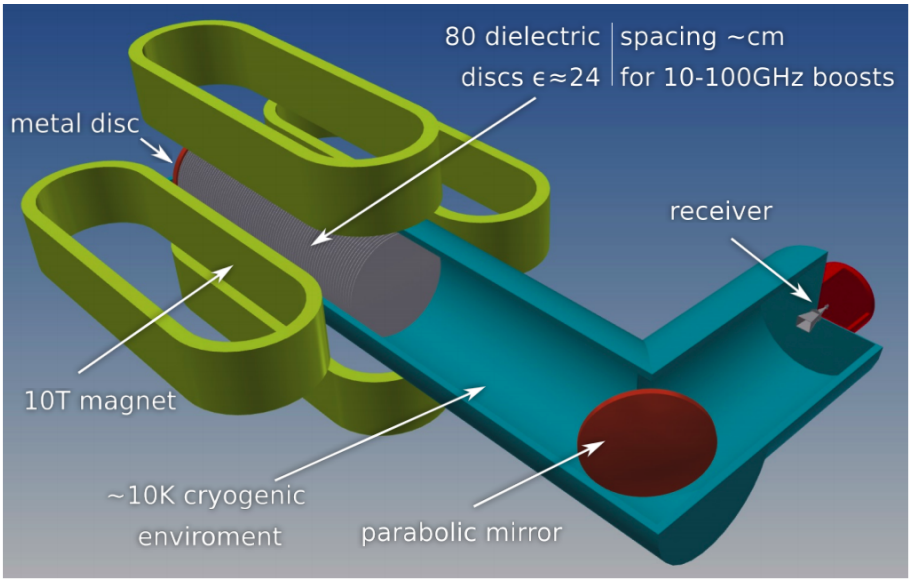

Figure 4.16: Proposed MADMAX apparatus, shown at Patras 2017. See (Majorovits & Javier Redondo for the MADMAX Working Group, 2016) for a review.

where α is the fine structure constant, f_a is the symmetry-breaking scale, N is the number of quark flavors, and g_γ is a model-dependent constant of value -0.97 and 0.36 for KSVZ and DFSZ respectively. The magnetic and axion configurations on the scale of the cavity are composed of many quanta, so we subsume them here with their average fields, reducing the Lagrangian to its classical form. In MKS units the Primakov lagrangian contribution to the cavity volume is

$$L_{g_{a\gamma\gamma}} = \epsilon_0 \int_V dV \frac{a}{16\pi^2} \vec{E} \cdot \vec{B} \tag{4.18}$$

where ϵ_0 is the electric permittivity of the vacuum. This coupling implies that only the field configurations with non-trivial

$$f = \frac{\left(\int_V dV \vec{E} \cdot \vec{B}\right)^2}{\int_v dV |\vec{E}|^2 \int_V dV |\vec{B}|^2} \tag{4.19}$$

are driven by axion decays, where $|\vec{E}|_{max}$ and $|\vec{B}|_{max}$ are the maximum magnitudes of the

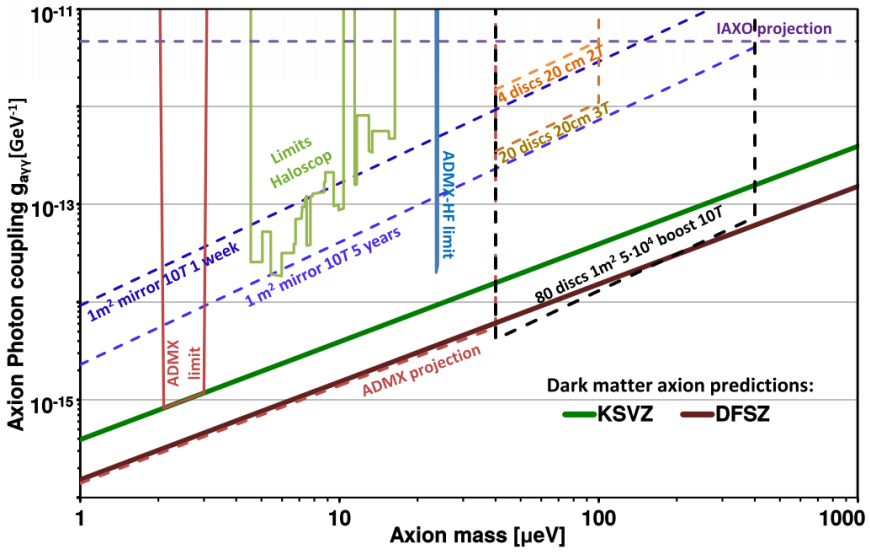

Figure 4.17: Projected sensitivity of MADMAX to DM axions (Majorovits & Javier Redondo for the MADMAX Working Group, 2016).

electric and magnetic fields respectively. We call f the form factor.

The lagrangian contributions from the cavity are

$$L_{cavity} = L_L + L_C \tag{4.20}$$

where L_L is the inductance energy, which has response $\propto |\dot{\vec{E}}|^2$, and L_C is the stored energy in the cavity

$$L_C = \frac{\epsilon_0}{2} \int_V dV \left(E^2 + c^2 B^2\right) \tag{4.21}$$

The total Lagrangian for the cavity-axion system is the sum $L_{cavity} + L_{g_{a\gamma\gamma}}$.

There are a few further simplifying assumptions we make before solving for the dynamics. Axion decay power to non-resonant configurations is quickly dissipated on the cavity walls, so we shall concentrate only on configurations close to resonant modes. For this example we use a right-cylindrical cavity and vertical homogeneous magnetic field $\vec{B} = B\hat{z}$. The form

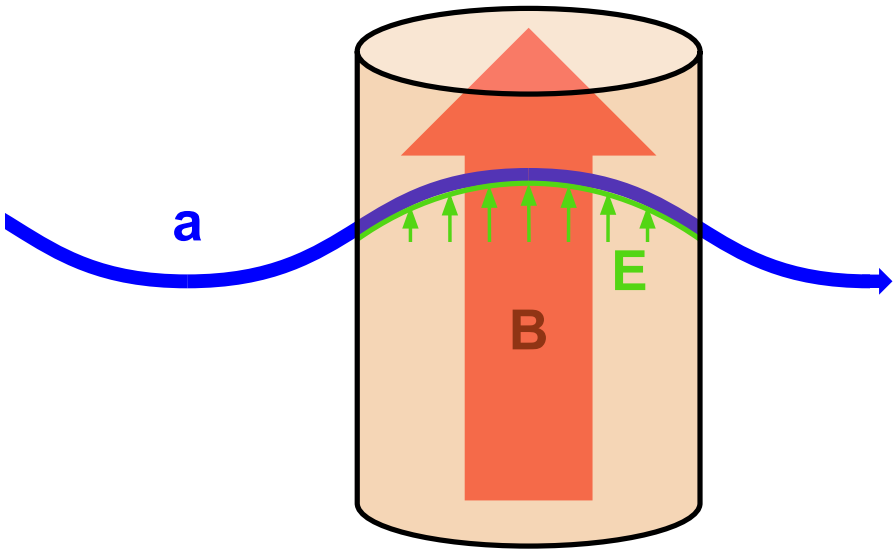

Figure 4.18: Illustration of cavity-facilitated Primakov conversion of DM axions.

factor formula is simplified

$$f = \frac{\left(\int_V dV \vec{E} \cdot \hat{z}\right)^2}{\int_v dV |\vec{E}|^2 V} \tag{4.22}$$

reducing the modes with non-0 form factor to be of Transverse Magnetic (TM) type. We also assume that non-static magnetic contributions to the lagrangian are minimal, true for TM modes in the expected power range, and are ignored. The only remaining degrees of freedom are in the mode's electric field $\vec{E}$.

The resulting mode dynamics obey the Euler-Lagrange equation

$$\frac{d}{dt}\left(\frac{\partial L}{\partial \dot{q}}\right) - \frac{\partial L}{\partial q} + \frac{\partial F}{\partial \dot{q}} = 0 \tag{4.23}$$

where q is a degree of freedom of the Lagrangian, and F is an introduced dissipative term representing energy losses to the cavity walls and antennae. We parameterize the time dependence of the mode relative to the stationary dimensionless waveform normalized to unity

$$\vec{E}_{\omega_0}(\vec{x}, t) = q(t)\vec{W}_{\omega_0, norm}(\vec{x}) \tag{4.24}$$

The Euler-Lagrange equation then gives

$$L\ddot{q} + R\dot{q} + q/C = F(t) \tag{4.25}$$

where we have consolidated the coefficients into an effective inductance L for the kinetic term, resistance R for the energy loss, and capacitance C for the stored energy. The driving term $F(t)$ is from axion decay and is time dependent as the axion field oscillates according to its energy. We may also write F in terms of the form factor and C

$$F(t) = -g_{a\gamma\gamma}a(t)cB\sqrt{\frac{fV\epsilon_0}{C}} \tag{4.26}$$

Solutions to such equations generally have both a transient and steady state contributions. We consider only the steady state solution due to the anticipated long observation time. For a monotonic axion field $F(t) = F_0\cos(\omega_a t)$ and waveform parameter takes the form

$$q(t) = q_f\cos(\omega_a t - \varphi) \tag{4.27}$$

where q_f is the amplitude and φ is the phase lag. These quantities can be calculated by inserting $q(t)$ into the equation of motion. The unique values are

$$q_f = \frac{F_0/L}{\sqrt{\left(\omega_0^2 - \omega_a^2\right)^2 + R^2\omega_a^2/L^2}} \tag{4.28}$$

$$\varphi = \arctan\left(\frac{R\omega_a}{1/C - L\omega_a^2}\right) \tag{4.29}$$

where $\omega_0 = 1/\sqrt{LC}$. From here it is easy to see an amplification of q_f about the resonance ($\omega_a \approx omega_0$). Amplifications of high degree are allowed as halo axions are an inexhaustible compared to deposited power, expected to be in the yocto-watt range. The square amplification's full width at half maximum may be parameterized by a dimensionless quality factor

$$Q = \frac{1}{\omega_0 RC} \tag{4.30}$$

The power deposited in the cavity is found to be

$$\begin{aligned} P(t) = F(t)\dot{q}(t) &= -F_0 x_f\omega_a\cos(\omega_a t)\sin(\omega_a t - \varphi) \\ &= -F_0 x_f\omega_a\left(\cos(\omega_a t)\sin(\omega_a t)\cos(\varphi) - \cos^2(\omega_a t)\sin(\varphi)\right) \end{aligned} \tag{4.31}$$

Averaging over an oscillation cycle gives the long-term power absorption

$$\langle P\rangle = \frac{F_0 x_f \omega_a}{2}\sin(\varphi) = \frac{F_0^2\omega_a^2 R}{2L^2\left(\left(\omega_0^2-\omega_a^2\right)^2 + R^2\omega_a^2/L^2\right)} \tag{4.32}$$

Writing the average power in terms of the resonance frequency, resonance width, and parameters of the axion-cavity interaction, the average power simplifies to

$$\begin{aligned}\langle P\rangle &= \frac{F_0 x_f \omega_a}{2}\sin(\varphi) = g_{a\gamma\gamma}^2|a_{\omega_a}|^2 c^2 B^2 f V\epsilon_0 \frac{\omega_a^2 R}{2CL^2\left(\left(\omega_0^2-\omega_a^2\right)^2 + \omega_0^2\omega_a^2/Q^2\right)} \\ &= \frac{F_0 x_f \omega_a}{2}\sin(\varphi) = g_{a\gamma\gamma}^2|a_{\omega_a}|^2 c^2 B^2 f V\epsilon_0 \frac{\omega_a^2\omega_0^3/Q}{2\left(\left(\omega_0^2-\omega_a^2\right)^2 + \omega_0^2\omega_a^2/Q^2\right)}\end{aligned} \tag{4.33}$$

Near the resonance the response profile may be simplified further

$$\langle P\rangle \approx g_{a\gamma\gamma}^2 c^2 B^2 f V\epsilon_0\omega_0 Q|a_{\omega_a}|^2/2 \frac{\frac{\omega_0^2}{4Q^2}}{\left(\left(\omega_0-\omega_a\right)^2 + \omega_0^2/(4Q^2)\right)} \tag{4.34}$$

$$= g_{a\gamma\gamma}^2 c^2 B^2 f V\epsilon_0\omega_0 Q|a_{\omega_a}|^2/2\Gamma_{\omega_0}(\omega_a) \tag{4.35}$$

where Γ_{ω_0} is the Lorentzian profile about the ω_0 resonance, normalized to have unit maximum value. The coupling and axion field terms may be re-expressed using the halo density

$$g_{a\gamma\gamma}^2|a_{\omega_a}|^2/2 = \frac{g_{a\gamma\gamma}^2\rho_a}{m_a^2} \tag{4.36}$$

Using the model-dependent coupling form of Eqn. 4.17 and figures from (Daw, 1998), we may calculate the deposited axion power in terms of physical parameters reasonable for a cavity receiver

$$\langle P\rangle \approx 2.09\times10^{-22}\text{Watts}\left(\frac{V}{220\text{liters}}\right)\left(\frac{B}{7.6\text{tesla}}\right)^2\left(\frac{g_\gamma}{0.36}\right)^2\left(\frac{\rho_a}{0.45\text{GeV/cc}}\right)\left(\frac{\omega_0}{750\text{MHz}}\right)\left(\frac{Q}{70000}\right) f\Gamma_{\omega_0} \tag{4.37}$$

assuming the axion spectra is restricted to a single frequency. Generalization to more distributed axion spectra is straightforward.

Estimating sensitivity is again done using SNR. Power is extracted from the cavity mode of interest by a critically-coupled antenna, pulling half of the deposited power from Eqn. 4.37.

A receiver chain then amplifies the signal and digitizes it to memory. Noise power comes from the cavity, antenna, and induced by the receiver chain by Eqn. 4.12, resulting in a Johnson spectra with effective system temperature of Eqn. 4.14. We assume no interference from other radio sources. An integration time of $t \approx 160$ seconds is required for an experiment of our reasonable parameters to reach DFSZ with an $SNR = 3$, bandwidth $B = 1kHz$, and system temperature of $T_{sys} = 1K$.

A single scan is only effective over one Q-width, or about 10 kHz for our example apparatus. The viable axion DM mass range is much wider. Tuning mechanisms to alter the cavity's mode structure in a continuous manner are inserted into the cavity, allowing modes to cover many hundreds of MHz. The ideal tuning rate of a cavity averages to

$$\frac{d\omega_0}{dt} = 4.14 \times 10^2 \mathrm{Hz}^2 \left(\frac{T_{sys}}{1K}\right)^{-2} \left(\frac{V}{220\mathrm{liters}}\right)^2 \left(\frac{B}{7.6\mathrm{tesla}}\right)^4 \left(\frac{g_\gamma}{0.36}\right)^4 \left(\frac{\rho_a}{0.45\mathrm{GeV/cc}}\right)^2 \times \left(\frac{\omega_0}{750\mathrm{MHz}}\right)^2 \left(\frac{Q}{70000}\right) \left(\frac{Q_a}{10^6}\right) \frac{f \times D}{SNR^2} \tag{4.38}$$

where D is the duty factor of a scan cycle, Q_a is the axion signal quality factor, and we assumed the effective coverage of a single scan is half the mode bandwidth. Such a figure implies that our example cavity is capable of covering a 100 MHz bandwidth on the order of a month!

Several collaborations are currently implementing the resonant cavity haloscope technique to search for relic axions. At the high mass range are the ORGAN and high-frequency CAPP groups whose operations currently lie on the $50 - 200\mu$eV range (McAllister et al., 2017; Petrakou, 2017). Below that are the HAYSTAC and low-frequency CAPP groups in the $20 - 100\mu$eV range (Brubaker et al., 2017; Petrakou, 2017). At the low end of the mass spectrum are ABRACADABRA and ADMX, working the sub-μeV to 50μeV. ADMX is the only search to have reached benchmark sensitivity in the viable DM range. We concentrate on the apparatus and analysis of ADMX in the next chapter.

4.5 Design of ADMX: Main Experiment

We concentrate on the most developed ADMX apparatus. In this section we cover the basic elements of the main experiment design and functionality, focusing on elements most pertinent to axion detection. Only figures and equipment relevant ADMX's latest data taking period, Run 1A, are discussed.

The main experiment infrastructure is divided into a cold space and a warm space, though this convention is somewhat specious as there are cold elements in the warm space. The cold space is distinguished by the region inside the primary magnet cylinder, Fig. 4.19. The outer steel housings act as shields against heat and Radio Frequency Interference (RFI) leakage. Under the first four shields are the main magnet and its liquid helium reservoir. The main magnet produces a solenoid field, capable of reaching central field strengths of 8.5 tesla. The high field is The magnet is composed of composite superconducting materials with critical temperature $\sim$ 10K, accommodating the high field while at liquid helium temperatures. A dedicated cryogenic system regulates the helium bath, maintaining the magnet's superconducting state. When in use, the total stored energy of the magnet runs into the megajoules, requiring numerous electrical and thermodynamic safety features in the case the magnet temperature rises above the critical point. The magnet is built with an uncharacteristically wide bore ideal for housing a high volume resonator.

Inside the magnet bore housing is the detector insert, containing the cavity, cold electronics, and sub-Kelvin cryogenics. Inside the heat/RFI shields protecting the coldest elements from the 4.2K magnet is the resonant cavity. The cavity casing is a steel right-cylindrical drum plated on both sides with highly conductive copper and put in knife-edge contact with two endplates, also composed of copper-plated steel. The inner surfaces of the cavity are polished to produce an uncoupled $Q \approx 10^5$. The cavity is placed at the center of the solenoid field and oriented concentrically with the bore. Inside the cavity are two identical right-cylindrical tuning rods, oriented with cylindrical axes parallel to the cylinder's. Also with copper exterior, each rod is suspended by top and bottom dielectric arms, which both

run horizontally to vertical axles in the cavity plates allowing for rotational motion. Mode tuning occurs by the different geometric configurations of the cavity. Three antennae are also attached to the cavity endplates, one weakly coupled port on the lower endplate, and two tunable antennas on the top plate and out of reach of the armatures. Fig. 4.20 shows the geometric features of the cavity, which have been optimized for minimal mode crowding and crossing and maximal tuning range and form factor. The effective volume of the cavity is 129 liters (Asztalos et al., 2010).

The cavity contains a series of modes that couple to axions. Recall that nontrivial power conversion from axions requires a non-zero form factor

$$f = \frac{\left(\int_V \vec{E} \cdot \vec{B} dV\right)^2}{\int_V |\vec{E}|^2 dV \int_V |\vec{B}|^2 dV} \tag{4.39}$$

We use the full form of the form factor as the due to small deviations in homogeneity and verticality of the main magnet's field. The decaying axion's electric field excites those modes, which have field with net alignment with the magnet's field. As the B field in the cavity is near-homogeneous and vertical w/r/t the cylindrical axis, the modes most coupled to will be of transverse-magnetic (TM) type. The specific TM modes chosen for observation are labeled TM_{010} and TM_{020c}, drawing analogy from the bare (rod-less) cylindrical cavity mode structure (Daw, 1998; Lyapustin, 2015; Boutan, 2015). The analysis section of this work will concern data taken on the TM_{010} mode over 645-680 MHz, gathered over five months during January-June 2017.

The antennae built into both the top and bottom end-caps serve multiple purposes. The single antenna shown on the bottom end-cap in Fig. 4.20 is intentionally weakly coupled to the cavity, meaning very little power may exit the cavity through that line. This weak port is for broad and narrow band signal injection to build mode maps and mode structures during data taking. The weak port also allows for injection of synthetic axions for the purpose of sensitivity calibration and axion detection testing. Synthetic Axion Generation (SAG) via the weak port is a robust test of sensitivity as the synthetic signal takes the same path from the cavity through the receiver chain as a microwave from an axion decay, allowing

for a near-direct comparison of the receiver electronics. The other straight-line antennae are located on the top plate and are for coupling to the resonant modes, placed perpendicular to the plane of the plate to maximize exposure to TM mode electric fields. These antennae are tunable via mechanical insertion/extraction by stepper motor. This allows the antennae to adjust between weak and strong coupling as needed. During data taking operations the antenna in use establishes critical coupling with the cavity, meaning that the cavity and RF impedances match. Such a configuration allows half of the resonant power to be transmitted while the remainder is dissipated on the cavity walls.

The tuning of the rods and antennae are run through an array of independent stepper motors located in room temperature at the top of the insert. Insulating G10 rods attached to the motors run from the top of the insert to the 1K plate immediately above the cavity. At the 1K plate the G10 rotational motion is geared down by factors of 20,000:1 and 141:1 for the rods and antennae respectively before being transfered to the rod armatures and linear drives. Tuning precisions are to the sub-mm level for the antennae and the 10^{-3} degree level for the rods.

Power from the cavity is transmitted through the critically-coupled antenna and out of the cold space through a highly-calibrated transmission and amplification chain. We concentrate on the only receiver chain used in Run 1A, for the TM_{010} channel. Recall from earlier in this chapter that it is the earliest stage of amplification that contributes most to the system noise power. The first amplifier in the the amplification chain is a Multi-strip SQUID Amplifier (MSA), limited in noise by the quantum uncertainty principle of the microwave state, or half the physical temperature as was the case for Run 1A. MSAs are also very sensitive to magnetic fields, creating tension as logistically they can only lie about a meter from an 8 tesla magnet. To mitigate the magnetic field in the vicinity of the amplifiers a bucking coil is placed around the cold electronics package to counteract the main magnet's field within the coil bore. The signal is amplified several more times both cryogenically by High Electron Mobility Transistors (HEMTs) and at room temperature by more classical amplifiers, but the noise introduced is minor, typically adding up to only 10% of the total system noise.

Cooling the cavity and early-stage amplification is crucial. ADMX employs a sophisticated cryogenic system to keep the temperature-dominating components at sub-Kelvin levels. Standard liquid helium pumping is insufficient and other more sophisticated cooling techniques such as laser pumping are poorly suited for such large masses, so to reach the required low temperatures ADMX utilizes a high-powered Dilution reFrigerator (DF), Fig. 4.22. Operating on the principle that a pair of isotopes of bosonic and fermionic types must exist either both as superfluids or in a normal state, useful cooling power may be rendered through osmotic pressure mixing. He_3 and He_4 respectively are used as the fermionic and bosonic isotopes in the ADMX DF. Surrounding the DF is an extensive cryogenics staging and recycling system.

The warm space includes all equipment outside the magnet shield. The majority of cryogenics and gas handling infrastructure is in the warm space. Gas equipment includes He_3 and He_4 storage in gas and liquid phases as well as pumps, compressors, and liquefiers to recycle the helium isotopes after their cooling run through the DF. To monitor and control both the warm and cold components of this complex system is a Data AcQuisition (DAQ) infrastructure, Fig. 4.23. Custom built and programmed for ADMX operations, the DAQ oversees the main experiment, cryogenics, magnets, and a litany of sensors to monitor magnetic field strength, pressures, cryogen levels and temperature at every stage of the apparatus. The end result is a cavity and quantum-limited amplifier system which is cooled to the 150 mK level for Run 1A, implying a potential DFSZ scanning rate of ~ 2 MHz/day. In the next chapter we put to use ADMX operations and scan data from Run 1A to perform an in-depth axion search, featuring new limits on a well-motivated, fully articulated axion lineshape.

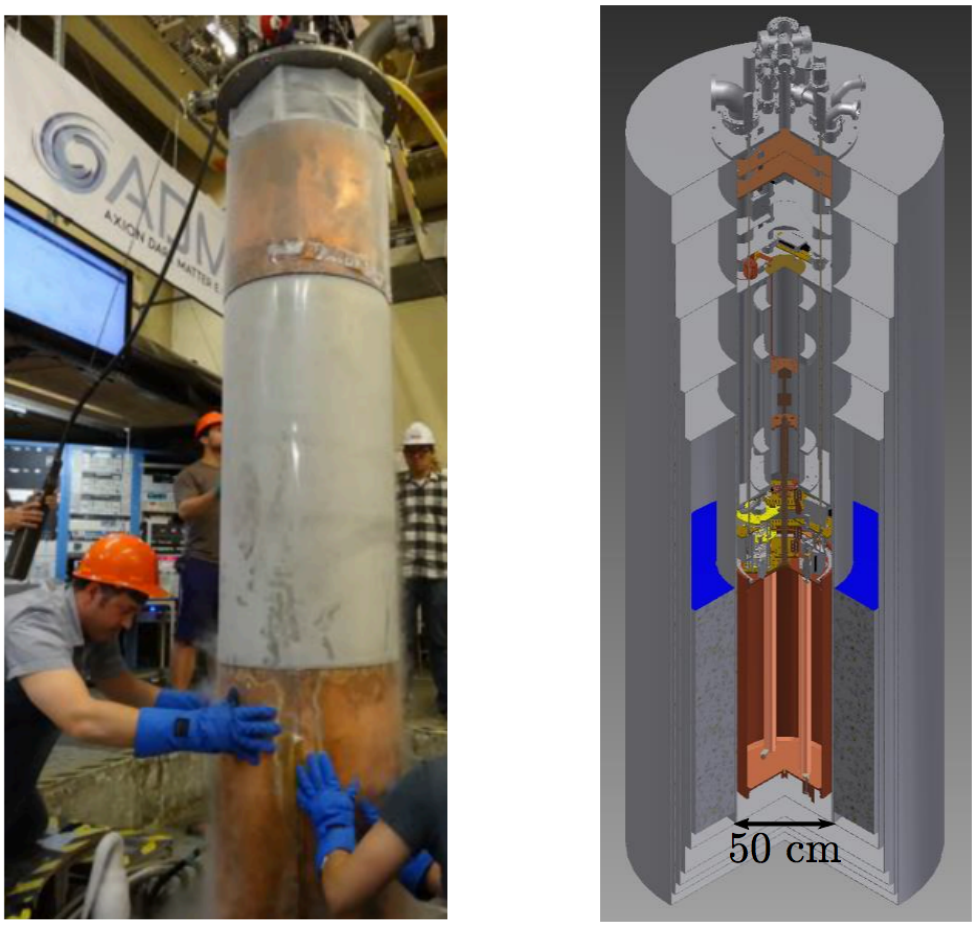

Figure 4.19: The ADMX cold-space. Left figure is photo taken during extraction at the end of Run 1A (author background center). Right is a cutaway view of the cold-space, with the insert portion occupying the space down from the fixture-filled con-flat.

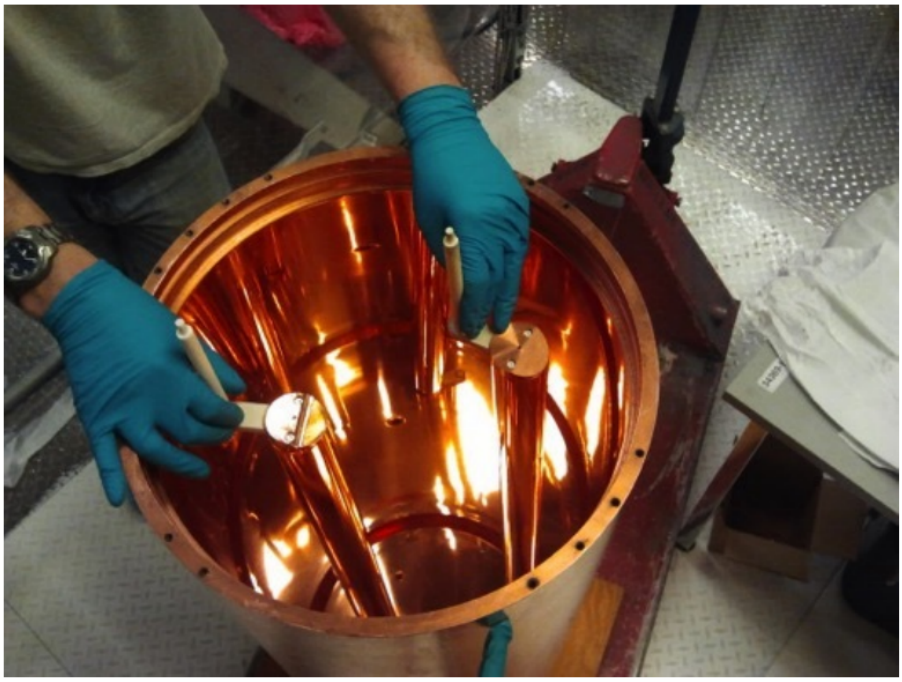

Figure 4.20: View of the open ADMX cavity with armatures.

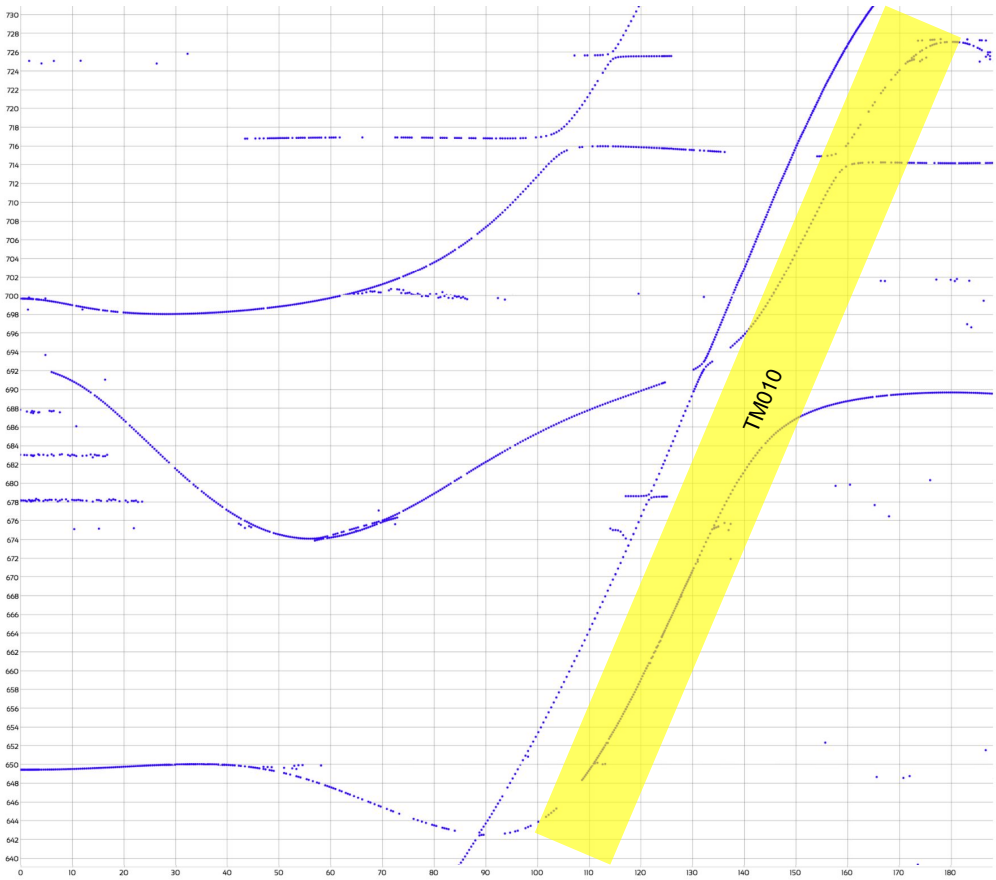

Figure 4.21: A truncated physical tuning map of the ADMX cavity, taken by rotating one rod through a half cycle and leaving the second stationary nearest the cavity wall. TM_{010} is highlighted.

Figure 4.22: Picture of the ADMX DF mixing chambers after installation into the insert. Also in frame are the tuning mechanisms for an antenna (right) and cavity tuning rod (left).

Figure 4.23: Compilation pictures of the ADMX main receiver and DAQ.

Chapter 5

ANALYSIS OF ADMX RUN 1A

We now search for our well-vetted halo line-shape in ADMX data. In this chapter we concentrate on ADMX's newest data run, Run 1A, which took place from January 18 to June 11, 2017 and spans axion masses 2.65μeV (645MHz) to 2.81μeV (680MHz). The chapter is organized as follows: Sections 5.1 5.2 discuss the goals of Run 1A and its reality, which include a review of the live axion search used to characterize candidates during data taking; Section 5.3 reviews of the data structures types pertinent to our offline axion search; Sections 5.4 5.5 5.6 5.7 present optimized schemes for conditioning scan data, analyzing individual scans, and combining single analysis results into a cumulative spectrum; Section 5.8 discusses the cuts made to Run 1A data; Section 5.9 presents the final results of the off-line analysis. The results of this chapter are preliminary.

5.1 Goals of Axion Search Analysis for Run 1A

ADMX operators set a number of derived science goals to focus Run 1A data-taking operations and achieve the project goal of being the first and preeminent DFSZ-sensitivity axion DM experiment.

- Cover the hardware limited scan range (645-715 MHz) to DFSZ sensitivity.
- Operate at a scan rate commensurate with the completion of the projected plan of scanning 6 GHz over four years. This comes to an average of ~ 2 MHz/day.
- Identify and address potential axion candidates.

A number of axion search analysis goals are derived from the science goals. The cold electronics operators require feedback on the operating sensitivity during data-taking in order to calibrate cryogenics, amplifiers, and set the cavity tuning rate. Further, a live rendering of axion candidates in the operating bandwidth allows for faster turn-around on potential candidates than delaying candidate procedures to the end of the run. A more in-depth analysis, complete with realistic line-shape, is desired for final word on sensitivity and candidates. A number of analysis goals are made from these needs.

- Construct and operate a 'live analysis' infrastructure capable of handling day-to-day operations of data taking and candidate analysis.

- Construct and operate a post data-taking axion search which incorporates realistic line-shape and operates at sufficient resolution to exploit the detail of those shapes.

- Make axion search noise-limited, meaning that statistical errors dominate over systematic errors in determining the experiment's sensitivity.

5.2 Data Taking Overview

To fulfill the Run 1A goals data taking is organized into a number of cadences, with the shortest cadences being the most robust to changing objectives. The shortest is the scan cadence on the timescale of $\sim$ 150 seconds. During a scan the DAQ sequentially transmits a spectrum of white noise through the weak port and receiver lines and sweeps the result. From this transmission the target mode locations and properties are found. Next is a white-nose reflection and scan of the receiver to measure coupling strength to the target mode. A third passive scan of the receiver records mode transmissions over 100 seconds. This integration is the axion scan. The last step of the cadence tunes the cavity into position for the next scan iteration. Every hour a wide transmission scan is taken for mode mapping and a minor calibration of the cold amplifiers is taken to maximize SNR. Major calibrations of the amplifiers are performed as needed, usually every few days.

Longer timescale cadences are more sensitive to the dynamic objectives of a working experiment. The run plan of Run 1A is largely dictated by hardware constraints, including the tuning and mixing properties of the target TM_{0n0} modes, the MSA tuning range, and other electronic operating properties. Deference is given to the highest form factor TM_{010} mode. Tuning restrictions on TM_{010} come from the quantum-limited MSA (645-745 MHz) and receiver circulators (600-715 MHz). A run plan is constructed from these parameters, Fig. 5.1, which aims to scan the entire 645-715 MHz TM_{010} range sans a mode crossing at 685 MHz. This run plan also sets to observe the TM_{020} mode over its corresponding range of 1300-1400 MHz.

Several hardware failures reshaped the reality of Run 1A. A catastrophic failure in the cold electronics vacuum feedthrough resulted in the disconnection of the TM_{020} channel. Limitations in MSA tuning reduced the effective amplification range of the TM_{010} channel to 645-680 MHz. Further, a main cavity tuning rod experienced a mechanical failure at cryogenic temperatures, while the second showed an increase in mechanical noise to the level of a TM_{010} Q width. Magnet and cryogenic systems held steady during data taking operations, with a central field of ~ 6.8 Tesla core temperature of $\lesssim 150$ mK respectively. In effect, the main experiment has only one channel to observe axions, with half of its designed mobility. In light of these malfunctions the duration of Run 1A is uncertain.

To improve our chances of achieving our science goals of reaching DFSZ sensitivity and addressing candidates the tuning cadence must be updated. Several tuning passes are required to thoroughly search a frequency band for an axion signal. A safe solution is to divide up the region into many segments, scanning one at a time to completion, at the loss of scan speed due to delays on tuning turn-arounds. An optimized solution is to divide the 35 MHz tuning range into segments 10 MHz in size, scanned in serial. Operations proceed as follows within a segment:

1. A baseline scan pass is taken across the segment at a rate estimated sufficient for DFSZ sensitivity

2. A selective pass is taken to level the SNR over the segment

3. Candidates for axion signals are identified and rescanned

    - Rescans and analyses are taken in accordance with candidate protocol outlined in Section 5.2.1.

Once the last of the candidates are addressed, that segment is closed and the next is initiated. This cadence is repeated until the run is complete.

Fortunately, the reduced tuning range falls within an opportune band of high TM_{010} form factor, Fig. 5.2. Revising the segments becomes a simple matter. We choose to start segment 1 at the high form-factor point of 650 MHz and run upwards until MSA tunability or mode crossings make data taking unfeasible, then resume a final segment in the lowest tuning range of the MSA. The residual tuning noise in the working rod also required a revision of the segment run plan, including a second baseline pass of the segment to smooth the tuning noise and SNR coverage.

5.2.1 Baseline Scan Operations

Given the axion scan rate of Eqn. 4.38, we calculate a scan rate of 1 MHz/day at DFSZ sensitivity for our operating conditions of $Q \sim 40,000$, $B = 6.8$ Tesla, $T_{sys} = 0.5$ K, form factor averaging at $f = 0.45$, duty factor of ~ 0.7, and axion bandwidth of 1 kHz. Broken up over 150 second scan cycles, a tuning rate of 0.002 kHz/scan is chosen for the baseline passes, well within the width of a typical TM_{010} resonance.

A Low Resolution (LR) sensitivity analysis and axion search is run in near real-time during main operations, enabling dynamic adjustment of cavity tuning and RF chain calibration to meet science and engineering goals. This 'live analysis' supplies operations with estimates of segment sensitivity and candidate identification. Live analysis is used in a consistent configuration throughout Run 1A with 5 kHz resolution and a 700 Hz top-hat axion line-shape. Output is sensitive to fluctuations in the system temperature during baseline

operations like $g_{a\gamma\gamma} \propto T_{sys}^{1/2}$. Such fluctuations occur regularly in Run 1A due to the unexpected temperament of the MSA, and often dominate variations in the baseline sensitivity, Fig. 5.3. Once a segment's baseline scans are complete, a leveling pass initiates. Using the live analysis rendering of a segment's potential SNR, regions of poor sensitivity are rescanned at a rate appropriate to improve their sensitivity to the DFSZ level. Once an acceptable leveling occurs the segment passes to candidate operations.

5.2.2 Candidate Operations

The live analysis also provides a measure of significance for power excesses, which serves as a basic estimator for axion candidacy, Fig. 5.4. Protocol for candidate operations are set prior to Run 1A and are held throughout.

1. Candidate Scan
    a Identify candidates using live analysis and prescribed candidate criterion
    b Perform an accelerated pass of the segment, slowing over candidates to allow for equivalent sensitivity
    c Analyze candidate data under same parameters as baseline
2. Persistent Candidates
    a Identify any candidates which persist through 1
    b Perform an accelerated pass of the segment, rescanning persistent candidates with period consistent with prescribed level of enhanced statistical significance.
    c Analyze rescan data under enhanced parameters
3. Continued Candidates
    a Identify any candidates which persist through 1 and 2

   b Perform search for RFI using means independent for the main experiment

   c Investigate structure of candidate for comparison against detected RFI and potential axion line-shapes

   d Analyze and present findings to Detection Committee (DC)

4. Magnet Ramp

   a Identify remaining candidates which pass DC scrutiny

   b Perform magnet ramps while scanning candidates to track magnetic response

   c Analyze for $P \propto B^2$ response

5. Deconstruction of Unknown Systematics

   (If this stage is triggered, an intense round of analysis of the apparatus and its environment are preformed to rule out any false positives. The details of this stage are yet to be specified.)

Candidates are identified using a cutoff above the one-sided 3σ (99.8%) level, and scanned to equivalent sensitivity to the baseline and leveling scans. Candidate rescans are scrutinized with scan times of size $5^2/3^2$ times that of the first candidate scan. A proportionate cutoff of 5σ is used to determine persistence. During the course of data taking, candidates were detected slightly above the expected normal statistics rate.RFI and anomalous correlated structures unable to be subtracted by the live analysis 6-order polynomial background-subtraction scheme dominate the a-statistical candidate deviations, Figs. 5.5 5.6. No persistent candidates survived step 3 of the candidate procedure. The 90% Confidence Limits (CL) calculated by the live analysis tell us that sensitivity lies almost unanimously below DFSZ.

5.2.3 Run 1A Summary

Over nearly six months of Run 1A operations, ADMX successfully scanned 35 MHz (0.15 μeV) of viable axion DM parameter space to DFSZ sensitivity, becoming the first axion

search to definitively test axions as a DM candidate. The value of this achievement cannot be understated, but practically speaking there is significant progress to be made. To summarize let us review the Run 1A science goals. (*Cover the hardware-limited scan range (645-715 MHz) to DFSZ sensitivity.*) The actual range set by hardware constraints limiting the scan range to 645-680 MHz. Run 1A did scan the entire viable range, even if it was not as large as anticipated. (*Operate at a fractional scale range commensurate with the completion of the projected scan plan of reaching 6 GHz over four years. This comes to an average of* $\sim$ 2 *MHz/day.*) The observed average scan rate came out to be 0.2 MHz/day, an order of magnitude below the target. Several factors let to anticipated delays, which are being addressed for the next data run. (*Identify and address potential axion candidates.*) Candidate identification and examination proceeded smoothly. A large portion of the candidate protocol was exercised and successfully classified every significant excursion.

It should also be noted that artificial axion signals were injected into the cavity to test detection sensitivity. At this point in the ADMX project the synthetic axion signals are analyzed separately and do not contribute to the candidate lists. Multiple publications are in progress examining the details of this run and analyzing its data (ADMX Collaboration, 2017a,b).

5.3 Data Types Overview

Many different data types are logged by the ADMX DAQ to record both a potential axion transmission and the general state of the experiment. Together these measurements pinpoint the RF signal and noise temperature, cavity and RF state, magnetic field, cryogenic conditions, and the time at which these observations are made. The data pertinent for signal analysis is initially organized into two categories for this section: digitizer scans and experiment status conditions. We review these data types in preparation for the technical presentation of the analysis to follow.

5.3.1 Experiment Status Data

A number of measurements are recorded by the DAQ to monitor the state of the insert, magnet and supporting cryogenics. Here we concentrate primarily on the data types that are relevant to the axion search.

The main magnet's state is captured by several monitors of the magnet's power supply as well as several Hall probes which directly measure $B_{||}$ in areas of high magnetic field as well as low-field/high-sensitivity areas like the cold electronics housing (squidadel). The power supply monitors record the input voltage and current of the main magnet with a periodicity of a few minutes. From the manufacturer, the peak magnetic field scales with input current like

$$B_{peak} = \frac{8.5T}{250A} I \tag{5.1}$$

for an empty magnet bore, though we expect minimal impacts to the magnetic field from the insert media or the bucking coil in the vicinity of the cavity. Hall probes set throughout the insert directly record the magnetic field component parallel to the probe wire with a period closer to an hour. Using the combined data, the magnetic field throughout the cavity may be modeled and is utilized in the calculation of the form factor used later in this analysis.

Numerous temperature sensors line the different stages and devices of the insert and shielding, recording measurements with periodicity up to ten minutes. From monitoring the magnetic casing temperature, the main cavity, the 1K pots, to the DF mixing chamber of the dilution refrigerator, most every stage is redundantly checked. For the axion search, there are many opportunities to directly or near directly measure the state of the cavity and early stage receiver lines. Calibrations for temperature ranges and magnetic field are crucial for the most sensitive and exposed sensors.

As part of the data-taking cadence, several active cavity measurements are taken once every scan cycle, or about every 2.5 minutes. These measurements include transmission sweeps (S_{12}) from the main cavity weak port through a receiver channel, of both narrow bandwidth high resolution and wide bandwidth low resolution types, and a narrow reflection

through the receiver antenna (S_{11}). The injected sweep signals are far more powerful than a potential axion signal or impinging RFI making them easier to see, while still conforming to the receiver operating parameters optimized for the 100 second passive scans. From these power traces various resonance qualities are measured, such as the local mode map, the Lorentzian response function of the tracked resonance, and the reciprocal Lorentzian spectra in the reflection.

For each measurement the DAQ ascribes it a time stamp at the time of logging. Under optimal operating conditions the various machines involved would have clocks synced to the microsecond level. Synchronous operation was not available during the run, resulting in a best estimate of order 1 second cooperation between clocks. While less important for sensors logged on minute timescales, single second asynchronicity becomes important when tracking the digitized high-frequency axion scans. Experiment status data is packaged during data taking alongside the digitized spectra. The latest active cavity, temperature, and main magnet measurements are collected during each iteration of the data taking cadence, labeled with the scan number and stored in an independent section of the DAQ database. The utility of these quantities are demonstrated in Section 5.5.

5.3.2 Digitizing Scans and RF Mixing

During most of each data-taking cycle, the cavity listens for the axion. The power out of the cavity during this passive phase is dominated by thermal contributions. On its way through the receiver chain the signal is amplified and mixed before being digitized into several data formats. Here we give a brief overview of the mixing and digitizing procedure to provide clarity on the resulting spectra used in axion searches. The power propagating out of the cold RF and into the digitizer chain goes through several (non-linear) operations before being stored to disk, Fig. 5.8, a necessary process as we require efficient high-resolution images of a relatively narrow band. The process generally parallels that of (Asztalos et al., 2010).

The first stage in the digitizer chain uses the resonance's measured frequency and a local oscillator to mix the signals down from hundreds of MHz to the vicinity of 10.7 MHz via super-

posing a stable signal of frequency $f_r + 10.7$. We may see the effect of this transformation using trigonometric identities on the voltages

$$\begin{aligned} g_{LO}(f_r - 10.7)V(f_r + \delta) &\propto \cos{(f_r - 10.7)t} + \phi\cos{(f_r + \delta)t} \\ &= \cos{(10.7 + \delta)t} + \cos{(2f_r - 10.7 - \delta)t} \end{aligned} \tag{5.2}$$

where δ is the difference between the central frequency f_r and the observed frequency. The first term on the RHS is mixed down and the second is mixed up. To remove the mixed-up signal, a bandpass filter of 30 kHz width is implemented about 10.7 MHz. Now the analogue signal exists purely in the vicinity of 10.7 MHz and is capable of being sampled quickly enough to resolve structures well below the expected axion width.

The first round of digitization occurs at a sampling rate of $400MHz$, meaning signals about 10.7 MHz are sampled nearly 40 times per cycle. Such a fast sampling rate does come at a cost, and each of these samples are evaluated only to a precision of ten bits. To optimize the resolution/precision function of our potential analyses, digitized samples are placed in bins 8-wide and averaged, improving the precision by $\sqrt{8} \sim 3$ times. The resulting re-binned sample has an effective rate of 25 MHz, well above the 2×10.7 MHz Nyquist frequency.

These rebinned time series are split into $\approx$ 10 ms chunks and temporarily stored to a circular RAM bank where they wait to be offloaded for the next stage of conditioning. Lag in the throughput of the next conditioning stage can fill the bank and cause backup in the RAM queue. No safety mechanism exists to preserve the oldest unprocessed chunks, which are overwritten by the newest recordings. If overwriting occurs, unpassed scans are lost and a flag is raised in the sub-data, indicating that scans processed are not necessarily consecutive. This will become important for the high-resolution data, as we will see later. Once the 10 ms series are pulled off the RAM, an FFT is performed to 12 MHz resolution, near Nyquist-limited. With the well-resolved contributions about resonance still centered at 10.7 MHz, a digital mixer windows 30 kHz and shifts these contributions down to begin at 0 Hz, performing a high pass filter above 30 kHz. Now we have drastically down-sampled the coherent frequency space data set of a 10ms sample at a rate resolving the full 30kHz.

Then, the sample is squared and averaged over the 100 second scan time ($\sim 10^4$ sample averages) to form the medium resolution data scans. These are the data sets we will be concerned with and after removal of edge effects are in the form of a 256 bin wide power spectrum array with bins width of $\sim$ 100 Hz, the natural FFT limit from the individual integrations. To form the high-resolution data sets a copy of the unsquared spectra is inverse FFT-ed back to the time domain, where it is effectively mixed down to approximately 15 kHz, and sampled at 30 kHz. The still-coherent time series is concatenated with other 10 ms integrations to form a single well-ordered scan over the full 100 second period. If one of these 10 ms scans is overwritten while in the circular RAM bank, gaps in the otherwise well-ordered data prevent it from forming a coherent series. The aforementioned flag is fixed to such sets, indicating that the time-series has been corrupted.

5.4 Background Subtraction

Before searching the integrated spectra for axion signals, we must first accurately measure the power transmitted out of the cavity. The complex interplay between components in the RF and digitization chain often produces a non-flat transfer function over the scan range, making transmission identification nontrivial. Modeling the true RF response of this complex system is a difficult task, met with limited success by previous ADMX analyzers and other axion cavity searches (Daw, 1998; Asztalos et al., 2010; Brubaker et al., 2017). Here we attempt to improve upon past efforts.

One of the derived goals of this analysis is that uncertainties be dominated by noise with systematic errors being sub-dominate. The power spectra noise error is encapsulated in a Johnson profile covered in 4.3.1, and the systematic error is given by correlated background structures. We expect the two sources of error to be distinguishable. Physical models of receiver chains both past and present have yet to meet this level of accuracy with any consistency (Daw, 1998; Asztalos et al., 2010), though we do glean from these physical studies that the device structures/responses are much broader than the axion width. Instead, a structure-agnostic scheme is used here for background removal.

To choose an appropriate Background Subtraction (BS) procedure we first consider the objectives and measures to gauge the accuracy of the result. After the cavity power is transmitted through the receiver antenna and before its first amplification, it is combined with spectra from the antenna and pre-circulator receiver chain. When these devices are at the same temperature as the cavity they produce the same radiometer and Johnson spectra and the pre-amplification spectra has uniform response. There is no evidence of such a thermal imbalance in Run 1A and we therefore assume uniform noise. This flat response, sans axion signal, is what we want to recover through BS.

The goal of regaining the cavity spectrum is ruined slightly by additional contributions of thermal noise to the transmitted spectra by each receiver device. Recall from 4.3.1 that these additions effectively increase the electronic system temperature. We cannot simply remove this noise as it is uncorrelated, so we revise our goal to recovering the flat system thermal spectrum plus the axion spectrum. To place the above on a precise mathematical footing, consider the digitized spectra and its relation to the earlier stages

$$f_{dig} = S_A(S_{MD}(f_a)) = S_A(S_{MD}(S_C(f_c))) \tag{5.3}$$

where f_c is the power spectra deposited in the cavity, f_a is the transmission spectra at the antenna, f_{dig} is the final digitized spectra, S_A is the amplification transition function, S_{MD} is the mixing-digitizing transition function, and S_C is the cavity transition function, which we already recognize as the Lorentizian. We concentrate on reproducing the antenna power spectra f_a.

Ideally we would find inverse functions for the amplification and mixing-digitizing phases

$$f_a = S_{MD}^{-1}(S_A^{-1}(f_{dig})) \tag{5.4}$$

but this is impossible due to the many-to-one nature of digitizing maps. Instead we modify our end goal to be a digitized form of the spectra using the same idealized digitizing procedure as described in Section 5.3.2, making the transition function of interest

$$f_{ad} = S_D(f_a) = S_D(S_{MD}^{-1}(S_A^{-1}(f_{dig}))) \tag{5.5}$$

where S_D is the ideal digitizer mapping. We may compare our ideal digitized structures to those recorded.

Each physical transition function also adds some non-invertible noise component to the signal so we concentrate primarily on removing the coherent contribution. If the coherent contribution is described by linear gain, then the various transition functions can be commuted to find a more ideal organization

$$\tilde{f}_{ad} = S_{D,gain}(S^{-1}_{MD,gain}(S^{-1}_{A,gain}(f_{dig}))) = \frac{S_{D,gain}}{S_{MD,gain} \times S_{A,gain}} \times f_{dig} \tag{5.6}$$

where

$$\tilde{f}_{ad} = S_{A,noise}(S_{MD,gain}(f_{ad})) \tag{5.7}$$

is the ideally digitized component including all noise contributions. BS is now defined as the construction of the reciprocal of the composite gain.

Before constructing a BS technique let us recall the structures we are trying to preserve. First and by far the most prevalent in our data is the uncorrelated noise, given by a Johnson spectra, and the second is the rare and highly collimated axion signal; two very different structures. Our only remaining hint to help in identifying the background is that the length scales of its structures start several times longer than the axion. To quantify this, let us take a look at some example digitized signals, Fig. 5.9. The frequency spectra for both examples show the expected uniform autocorrelation for the background, a columnated but tail-heavy autocorrelation for the background, and an unusually wide spread for simulated axion signal.

The last can be explained using an uncertainty relation: as the width of the signal approaches the resolution limit of the spectra, its FFT representation expands to fill the complementary space via the relation

$$\Delta f \Delta \tilde{f} \sim \frac{\delta f_{bin}}{\delta f_{scan}} \tag{5.8}$$

where $\Delta \tilde{f}$ is the size of the complementary structure. The background autocorrelation result is explained by the limited ability of the function space $F(N)$ to describe functions in an Fourier basis whose length-scales exceed its span. For example consider a digitized quarter

cosine function $\propto \cos(\pi k/4N)$ and its FFT $\propto 1/k$, which captures the function fully but not concisely. This $1/k$ tail creates problems when trying to use an FFT to separate the contributions of our signal.

A work-around is to expand the space in such a way to allow the analogous Fourier decomposition to better distinguish between background, signal, and noise. We concentrate on the class of expanded function spaces, $F((2n+1)N)$. The class of filters we construct use an inclusion made made up of copies of the original data. How these copies are handled and adjoined to construct the inclusion is the crux of these filters. Each injection q is paired with a projection p such that the composition $p \circ q = I_N$.

- Clone: About a central scan, append pairs of of forward-oriented copies

$$f_{clone}(k) = q_{clone}(f(k)) = f(k \bmod N) \tag{5.9}$$

- Mirrored Clone: About a central scan, append pairs of $(-1)^l$-oriented copies where $l = 1, ..., n$,

$$f_{mirror}(k) = q_{mirror}(f(k)) = f(sign((-1)^n \sin(k\pi/N))k \bmod N) \tag{5.10}$$

  which matches boundaries for the central copies.

- Reciprocated Clone: About a central scan, append pairs of $(-1)^l$-oriented copies where $l = 1, ..., n$ modulated by a forming function

$$f_{mirror}(k) = q_{clone}(f(k)) = \begin{cases} f(k \bmod N) & \text{if } sign((-1)^n \sin(k\pi/N)) > 0 \\ \frac{r(k \bmod N)}{f(-k \bmod N)} & \text{if } sign((-1)^n \sin(k\pi/N)) < 0 \end{cases}$$

  where

$$r = \left(f(N)^2 - f(1)^2\right) \cos^2((k \bmod N)\pi/N) + f(1)^2 \tag{5.11}$$

  which matches both the boundary values and slopes for the central copies.

Once injected the expanded FFTs show greater separation between the background, signal and noise, Fig. 5.11. Here a simple high-pass filter can almost completely remove the background and modulating structures while minimally affecting the signal and noise components over the center scan copy. Once the background is isolated, inverse FFT'ed and divided out from the base signal, we are ostensibly left with forward and reversed copies of the spectra in units of fraction of the mean thermal power. Using the appropriate projection back to $F(N)$ gives our result for the original spectra at the antenna.

To test the viability of these filters we perform several experiments, comparing them not only against each other but also against several accepted practices within the field.

Performing BS on an ensemble of simulated raw spectra of backgrounds, signals, and Johnson noise, we may measure the preservation of the signal and the noise, Figs. 5.12 5.13. Results from BS on $O(10^6)$ simulated scans are summarized in Table 5.1. The Reciprocated Clone High-Pass Filter (RCHPF) is found to outperform all other tested procedures in isolating background and preserving axion signals, producing high-fidelity noise-limited scans for the wide range of structures experienced by ADMX.

	6-Order Polynomial	Savitzky-Golay	CHPF	RCHPF
Benign Structure				
Dispersion Error	$0 \pm 1\%$	$-4 \pm 2\%$	$-2 \pm 3\%$	$0 \pm 2\%$
Recovered Axion Power	$95 \pm 5\%$	$100 \pm 10\%$	$95 \pm 4\%$	$97 \pm 2\%$
Significant Structure				
Dispersion Error	$500 \pm 100\%$	$-5 \pm 2\%$	$7 \pm 4\%$	$0 \pm 3\%$
Recovered Axion Power	$40 \pm 10\%$	$92 \pm 20\%$	$90 \pm 10\%$	$95 \pm 5\%$

Table 5.1: Comparison of several BS schemes on a set of 800,000 simulated scans, half with backgrounds generated by a low-order polynomial with random coefficients (benign), and the other a composition of low-order polynomial and Lorentzian profile (significant). Half the scans in each background class have a noise-level axion signal, the other half have no signal. Dispersion error is calculated by clustering an axion-free scan set into groups of 100, averaging the background-subtracted signals point-wise, measuring their dispersion and comparing the result to pure noise coaddition. Recovered axion power performs the same process as the dispersion error calculation with the axion scan set, with the dispersion step replaced by an integration of power over the axion bandwidth. The Savitzky-Golay filter is calibrated to $d = 5$ and $W = 101$. Cloning is of order $n = 3$ and the High-Pass Filters (HPFs) use a top-hat of size $w = 20$. The analysis reported at the end of this chapter uses a dynamic parameterization of the RCHPF, which improves its stability.

Now we prepare the BS-ed scan for axion search. The spectra post-BS is a dimensionless distribution of mean 1 with Johnson-distributed fractional fluctuations relative to the mean thermal contribution. As we search only for signals with limited bandwidth, we are only concerned with excesses in power over the mean, making the relevant quantity

$$\delta = R - 1 \tag{5.12}$$

where R is the mean-normalized spectra. To find the unit-full power excesses recall that the mean is identified with the average thermal power out or

$$\bar{P} = kTB \tag{5.13}$$

where T is the system noise temperature, producing fluctuation power in watts

$$\delta_w = kTB\delta \tag{5.14}$$

We have now reproduced the cavity transmission between the cavity and the MSA. Analysis of the post-BS scan for axion signals follows in the next section.

5.5 Scan Analysis

The scan package it the basic unit of ADMX data from which we can search for axions. This single iteration of data taking includes both the digitized scan, assumed to already be conditioned, and the packaged experiment status including sensor readings estimates of the system noise temperature and cavity magnetic field strength. This section analyzes the single scan and derives formulae governing the axion search.

5.5.1 Probability of Observation

The normalized scan presented in the previous section represents power moving up the receiver at the point immediately above the antenna, Fig. 5.14. This power spectrum contains ambient thermal noise and potentially a persistent signal. In this regime, the probability of an observation being realized is of the frequentist form

$$P(obs|model) \propto e^{\left(-\chi^2(obs|model)\right)} \tag{5.15}$$

where

$$\chi^2(obs|model) = |\frac{x_{obs} - x_{model}}{\sqrt{2}\sigma_x}|^2 \tag{5.16}$$

where x_{obs} are the figures from observation, x_{model} is the underlying behavioral model, and σ_x are the uncertainties inherent to the observation. For the case of analyzing the power transmitted through the strongly-coupled antenna, a χ^2 form based on transmitted power is adopted

$$\chi^2 = \sum_i \left(\frac{\delta_{w,i} - p_{model,i}}{\sqrt{2}\sigma_{\delta_{w,i}}} \right)^2 \tag{5.17}$$

where $p_{model,i}$ is the signal shape power, $\sigma_{\delta_{w,i}}$ is the uncertainty in noise power, and we take a sum over the bins of a scan's digitized power spectra. The uncertainty can be calculated directly from the δ_w, under our assumption of a Johnson spectra of uniform temperature and so long as the signal power is weak by comparison

$$\sigma_{\delta_{w,i}} = \sum_j \frac{\delta_{w,j}^2}{N-1} \tag{5.18}$$

Before determining the likelihood of a particular model given the data, let us first codify the parameterization of our axion transmission model. In the noiseless and background-less limit only the deposited axion power is transmitted, with intensity

$$p_{model}(\nu) = \langle P \rangle f(\nu) = \Gamma_{\omega_0}(\nu) P_{total} f(\nu) \tag{5.19}$$

where P_{total} is the total axion power sans cavity and halo response, Γ is the cavity transition function, and f is the continuous form of the normalized spectral density from a prescribed line-shape such as the SHM. Unless otherwise stated, we will be using a local axion density of 0.45 GeV/cc. Parameterizing the spectra in terms of fractional power relative to the total power from a DFSZ axion halo

$$p_{model}(\nu) = A P_{DFSZ} \Gamma(\nu) f(\nu) = A \Gamma p_{DFSZ}(\nu) \tag{5.20}$$

The signal is then digitized using integral techniques

$$p_{model,i} = A \Gamma_i p_{DFSZ,i} \tag{5.21}$$

where ρ_i is the probability that an axion is in the i-th bin. The cavity transition function is composed of both the Lorentzian resonance profile and the cavity-receiver coupling strength

$$\Gamma(\nu) = C\Gamma_{\omega_0} = \frac{C}{1 + 4\left(\nu - \omega_0\right)^2 Q^4/\omega_0^2} \tag{5.22}$$

where C is the coupling strength, ω_0 is the resonance frequency and Q is the resonance quality factor. For a critically-coupled mode $C = 1/2$. Each of these components is well-measured during data taking via the active S_{12} and S_{11} scans stored in the experiment status data package.

As we consider no priors for the axion mass the starting frequency of the signal is initially perceived to be of uniform likelihood. This uniformity implies that instead of optimizing a scan's χ^2 over axion mass, we consider the likelihood of every possible signal, picking out axion candidates based on deviations in overall power from the null hypothesis. To identify the probability distribution of measuring a particular shape, let us take our parameterization of the hypothesized signal to its natural conclusion. Each term in the scan χ^2 becomes a quadratic in A, with the sum also being a quadratic

$$\chi^2 = \sum_i \frac{\delta_{w,i}^2}{2\sigma_{\delta_{w,i}}} - 2A\sum_i \frac{\Gamma_i p_{DFSZ,i}\delta_{w,i}}{2\sigma_{\delta_{w,i}}} + A^2\sum_i \frac{\Gamma_i^2 p_{DFSZ,i}^2}{2\sigma_{\delta_{w,i}}} \tag{5.23}$$

with minima-centered form

$$\chi^2 = \frac{\left(A - A_{ml}\right)^2}{2\sigma_A} + Const. \tag{5.24}$$

This form implies that the probability of measurement is also normal about A

$$P(obs|model) \propto \exp\left(-\frac{\left(A - A_{ml}\right)^2}{2\sigma_A}\right) \tag{5.25}$$

making A_{ml} the most likely fractional power described by the scan, and σ_A the uncertainty in the fractional power. Such a parameterization does not determine how 'good' the fit is between model and observation, just which is the best among those sampled. These two parameters are very powerful and many statistical questions may be answered using only these two quantities only.

Measuring A_{ml} and σ_A is a straightforward task. A_{ml} being the most likely outcome occurs when the χ^2 is minimized. This occurs only once for a quadratic, so we simply solve for the root of $\partial_A \chi^2$

$$A_{ml} = \frac{\sum_i \frac{p_{DFSZ,i}\delta_{w,i}}{2\sigma_{\delta_{w,i}}}}{\sum_i \frac{p^2_{DFSZ,i}}{2\sigma_{\delta_{w,i}}}} \tag{5.26}$$

σ_A follows soon after by evaluating χ^2 at convenient locations

$$\sigma_A = \frac{1}{\sqrt{2\Delta\chi^2}} \tag{5.27}$$

where

$$\Delta\chi^2 = \chi^2\left(A_{ml}+1\right) - \chi^2\left(A_{ml}\right) \tag{5.28}$$

The questions we want answered concern the sensitivity of the scan to axions and the significance of the most likely models when compared to the null hypothesis. To gauge a scan's sensitivity to axion signals we ask what power would the axion have to take to be invisible is the probability that an axion with prescribed power"What axion powers are we confident in detecting?" is the first question we wish to answer. Taking a prescribed level of confidence X, we define detection to mean to lay outside the double-sided confidence interval about the null condition of the population of observations.

$$P(|A| \leq A_X) = X \tag{5.29}$$

Using the estimate population centered around $A = 0$ with width σ_A, the X confidence level is given in terms of the width

$$-C(X)\sigma_A \leq A \leq C(X)\sigma_A \tag{5.30}$$

where $C(X)$ gives the number of width lengths. The detection limits presented in this work are at the 90% confidence level, giving $C(X) = 1.64485$. Translating the power limits to coupling limits is a simple matter of algebra, using the power-coupling relation

$$P_{tot} \propto g^2_{a\gamma\gamma} \tag{5.31}$$

The fractional confidence interval may be calculated to be

$$g_A\left(XC.L.\right) = \sqrt{A\left(XC.L.\right)} \tag{5.32}$$

where g_A is the dimensionless coupling ratio relative to DFSZ.

"What is the probability that the power of maximum likelihood is indiscernible from the null condition" is our second question. For a null-centered population the result is found by computing the probability connecting the null condition to the most likely power

$$P_{sig} = P(|A| \leq A_{ml}) \tag{5.33}$$

which gives the significance of a particular observed power deviation. For our normal distribution this result may be placed in units of population width

$$Sig_\sigma = \frac{A_{ml}}{\sigma_A} \tag{5.34}$$

with the associated probability

$$P_{sig} = P(|A| \leq Sig_\sigma \sigma_A) \tag{5.35}$$

High significance of a positive power deviation is the primary means by which we identify candidates. A significance of 3σ was used during data taking operations for identification of primary and persistent candidates. Note that this is a single choice of sensitivity and significance measurement. Other techniques that use the full χ^2 statistic as an objective goodness-of-fit may provide improved limits and behavior over our simple but robust variational technique. Future work may implement such methods. Next, we discuss the calculation of these quantities.

Calculating the Figures of Merit

The combinations of A_{ml} and σ_A used to calculate sensitivity and fit significance involve several layers of computation. There are multiple paths that we may take in calculating these figures of merit, some more efficient than others. In the interest of efficiency, especially

in light of the massive influx of ADMX data expected in the next several years, we take advantage of several numerical principles to enhance analysis speed and accuracy. The most important algorithms employed are covered here.

Starting from the power excesses δ_w, their dispersion σ_{δ_w}, and the DFSZ power distribution p_{DFSZ} we calculate the coefficients of χ^2. The constant term

$$\chi^2_{A^0} = \sum_i \frac{\delta^2_{w,i}}{2\sigma_{\delta_{w,i}}} \tag{5.36}$$

is the most trivial, as it does not change with respect to the various axion models that we search for, so performing the sum as shown is sufficient for our purposes. The $-2A$ coefficient

$$-\frac{1}{2}\chi^2_{A^1} = \sum_i \frac{p_{DFSZ,i}\Gamma_i\delta_{w,i}}{2\sigma_{\delta_{w,i}}} \tag{5.37}$$

does respond to the choice of axion model. In the limit where the range in rest mass frequency covered by the scan is far smaller than the central mass, $\Delta m_{scan}/m_{center} \ll 1$, the line-shape effectively translates under the rest mass frequency

$$f\left(\frac{\nu-\nu_o}{\nu_o}\right) \approx f\left(\frac{\nu-\omega_0}{\omega_0}\right) \tag{5.38}$$

where we set the central frequency to the resonance frequency. This translational form of the signal elevates the A^1 inner product between data and signal shape a discrete convolution between the data and a whole range of signal shapes, which may be calculated at a nearly equivalent cost. To effectively evaluate this convolution we would like to use the discrete convolution theorem

$$\sum_i \delta_{w,i}\Gamma_i p_{DFSZ,i}(\nu_o) \rightarrow (\delta_w\Gamma) * p_{DFSZ}(\nu_o) = FFT^{-1}\left(FFT(\delta_w\Gamma)FFT(p_{DFSZ})\right) \tag{5.39}$$

however we must be careful with its implementation on finite data sets. For sets with a finite number of bins, the discrete convolution theorem takes on a periodic definition over the scan range

$$FFT^{-1}\left(FFT(\delta_w\Gamma)FFT(p_{DFSZ})\right) = (\delta_w\Gamma) * p_{DFSZ}(\nu_o \bmod \Delta\nu_{scan}) \tag{5.40}$$

This periodic nature gives inaccurate results for rest mass frequencies within one signal width of the scan's upper limit, often leading to inaccurate fit estimation or a loss of data, Fig. 5.15. To mitigate data loss we first acknowledge that axions with any significant scan overlap contribute to the separation of the chi^2 from the null state, sending the range of masses considered in the scan analysis to extend beyond the scan by a full axion width above and below. Inspired by this expansion in relevance we construct a means to both invoke the finite range convolution theorem and extend a scan's range of efficacy. The algorithm extends the scan by an axion width on either end with zero weight on the extensions

$$\delta_w\Gamma \rightarrow \delta'_w\Gamma' = \begin{cases} \delta_{w,i}\Gamma_i & \text{for} i = 1, 2, ..., N \\ 0 & \text{otherwise} \end{cases}$$

The extended inner product obviously produces the same result. The discrete finite convolution theorem is also seen to reproduce the product as the axion line-shape has enough room to leave the non-zero region of the scan before wrapping around, Fig. 5.16.

The last term of the chi-squared

$$\chi^2_{A^2} = \sum_i \frac{\Gamma_i^2 p^2_{DFSZ,i}}{2\sigma_{\delta_{w,i}}} \tag{5.41}$$

also involves a discrete convolution, but between the square cavity transfer function and the squared DFSZ signal

$$\Gamma_i^2 p^2_{DFSZ,i}(\nu_o) \rightarrow \Gamma^2 * p^2_{DFSZ}(\nu_o) \tag{5.42}$$

We may again implement the discrete finite convolution theorem by using the same extension on the squared transition function, accurately calculating the numerous inner products at a fraction of the computational cost. This calculation completes the single scan analysis. The next section considers how to optimally integrate multiple scans.

5.6 Coaddition of Scans

Now that we have a handle on how individual scans are analyzed, we must intelligently include coincident data from multiple scans to boost the power of the single scan result. In

combining scans we also extend the search's spectral range to the union of all scan searches, creating a grand spectrum. This coaddition procedure is based on the assumption that every loop of the data-taking cadence produces a unique measurement of the axion spectra. Statistical independence allows us to construct measures of fit for which the addition/subtraction of a new scan follows simple algebraic rules, making the analysis modular to the single scan level. The remainder of this section provides an overview of how the figures of interest are calculated are combined.

At the population level a collection of statistically independent scans are introduced as trivial extensions of the χ^2 kernel. For two scans incorporation looks like

$$\chi^2_{12} = \sum_{i \in S_1, S_2} \left(\frac{\delta_{w,i} - p_{model,i}}{\sqrt{2}\sigma_{\delta_{w,i}}} \right)^2 \tag{5.43}$$

$$= \sum_{S_1} \left(\frac{\delta_{w,i} - p_{model,i}}{\sqrt{2}\sigma_{\delta_{w,i}}} \right)^2 + \sum_{S_2} \left(\frac{\delta_{w,i} - p_{model,i}}{\sqrt{2}\sigma_{\delta_{w,i}}} \right)^2 \tag{5.44}$$

$$= \chi^2_1 + \chi^2_2 \tag{5.45}$$

where S_k are the bins of the k-th scan, recalling that the model may take on trivial value over one or more of the scans. Extensions for larger collections of scans is straightforward. Optimally adding in a new scan is that simple. The tricky part appears when we consider that not all scans cover the same frequency range or necessarily even have bins whose boundaries match over their intersection, making direct bin-wise arithmetic difficult. To ameliorate this issue, we will turn the problem on its side and instead set the grand spectrum by performing the axion search at a prescribed collection of axion rest mass frequencies.

To track how the set of scans influences the figures of merit, a number of grand spectra are created, each with its own rule governing the addition/subtraction of a new scan. Arithmetic occurs on the basis of coincident axion rest mass. The first is the simple statistic of effective number of scans which contribute to a signal's fit significance

$$C(\nu_i) = (\text{number of scans}) \tag{5.46}$$

Each contributing scan will changes the statistic by the Lorentzian weight averaged over the signal

$$C = C_o \pm \bar{\Gamma} \tag{5.47}$$

The various coefficients of the χ^2 update as one would expect

$$\chi^2_{A^k} = \chi^2_{A^k,o} \pm \chi^2_{A^k,scan} \tag{5.48}$$

and from these rules we may derive the arithmetic necessary to update the remaining figures of significance.

The σ_A and sensitivity limits utilize χ^2 differences, making their update rules behave like reciprocal summations

$$\sigma_A = \left(\frac{1}{\sigma^2_{A,o}} \pm \frac{1}{\sigma^2_{A,scan}} \right)^{-1/2} \tag{5.49}$$

$$A(XC.L.) = \left(\frac{1}{A(XC.L.)^2_o} \pm \frac{1}{A(XC.L.)^2_{scan}} \right)^{-1/2} \tag{5.50}$$

$$g_A(XC.L.) = \left(\frac{1}{g_{A,o}(XC.L.)^4} \pm \frac{1}{g_{A,scan}(XC.L.)^4} \right)^{-1/4} \tag{5.51}$$

More complex quantities such as the maximum likelihood powers and and fit significances may utilize the previous updated quantities if performed as ordered here

$$A_{ml} = \frac{-\chi^2_{A^1}}{2\chi^2_{A^2}} \tag{5.52}$$

$$Sig = \frac{A_{ml}}{\sigma_A} \tag{5.53}$$

Other statistics such as the SNR and cumulative noise power have similar modular definitions, but we do not derive them here as they are inconsequential to our offline analysis.

5.7 Signal Modulation and Run-Time Level Parameters

Over the course of gathering data, many aspects of the axion search may change. Over the previous sections we have accounted for those features intrinsic to the experimental

apparatus. Here we address one external factor: orbital signal modulation. Over the period of hours and months, the aparatus accumulates a peculiar velocity relative to the galactic center as it moves with the Earth's surface. The diurnal spin of the earth's surface and the earth-sun orbit change the frame of reference from which an axion spectra is measured, changing the axion halo line-shape. Using such articulated line-shapes enhances the fit significance of an axion signal and reduces the significance of comoving signals such as Earth-bound RFI. The axion search presented in this chapter is the first to have a fully-articulated and well-motivated line-shape at DFSZ sensitivity.

For simple signal shapes such as the one presented in Section 3.6.2 and the SHM the peculiar velocity changes the width by order

$$\delta W \sim 2W \frac{v_{pec}}{v_{circ}} \tag{5.54}$$

which amounts to $O(10\%)$ for orbit and $O(1\%)$ for spin.

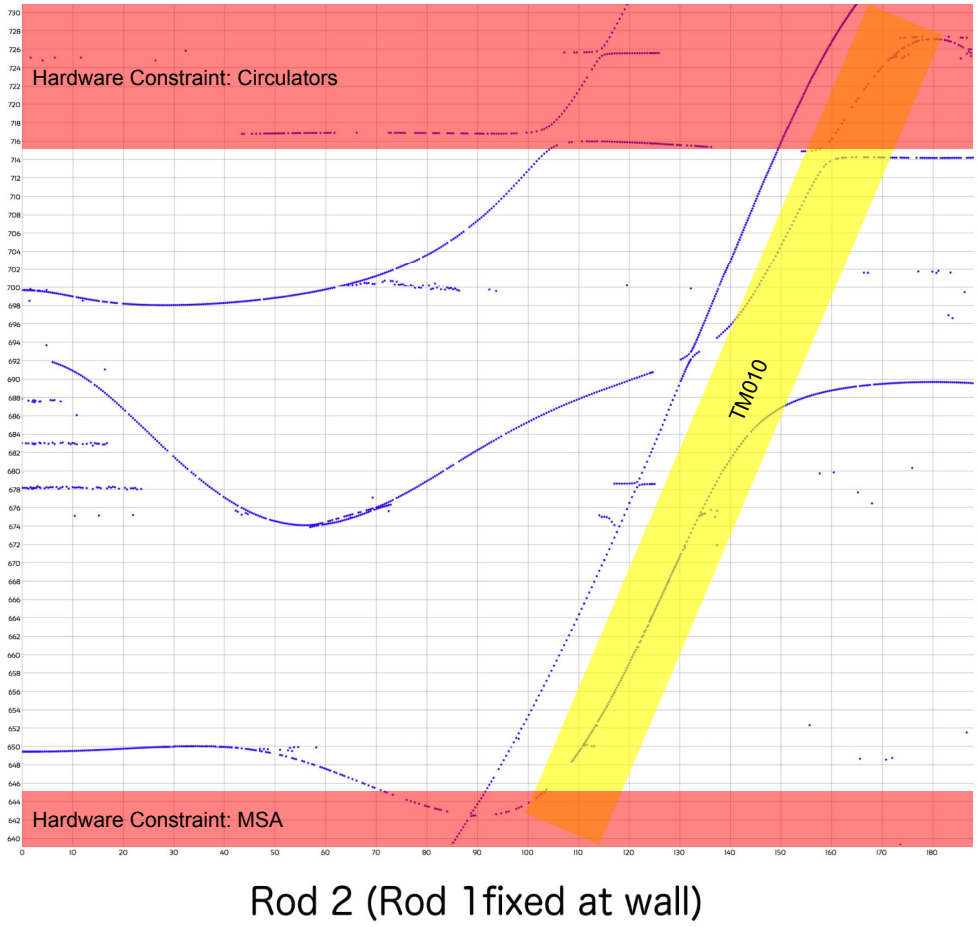

Figure 5.1: Physical mode map of main cavity over Run 1A TM_{010} frequencies. TM_{010} mode highlighted. Hardware constraints are show in red. Cavity configurations have one rotating rod with the other rod held at the cavity wall.

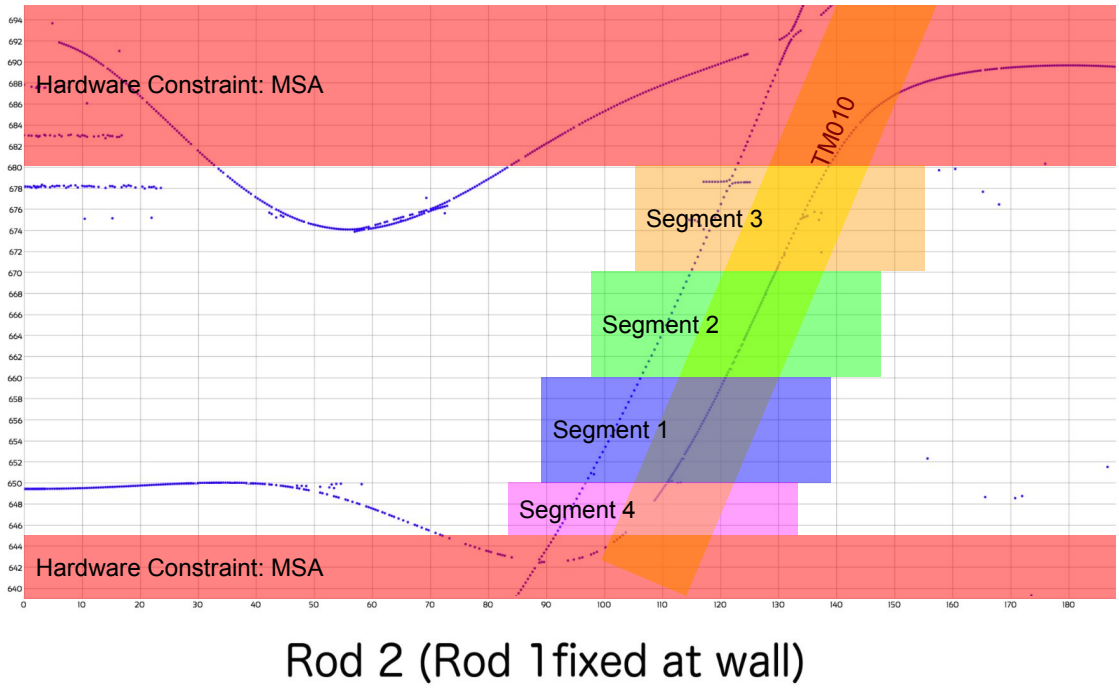

Figure 5.2: A zoom-in of Fig. 5.1 with operation-time constraints and viable scan range segmentation imposed. Form factors within this band range from 0.4-0.5.

tune (B field on).png tune (B field on).png

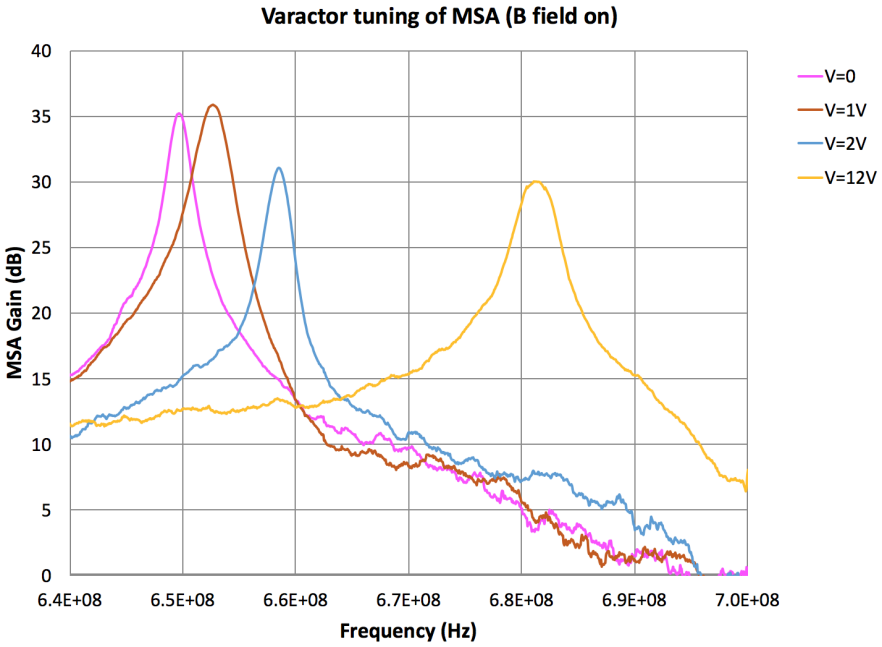

Figure 5.3: Selection of MSA transmission spectra over the realized tuning range. The narrow gain peak provides a limited range of quantum-limite amplification. Height of gain peak is highly sensitive to MSA environment at the time of tuning, making consistent calibration difficult.

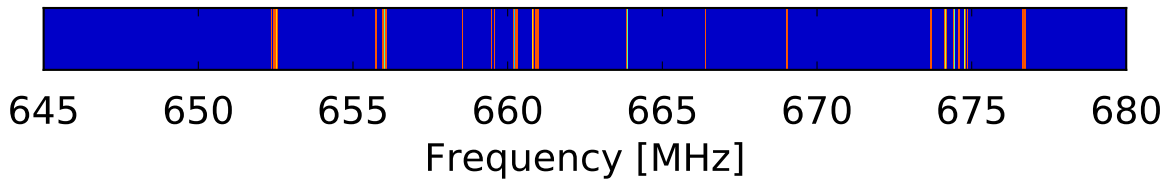

Figure 5.4: Run time candidates for Run 1A, as calculated by the live analysis.

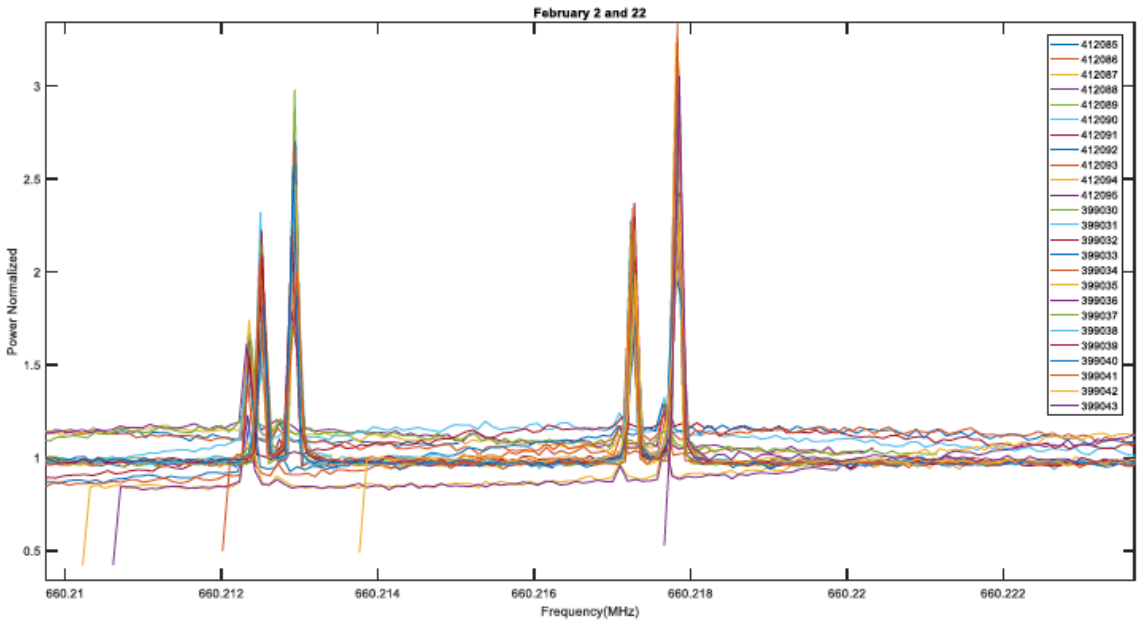

Figure 5.5: Example of RFI in Run 1A. Several scans are displayed to show range of prominence and persistence.

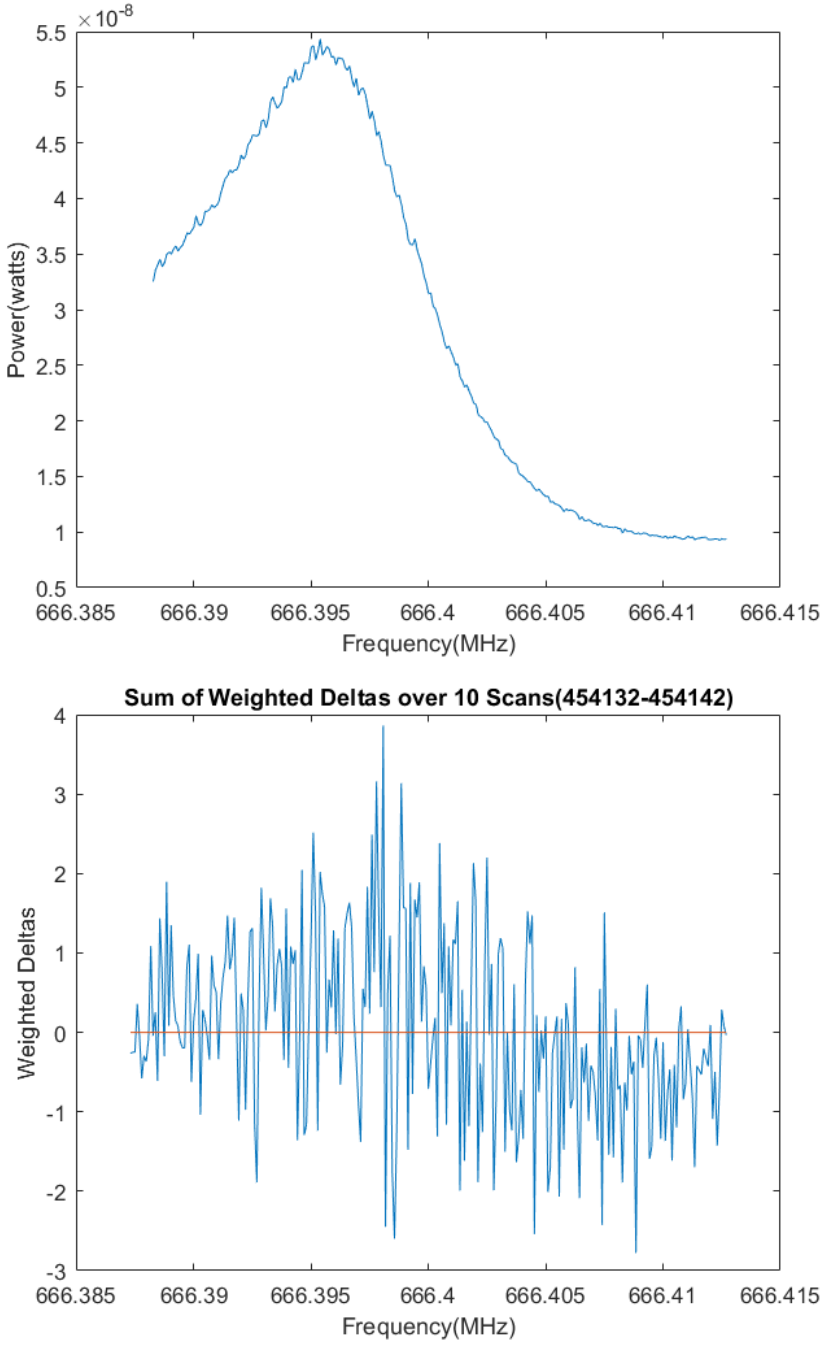

Figure 5.6: Example of significant residual background structure after poor background subtraction performed by the live analysis six-order polynomial scheme. The top figure shows a raw scan with significant correlated structure. The bottom figure shows the weighted average of ten adjacent scans with significant backgrounds, with notable remaining correlated structure.

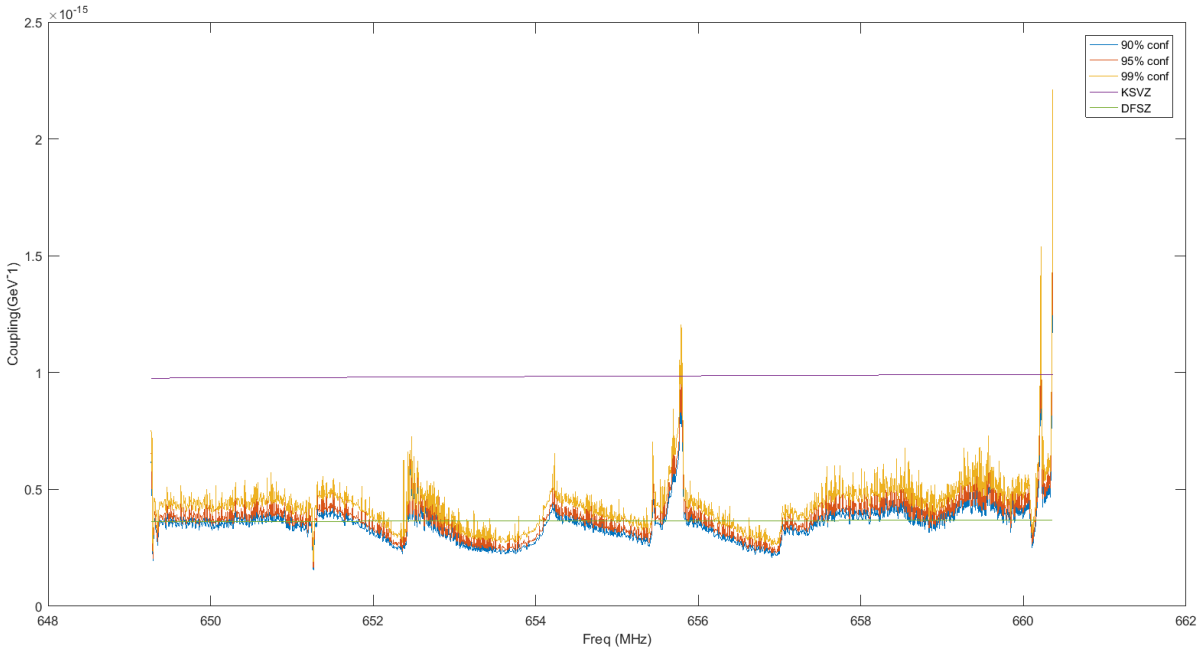

Figure 5.7: Example of live analysis coupling limits for Segment 1 at 90 %, 95 %, 99 % confidence for 100% DM axions. Limits were generated using an early form of system temperature estimation.

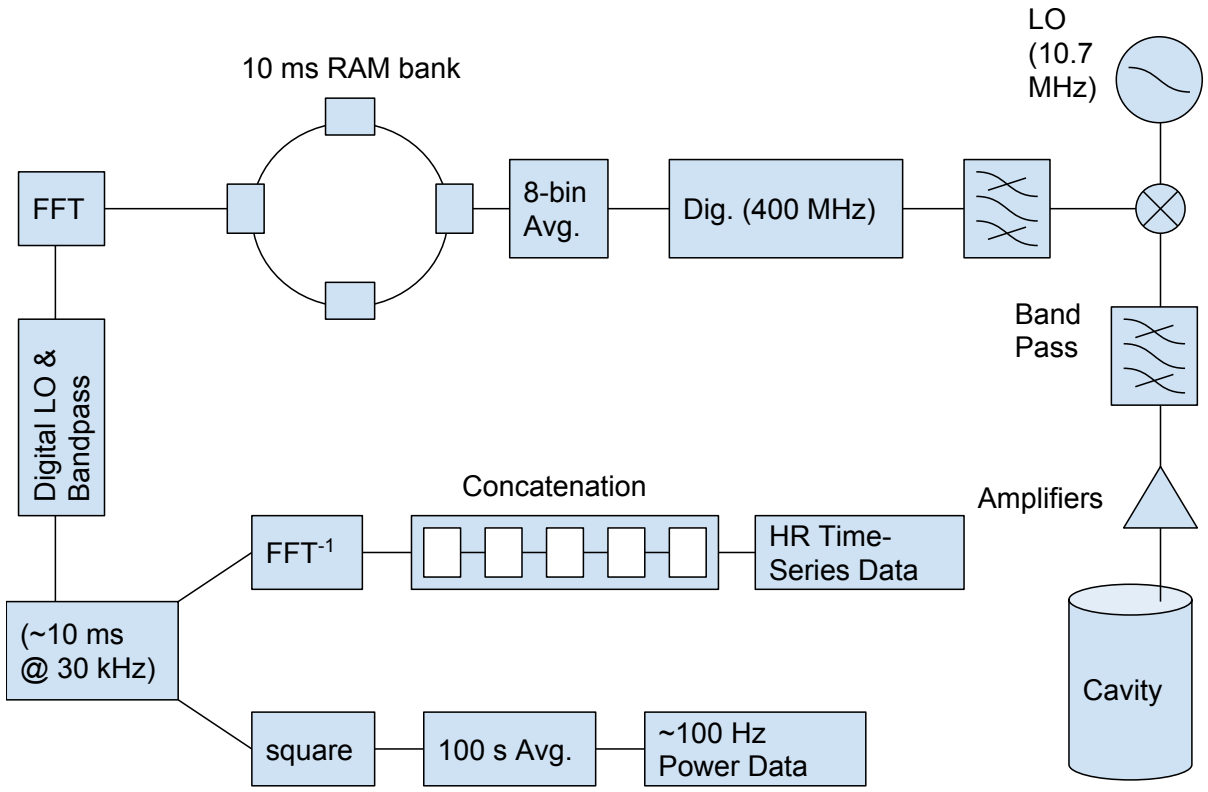

Figure 5.8: Schematic for the TM_{010} digitizer chain.

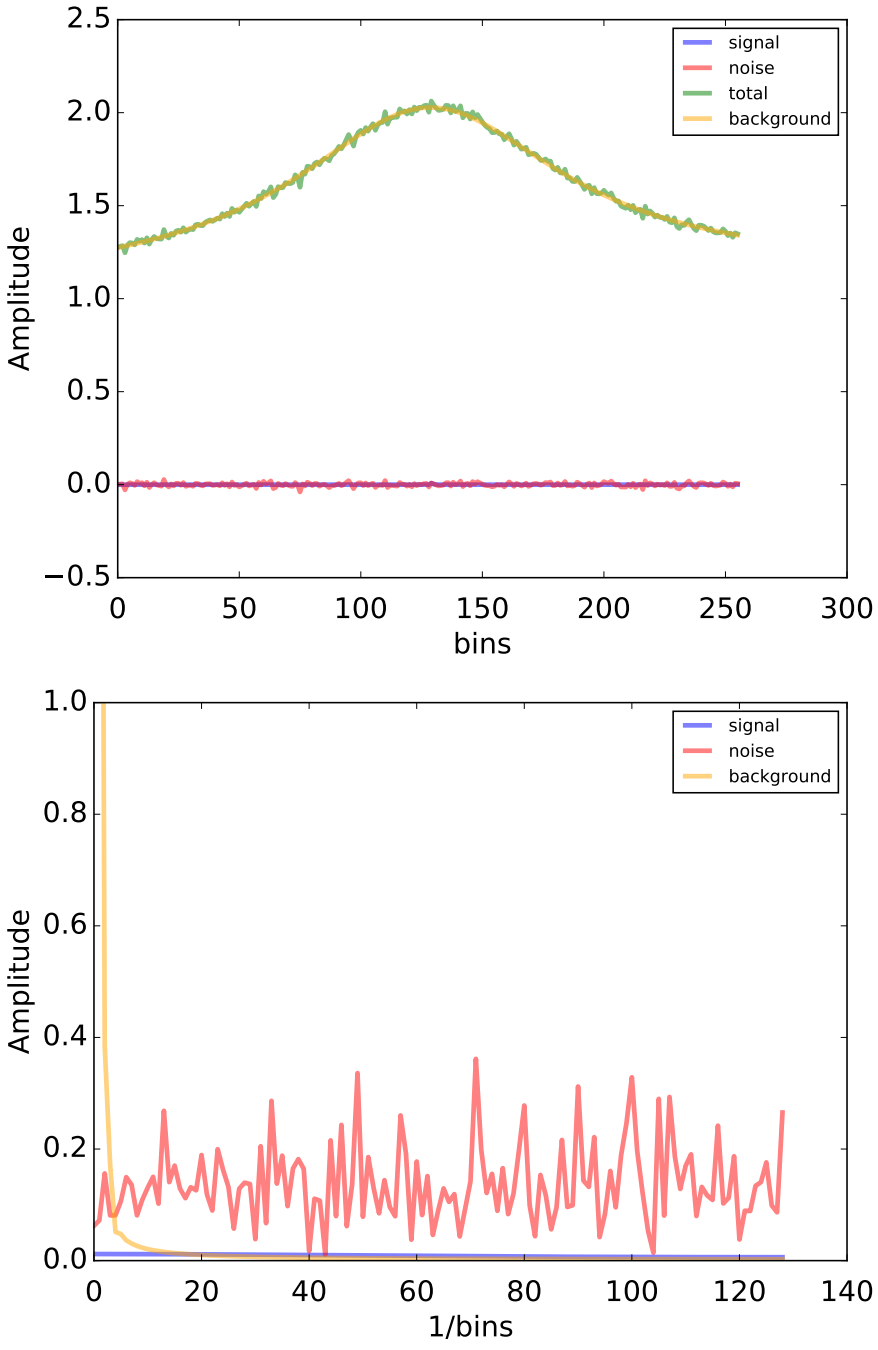

Figure 5.9: Simulated sample raw digitizer power spectra with significant background structure and a sub-noise level axion signal. The top panel shows the incoherent spectra in its recorded parameterization of [power]/[Hz] and the bottom panel shows the FFT-ed spectra in autocorrelated [power]/[sec].

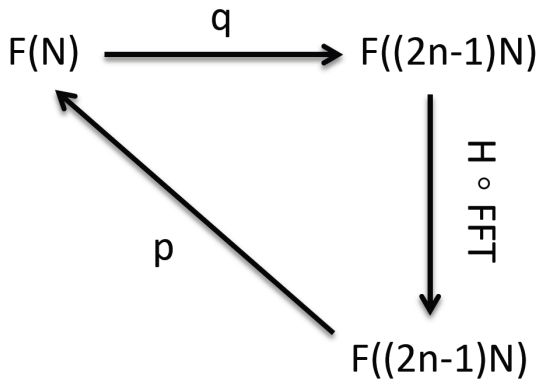

Figure 5.10: Diagram maps clone filter class. The total filter is traced by the counterclockwise cycle starting/ending with $F(N)$. The H map is a filter on functions of the $F((2n+1)N)$ space.

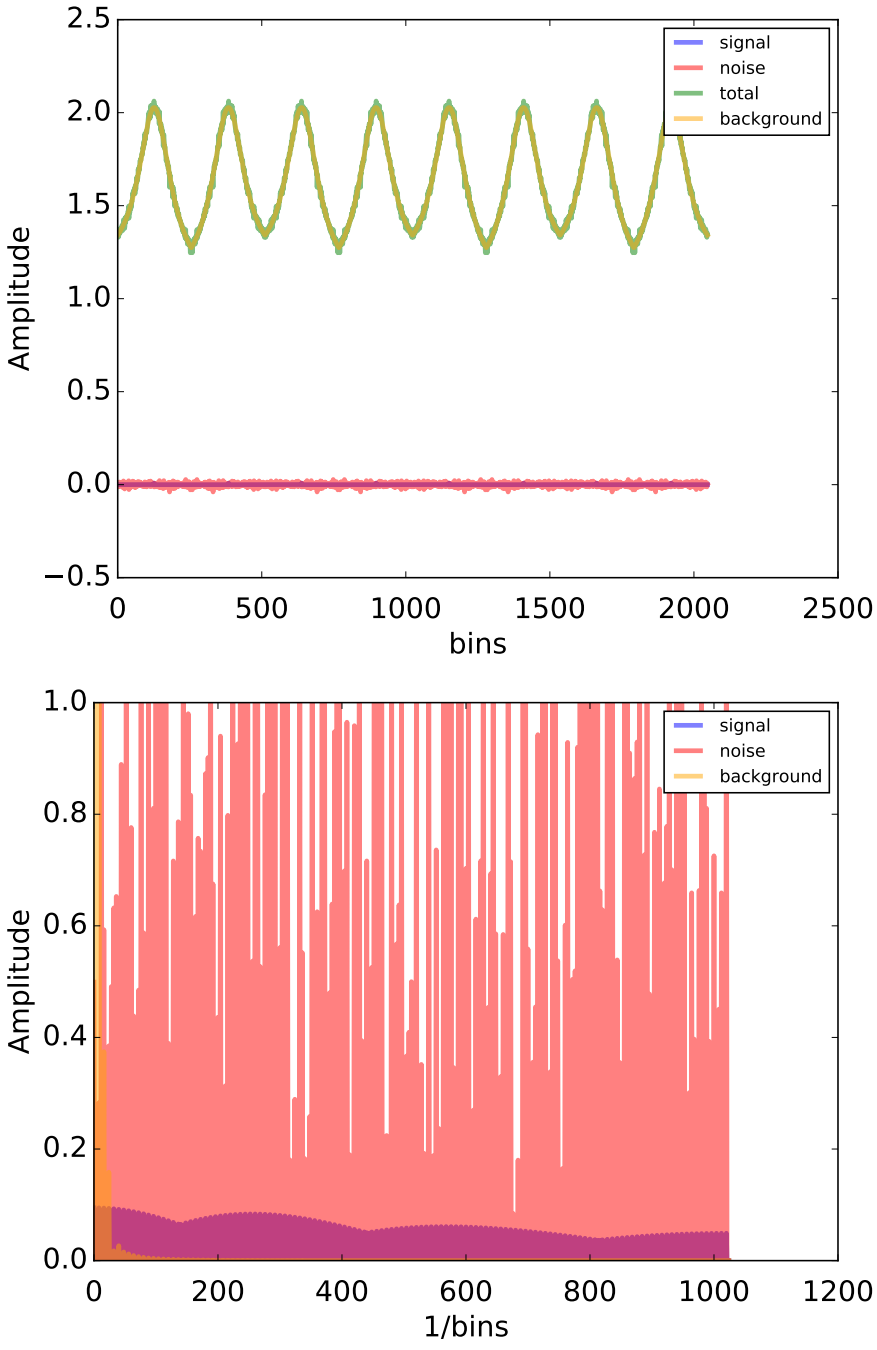

Figure 5.11: Mappings of simulated sample raw spectra from 5.9 into the expanded function space for the basic clone filter, and its autocorrelated counterparts. Background on the autocorrelation figure has been rescaled to make structure visible.

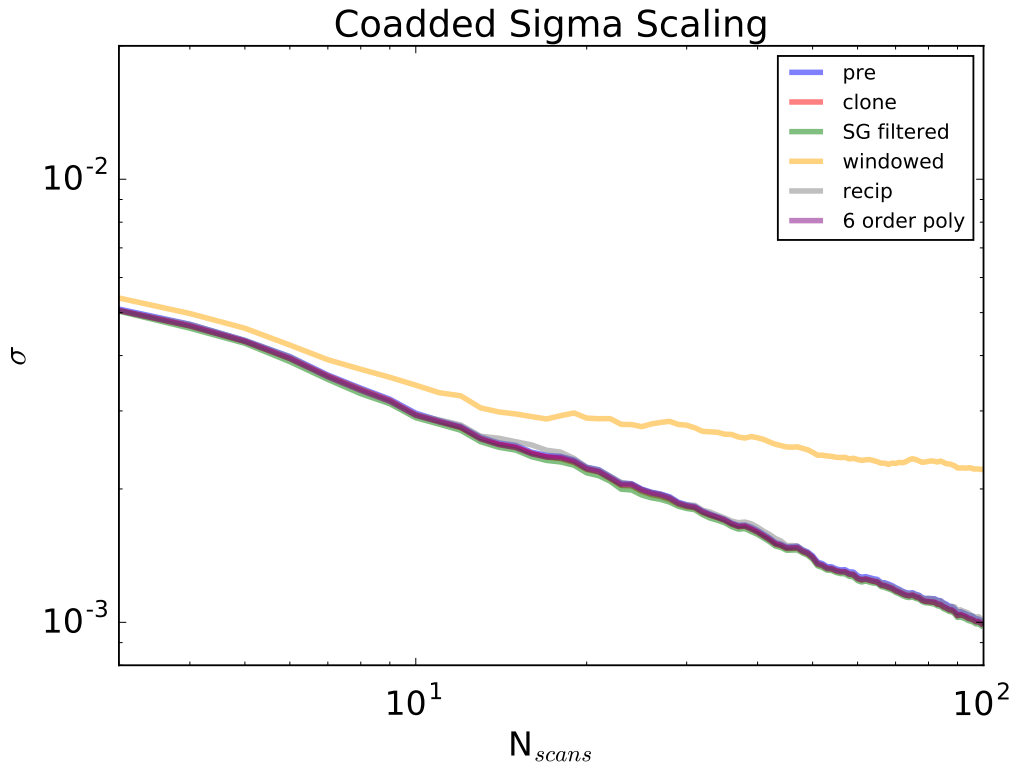

Figure 5.12: Sample standard deviation scaling of co-added simulated scan spectra after BS. Original backgrounds are in the benign category. Co-additions are done point-wise without offset. Scaling is expected to obey a $\propto 1/\sqrt{N_{scans}}$ law for a uncorrelated normal distribution. True standard deviation scaling of the simulated noise is also calculated for comparison.

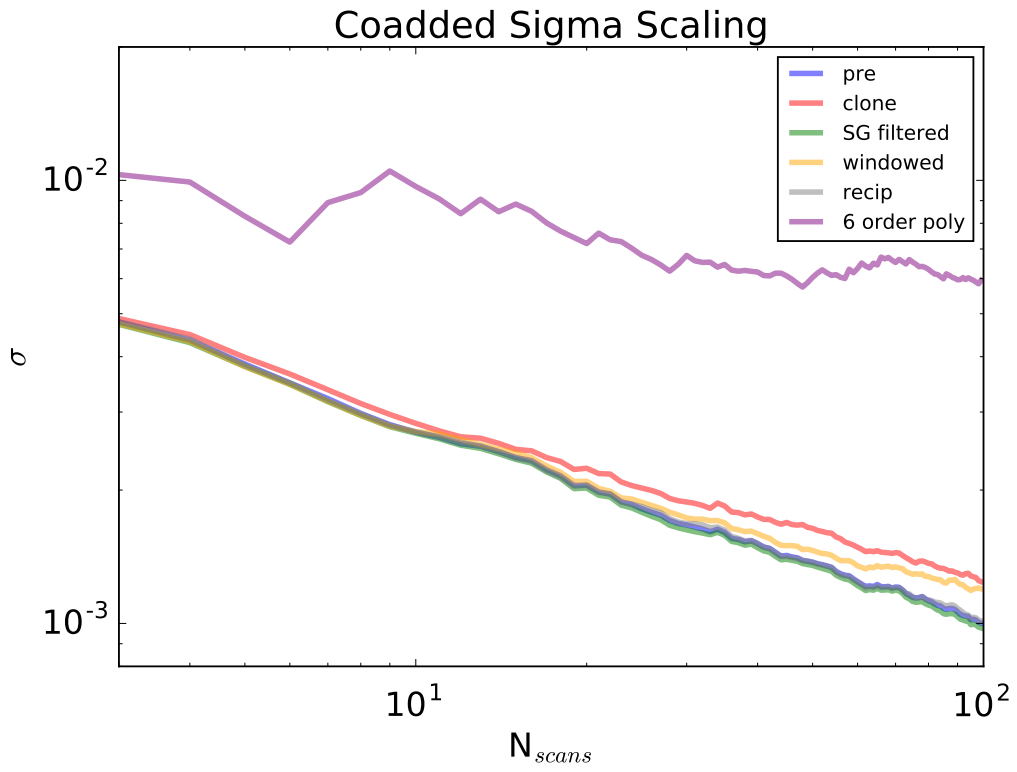

Figure 5.13: Sample standard deviation scaling of co-added simulated scan spectra after BS. Original backgrounds are in the significant category. Co-additions are done point-wise without offset. Scaling is expected to obey a $\propto 1/\sqrt{N_{scans}}$ law for a uncorrelated normal distribution. True standard deviation scaling of the simulated noise is also calculated for comparison.

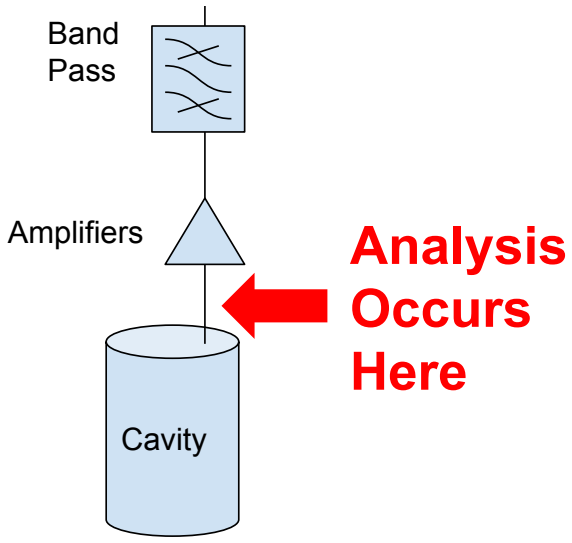

Figure 5.14: Zoom-in of the TM_{010} channel ADMX receiver chain, indicating where the axion search analysis effectively occurs.

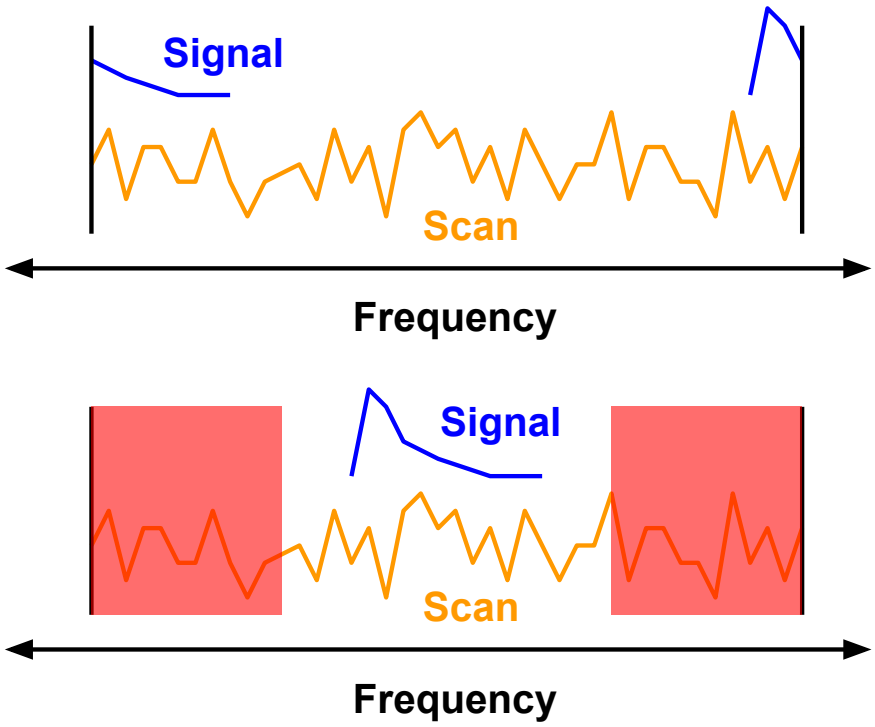

Figure 5.15: Common errors in using discrete convolution theorem on finite data sets. The left figure shows the wrap-around effect of the finite convolution theorem. The right figure gives a potential if inefficient solution: remove the axion-width segments impacted from the wrap-around effect from the convolution result. This constitutes about a 10% loss of data when applied to Run1A spectra.

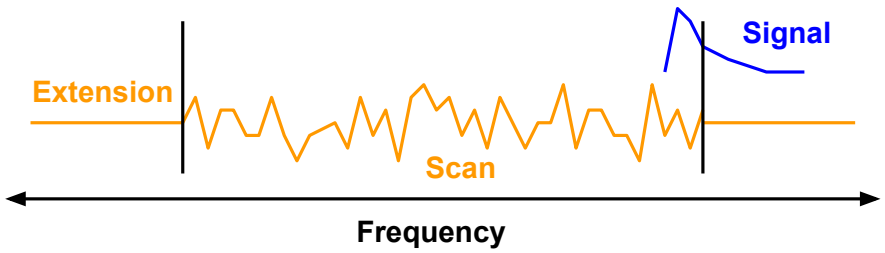

Figure 5.16: A solution to the discrete convolution theorem problem. Adding zero-weighted wings of axion width to both sides of the scan before implementing the convolution theorem produces the correct result over the full range of interest. This is evident by the absence of wrap-around when the axion signal is in the original scan range.

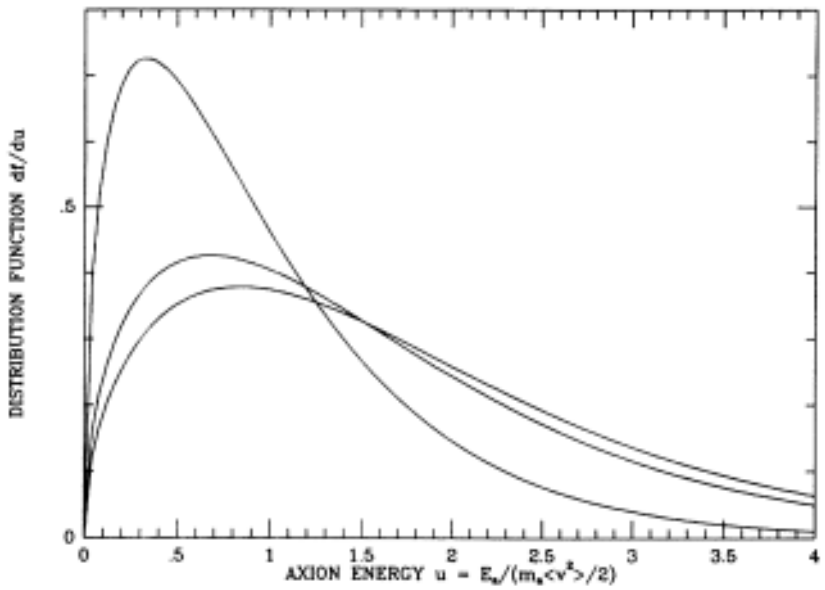

Figure 5.17: Line-shape modulation of the SHM due to the peculiar motion of an earth-borne apparatus (Turner, 1990). Traces shown are for times of maximum aligned motion, orthogonal motion, and anti-aligned motion relative to the solar velocity.

The line-shapes considered in this work are robust, changing appreciably on the timescale of months. For more complex signal shapes, such as those of a non-virialized halo comprised of highly compact energy levels, the signal appreciably changes its shape on a much shorter timescale, on the order of minutes to hours. Such a short timescale implies that each scan must utilize its own shape, though within a scan the convolution limit still applies as $Q_a \sim 10^{-6} \ll \Delta\nu_{caustic}/\Delta\nu_{scan}$.

The signal used for each scan's axion search is generated using the kinematic conditions of the apparatus relative to the galactic center. Digitizer time-stamps are used to specify the orbital phase. Realistic orbital and spin parameters are used to specify the magnitude and orientation of the orbital motion at the time of the scan (Turner, 1990; Gelmini & Gondolo, 2001; Freese et al., 2013). Calculating the new line-shape is quite easy for the SHM as a

simple boost may be taken to change the distribution's frame of reference. The new N-Body line-shape is not so straightforward. The full N-Body distributions that generated the line-shape may be boosted to provide new shapes, but this is very costly. Instead a simple yet effective estimate for small modulations is used

$$f(\frac{\nu - \nu_o}{\nu_o}) \rightarrow f(\frac{(\nu - \nu_o)\,(\vec{v}_{pec} \cdot \vec{v}_{sol}/v_{sol}^2 + 1)}{\nu_o}) \tag{5.55}$$

5.8 Data Cuts

Not all data taken during Run 1A operations is qualified to enter into the axion search. Scans taken as part of receiver studies, mode navigation errors, during abnormal cryogenics conditions, and a number of other conditions are marked as unfit for analysis. Further, scans for which the logs are incomplete or BS does not pass quality checks are also omitted. Altogether approximately 2% out of $\sim 2 \times 10^5$ scans during Run 1A. See Table 5.8 for data cut details.

Reason	Number of Scans Cut
Receiver Tests	1284
Navigation	1940
Electronics	965
Other	485

5.9 Run 1A Results

We now use the machinery and data cuts of the previous sections to compile our search results. The Run 1A axion search is performed using the natural power spectrum bin width of $\approx$ 96.5 Hz for the mass resolution and is conducted for both the new line-shape and the SHM. Fit significance showed no new candidates relative to the live analysis.In the candidate-less context the sensitivities power, coupling, etc. become confidence limits on the detectability of axions. Figure 5.18 shows detectability limits in axion-photon coupling, power, and DM density, averaged in 1MHz intervals.

In each form of the limits we see the new line-shape outperform the SHM by a factor of $1.8^{1/2}$ in power and DM density and $1.8^{1/4}$ in $g_{a\gamma\gamma}$. This behavior falls short of the upper bound in sensitivity augmentation by a power of 2. Future analyses will attempt to improve on this enhancement.

Even with current techniques the new line-shape represents an impressive increase in the discovery potential of Run 1A, which is used to improve limits. This line-shape may be used with equal efficacy to enhance previous ADMX data as well as data from other axion cavity searches. Future ADMX runs have the choice of using this new potential as a sensitivity enhancement over the robust SHM or as a liberty to increase their scanning rate. There is a linear relationship between our analysis' power enhancement and integration time, implying that scan rates may be increased by a factor of 1.8 relative to the SHM at the same sensitivity. Such an accelerated pace pushes ADMX much closer to covering the viable DM parameter space at an auspicious rate. Our N-Body-motivated line-shape has already proven to be quite a boon for the axion search community!

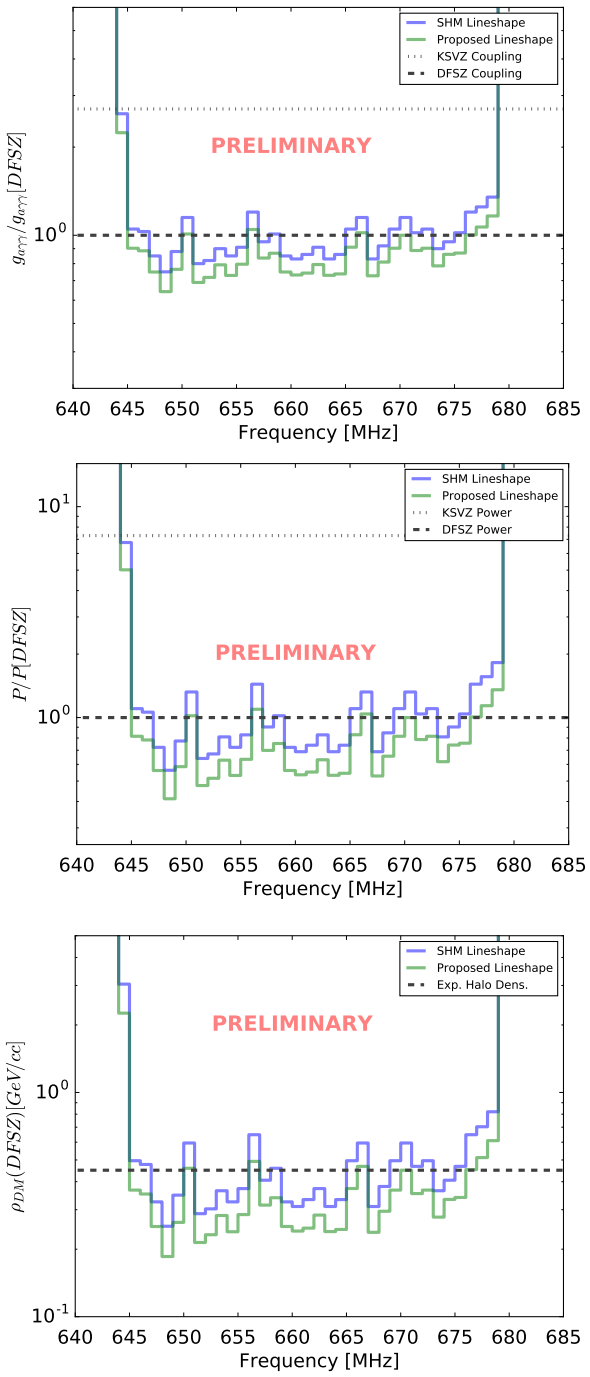

Figure 5.18: Sensitivity of 96.5 Hz axion searches of Run 1A, averaged over 1 MHz intervals. Both SHM and the new line-shape are tested. The top panel represents the sensitivity in converted power, the middle represents sensitivity in coupling $g_{a\gamma\gamma}$ assuming axions are the DM, and the bottom represents sensitivity to the local DM density assuming DFSZ coupling. All sensitivities are to the 90% confidence level.

Chapter 6

SUMMARY AND FUTURE WORK

This dissertation addresses the utility of cosmological structure formation simulations on the search for QCD axion DM. The well-motivated axion DM candidate has properties that make it versatile to detect and place it in a state unique from material science. The rigorous study of axion structures from the perspective of N-Body simulations has already proven to be a windfall for the astronomy and DM search communities, revealing deep qualities of both CDM and Bose infall. Inspired by the progress to date, a significant research effort is scheduled to take place over the next several years, with the potential of resolving a controversy of increasing relevance to the DM search community.

6.1 A Path to Ending the USP Controversy

Our contribution is the formation of a research program whose prime requirement is resolving the unique structure controversy. The project derives from first principles a comprehensive and computationally effective model of axion infall. From the starting point of a quantum axion field in the presence of a cosmological spacetime, dynamics of relic axions during the structure formation epochs are formed. A continuum distribution description of the salient degrees of freedom of the Bose fluid

$$\partial_t f^{(1)} + \frac{\vec{p}}{m_a} \cdot \vec{\nabla} f^{(1)} - (1 - \epsilon S)\, \vec{\nabla}\Phi \cdot \vec{\nabla}_p f^{(1)} - \epsilon \vec{\nabla}\Theta \cdot \vec{\nabla}_p f^{(1)} = 0$$
$$\nabla^2 \Phi = 4\pi G \int d^3 p f^{(1)}$$
$$\nabla^2 \Theta = 4\pi G \int d^6 w_2 \delta^3 \left(\vec{x}_1 - \vec{x}_2\right) \frac{C^\mu \partial_\mu f_+}{f_+} f^{(1)}(w_2, t)$$

shows distinct departures from the standard collision-less Boltzmann equation of CDM due to the presence of a cross-correlation measure ϵS and potential Θ. This departure fulfills the

expected CDM limit when axions de-cohere.

Solutions to the axion structure problem are needed to definitively test the assertion that axions form structure unique from CDM. The axion Boltzmann equation becomes too non-linear during the strongly-coupled collapse and equilibration phases of structure formation to solve analytically, instead requiring a sophisticated computational approach. Using the Method of Characteristics to discretize the continuum DF into integral particles, each with an equation of motion

$$\begin{aligned}\dot{f} &= 0 \\ \dot{\vec{x}} &= \frac{\vec{p}}{\mu} \\ \dot{\vec{p}} &= -\vec{\nabla}\Phi' - (1-\epsilon S)\vec{\nabla}\Phi - \epsilon\vec{\nabla}\Theta\end{aligned}$$

which are obviously disparate from Newton's "$-\vec{\nabla}\Phi = m\vec{a}$". Small scale computational experiments on the N-Body equations give us some experience with solving the equations and probing the extent of the extra-classical physics. The Axions in eXternal Potential infrastructure performs this task exploring the low degeneracy and coherent limit. Several experiments run in this practice regime show structures unique from their classical counterparts are capable of surviving the chaotic infall process. Isolated collapses in three dimensions showed the suppression of the classical Radial Orbit Instability, improving particle-wise conservation of angular momentum after the initial collapse. Further, the density and angular momentum profiles of Bose infall also appear to be distinct from the universal profiles of CDM.

Even with all this development, we are far from providing definitive answers to the question of unique Bose structure on galactic scales. Simulations of full collapse from the radiation-matter transition to modern times are needed. Further, the simple and poorly-resolved structures of AXP are straightforward to analyze, but halos of cosmological origin require more thought. Understanding these structures, both Bose and CDM, is paramount to extracting the science from the simulation data.

6.2 Understanding DM Halos

In preparation for the simulations of Bose SF the research program has a parallel path setting to better understand the structures of CDM simulations. The process of classical formation and equilibration, still highly non-linear, is not well understood by the SF community, making our work an open topic. We choose to approach from the perspective of a potential terrestrial experiment or astronomer in a MW halo.

We first study a range of bulk perturbations to idealized cosmological infall, testing our confidence in the structures expected from CDM halos. Imparting a halo progenitor with solid-body spin produces a halo with robust density and angular momentum profiles over all reasonable cosmological spins and well into extreme spins. The robust profiles appear to be closely related to an axial symmetry-breaking bar structure similar to that created by the Radial Orbit Instability. These near-universal structures serve as a reliable control to compare Bose halos against. In the case of Bose infall we may speculate that the condensed axions either resist dispersing their angular momentum or more energetically form symmetry-breaking structures like the observed bar, which may have already been seen in the Axions in eXternal Potential results.

In the eventual context of cosmological halo formation, the role of these instabilities becomes less clear. A halo's history consists of periods of gentle minor mergers, interrupted occasionally by more violent major mergers. (Bellovary et al., 2008) performs preliminary simulations of halos subject to controlled minor and major mergers to investigate the realistic role of the Radial Orbit Instability, where they speculate that it does not play a significant role in the subsequent relaxation process after a major merger. However, they also state that there are indications of an operational instability during the minor merger periods, acting on nearly radial tidal streams associated with disrupted subhalos. A similar study with non-radial inflow and torqueing may provide insight into the rotational regime. Whether any findings of symmetry(-breaking) structures carry over to observational tests remains to be seen.

Expanding to cosmological volumes and a more complete set of physics allows for the formation of MW-like galaxies, our ultimate case study. Our first study of such simulations is the Romulus 25 data set, describing the evolution of the 25 Mpc cosmological box using the state-of-the-art N-Body code CHaNGa. The lowest hanging fruit of axion analysis in such a data set is the calculation of the axion signal shape. Selecting Romulus 25's most MW-like halos, we find that the kinematic spectra for a terrestrial observer do not comply with the widely accepted Standard Halo Model, but instead show a much narrower profile. This in and of itself is a significant discovery both for the astronomy of DM and our eventual structure comparisons, but also to current axion searches.

We analyze data using the narrow line-shape, which is our current best guess to the true axion spectra, from the most recent run of the leading axion cavity search ADMX. Features new to the cavity search community are used here, including a novel background subtraction scheme specially suited to the ADMX receiver chain and modulation of the line-shape due to the peculiar motion of the apparatus on the earth's surface. For a preliminary axion search using uncertainty-significance statistics, robust limits are placed on the axion coupling using the most realistic axion signal shape to date. Even at this early stage the advantage of the new line-shape are obvious as they enhance the Run 1A limits to well beyond the viable DM region. Such enhancements drastically improve cavity searches' discovery potential. Other approaches to calculating confidence limits may produce improved sensitivity and fully exploit the narrower line-shape, which are to be pursued in future work. Further, spectra and line-shapes will also be of great utility to non-terrestrial axion DM searches, such as the proposed radio telescope searches. Forming these spectra given the intra-galactic magnetic field is a straightforward task.

The surprising narrowness of the expected MW DM spectra guides our halo study to understanding the underlying mechanisms, and how they may change under Bose dynamics. Beyond the standard profiles and analyses of the DM and baryons, Romulus 25 affords the ability to probe modern and historical structures. Preliminary work shows that velocity anisotropy and bulk co-rotational motion at peak density are the primary differentiators

from the SHM, which often exist through the DE epoch and into the progenitors 8 Gyr previous. Dark Disk conjectures are ruled out when one removes the baryonic matter from the simulation, using the DM-only version of Romulus 25, and find an additional enhancement of the signal, implying that this is a feature of DM-only collapse, and not wholly caused by baryonic interactions.

While conserved macroscopic properties such as halo angular momentum are directly tied to the same properties in the infall components and environmental impact, intrinsic figures such as anisotropy are due to scattering off gravitational potentials and the nature of virialization. To prove this out we performed a number of experiments on isolated halo formation. These tests show that the majority of kinematic properties unique to the DM spectra can be described by an isolated halo, with the underlying dynamics dominated by a highly resonant triaxial potential. The expected mobility of the spectra with baryons is also observed via the introduction of rudimentary galactic potentials, which scatter the highly resonant distribution into the observed shapes. The resulting spectra still hold distinct non-thermal characteristics, retaining the distinctive narrow line-shape of Romulus 25. The identification of resonant dynamics as the underlying cause of the signal shape also directs us as to where differences may arise in Bose structures; giving us a first glimpse as to what orbits survive the relaxation process and what are disrupted. The survival of resonances and other columnated features has significant implications for axion fine structure.

6.3 Resolving the USP

The most crucial stages of the project are still ahead. Having proved the viability of the Bose infall model on a small scale the N-Body algorithms are to be adapted for use in the N-Body Shop's flagship code ChaNGa. When complete a series of small simulations are to be run, both as a test of the software and the upscaled physics. Isolated spherical collapse simulations are a natural first step, with one-to-one CDM counterparts in the spun-up and baryon-potential simulation series. The simple nature of such initial conditions reduces the potential influences affecting the final state of axions. The virialization process, instabilities,

halo profile shape, and the local statistical behavior of the axions can all be studied in isolation. Adjustments to the implemented model are to be made based on the results of these collapses and knowledge of limiting behavior of the model, Fig. 6.1. Once the model of axion-only collapse is complete more species are to be integrated. The survival of any unique structures to the introduction of baryons from axion-only simulations is crucial to its survival in more realistic contexts. If new structures are found to be present, larger and more complex simulations are needed to determine the extent of Bose effects in more realistic cosmologies.

Next is the small cosmological volume stage. Axions evolved alone from well-motivated over-densities inside a periodic box of cosmological size improve our understanding of how realistic tidal torquing, mergers and inflows function with the axions' statistical behavior. This step completes our stand-alone tests of would-be bosonic effects to the natural cosmological environment. We can have some confidence in the axion-specific structures if they survive both scattering off of isolated baryonic potentials and an impinging environment.

Zoom-in simulations provide effectively complete infall one galaxy at a time. Cosmological context introduces the full suite of environmental impacts on structure formation. Response to tidal torquing, mergers, and other input round out our grasp of Bose physics effects. This relatively inexpensive phase is also a critical stage to converge upon the proper means to track dispersion of the bosonic density matrix; the accurate tracking condensed and non-condensed axion components is crucial to calibrating the degree of impact for cross-correlation dynamics. Resolution in the physical model is bound to be a prominent topic due to the fine nature of proposed unique axion structures. The first instance of a next-generation axion spectra may also be calculated from this volume from a reasonable MW analogue.

Continuing progress towards comprehensive cosmological samples, a series of small and intermediate volume runs are then performed. Eight and 25 Mpc runs are made in the footsteps of the Romulus series and compared to their CDM counterparts. A number of other observations may be made among the fully-resolved baryons to tally the differences between CDM and Bose DM. With the larger volumes, there may be sufficient statistics

to begin comparing against observation. Cosmological power spectra, galaxy luminosities and star formation history, merger histories, scattering off DM features, and many other observables will be accessible. Further, more statistical accounts of axion spectra in MWs may be made.

How a simulation is analyzed is as important as the test itself. Identification of structural differences between DM models is paramount to the project's success in resolving the unique structure controversy. Once the profile and line-shape tools of this dissertation are exhausted, we will progress with more direct measures starting the impetus for this project: caustic rings. As a CDM halo may contain caustics of its own, the analysis must differentiate axion-specific singularities in density from a base set. A hallmark feature of the supposed caustic rings is their very finite z-profile, as opposed to the relatively spherical caustics of CDM, Fig. 6.2. This allows for projections in/out of the caustic ring space via z-slices to provide a graded means of comparison over multiple sample representations. Fine structure in the axion energy spectra of terrestrial searches, Fig. 6.3, physical rings of over-density matter along self-similar lines, Fig. 6.4, phase-space discontinuities, Fig. 6.5, and orbit classifications, Fig. 6.6, are all promising approaches to seek out differences.

If no singular structures are found to display sensitivity to Bose physics, there is a definitive if expensive means to identifying differences: a direct study of two simulations' global phase-spaces, differing only in their DM physics. Simulations that share initial particle distributions and conditions may be compared on a particle-by-particle basis, measuring the differences in the manifolds' structures, Fig. 6.7. For example the χ^2 figure

$$\Delta_{CDM,axion} = \sum_{i \in P} \sum_{j} \frac{\left(w_{CDM,i,j} - w_{axion,i,j}\right)^2}{2\sigma^2_{w_{i,j}}} \tag{6.1}$$

where P is the set of particles, $w_{i,j}$ is the j-th component of the i-th particles phase space and $\sigma_{w_{i,j}}$ is its numerical uncertainty is capable of determining the "goodness of fit" of one manifold to the other. Tests on this statistic are capable of determining if differences exist and the significance of the poor fit. If significant differences are found, those regions of phase space that contribute most are identified and studied. If no significant differences are found

then statistically the classical and Bose physics are interchangeable. Such an analysis is very involved as the $6|P|$ dimensionality of the data is taken wholesale instead of using one of an infinite number of projections. This technique not viable for the highly resolved cosmological simulations, so we hope to use it either as a test of the null condition at low resolutions or as a utility to create the structure-finding tools of the next generation of simulations.

6.4 Future ADMX Analyses

ADMX is on the verge of a great data renaissance. In the next year coverage from 500 MHz to 1000 MHz will be completed. Construction is already underway for a new cavity array to cover the 1-2 GHz bandwidth, scheduled to occur in the following two years. In total ADMX plans to reach 10 GHz by the early 2020s, Fig. 6.8.

With this extensive coverage comes much larger data sets and larger demands on the sophistication of axion search analyses. As mentioned in 5.3.2, coherent time-series of each scan are stored alongside the MR power spectra. These time series are capable of resolving spectra to the 10 mHz. Such a resolution was chosen as an optimum of signal modulation from annual and daily motions and the minimum resolution needed to resolve Pierre Sikivie's caustic rings. Adopting the analysis chain for these high resolutions is procedurally straightforward. Much of the hard work to incorporate signal modulation and an advanced background subtraction are already complete, leaving a single fast fourier transform to convert time-series data into power. Once in this form background subtraction, noise calibration, and significance calculations all progress in the same fashion.

Increased resolution allows for the analysis of more sophistication axion models. To exploit this, all elements of signal shape calculation will have to be improved from signal modulation to the local axion distribution. A side effect of these is a commensurate increase in the storage and computational resources necessary to perform such high-resolution analyses. This resolution inflation compounds with the expected increase of data taking will eventually require more advanced computer systems to keep pace.

6.5 Axion Astronomy

In the event of axion DM detection, the high-resolution ADMX data will be crucial in classifying the local DM spectra, which has yet been observed directly. A great deal of new information may be extracted about the formation history of the MW from the DM distribution. The collision-less nature of axion DM allows its local distribution to retain far more detail of the MW's formation than current gas and stellar observations. Evidence of distant merger history, tidal disruption, accretion, cold flows, caustic rings, etc. may be present in the axion spectra. ADMX's 10 mHz data is able to resolve cold flows to the level of tens of m/s, far beyond the Romulus 25 findings. Local energy resolutions $10^3 - 10^4$ times greater than today's are needed to fully exploit the time-series data, though intermediate resolutions may still reveal a great deal about our galaxy's history. To accomplish the requisite mass resolution with modern resources, simulations of MW formation would need to be both zoomed-in and have larger particle number than Romulus 25 (zoom-in would account for $4^3 = 64$ of the 1000, but mass resolution would have to make up the other $1000/64 \sim 16$), Fig. 6.9.

Conversely if axion-specific structures are shown to survive in MW-like halos prior to detection, an independent axion astronomy is born. At this stage we are likely to have a firm enough grasp of the Bose differences from CDM to be confident in deriving a more rigorous class of axion initial conditions. To do so would involve a tracking of correlations from the QCD phase transition through the radiation dominated epoch and into the linear regime of structure formation after radiation-matter transition. This step completes our description of axion dynamics, linking the fluctuations in the early universe axion field to the present structures of axion particles.

At this stage of the research, it is expected that larger cosmological volumes such as Romulus 50 will be complete and well-studied. A 50 Mpc volume would be quite powerful in surveying structures up to the cluster scale. Performing a similar simulation using axion physics would perform a similar task for the axion community. Beyond expanding the statis-

tics of MW spectra for terrestrial experiments, the simulation would provide opportunities for a whole new astronomy and potentially cosmology. Realistic renderings of axion-unique structures and their impact on baryon structure on galactic and larger scales would provide candidate-specific means of identifying DM using direct observations and/or indirect gravitational lensing techniques. Such observations allow for independent tests of axion DM, providing limits on axion attributes like particle mass and overall density. On multiple fronts the continuation of this research project promises to significantly advance axion DM science.

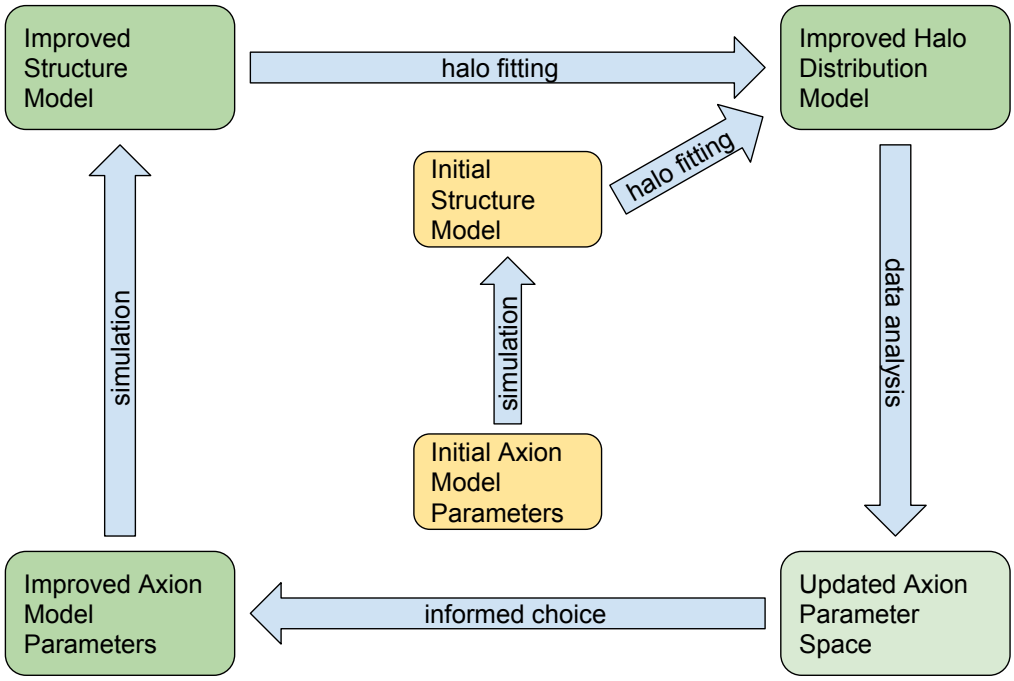

Figure 6.1: Axion search enhancement workflow diagram. The workflow begins with a reasonable guess for the relic axion model parameters, which leads to an initial structure model through structure formation simulation. A fitted axion distribution for a MW analogue halo gives ADMX an improved model against which it can compare its signal data. The results of the data analysis will be used to refine the parameter space available in which the axion can exist – or possibly confirm where the axion does exist. A feedback loop can be established once the ADMX provides an improved axion parameter space.

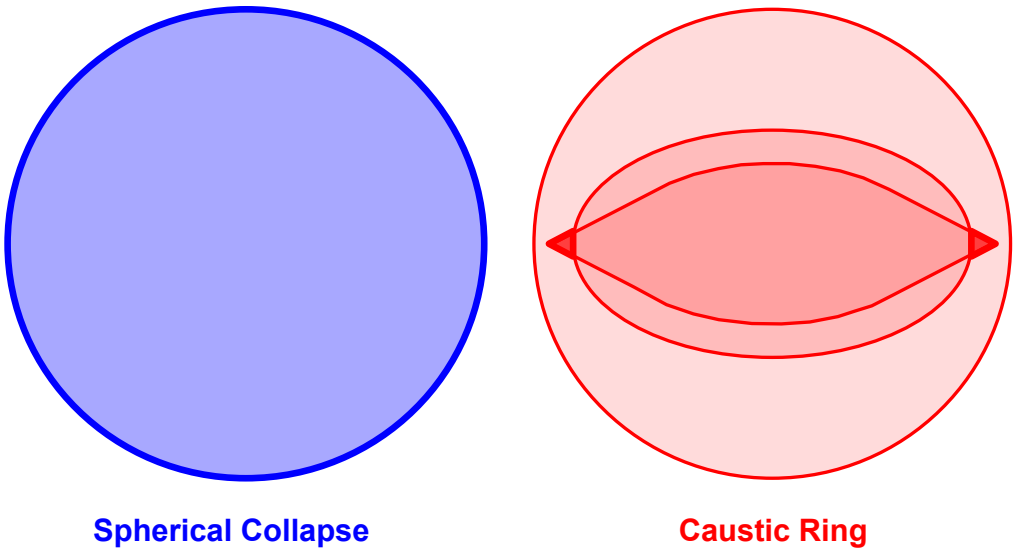

Figure 6.2: Comparison of potential caustic features to be found in simulations of CDM and Bose infall. While both types of DM physics may produce spherical caustics from ideal infall, Bose physics may produce new or altered features such as caustic rings.

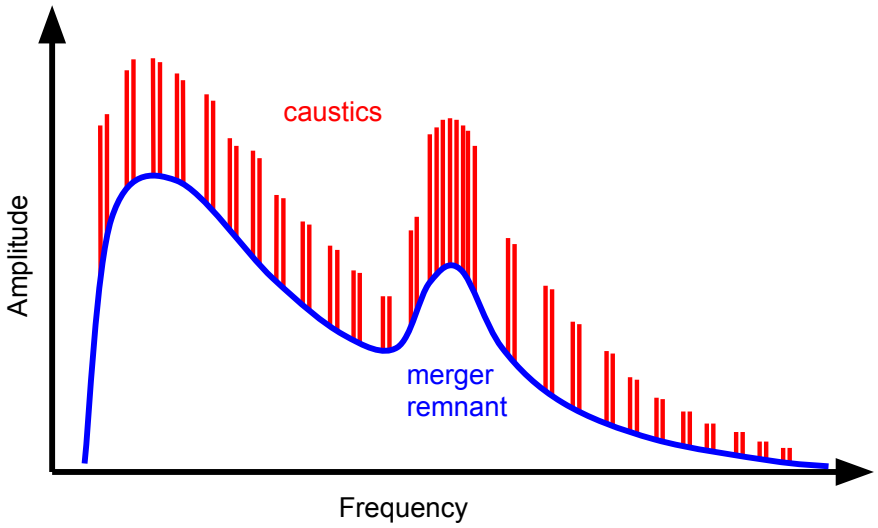

Figure 6.3: Axion energy spectra for one halo calculated using both CDM (blue) and Bose (red) physics. A number of features may be present in the halo spectrum, including historical events like mergers and dynamics footprints such such fine structure from caustics.

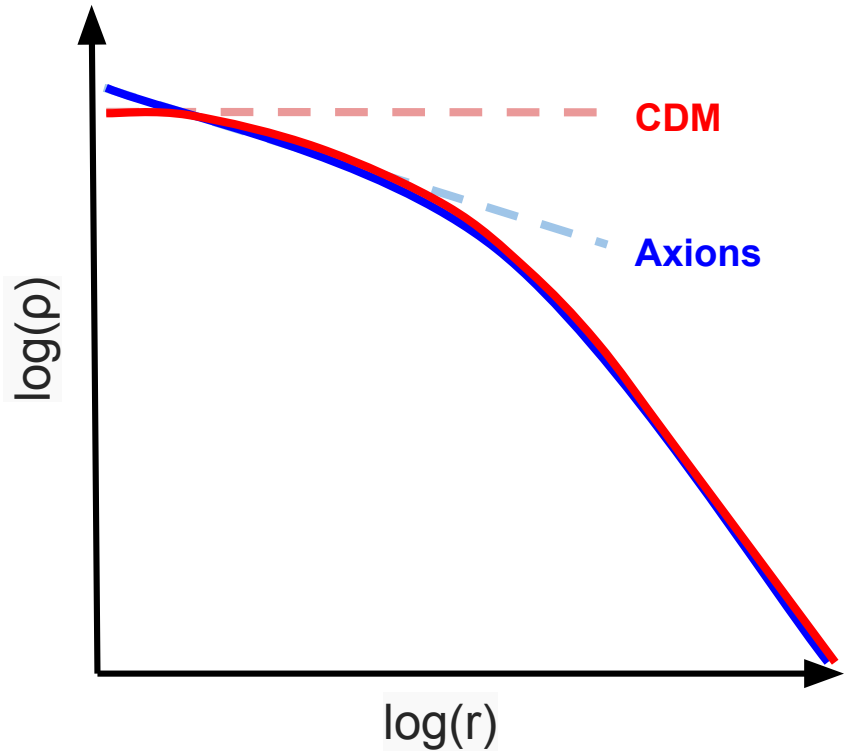

Figure 6.4: Density versus radius profiles for one halo calculated using both CDM (blue) and Bose (red) physics. Unique structures may exist here in the form of new core structure due to stricter particle-wise angular momentum conservation.

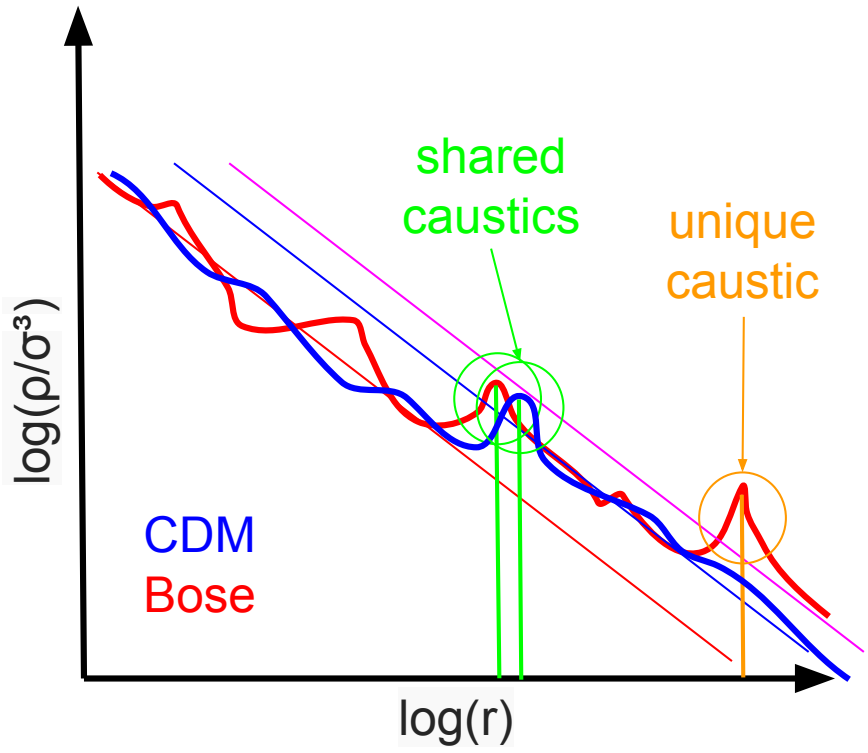

Figure 6.5: Phase-space density versus radius profiles for one halo calculated using both CDM (blue) and Bose (red) physics. Caustic events are circled, with unique events in red.

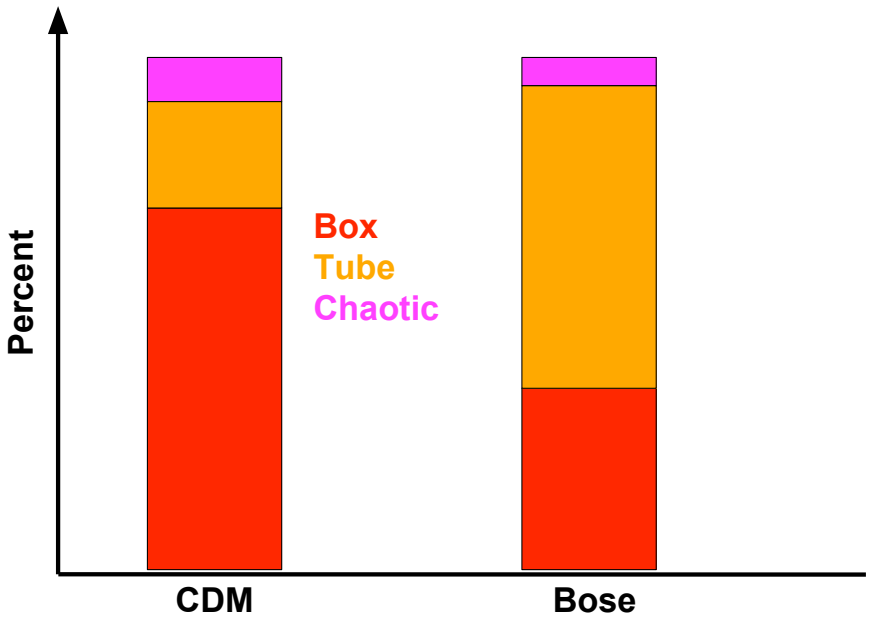

Figure 6.6: Orbit populations for one halo calculated using both CDM and Bose physics. New angular momentum physics may alter the box-dominated classical halo to something closer to tube-dominated.

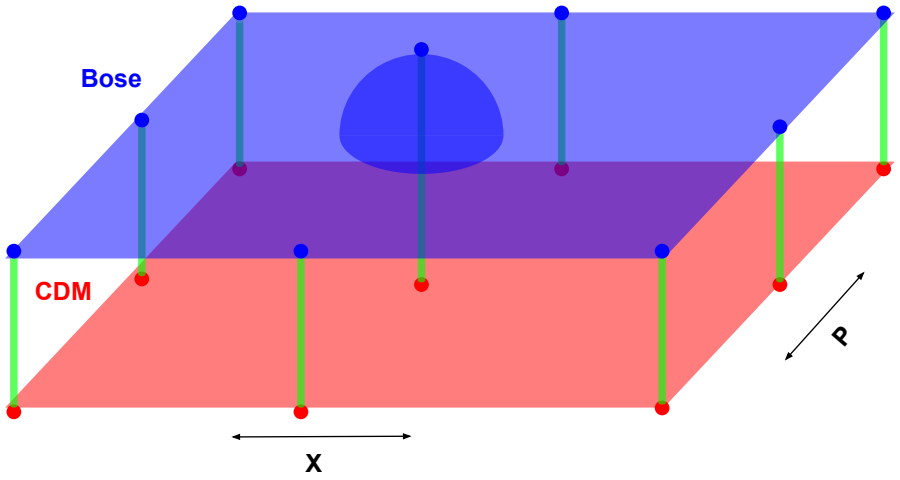

Figure 6.7: Illustration of possible phase-space manifolds created by simulations of CDM and Bose infall. A potential comprehensive analysis of these simulations is to measure point-wise differences between the two hyper-surfaces.

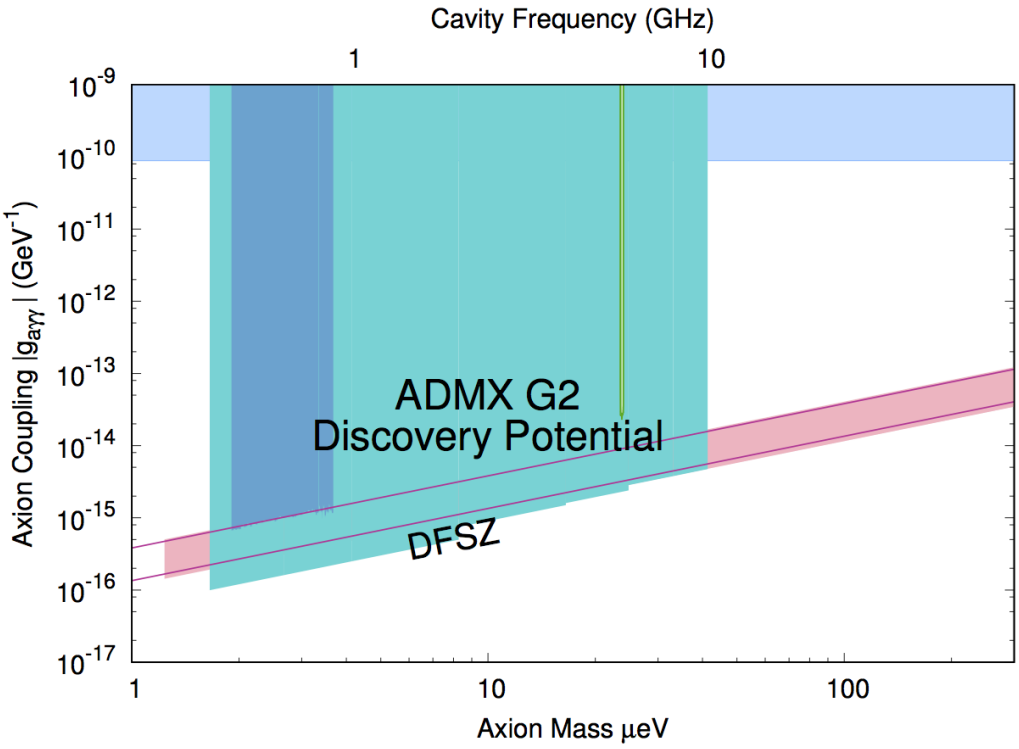

Figure 6.8: Projected sensitivity of ADMX searches through Department of Energy's Generation 2 operations plan.

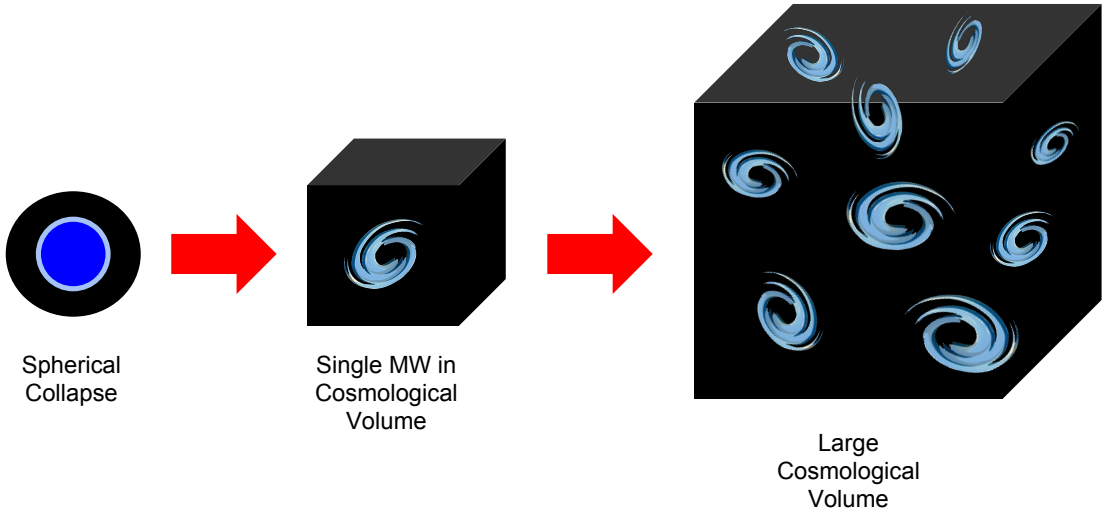

Figure 6.9: Illustration of expected simulation progression to produce realistic line-shapes capable of solving the USP and capitalizing on ADMX's high-resolution data.

Appendix A
STATISTICS OF MFT AXION MODEL

The occupation statistics of a system of identical scalar axions follow that of a Bose system, condensed or not. Here we explicitly track the statistics of the Schroedinger MFT axion model and a full Bose system.

A.1 Quantum Field Axions

Let the axions be contained in a cubic box of side length L and periodic boundary conditions (this train of thought parallels Erken et al. (2012)). Then the quantum axion field may be expanded in the plane wave orthonormal basis

$$\theta(\vec{x},t)=\sum_{\vec{n}}\sqrt{\frac{\hbar^2}{2L^3c\epsilon_{\vec{n}}}}\left(a_{\vec{n}}(t)e^{i2\pi\vec{n}\cdot\vec{x}/L}+a^{\dagger}_{\vec{n}}(t)e^{-i2\pi\vec{n}\cdot\vec{x}/L}\right) \tag{A.1}$$

where $\vec{n}$ is a vector of integers, $a^{\dagger}_{\vec{n}}$ and $a_{\vec{n}}$ are the creation and annihilation operators, and $\epsilon_{\vec{n}}$ is the energy of the state. The creation and annihilation operators satisfy the equal-time commutation relations

$$[a_{\vec{n}}(t),a^{\dagger}_{\vec{n'}(t)}]=\delta_{\vec{n},\vec{n'}}\ ,\ [a_{\vec{n}}(t),a_{\vec{n'}(t)}]=0 \tag{A.2}$$

For the case of a highly degenerate system of axions, the Schroedinger equation can be used with Hamiltonian in Eqn. 3.56, written in the plane wave expansion as

$$H=\sum_{\vec{n}}\hbar\omega_{\vec{n}}a^{\dagger}_{\vec{n}}a_{\vec{n}}+\sum_{\vec{n_1},\vec{n_2},\vec{n_3},\vec{n_4}}\Lambda^{\vec{n_3},\vec{n_4}}_{\vec{n_1},\vec{n_2}}a^{\dagger}_{\vec{n_1}}a^{\dagger}_{\vec{n_2}}a_{\vec{n_3}}a_{\vec{n_4}} \tag{A.3}$$

where $\Lambda^{\vec{n_3},\vec{n_4}}_{\vec{n_1},\vec{n_2}}$ describes the interactions between plane waves. The interaction term may be expanded into self-interaction and gravity parts

$$\Lambda^{\vec{n_3},\vec{n_4}}_{\vec{n_1},\vec{n_2}}=\Lambda_s\ {}^{\vec{n_3},\vec{n_4}}_{\vec{n_1},\vec{n_2}}+\Lambda_g\ {}^{\vec{n_3},\vec{n_4}}_{\vec{n_1},\vec{n_2}} \tag{A.4}$$

where the self-interaction term takes the form

$$\Lambda_s \begin{smallmatrix}\vec{n_3},\vec{n_4}\\ \vec{n_1},\vec{n_2}\end{smallmatrix} = \frac{\lambda\hbar^4}{4^2 m^2 c^4 L^3}\delta_{\vec{n_1}+\vec{n_2}=\vec{n_3}+\vec{n_4}} \tag{A.5}$$

and the gravity interaction may be written as

$$\Lambda_g \begin{smallmatrix}\vec{n_3},\vec{n_4}\\ \vec{n_1},\vec{n_2}\end{smallmatrix} = -\frac{\pi G m^2\hbar^2}{L^3}\delta_{\vec{n_1}+\vec{n_2}=\vec{n_3}+\vec{n_4}}\left(\frac{1}{|\vec{p}_{\vec{n_1}}-\vec{p}_{\vec{n_3}}|^2}+\frac{1}{|\vec{p}_{\vec{n_2}}-\vec{p}_{\vec{n_4}}|^2}\right) \tag{A.6}$$

where $\vec{p}_{\vec{n}} = 2\pi\vec{n}/L$.

The Hiesenberg equation of motion for the annihilation operators are derived to be

$$-i\hbar\dot{a}_{\vec{n_1}} = [H, a_{\vec{n_1}}] = -\epsilon_{\vec{n}} - 2\sum_{\vec{n_2},\vec{n_3},\vec{n_4}} \Lambda^{\vec{n_3},\vec{n_4}}_{\vec{n_1},\vec{n_2}} a^\dagger_{\vec{n_2}} a_{\vec{n_3}} a_{\vec{n_4}} \tag{A.7}$$

The creation operator's equation of motion may be derived similarly. Applying the equations of motion to the state number operators, $\mathcal{N}_{\vec{n}} = a^\dagger_{\vec{n}} a_{\vec{n}}$, the occupation values' evolution can be found to lowest non-trivial order in Λ

$$\begin{aligned}\dot{\mathcal{N}}_{\vec{n_1}} = 2\sum_{\vec{n_2},\vec{n_3},\vec{n_4}} &\left|\Lambda^{\vec{n_3},\vec{n_4}}_{\vec{n_1},\vec{n_2}}\right|^2 \left(\mathcal{N}_{\vec{n_3}}\mathcal{N}_{\vec{n_4}}\left(\mathcal{N}_{\vec{n_1}}+1\right)\left(\mathcal{N}_{\vec{n_2}}+1\right) - \mathcal{N}_{\vec{n_1}}\mathcal{N}_{\vec{n_2}}\left(\mathcal{N}_{\vec{n_3}}+1\right)\left(\mathcal{N}_{\vec{n_4}}+1\right)\right)\\ &\times\frac{2\pi}{\hbar}\delta\left(\epsilon_{\vec{n_1}}+\epsilon_{\vec{n_2}}-\epsilon_{\vec{n_3}}-\epsilon_{\vec{n_4}}\right)\end{aligned} \tag{A.8}$$

where the particle kinetic regime has been assumed, namely that the dispersion $\delta\omega$ of highly occupied states is much larger than the relaxation rate Γ, making ϵ terms sub-leading.

Once the quantum system has come into equilibrium, all $\dot{\mathcal{N}}_{\vec{n}} = 0$, its distribution must satisfy the relation

$$N_{\vec{n_3}}N_{\vec{n_4}}\left(N_{\vec{n_1}}+1\right)\left(N_{\vec{n_2}}+1\right) - N_{\vec{n_1}}N_{\vec{n_2}}\left(N_{\vec{n_3}}+1\right)\left(N_{\vec{n_4}}+1\right) \tag{A.9}$$

or

$$\left(1+\mathcal{N}^{-1}_{\vec{n_1}}\right)\left(1+\mathcal{N}^{-1}_{\vec{n_2}}\right) = \left(1+\mathcal{N}^{-1}_{\vec{n_3}}\right)\left(1+\mathcal{N}^{-1}_{\vec{n_4}}\right) \tag{A.10}$$

for every quartet of states satisfying the energy conservation relation $\epsilon_{\vec{n_i}}+\epsilon_{\vec{n_j}} = \epsilon_{\vec{n_k}}+\epsilon_{\vec{n_l}}$. The quartet relation is satisfied by

$$\epsilon_{\vec{n}} = C\ln\left(1+\mathcal{N}^{-1}_{\vec{n}}\right) \tag{A.11}$$

which is equivalent to the equilibrium Bose-Einstein distribution in this regime

$$\mathcal{N}_{\vec{n}} = \frac{1}{e^{\epsilon_{\vec{n}}/C} - 1} \tag{A.12}$$

A.2 MFT Axions

For the case of a classical field, the order parameter θ may be expanded similarly

$$\theta(\vec{x}, t) = \sum_{\vec{n}} \sqrt{\frac{\hbar^2}{2L^3 c\epsilon_{\vec{n}}}} \left(a_{\vec{n}}(t) e^{i2\pi\vec{n}\cdot\vec{x}/L} + a^{\dagger}_{\vec{n}}(t) e^{-i2\pi\vec{n}\cdot\vec{x}/L} \right) \tag{A.13}$$

Likewise, the Schroedinger equation may be solved via a similar expansion

$$\theta(\vec{x}, t) = \sum_{\vec{n}} \sqrt{\frac{\hbar}{2L^3\omega_{\vec{n}}}} \left(A_{\vec{n}}(t) e^{i2\pi\vec{n}\cdot\vec{x}/L} + A^{*}_{\vec{n}}(t) e^{-i2\pi\vec{n}\cdot\vec{x}/L} \right) \tag{A.14}$$

which may be used to rewrite the classical Hamiltonian

$$H = \sum_{\vec{n}} \hbar\omega_{\vec{n}} A^{*}_{\vec{n}} A_{\vec{n}} + \sum_{\vec{n_1},\vec{n_2},\vec{n_3},\vec{n_4}} \Lambda^{\vec{n_3},\vec{n_4}}_{\vec{n_1},\vec{n_2}} A^{*}_{\vec{n_1}} A^{*}_{\vec{n_2}} A_{\vec{n_3}} A_{\vec{n_4}} \tag{A.15}$$

The Fourier components satisfy their own equations of motion

$$-i\dot{A}_{\vec{n_1}} = -\omega_{\vec{n}} - 2 \sum_{\vec{n_2},\vec{n_3},\vec{n_4}} \Lambda^{\vec{n_3},\vec{n_4}}_{\vec{n_1},\vec{n_2}} A^{*}_{\vec{n_2}} A_{\vec{n_3}} A_{\vec{n_4}} \tag{A.16}$$

The analogous classical occupation values

$$N_{\vec{n}} A^{*}_{\vec{n}} A_{\vec{n}} \tag{A.17}$$

satisfy their own dynamics equations

$$\begin{aligned} \dot{N}_{\vec{n_1}} = 2 \sum_{\vec{n_2},\vec{n_3},\vec{n_4}} \left| \Lambda^{\vec{n_3},\vec{n_4}}_{\vec{n_1},\vec{n_2}} \right|^2 & \left(N_{\vec{n_3}} N_{\vec{n_4}} N_{\vec{n_1}} + N_{\vec{n_3}} N_{\vec{n_4}} N_{\vec{n_2}} - N_{\vec{n_3}} N_{\vec{n_1}} N_{\vec{n_2}} - N_{\vec{n_4}} N_{\vec{n_1}} N_{\vec{n_2}} \right) \\ & \times 2\pi\delta \left(\omega_{\vec{n_1}} + \omega_{\vec{n_2}} - \omega_{\vec{n_3}} - \omega_{\vec{n_4}} \right) \end{aligned} \tag{A.18}$$

After sufficient time has passed for an equilibrium to be found, $\dot{N}_{\vec{n}} = 0$, the distribution satisfies

$$N_{\vec{n_1}} N_{\vec{n_2}} \left(N_{\vec{n_3}} + N_{\vec{n_4}} \right) = N_{\vec{n_3}} N_{\vec{n_4}} \left(N_{\vec{n_1}} + N_{\vec{n_2}} \right) \tag{A.19}$$

or

$$N_{\vec{n_1}}^{-1} + N_{\vec{n_2}}^{-1} = N_{\vec{n_3}}^{-1} + N_{\vec{n_4}}^{-1} \tag{A.20}$$

for $\omega_{\vec{n_1}} + \omega_{\vec{n_2}} = \omega_{\vec{n_3}} + \omega_{\vec{n_4}}$. This distribution is solved by the standard equipartition solution

$$N_{\vec{n}}\omega_{\vec{n}} = C \tag{A.21}$$

which is distinct from the expected Bose-Einstein distribution for identical bosons, and in fact recreates the classical ultraviolet catastrophe. In review, the difference between the quantum and the classical approaches to the axions occur when the all-in-condensate expectation is made, and Schroedinger equation is converted from an operator to a c-number equation.

Appendix B

MULTI-FLUID THEORY

The approach below in many ways parallels the work of Zaremba, Nikuni, and Griffin (Zaremba et al., 1999).

B.1 Component Separation

Take as a starting point the Heisenberg equation of motion for the quantum field operator under the influence of self-gravity and a contact interaction

$$i\hbar\partial_t\hat{\psi}(\vec{x},t) = [\hat{\psi}(\vec{x},t),\hat{H}] = -\frac{\hbar^2\vec{\nabla}^2}{2m}\hat{\psi}(\vec{x},t) + m\Phi(\vec{x})\hat{\psi}(\vec{x},t) + g\hat{\psi}^\dagger(\vec{x},t)\hat{\psi}(\vec{x},t)\hat{\psi}(\vec{x},t) \quad \text{(B.1)}$$

where the strength of the contact term can be related to the spherical scattering length a by $g = 4\pi a\hbar^2/m$. To reduce the degrees of freedom to be solved for from N, the number of identical bosons, to something more manageable, consider the expectation value of the quantum field with respect to a broken (Bose) symmetry non-equilibrium ensemble

$$\theta(\vec{x},t) = \left\langle\hat{\psi}\right\rangle = \frac{1}{N!}\left\langle 0\right|(\hat{a})^N\hat{\psi}(\hat{a}^\dagger)^N\left|0\right\rangle \quad \text{(B.2)}$$

and the remainder operator

$$\hat{\tilde{\psi}} = \hat{\psi} - \theta\hat{I} \quad \text{(B.3)}$$

where $\hat{I}$ is the identity operator over the broken symmetry ensemble. From this point on, the expectation value and remainder will be refereed to as the condensate and non-condensate respectively. The expectation value of Eqn. B.1 provides the first of two motive equations

for the divided system

$$i\hbar\partial_t\theta(\vec{x},t) = -\frac{\hbar^2\vec{\nabla}^2}{2m}\theta(\vec{x},t) + m\Phi(\vec{x})\theta(\vec{x},t) \tag{B.4}$$

$$+ gn_c(\vec{x},t)\theta(\vec{x},t) + 2g\tilde{n}(\vec{x},t)\theta(\vec{x},t) + g\tilde{m}(\vec{x},t)\theta^*(\vec{x},t) + g\left\langle\hat{\tilde{\psi}}^\dagger(\vec{x},t)\hat{\tilde{\psi}}(\vec{x},t)\hat{\tilde{\psi}}(\vec{x},t)\right\rangle \tag{B.5}$$

where $n_c = |\Phi|^2$ is the non-equilibrium condensate density, $\tilde{n} = \left\langle\hat{\tilde{\psi}}^\dagger\hat{\tilde{\psi}}\right\rangle$ is the non-condensate density, $\tilde{n} = \left\langle\hat{\tilde{\psi}}\hat{\tilde{\psi}}\right\rangle$ is the off-diagonal non-condensate density, and $\tilde{n} = \left\langle\hat{\tilde{\psi}}^\dagger\hat{\tilde{\psi}}\right\rangle$ is a three field correlation function. Note that all expectation values thus far are with respect to the non-equilibrium ensemble and are capable of having non-zero expectations due to the Bose broken symmetry. The effective Hamiltonian for the condensate is given by

$$\hat{H}_c = \hat{H}_{c,0} + \hat{H}'_c \tag{B.6}$$

$$\hat{H}'_c = \hat{H}'_{c,1} + \hat{H}'_{c,2} + \hat{H}'_{c,3} + \hat{H}'_{c,4} + \hat{H}'_{c,5} \tag{B.7}$$

where

$$\hat{H}_{c,0} = -\int d^3x\theta^*\frac{\hbar^2\vec{\nabla}^2}{2m}\theta \tag{B.8}$$

$$\hat{H}'_{c,1} = \int d^3x\theta^* m\Phi(\vec{x})\theta \tag{B.9}$$

$$\hat{H}'_{c,2} = \int d^3x\theta^* gn_c(\vec{x},t)\theta \tag{B.10}$$

$$\hat{H}'_{c,3} = \int d^3x\theta^* 2g\tilde{n}(\vec{x},t)\theta \tag{B.11}$$

$$\hat{H}'_{c,4} = \frac{1}{2}\int d^3x\left(\theta^* g\tilde{m}(\vec{x},t)\theta^* + \{h.c.\}\right) \tag{B.12}$$

$$\hat{H}'_{c,5} = \frac{1}{2}\int d^3x\left(\theta^* g\left\langle\hat{\tilde{\psi}}^\dagger\hat{\tilde{\psi}}\hat{\tilde{\psi}}\right\rangle + \{h.c.\}\right) \tag{B.13}$$

The difference between Eqn. B.1 and Eqn. B.5 provide the second equation of motion

$$i\hbar\partial_t\hat{\tilde{\psi}} = -\frac{\hbar^2\vec{\nabla}^2}{2m}\hat{\tilde{\psi}} + m\Phi\hat{\tilde{\psi}} + 2gn_c\hat{\tilde{\psi}} + \theta^2\hat{\tilde{\psi}}^\dagger$$
$$+ g\theta^*\left(\hat{\tilde{\psi}}\hat{\tilde{\psi}} - \tilde{m}\right) 2g\theta\left(\hat{\tilde{\psi}}^\dagger\hat{\tilde{\psi}} - n\right) + g\left(\hat{\tilde{\psi}}^\dagger\hat{\tilde{\psi}}\hat{\tilde{\psi}} - \left\langle\hat{\tilde{\psi}}^\dagger\hat{\tilde{\psi}}\hat{\tilde{\psi}}\right\rangle\right) \tag{B.14}$$

The effective Hamiltonian for the system can be written as

$$\hat{H} = \hat{H}_0 + \hat{H}' \tag{B.15}$$

$$\hat{H}' = \hat{H}'_1 + \hat{H}'_2 + \hat{H}'_3 + \hat{H}'_4 + \hat{H}'_5 \tag{B.16}$$

where

$$\hat{H}_0 = -\int d^3x \hat{\tilde{\psi}}^\dagger \frac{\hbar^2 \vec{\nabla}^2}{2m} \hat{\tilde{\psi}} \tag{B.17}$$

$$\hat{H}'_1 = \int d^3x \hat{\tilde{\psi}}^\dagger \left(m\Phi(\vec{x}) + 2gn\right) \hat{\tilde{\psi}} \tag{B.18}$$

$$\hat{H}'_2 = \int d^3x \left(L_1 \hat{\tilde{\psi}}^\dagger + \{h.c.\}\right) \tag{B.19}$$

$$\hat{H}'_3 = \frac{1}{2}\int d^3x g \left(\theta^2 \hat{\tilde{\psi}}^\dagger \hat{\tilde{\psi}}^\dagger + \{h.c.\}\right) \tag{B.20}$$

$$\hat{H}'_4 = \frac{1}{2}\int d^3x g \left(\theta^* \hat{\tilde{\psi}}^\dagger \hat{\tilde{\psi}} \hat{\tilde{\psi}} + \{h.c.\}\right) \tag{B.21}$$

$$\hat{H}'_5 = \frac{1}{2}\int d^3x g \hat{\tilde{\psi}}^\dagger \hat{\tilde{\psi}}^\dagger \hat{\tilde{\psi}} \hat{\tilde{\psi}} - 2g \int d^3x \tilde{n} \hat{\tilde{\psi}}^\dagger \hat{\tilde{\psi}} \tag{B.22}$$

$$L_1 = -g\left(2\tilde{n}\theta + \tilde{m}\theta^* + \left\langle \hat{\tilde{\psi}}^\dagger \hat{\tilde{\psi}} \hat{\tilde{\psi}} \right\rangle\right) \tag{B.23}$$

This coupled system of PDEs can now be used to effectively evolve of the Bose system.

So maybe not, but with some more massaging this system can be placed in a form suitable for ChaNGa: a collection of Boltzmann equations capable of handling the expected dispersive configurations. This will be done in a similar manner to the MFT case, but with very different results.

B.2 Boltzmann Equations

B.2.1 Non-condensate BE

This approach avoids assumptions of axions remaining in a single coherent state in order to satisfy those who believe that the paradigm of an axion condensate is a red herring, while still allowing for the formation of one. Therefore, we utilize a density matrix description

$$\hat{\rho} = \sum_J |C\rangle_J \, p_J \, \langle C|_J \tag{B.24}$$

where $\{|C\rangle_J\}$ is an orthonormal basis of the many body space and $\{p_J\}$ are the corresponding probabilities that the system exists in a given state. The expectation value of an operator in the presence of a mixed state is given by

$$\left\langle \hat{O} \right\rangle = \mathrm{Tr}\left(\hat{\rho}\hat{O}\right) \tag{B.25}$$

An equation of motion for the operator is given in the Heisenberg form

$$i\hbar\partial_t\hat{\rho} = [\hat{H}, \hat{\rho}] \tag{B.26}$$

though its evaluation is ambiguous without knowledge of each state's evolution.

If we are only interested in a subset of the possible states ($\{|D\rangle\}_K \subset \{|C\rangle\}_J$), the density matrix equations shift to an effective form. The operator expectation value equation applies only to operators restricted to the subspace of interest

$$\left\langle \hat{O}' \right\rangle = \mathrm{Tr}\left(\hat{\rho}'\hat{O}'\right) \tag{B.27}$$

The equation of motion for the restricted density matrix also shifts

$$i\hbar\partial_t\hat{\rho}' = [\hat{H}_{eff}, \hat{\rho}'] \tag{B.28}$$

where $\hat{H}_{eff}$ is the effective Hamiltonian of the subset, which drives its evolution. This effective density matrix formalism will be used to help derive Boltzmann equations for both the condensate and the non-condensate.

To derive a quantum kinetic equation for the non-condensate component, we introduce the non-condensate Wigner operator

$$\hat{f}(\vec{x}, \vec{p}) = \int d^3x' e^{i\vec{p}\cdot\vec{x}'} \hat{\tilde{\psi}}^\dagger(\vec{x} + \vec{x}'/2)\hat{\tilde{\psi}}(\vec{x} - \vec{x}'/2), \tag{B.29}$$

The effective distribution function is found to be

$$f = \mathrm{Tr}\hat{\tilde{\rho}}\hat{f} \tag{B.30}$$

Using the non-condensate density's equation of motion, the distribution equation of motion is found to be

$$\begin{aligned}\partial_t f &= \frac{1}{i\hbar}\mathrm{Tr}\left(\hat{\tilde{\rho}}[\hat{f},\hat{H}_{eff}]\right)\\ &= \frac{1}{i\hbar}\mathrm{Tr}\left(\hat{\tilde{\rho}}[\hat{f},\hat{H}_0]\right)+\frac{1}{i\hbar}\mathrm{Tr}\left(\hat{\tilde{\rho}}[\hat{f},\hat{H}']\right)\end{aligned} \tag{B.31}$$

Utilizing the equal-time commutation relations, the first commutator gives the free streaming term in the kinetic equation

$$\frac{1}{i\hbar}\mathrm{Tr}\left(\hat{\tilde{\rho}}[\hat{f},\hat{H}_0]\right)=\frac{1}{i\hbar}\mathrm{Tr}\left(\hat{\tilde{\rho}}[\hat{f},-\frac{\hbar^2}{2m}\int d^3x''\hat{\tilde{\psi}}^\dagger(\vec{x}'',t)\vec{\nabla}^2_{\vec{x}''}\hat{\tilde{\psi}}(\vec{x}'',t)]\right) \tag{B.32}$$

$$=\frac{-1}{i\hbar}\mathrm{Tr}\left(\hat{\tilde{\rho}}\frac{\hbar^2}{2m}\int d^3x''d^3x'e^{i\vec{p}\cdot\vec{x}'/\hbar}[\hat{\tilde{\psi}}^\dagger(\vec{x}+\vec{x}'/2,t)\hat{\tilde{\psi}}(\vec{x}-\vec{x}'/2,t),\hat{\tilde{\psi}}^\dagger(\vec{x}'',t)\vec{\nabla}^2_{\vec{x}''}\hat{\tilde{\psi}}(\vec{x}'',t)]\right) \tag{B.33}$$

$$=\frac{-1}{i\hbar}\mathrm{Tr}\hat{\tilde{\rho}}\frac{\hbar^2}{2m}\int d^3x''d^3x'e^{i\vec{p}\cdot\vec{x}'/\hbar}\times$$

$$\left(\delta_{(\vec{x}''-\vec{x}+\vec{x}'/2)}\hat{\tilde{\psi}}^\dagger(\vec{x}+\vec{x}'/2,t)\vec{\nabla}^2_{\vec{x}''}\hat{\tilde{\psi}}(\vec{x}'',t)-\delta_{(\vec{x}''-\vec{x}-\vec{x}'/2)}\hat{\tilde{\psi}}^\dagger(\vec{x}'',t)\vec{\nabla}^2_{\vec{x}''}\hat{\tilde{\psi}}(\vec{x}-\vec{x}'/2,t)\right) \tag{B.34}$$

$$=\frac{-1}{i\hbar}\mathrm{Tr}\hat{\tilde{\rho}}\frac{\hbar^2}{2m}\int d^3x'e^{i\vec{p}\cdot\vec{x}'/\hbar}\times$$

$$\left(\hat{\tilde{\psi}}^\dagger(\vec{x}+\vec{x}'/2,t)\vec{\nabla}^2_{(\vec{x}-\vec{x}'/2)}\hat{\tilde{\psi}}(\vec{x}-\vec{x}'/2,t)-\hat{\tilde{\psi}}^\dagger(\vec{x}+\vec{x}'/2,t)\vec{\nabla}^2_{(\vec{x}+\vec{x}'/2)}\hat{\tilde{\psi}}(\vec{x}-\vec{x}'/2,t)\right) \tag{B.35}$$

$$=\frac{\vec{p}}{m}\cdot\vec{\nabla}_{\vec{x}}f(\vec{x},\vec{p},t)+i\frac{2\hbar}{m}\vec{p}^2 f \tag{B.36}$$

where in the last step, we used integration-by-parts multiple times and canceled boundary terms based on periodic boundary condition considerations. The existence of the imaginary term is unusual, and will be addressed once the all commutators have been addressed. The second commutator is interpreted as a collection of interactions

$$\frac{1}{i\hbar}\mathrm{Tr}\left(\hat{\tilde{\rho}}[\hat{f},\hat{H}']\right)=\Gamma'(\vec{x},\vec{p},t) \tag{B.37}$$

The result produces something closer to the standard Boltzmann form

$$\partial_t f+\frac{\vec{p}}{m}\cdot\vec{\nabla}f+i\frac{2\hbar}{m}\vec{p}^2 f=\Gamma'(\vec{x},\vec{p},t) \tag{B.38}$$

Looking at the interaction terms more closely, it is clear that the most of them are of contact type and cannot be interpreted as 'slowly varying' or otherwise suited for transport. The gravitational term stands out as the force is mediated by a scale-invariant field, the gravitational potential. The gravitational contribution to the Boltzmann equation is of the form

$$\Gamma'_g(\vec{x},\vec{p},t) = \frac{1}{i\hbar}\mathrm{Tr}\left(\hat{\rho}\left[\hat{f}, \int d^3x \hat{\tilde{\psi}}^\dagger \left(m\Phi(\vec{x})\right)\hat{\tilde{\psi}}\right]\right) \tag{B.39}$$

Evaluating the commutator and condensing the result gives

$$\Gamma'_g(\vec{x},\vec{p},t) = \frac{-1}{i\hbar}\mathrm{Tr}\hat{\tilde{\rho}}\int d^3x'' d^3x' e^{i\vec{p}\cdot\vec{x'}/\hbar}[\hat{\tilde{\psi}}^\dagger(\vec{x}+\vec{x}'/2,t)\hat{\tilde{\psi}}(\vec{x}-\vec{x}'/2,t), \hat{\tilde{\psi}}^\dagger(\vec{x}'',t)m\Phi(\vec{x}'')\hat{\tilde{\psi}}(\vec{x}'',t)] \tag{B.40}$$

$$= \frac{-m}{i\hbar}\mathrm{Tr}\hat{\tilde{\rho}}\int d^3x'' d^3x' e^{i\vec{p}\cdot\vec{x'}/\hbar}\times$$
$$\left(\delta_{(\vec{x}''-\vec{x}+\vec{x}'/2)}\hat{\tilde{\psi}}^\dagger(\vec{x}+\vec{x}'/2,t)\Phi(\vec{x}'')\hat{\tilde{\psi}}(\vec{x}'',t) - \delta_{(\vec{x}''-\vec{x}-\vec{x}'/2)}\hat{\tilde{\psi}}^\dagger(\vec{x}'',t)\Phi(\vec{x}'')\hat{\tilde{\psi}}(\vec{x}-\vec{x}'/2,t)\right) \tag{B.41}$$

$$= \frac{-m}{i\hbar}\mathrm{Tr}\hat{\tilde{\rho}}\int d^3x' e^{i\vec{p}\cdot\vec{x'}/\hbar}\times$$
$$\left(\hat{\tilde{\psi}}^\dagger(\vec{x}+\vec{x}'/2,t)\Phi(\vec{x}-\vec{x}'/2)\hat{\tilde{\psi}}(\vec{x}-\vec{x}'/2,t) - \hat{\tilde{\psi}}^\dagger(\vec{x}+\vec{x}'/2,t)\Phi(\vec{x}+\vec{x}'/2)\hat{\tilde{\psi}}(\vec{x}-\vec{x}'/2,t)\right) \tag{B.42}$$

The potentials expanded in first order Taylor series about $\vec{x}$ produce a force term plus a higher order contribution

$$\Phi(\vec{x}-\vec{x}'/2)-\Phi(\vec{x}+\vec{x}'/2) = -\vec{x}'\cdot\vec{\nabla}_{\vec{x}}\Phi(\vec{x})+\frac{|\beta|}{\beta!}\int_0^1 dl(1-l)\left(x/2\right)^\beta \partial_\beta\left(\Phi(\vec{x}-l\vec{x}'/2)-\Phi(\vec{x}+l\vec{x}'/2)\right) \tag{B.43}$$

where β is a multi-index of order 2. Γ'_g may be split into two contributions

$$\Gamma'_g(\vec{x},\vec{p},t) = \frac{1}{i\hbar}\mathrm{Tr}\hat{\tilde{\rho}}\int d^3x' e^{i\vec{p}\cdot\vec{x'}/\hbar}\hat{\tilde{\psi}}^\dagger(\vec{x}+\vec{x}'/2,t)m\left(\Phi(\vec{x}-\vec{x}'/2)-\Phi(\vec{x}+\vec{x}'/2)\right)\hat{\tilde{\psi}}(\vec{x}-\vec{x}'/2,t) \tag{B.44}$$

$$\begin{aligned}&= \frac{-m}{i\hbar}\mathrm{Tr}\hat{\tilde{\rho}}\int d^3x' e^{i\vec{p}\cdot\vec{x'}/\hbar}\times \\ &\hat{\tilde{\psi}}^\dagger(\vec{x}+\vec{x}'/2,t)\left(\vec{x}'\cdot\vec{\nabla}_{\vec{x}}\Phi(\vec{x}) - \int_0^1 dl(1-l)\left(\frac{x}{2}\right)^\beta \partial_\beta\left(\Phi(\vec{x}-l\vec{x}'/2)-\Phi(\vec{x}+l\vec{x}'/2)\right)\right)\hat{\tilde{\psi}}(\vec{x}-\vec{x}'/2,t)\end{aligned} \tag{B.45}$$

$$\begin{aligned}&= -\frac{1}{i\hbar}\mathrm{Tr}\left(\hat{\tilde{\rho}}\int d^3x' m\vec{\nabla}_{\vec{x}}\Phi(\vec{x})\cdot\vec{x}' e^{i\vec{p}\cdot\vec{x'}/\hbar}\hat{\tilde{\psi}}^\dagger(\vec{x}+\vec{x}'/2,t)\hat{\tilde{\psi}}(\vec{x}-\vec{x}'/2,t)\right) \\ &+ \frac{-1}{i\hbar}\mathrm{Tr}\hat{\tilde{\rho}}\int d^3x' e^{i\vec{p}\cdot\vec{x'}/\hbar}\times \\ &\hat{\tilde{\psi}}^\dagger(\vec{x}+\vec{x}'/2,t)m\left(\frac{|\beta|}{\beta!}\int_0^1 dl(1-l)\,(x/2)^\beta\,\partial_\beta\left(\Phi(\vec{x}-l\vec{x}'/2)-\Phi(\vec{x}+l\vec{x}'/2)\right)\right)\hat{\tilde{\psi}}(\vec{x}-\vec{x}'/2,t)\end{aligned} \tag{B.46}$$

$$\begin{aligned}&= -m\vec{\nabla}_{\vec{x}}\Phi(\vec{x})\vec{\nabla}_{\vec{p}}f(\vec{x},\vec{p},t) \\ &+ \frac{-1}{i\hbar}\mathrm{Tr}\hat{\tilde{\rho}}\int d^3x' e^{i\vec{p}\cdot\vec{x'}/\hbar}\times \\ &\hat{\tilde{\psi}}^\dagger(\vec{x}+\vec{x}'/2,t)m\left(\frac{|\beta|}{\beta!}\int_0^1 dl(1-l)\,(x/2)^\beta\,\partial_\beta\left(\Phi(\vec{x}-l\vec{x}'/2)-\Phi(\vec{x}+l\vec{x}'/2)\right)\right)\hat{\tilde{\psi}}(\vec{x}-\vec{x}'/2,t)\end{aligned} \tag{B.47}$$

The first of these terms may be interpreted as long distance (transport) interaction

$$\Gamma'_{g,tr}(\vec{x},\vec{p},t) = -m\vec{\nabla}_{\vec{x}}\Phi(\vec{x})\vec{\nabla}_{\vec{p}}f(\vec{x},\vec{p},t) \tag{B.48}$$

Before interpreting the second term, the remainder should be expanded to reveal the next

term

$$\begin{aligned}\Gamma'_{g,mx}(\vec{x},\vec{p},t) &= \frac{-m}{i\hbar}\mathrm{Tr}\hat{\tilde{\rho}}\int d^3x' e^{i\vec{p}\cdot\vec{x'}/\hbar}\times \\ &\hat{\tilde{\psi}}^\dagger(\vec{x}+\vec{x}'/2,t)\left(\int_0^1 dl(1-l)\,(x/2)^\beta\,\partial_\beta\left(\Phi(\vec{x}-l\vec{x}'/2)-\Phi(\vec{x}+l\vec{x}'/2)\right)\right)\hat{\tilde{\psi}}(\vec{x}-\vec{x}'/2,t) \\ &= \frac{-m}{i2\hbar}\mathrm{Tr}\left(\hat{\tilde{\rho}}\int d^3x' e^{i\vec{p}\cdot\vec{x'}/\hbar}\hat{\tilde{\psi}}^\dagger(\vec{x}+\vec{x}'/2,t)\hat{\tilde{\psi}}(\vec{x}-\vec{x}'/2,t)\vec{x}'\cdot\vec{\nabla}\left(\vec{x}'\cdot\vec{\nabla}\Phi(\vec{x})\right)\right)+O\left((\partial)^3\Phi\right) \\ &= \frac{-im\hbar}{2}\partial_\beta\Phi\partial^\beta_{(p)}f+O\left((\partial)^3\Phi\right) \end{aligned} \tag{B.49}$$

where again summation over the rank 2 multi-index β is implied. Ignoring the third order and higher potential contributions, the Boltzmann equation can be consolidated again

$$\partial_t f+\frac{\vec{p}}{m}\cdot\vec{\nabla}f-\vec{\nabla}\Phi\cdot\vec{\nabla}_{\vec{v}}f+i\left(\frac{2\hbar}{m}\vec{p}^2 f-\frac{m\hbar}{2}\partial_\beta\Phi\partial^\beta_{(p)}f\right)=\frac{1}{i\hbar}\mathrm{Tr}\left(\hat{\rho}[\hat{f},\left(\hat{H}'_1\right)_{rm}+\hat{H}'_2+\hat{H}'_3+\hat{H}'_4+\hat{H}'_5]\right) \tag{B.50}$$

where

$$\left(\hat{H}'_1\right)_{rm}=\int d^3x\hat{\tilde{\psi}}^\dagger 2gn\hat{\tilde{\psi}} \tag{B.51}$$

which looks very similar to the classical Boltzmann equation, save for the imaginary terms. The right hand side of this equation represents the effect of close-range collisions between axions.

B.2.2 Condensate BE

The condensed component follows similarly. Defining an independent Wigner form

$$f_c(\vec{x},\vec{p})=\int d^3x' e^{i\vec{p}\cdot\vec{x}'/\hbar}\theta^*(\vec{x}+\vec{x}'/2)\theta(\vec{x}-\vec{x}'/2), \tag{B.52}$$

the equation of motion for the distribution is found by straightforward differentiation

$$\partial_t f_c(\vec{x},\vec{p})=\frac{1}{i\hbar}\int d^3x' e^{i\vec{p}\cdot\vec{x}'/\hbar}\left(\partial_t\theta^*(\vec{x}+\vec{x}'/2)\theta(\vec{x}-\vec{x}'/2)+\theta^*(\vec{x}+\vec{x}'/2)\partial_t\theta(\vec{x}-\vec{x}'/2)\right) \tag{B.53}$$

Again, a streaming term can be found from the kinetic contributions to the equation of motion

$$\frac{1}{i\hbar}\int d^3x' e^{i\vec{p}\cdot\vec{x}'/\hbar}\left(\frac{h^2}{2m}\vec{\nabla}^2_{\vec{x}+\vec{x}'/2}\theta^*(\vec{x}+\vec{x}'/2,t)\theta(\vec{x}-\vec{x}'/2,t)-\theta^*(\vec{x}+\vec{x}'/2,t)\frac{h^2}{2m}\vec{\nabla}^2_{\vec{x}-\vec{x}'/2}\theta(\vec{x}-\vec{x}'/2,t)\right) \tag{B.54}$$

$$=\vec{p}m\cdot\vec{\nabla}_{\vec{x}}f_c(\vec{x},\vec{p},t)+i\frac{2\hbar}{m}\vec{p}^2 f_c(\vec{x},\vec{p},t) \tag{B.55}$$

The gravitational term also reduces to a transport, imaginary, and higher order terms

$$\frac{1}{i\hbar}\int d^3x' e^{i\vec{p}\cdot\vec{x}'/\hbar}\left(m\Phi(\vec{x}+\vec{x}'/2)\theta^*(\vec{x}+\vec{x}'/2)\theta(\vec{x}-\vec{x}'/2)-\theta^*(\vec{x}+\vec{x}'/2)m\Phi(\vec{x}-\vec{x}'/2)\theta(\vec{x}-\vec{x}'/2)\right) \tag{B.56}$$

$$\begin{aligned}&=-\vec{\nabla}_{\vec{x}}m\Phi(\vec{x})\cdot\vec{\nabla}_{\vec{p}}f_c(\vec{x},\vec{p})\\&-\frac{m}{i\hbar}\int d^3x' e^{i\vec{p}\cdot\vec{x}'/\hbar}\theta^*(\vec{x}+\vec{x}'/2,t)\left(\int_0^1 dl(1-l)\left(x/2\right)^\beta\partial_\beta\left(\Phi(\vec{x}-l\vec{x}'/2)-\Phi(\vec{x}+l\vec{x}'/2)\right)\right)\theta(\vec{x}-\vec{x}'/2,t)\end{aligned} \tag{B.57}$$

$$=-\vec{\nabla}_{\vec{x}}\Phi(\vec{x})\cdot\vec{\nabla}_{\vec{p}}f_c(\vec{x},\vec{p})+\frac{-im\hbar}{2}\partial_\beta\Phi\partial^\beta_{(p)}f+O\left((\partial)^3\Phi\right) \tag{B.58}$$

The remaining interaction terms may be condensed into a form similar to the non-condensate, bringing the condensate equation of motion into a pseudo-Boltzmann form

$$\begin{aligned}&\partial_t f_c+\frac{\vec{p}}{m}\cdot\vec{\nabla}f_c-\vec{\nabla}m\Phi\cdot\vec{\nabla}_{\vec{p}}f_c+i\left(\frac{2\hbar}{m}\vec{p}^2 f_c-\frac{m\hbar}{2}\partial_\beta\Phi\partial^\beta_{(p)}f_c\right)\\&=-\frac{1}{i\hbar}\int d^3x' e^{i\vec{p}\cdot\vec{x}'/\hbar}\left(gn_c(\vec{x}+\vec{x}'/2,t)\theta(\vec{x}+\vec{x}'/2,t)+2g\tilde{n}(\vec{x}+\vec{x}'/2,t)\theta(\vec{x}+\vec{x}'/2,t)\right)\\&-\frac{1}{i\hbar}\int d^3x' e^{i\vec{p}\cdot\vec{x}'/\hbar}g\tilde{m}(\vec{x}+\vec{x}'/2,t)\theta^*(\vec{x}+\vec{x}'/2,t)\\&-\frac{1}{i\hbar}\int d^3x' e^{i\vec{p}\cdot\vec{x}'/\hbar}g\left\langle\hat{\tilde{\psi}}^\dagger(\vec{x}+\vec{x}'/2,t)\hat{\tilde{\psi}}(\vec{x}+\vec{x}'/2,t)\hat{\tilde{\psi}}(\vec{x}+\vec{x}'/2,t)\right\rangle\theta(\vec{x}-\vec{x}'/2,t)\\&-\frac{1}{i\hbar}\int d^3x' e^{i\vec{p}\cdot\vec{x}'/\hbar}\theta^*(\vec{x}+\vec{x}'/2,t)\left(gn_c(\vec{x}-\vec{x}'/2,t)\theta(\vec{x}-\vec{x}'/2,t)+2g\tilde{n}(\vec{x}-\vec{x}'/2,t)\theta(\vec{x}-\vec{x}'/2,t)\right)\\&-\frac{1}{i\hbar}\int d^3x' e^{i\vec{p}\cdot\vec{x}'/\hbar}g\tilde{m}(\vec{x}-\vec{x}'/2,t)\theta^*(\vec{x}-\vec{x}'/2,t)\\&-\frac{1}{i\hbar}\int d^3x' e^{i\vec{p}\cdot\vec{x}'/\hbar}\left(g\left\langle\hat{\tilde{\psi}}^\dagger(\vec{x}-\vec{x}'/2,t)\hat{\tilde{\psi}}(\vec{x}-\vec{x}'/2,t)\hat{\tilde{\psi}}(\vec{x}-\vec{x}'/2,t)\right\rangle\right)\end{aligned} \tag{B.59}$$

The equation's special form and the interaction terms require interpretation before implementation.

B.3 Simplifying Interactions

Starting with gravity-only ($g = 0$), the system of Boltzmann equations reduce to

$$\partial_t f_c + \frac{\vec{p}}{m} \cdot \vec{\nabla} f_c - \vec{\nabla}\bar{\Phi} \cdot \vec{\nabla}_{\vec{v}} f_c + i \left(\frac{2\hbar}{m} \vec{p}^2 f_c - \frac{m\hbar}{2} \partial_\beta \Phi \partial^\beta_{(p)} f_c \right) = 0 \tag{B.60}$$

$$\partial_t f + \frac{\vec{p}}{m} \cdot \vec{\nabla} f - \vec{\nabla}\bar{\Phi} \cdot \vec{\nabla}_{\vec{v}} f + i \left(\frac{2\hbar}{m} \vec{p}^2 f - \frac{m\hbar}{2} \partial_\beta \Phi \partial^\beta_{(p)} f \right) = 0 \tag{B.61}$$

The real-ness of each of the distribution functions, and their derivatives, leads to a decoupling between the real and imaginary factors in each equation. The effective system of equations becomes

$$\partial_t f_c + \frac{\vec{p}}{m} \cdot \vec{\nabla} f_c - \vec{\nabla}\bar{\Phi} \cdot \vec{\nabla}_{\vec{v}} f_c = 0 \tag{B.62}$$

$$\frac{2\hbar}{m} \vec{p}^2 f_c - \frac{\hbar}{2} \partial_\beta \Phi \partial^\beta_{(p)} f_c = 0 \tag{B.63}$$

$$\partial_t f + \frac{\vec{p}}{m} \cdot \vec{\nabla} f - \vec{\nabla}\bar{\Phi} \cdot \vec{\nabla}_{\vec{v}} f = 0 \tag{B.64}$$

$$\frac{2\hbar}{m} \vec{p}^2 f - \frac{\hbar}{2} \partial_\beta \Phi \partial^\beta_{(p)} f = 0 \tag{B.65}$$

where the first equation of each component is of standard collision-less Boltzmann form, and the second may be interpreted as a constitutive equation governing the more net effects of Bose statistics on each component's distribution; it is these secondary equations that differentiate the system from purely classical behavior.

B.4 Summary

The two-fluid approach presents an interesting perspective on mixed Bose systems. The semi-classical limit, where only terms of degree $\hbar^0$ are considered, produces two classical Boltzmann equations with no apparent difference in physics between the condensate and normal components. The system produces identical solutions to the MFTs presented in

Chapter 3. Widening our consideration to include the imaginary constraint equations does seem to add a new dimension to the flow. However there again is no difference in physics of the two components, obfuscating any special contributions of a condensate. Further, preliminary computational work by the author shows unavoidable numerical difficulties in simulations over many dynamical crossing times that currently prohibit the the constraint's use. Our conclusion is that multi-fluid techniques are poorly suited to simulate axion structure formation.

Appendix C

BTDDFT

For a given interaction potential, the RG theorem shows that the external potential uniquely determines the axion density, Appx. D. In the case of axions, the external potential will be replaced by the long-range portions of the axion self-gravity, plus the mutual gravitational attraction between the axions and other massive components (gas, stars, etc.). The Kohn-Sham approach to TDDFTs chooses a non-interacting system, which is set to be equivalent to the full interacting system.

$$\Psi^{(N)}(\vec{x}_1, \vec{x}_2, ..., \vec{x}_N, t) \rightarrow \{\psi_i(\vec{x}, t)\}_{i=1,...,N} \tag{C.1}$$

The primary advantage of this division lies in the relative ease of solving a collection of non-interacting systems instead of the full exchanging, correlating, etc. system. We represent the system as a single permanent (symmetric version of the determinant) of single-particle orbitals, each obeying a Schroedinger-like equation

$$i\hbar\partial_t\phi_i = \left(-\frac{\hbar^2}{2m}\Delta + v_{eff}\right)\phi_i \tag{C.2}$$

and collectively generating the total density

$$\rho = \int d^3x_2 \cdots d^3x_N \Psi^{(N)\dagger}\Psi^{(N)} = \sum_i^N |\phi_i|^2 \tag{C.3}$$

The equation of motion of the permanent is then found to be

$$\begin{aligned} i\hbar\partial_t \Psi^{(N)} &= H^{(N)}\Psi^{(N)} \\ &= i\hbar\partial_t \sum_{\sigma\in S_N}\prod_i^N \phi_i\left(\vec{x}_{\sigma(i)}\right) \\ &= i\hbar \sum_{\sigma\in S_N}\sum_j^N \partial_t\phi_j\left(\vec{x}_{\sigma(j)}\right)\prod_{i\neq j}\phi_i\left(\vec{x}_{\sigma(i)}\right) \\ &= i\hbar \sum_{\sigma\in S_N}\sum_j^N \left(-\frac{\hbar^2}{2m}\Delta_{\vec{x}_{\sigma(j)}} + v_{eff}\right)\phi_j\left(\vec{x}_{\sigma(j)}\right)\prod_{i\neq j}\phi_i\left(\vec{x}_{\sigma(i)}\right) \\ &= -\sum_i^N \frac{\hbar^2}{2m}\Delta_{\vec{x}_{\sigma(i)}}\Psi^{(N)} + \sum_i^N v_{eff}\left(\vec{x}_{\sigma(i)},t\right)\Psi^{(N)} \end{aligned} \tag{C.4}$$

where we find that the kinetic contribution is equivalent to the full system. The problem of drawing an equivalence between the full Hamiltonian and the composite orbital Hamiltonian is then reduced to determining the appropriate potential, V_{eff}. In this way, we have reduced an equation of 3N variables into N equations of 3 variables.

This is an impressive reduction, but modeling structure formation of relic axions on any appreciable scale requires quite a bit more. Fortunately, the exchange symmetry shared by the identical axions allows for another drastic reduction in complexity. Reducing the number of unique degrees of freedom from N to K via freezing the number of attainable orbitals is one option. Setting each field entry of the permanent to an element of $\{\phi_j\}_{j=1,\ldots,K}$ via the index map $m(*)$, the many-body wave-function becomes

$$\Psi^{(N)} = \sum_{\sigma\in S_n}\prod_{i=1}^N \phi_i(\vec{x}_{\sigma(i)}) \rightarrow \sum_{\sigma\in S_n}\prod_{i=1}^N \phi_{m(i)}(\vec{x}_{\sigma(i)}) \tag{C.5}$$

The resultant density form then becomes

$$\begin{aligned} \rho &= \int d^3x_2\cdots d^3x_N \Psi^{(N)\dagger}\Psi^{(N)} \\ &= \sum_j^K N_j|\phi_i|^2 \end{aligned} \tag{C.6}$$

where N_j is the number of axions set to orbital ϕ_j, as determined by the pre-image of j via $m(*)$. The effective equations of motion remain with the individual orbitals restricted to the subset.

Note that transmission between orbitals is not possible by construction, so if we are to use the coherence school of thought for the BEC (Leggett, 2006), what is initially in a condensate remains in that same condensate. This is especially non-intuitive considering the possibility for shell-crossing (dispersive) orbital solutions. If we are to apply to the lowest energy state interpretation of BECs, then transmission in and out of such a state is possible so long as the orbitals do not provide stationary solutions themselves. To define the condensate at any given time, we would then need to establish a means of estimating the lowest energy solution form, which may depend on the size of the contemporary structures.

Determining the appropriate potential is quite challenging. Similarly to normal DFT, the effective potential is decomposed into external, self-gravity, and a cross-correlation term

$$v_{eff} = v_{ext} + v_{sg} + v_{xc} \tag{C.7}$$

where the external potential is composed of gravitational interactions with other massive species

$$v_{ext}(\rho_{ext}) = m\Phi_{ext} \tag{C.8}$$

and the self-gravity potential

$$v_{sg}(\rho) = m\Phi_{sg} \tag{C.9}$$

where each gravitational potential is due to external and axion densities respectively

$$\Delta\Phi_{ext} = 4\pi G\rho_{ext} \tag{C.10}$$

$$\Delta\Phi_{sg} = 4\pi G\rho \tag{C.11}$$

The cross-correlation potential v_{xc} is intended to make up for the remaining contributions. The task of finding a suitable v_{xc} is difficult and a great deal of research has been dedicated to such pursuits for fermionic systems, 3.4.

The bosonic case is slightly different, though we may take lessons from the electronic literature. The simplest analogous potential comes from the local density approximation, which takes the form

$$v_{xc} = \frac{\delta E_{LDA}}{\delta \rho} = \epsilon_{xc} + \rho \frac{\partial \epsilon_{xc}}{\partial \rho} \tag{C.12}$$

where, for a homogeneous electron gas,

$$\epsilon_{xc} = -\frac{3}{4}\left(\frac{3}{\pi}\right)^{1/3} \int \rho^{4/3} d^3x' + A \ln \rho + B + \rho^{-1}\left(C \ln \rho + D\right) \tag{C.13}$$

is the exchange-correlation kernel. It stands to reason that a re-derivation of the potential will be necessary to comply with the difference in exchange symmetry, but the fundamental principle of the LDA is an adequate place to start.

Appendix D

RUNGE-GROSS THEOREM

The Runge-Gross (RG) theorem, originally derived for electrons subject to an external scalar field, can be applied to bosonic systems equally as well. Let us construct a Hamiltonian for a system of N identical particles and external scalar field v. The evolution of the N-body wave-function is determined by the Schroedinger equation

$$\hat{H}_v(t)\,|\Psi^{(N)}(t)\rangle = i\hbar\partial_t\,|\Psi^{(N)}(t)\rangle \tag{D.1}$$

where $|\Psi^{(N)}(t)\rangle$ is the state of the identical system. The system's density at any given point in time is given through the integral

$$\rho(\vec{x},t) = N\sum_s \int d^3x_2\cdots d^3x_N |\Psi^{(N)}\left(\vec{x}_1,s_1,...,\vec{x}_N,s_N,t\right)|^2 \tag{D.2}$$

where $\Psi^{(N)}\left(\vec{x}_1,s_1,...,\vec{x}_N,s_N,t\right) = \langle\vec{x}_1,s_1,...,\vec{x}_N,s_N|\,|\Psi^{(N)}(t)\rangle$. These forms lead us to the RG theorem:

Theorem 1 *Given a system of N identical particles subject to a Schroedinger equation of motion, an external potential will map bijectively to the system's density modulo an additive homogenous potential*

$$v(\vec{x},t)+c(t) \to e^{-ic(t)}\,|\Psi^{(N)}(t)\rangle \to \rho(\vec{x},t) \tag{D.3}$$

Proof 1 *Given two external potentials with more than a homogeneous difference*

$$v_1(\vec{x},t) - v_2(\vec{x},t) = \Delta v(\vec{x},t) \tag{D.4}$$

consider their respective Schroedinger solutions for a system of N identical particles

$$i\hbar\partial_t\,|\Psi_1^{(N)}(t)\rangle = \hat{H}_{v_1}(t)\,|\Psi_1^{(N)}(t)\rangle \tag{D.5}$$

$$i\hbar\partial_t\,|\Psi_2^{(N)}(t)\rangle = \hat{H}_{v_2}(t)\,|\Psi_2^{(N)}(t)\rangle \tag{D.6}$$

such that they have the same initial condition $|\Psi^{(N)}\rangle = |\Psi_1^{(N)}(t_0)\rangle = |\Psi_1^{(N)}(t_0)\rangle$.

Given the Taylor series expansion of the external potential difference

$$\Delta v(\vec{x},t) = \sum_k \frac{u_k(\vec{x})}{k!}(t-t_0)^k \tag{D.7}$$

where

$$u_k(\vec{x}) = \partial_t^k \Delta v(\vec{x},t_0) \tag{D.8}$$

are not constant in space by construction.

The Heisenberg equation of motion for the current densities due to the external potentials v_1 *and* v_2 *are*

$$i\partial_t \vec{j}_1(\vec{x},t) = \langle \Psi_1^{(N)}(t)| \left[\hat{\vec{j}}, \hat{H}_{v_1}(t)\right] |\Psi_1^{(N)}(t)\rangle \tag{D.9}$$

$$i\partial_t j_2(\vec{x},t) = \langle \Psi_2^{(N)}(t)| \left[\hat{\vec{j}}, \hat{H}_{v_2}(t)\right] |\Psi_2^{(N)}(t)\rangle \tag{D.10}$$

The difference between the currents at the initial time is given by

$$i\hbar\partial_t \left(\vec{j}_1(\vec{x},t) - \vec{j}_2(\vec{x},t)\right)|_{t_0} = \langle \Psi^{(N)}(t_0)| \left[\hat{\vec{j}}, \hat{H}_{v_1}(t_0) - \hat{H}_{v_2}(t_0)\right] |\Psi^{(N)}(t_0)\rangle \tag{D.11}$$

$$= \langle \Psi^{(N)}(t_0)| \left[\hat{\vec{j}}, \hat{V}_1(t_0) - \hat{V}_2(t_0)\right] |\Psi^{(N)}(t_0)\rangle \tag{D.12}$$

$$= i\hbar\rho(\vec{x},t)\vec{\nabla}\Delta v(\vec{x},t_0) \tag{D.13}$$

where in the last step, we utilized the commutator result

$$\langle \Psi^{(N)}(t)| \left[\hat{\vec{j}}, \hat{V}(t)\right] |\Psi^{(N)}(t)\rangle = i\hbar\rho\vec{\nabla}v + \vec{j} \tag{D.14}$$

This divergence in the current densities shows that when the two external potentials diverge by more than a homogeneous term, differences will start to appear in the currents after some infinitesimal evolution. Even if the differences in potentials are higher order in time, differences will appear, as can be seen in higher-order Heisenberg equations

$$(i\hbar)^{k+1}\partial_t^{k+1}\left(\vec{j}_1(\vec{x},t) - \vec{j}_2(\vec{x},t)\right)|_{t_0} = i\hbar\rho(\vec{x},t)\vec{\nabla}(i\hbar)^k\partial_t^k\Delta v(\vec{x},t_0) \tag{D.15}$$

To prove that these differences in the current densities translate to different densities, consider the continuity equations satisfied by the systems

$$\partial_t \rho_1(\vec{x},t) + \vec{\nabla}\cdot\vec{j}_1(\vec{x},t) = 0 \tag{D.16}$$

$$\partial_t \rho_2(\vec{x},t) + \vec{\nabla}\cdot\vec{j}_2(\vec{x},t) = 0 \tag{D.17}$$

Taking repeated time derivatives of the difference of densities, the continuity equations yield

$$\partial_t^{k+2}\left(\rho_1(\vec{x},t) - \rho_2(\vec{x},t)\right)|_{t_0} = -\vec{\nabla}\cdot\partial_t^{k+1}\left(\vec{j}_1(\vec{x},t) - \vec{j}_2(\vec{x},t)\right)|_{t_0} \tag{D.18}$$

$$= -\vec{\nabla}\cdot\left(\rho(\vec{x},t)\vec{\nabla}\partial_t^k\left(v_1(\vec{x},t) - v_2(\vec{x},t)\right)\right)|_{t_0} \tag{D.19}$$

$$= -\vec{\nabla}\cdot\left(\rho(\vec{x},t_0)\vec{\nabla}u_k(\vec{x})\right) \tag{D.20}$$

Therefore, so long as the potential difference is for some k is such that the last term is non-zero, the two densities will have some non-trivial difference after some evolution past t_0. The guarantee of a non-zero u_k for some k is equivalent to the non-vanishing of D.20 due to the non-trivial differences between the potential's spatial dependence. For clarity, assume the contrary

$$\vec{\nabla}\cdot\left(\rho(\vec{x},t_0)\vec{\nabla}u_k(\vec{x})\right) = 0 \tag{D.21}$$

Green's theorem can be applied to a related form

$$0 = \int d^3x u_k(\vec{x})\vec{\nabla}\cdot\left(\rho(\vec{x},t_0)\vec{\nabla}u_k(\vec{x})\right) \tag{D.22}$$

$$= -\int d^3x \rho(\vec{x},t_0)\left(\vec{\nabla}\partial_t^k u_k(\vec{x})\right)^2 + \frac{1}{2}\int d^2S\hat{n}\cdot\vec{\nabla}u_k^2(\vec{x})\rho(\vec{x},t_0) \tag{D.23}$$

The surface integral vanishes so long as the net flux of material into the region, suitable for isolated systems and systems with periodic boundary conditions. Due to non-negativity of the volume integrand, the integrand must be identically zero over the region

$$\rho(\vec{x},t_0)\left(\vec{\nabla}\partial_t^k u_k(\vec{x})\right)^2 = 0 \tag{D.24}$$

which contradicts the assumption of a non-trivial u_k. The RG theorem is thus proved.

Appendix E

LIOUVILLE'S EQUATION AND THE COLLISION-LESS BOLTZMANN EQUATION

Consider the N-body classical distribution function

$$f^{(N)}(w_1, ..., w_N) \tag{E.1}$$

For a system interacting only through Newtonian gravity, the motive equation for the distribution may be derived in the traditional way: considering the dynamics for each classical particle within the distribution

$$\frac{df^{(N)}}{dt} = \frac{\partial f^{(N)}}{\partial t} + \sum_i^N \frac{\partial f^{(N)}}{\partial \vec{w}_i} \cdot \dot{\vec{w}}_i \tag{E.2}$$

$$= \frac{\partial f^{(N)}}{\partial t} + \sum_i^N \left(\frac{\partial f^{(N)}}{\partial \vec{x}_i} \cdot \dot{\vec{x}}_i + \frac{\partial f^{(N)}}{\partial \vec{p}_i} \cdot \dot{\vec{p}}_i \right) \tag{E.3}$$

$$= \frac{\partial f^{(N)}}{\partial t} + \{f^{(N)}, H_N\} = 0 \tag{E.4}$$

where $\{\cdot, \cdot\}$ is the classical Poisson bracket. In the case where the objects are attracted to one another via only their mutual gravity, Liouville's equation may be rewritten

$$0 = \frac{\partial f^{(N)}}{\partial t} + \sum_i^N \left(\frac{\partial f^{(N)}}{\partial \vec{x}_i} \cdot \vec{v}_i - \frac{\partial f^{(N)}}{\partial \vec{v}_i} \cdot \sum_{j \neq i} \partial_{\vec{x}_i} \Phi_{ij} \right) \tag{E.5}$$

To reduce the N-body DF into something more manageable, let us integrate over K of the single-particle phase-spaces. The result is the N-K DF

$$f^{(K)}(w_1, ..., w_K, t) = \int d^3 w_{K+1} \cdots d^3 w_N f^{(N)}(w_1, ..., w_N, t) \tag{E.6}$$

Specifically we consider the two-body DF, $f^{(2)}$, which may be written as a sum of a correlated and non-correlated part

$$f^{(2)}(w_1, w_2, t) = f(w_1, t) f(w_2, t) + g(w_1, w_2, t) \tag{E.7}$$

where g is the two-body correlation function. Integrating the N-body Liouville equation over N-1 single-particle phase-spaces straightforwardly simplifies the time-derivative and free-streaming terms

$$\frac{\partial f^{(1)}}{\partial t} = \int d^3w_2 \cdots d^3w_N \frac{\partial f^{(N)}}{\partial t} \tag{E.8}$$

$$\frac{\partial f^{(1)}}{\partial \vec{x}} \cdot \vec{v} = \int d^3w_2 \cdots d^3w_N \sum_i^N \frac{\partial f^{(N)}}{\partial \vec{x}_i} \cdot \vec{v}_i \tag{E.9}$$

where we use the divergence theorem and the assumption of PBC over the volume to eliminate the $i > 1$ terms. The transport term is similarly reduced to index $i = 1$, and may be further resolved by exploiting the exchange symmetry enjoyed by a collection of identical objects.

$$\sum_{i,j}^N \int d^6w_2 \cdots d^6w_N \frac{\partial f^{(N)}}{\partial \vec{v}_i} \cdot \sum_{j \neq i} \partial_{\vec{x}_i} \Phi_{ij} = \sum_{i=2}^N \int d^6w_2 \cdots d^6w_N \frac{\partial f^{(N)}}{\partial \vec{v}} \cdot \partial_{\vec{x}} \Phi_{i1} \tag{E.10}$$

$$= (N-1) \int d^6w_2 \partial_{\vec{x}} \Phi_{21} \partial_{\vec{v}} g(w, w_2, t) + (N-1) f^{(1)}(w,t) \int d^6w_2 \partial_{\vec{x}} \Phi_{21} f^{(1)}(w_2, t) \tag{E.11}$$

$$= \frac{N-1}{N} \partial_{\vec{x}} \bar{Phi} \partial_{\vec{v}} f^{(1)} + \frac{N-1}{N} \Gamma[f] \tag{E.12}$$

The Boltzmann equation is then

$$\frac{df^{(1)}}{dt} = \frac{\partial f^{(1)}}{\partial t} + \frac{\partial f^{(1)}}{\partial \vec{x}} \cdot \vec{v} - \frac{N-1}{N} \partial_{\vec{x}} \bar{Phi} \partial_{\vec{v}} f^{(1)} = \frac{N-1}{N} \Gamma[f] \tag{E.13}$$

The result is a system effectively described by a single-body equation over an averaged gravitational potential $\bar{\Phi}$, plus an impact term Γ due to two-body correlation contributions. The impact term is the encounter operator

$$\Gamma[f] = N \int d^6w_2 \partial_{\vec{x}} \Phi_{21} \partial_{\vec{v}} g(w, w_2, t) \tag{E.14}$$

and will be utilized extensively in the derivation of the closed multi-fluid Boltzmann equations.

Appendix F

THE MANY-BODY SCHROEDINGER EQUATION AND ONE SPECIAL SOLUTION

Let us consider the many-body problem of axion infall as a solution of the many-body Schroedinger equation under inter-particle Newtonian gravitation.

$$i\hbar\partial_t \Psi\left(\vec{x}_1, ..., \vec{x}_N; t\right) = \hat{H}\Psi\left(\vec{x}_1, ..., \vec{x}_N; t\right) \tag{F.1}$$

with the Hamiltonian of the form

$$\hat{H} = \hat{T} + \hat{V}_{int} + \hat{V}_{ext} = -\sum_i^N \frac{\hbar^2\nabla^2}{2m_a} - \sum_{i<j}^N \frac{Gm_a^2}{|\vec{x}_i - \vec{x}_j|} + \sum_i^N \phi\left(\vec{x}_i\right) \tag{F.2}$$

We will be ignoring the external potential for the rest of this section. The solution space for this PDE is covered by the

$$\mathcal{C}\left(\mathbb{R}^{3N+1}\right) \tag{F.3}$$

which has a dense Fock space

$$\mathcal{C}\left(\mathbb{R}^3\right) \times ... \times \mathcal{C}\left(\mathbb{R}^3\right) \times \mathcal{C}\left(\mathbb{R}\right) \tag{F.4}$$

meaning we may write any solution of the many-body Schroedinger equation as combinations of single-body products to arbitrary accuracy

$$\Psi = \prod_{i\in\{1,...,N\}\alpha\in A} \psi_\alpha\left(\vec{x}_i\right) + ... \tag{F.5}$$

Finding these combinations can be difficult. With such a strong correlated force, these linear combinations are often of infinite length and slowly converging, making computation difficult when faced with finite resources. As the goal of this research project is to succinctly describe the dynamics of the axion system, and additional tool is needed.

As the axions are Bosons, the anticommutaiton relations of the quantum field requires the system to only occupy fully symmetric states under particle exchange

$$\Psi\left(\vec{x}_1, ..., \vec{x}_i, ..., \vec{x}_j, ..., \vec{x}_N; t\right) = \Psi\left(\vec{x}_1, ..., \vec{x}_j, ..., \vec{x}_i, ..., \vec{x}_N; t\right) for some i, j \tag{F.6}$$

reducing the solution space to

$$\mathcal{C}\left(\mathbb{R}^{3N+1}\right)/S_N \tag{F.7}$$

and the dense Fock space to

$$\mathcal{C}\left(\mathbb{R}^3\right) \times ... \times \mathcal{C}\left(\mathbb{R}^3\right) \times \mathcal{C}\left(\mathbb{R}\right)/S_N \tag{F.8}$$

To find a more useful and concise form of the many-body solutions, let us rewrite the Hamiltonian in a form that showcases the unique shape of the potential. The kinetic term $\hat{T}$ describes the energy due to motion of axions relative to a prescribed frame of reference, but motion of the sum of particles can be equally described by the motion of the system's center of mass and the relative particle motions. A gradient can be written as

$$\vec{\nabla}_i = \frac{1}{N}\sum_j^N \left(\vec{\nabla}_j + \left(\vec{\nabla}_i - \vec{\nabla}_j\right)\right) \tag{F.9}$$

$$= \frac{1}{N} M_{total} \vec{\nabla}_{com} + \frac{1}{N}\sum_{i\neq j} \vec{\nabla}_{\Delta_{ij}} \tag{F.10}$$

where $\vec{\nabla}_{\Delta_{ij}} = \vec{\nabla}_i - \vec{\nabla}_j$, making

$$\nabla_i^2 = \frac{1}{N^2} M_{tot}^2 \nabla_{com}^2 + \frac{1}{N^2}\sum_{i\neq j} \nabla_{\Delta_{ij}}^2 \tag{F.11}$$

$$+ \frac{2}{N^2} M_{tot} \sum_{i\neq j} \vec{\nabla}_{com} \cdot \vec{\nabla}_{\Delta_{ij}} + \frac{2}{N^2} M_{tot} \sum_{k\neq j} \vec{\nabla}_{\Delta_{ij}} \cdot \vec{\nabla}_{\Delta_{ik}} \tag{F.12}$$

The last two terms are seen to vanish for $\hat{T}$ as a whole as each $\vec{\nabla}_{com} \cdot \vec{\nabla}_{\Delta_{ij}}$ may be matched with a $\vec{\nabla}_{com} \cdot \vec{\nabla}_{\Delta_{ji}} = -\vec{\nabla}_{com} \cdot \vec{\nabla}_{\Delta_{ij}}$ and each $\vec{\nabla}_{\Delta_{ij}} \cdot \vec{\nabla}_{\Delta_{ik}}$ can be matched with cycles of terms to reduce to center-of-mass contributions.

The alternate form of $\hat{T}$ can then be written as

$$\hat{T} = -\frac{1}{2M_{tot}}\nabla^2_{com} - \sum_{i<j}\frac{1}{2\mu}\nabla^2_{\Delta_{ij}} \tag{F.13}$$

where $\mu = m_a/N$.The many-body Hamiltonian can also be rewritten

$$\hat{H} = -\frac{1}{2M_{tot}}\nabla^2_{com} - \sum_{i<j}\frac{1}{2\mu}\nabla^2_{\Delta_{ij}} - \sum_{i<j}^{N}\frac{Gm_a^2}{|\vec{x}_i - \vec{x}_j|} \tag{F.14}$$

$$= \hat{H}_{com} + \hat{H}_{int} \tag{F.15}$$

where

$$\hat{H}_{com} = -\frac{1}{2M_{tot}}\nabla^2_{com} \tag{F.16}$$

$$\hat{H}_{int} = -\sum_{i<j}\frac{1}{2\mu}\nabla^2_{\Delta_{ij}} - \sum_{i<j}^{N}\frac{Gm_a^2}{|\vec{x}_i - \vec{x}_j|} \tag{F.17}$$

Note that $\hat{H}_{int}$ appears to be separable over the $\vec{\Delta}_{ij}$, however they are non-independent over the many-body solution space. To circumvent this, let use consider a slightly different problem: a system of N^2 particles with Hamiltonian H_{int} defined over function space $\mathscr{C}\left(\mathbb{R}^{3N^2+1}\right)$ with solution space defined using additional (Bose) modulation

$$\mathscr{C}\left(\mathbb{R}^{3N^2+1}\right)/S_{N^2} \tag{F.18}$$

In this case the Hamiltonian is separable and the stationary states may be written as a single permanent of single 'particle' states

$$\Phi'\left(\Delta_{ij}\right) = perm\left(\prod_{ij\,\alpha}\phi_\alpha\left(\Delta_{ij}\right)\right) \tag{F.19}$$

and the coherent states as

$$\Psi'\left(\Delta_{ij};t\right) = perm\left(\prod_{ij\,\alpha}\psi_\alpha\left(\Delta_{ij},t\right)\right) \tag{F.20}$$

This finding can be utilized in the original use-case of N axions by applying an appropriate projection

$$p:\ \Delta_{ij} = \vec{x}_i - \vec{x}_j \forall i,j \tag{F.21}$$

on the Hamiltonian function space pair.

$$\{\hat{H}\left(\mathbb{R}^{3N^2+1}\right), \mathscr{C}\left(\mathbb{R}^{3N^2+1}\right)\} \rightarrow \{\hat{H}\left(\mathbb{R}^{3N+1}\right), \mathscr{C}\left(\mathbb{R}^{3N+1}\right)\} \tag{F.22}$$

It is apparent that this projection both respects the modulated many-body solution space and the required Schroedinger equation. What remains is to show that the span of solutions to the N^2 problem hold for all solutions to the N problem, which translates to proving the projected solution space $p\left(C\left(\mathbb{R}^{3N^2+1}\right)\right)$ is dense in $C\left(\mathbb{R}^{3N+1}\right)$. The proof of this is straightforward.

BIBLIOGRAPHY

Aaboud, M., Aad, G., Abbott, B., et al. 2017, Physics Letters B, 765, 11

Aad, G., Abajyan, T., Abbott, B., et al. 2012, Physics Letters B, 716, 1

Abbott, C. G., Valluri, M., Shen, J., & Debattista, V. P. 2017, Monthly Notices of the RAS, 470, 1526

Abbott, L. F., & Sikivie, P. 1983, Physics Letters B, 120, 133

ADMX Collaboration. 2017a

—. 2017b

Agnese, R., Anderson, A. J., Asai, M., et al. 2014, Physical Review Letters, 112, 241302

Akerib, D. S., Alsum, S., Araújo, H. M., et al. 2017, Phys. Rev. Lett., 118, 021303

Alcock, C., Allsman, R. A., Alves, D. R., et al. 2000, Astrophysical Journal, 542, 281

Anderson, L., Aubourg, É., Bailey, S., et al. 2014, Monthly Notices of the RAS, 441, 24

Anglin, J. R., & Ketterle, W. 2002, Nature, 416, 211

Aprile, E., Aalbers, J., Agostini, F., et al. 2017, ArXiv e-prints, arXiv:1705.06655

Arcadi, G., Dutra, M., Ghosh, P., et al. 2017, ArXiv e-prints, arXiv:1703.07364

Armengaud, E., Avignone, F. T., Betz, M., et al. 2014, Journal of Instrumentation, 9, T05002

Arvanitaki, A., Baryakhtar, M., & Huang, X. 2015, Physical Review D, 91, 084011

Asztalos, S. J., Carosi, G., Hagmann, C., et al. 2010, Physical Review Letters, 104, 041301

Baier, F. W. 1978, Astronomische Nachrichten, 299, 311

Baker, C. A., Doyle, D. D., Geltenbort, P., et al. 2006, Physical Review Letters, 97, 131801

Banik, N., Christopherson, A. J., Sikivie, P., & Todarello, E. M. 2015, Physical Review D, 91, 123540

Banik, N., & Sikivie, P. 2016, Physical Review D, 93, 103509

Barnes, E. I., Williams, L. L. R., Babul, A., & Dalcanton, J. J. 2006, Astrophysical Journal, 643, 797

Barnes, J., & Efstathiou, G. 1987, Astrophysical Journal, 319, 575

Barnes, J., Hut, P., & Goodman, J. 1986, Astrophysical Journal, 300, 112

Baudis, L. 2014, Physics of the Dark Universe, 4, 50 , dARK TAUP2013

Bellovary, J. M., Dalcanton, J. J., Babul, A., et al. 2008, Astrophysical Journal, 685, 739

Binney, J. 2017, ArXiv e-prints, arXiv:1706.01374

Binney, J., & Quinn, T. 1991, Monthly Notices of the RAS, 249, 678

Binney, J., & Tremaine, S. 2008, Galactic Dynamics: Second Edition (Princeton University Press)

Bondar, D. I., Cabrera, R., Zhdanov, D. V., & Rabitz, H. A. 2013, Physical Review A: General Physics, 88, 263

Boutan, C. 2015, PhD thesis, UW PhD Thesis, 2017

Bovy, J., Allende Prieto, C., Beers, T. C., et al. 2012, Astrophysical Journal, 759, 131

Bozorgnia, N., Calore, F., Schaller, M., et al. 2016, Journal of Cosmology and Astroparticle Physics, 5, 024

Brito, R., Ghosh, S., Barausse, E., et al. 2017, ArXiv e-prints, arXiv:1706.06311

Brown, D. A. 2007, PhD thesis, PhD Thesis, 2007

Brubaker, B. M., Zhong, L., Lamoreaux, S. K., Lehnert, K. W., & van Bibber, K. A. 2017, ArXiv e-prints, arXiv:1706.08388

Budker, D., Graham, P. W., Ledbetter, M., Rajendran, S., & Sushkov, A. O. 2014, Physical Review X, 4, 021030

Bullock, J. S., Dekel, A., Kolatt, T. S., et al. 2001, Astrophysical Journal, 555, 240

Callan, Jr., C. G., Dashen, R., & Gross, D. J. 1978, Physical Review D, 17, 2717

CAST collaboration, Anastassopoulos, V., Aune, S., et al. 2017, ArXiv e-prints, arXiv:1705.02290

Casuso, E., & Beckman, J. E. 2015, Monthly Notices of the RAS, 449, 2910

Catena, R., & Covi, L. 2014, European Physical Journal C, 74, 2703

Chakrabarty, S. S., & Sikivie, P. 2017, in APS April Meeting Abstracts

Chau, A., Mayer, L., & Governato, F. 2017, Astrophysical Journal, 845, 17

Codis, S., Pichon, C., & Pogosyan, D. 2015, Monthly Notices of the RAS, 452, 3369

Coleman, S. 1988, Aspects of Symmetry, 416

Collaboration, A. 2016, ALPS WISP DM Experiments, `https://alps.desy.de/e169399/`, accessed: 2017-09-30

Couchman, H. M. P., Thomas, P. A., & Pearce, F. R. 1995, Astrophysical Journal, 452, 797

Courant, R., & Hilbert, D. 1953, Methods of mathematical physics - Vol.1; Vol.2

Csáki, C., & Tanedo, P. 2016, ArXiv e-prints, arXiv:1602.04228

Dalfovo, F., Giorgini, S., Pitaevskii, L. P., & Stringari, S. 1999, Rev. Mod. Phys., 71, 463

Dar, S. 2000, ArXiv High Energy Physics - Phenomenology e-prints, hep-ph/0008248

Daw, E. J. 1998, PhD thesis, PhD Thesis, 1998

Dawson, K. S., Schlegel, D. J., Ahn, C. P., et al. 2013, Astronomical Journal , 145, 10

de Blok, W. J. G., McGaugh, S. S., & Rubin, V. C. 2001, Astronomical Journal , 122, 2396

de Naray, R. K., Martinez, G. D., Bullock, J. S., & Kaplinghat, M. 2010, The Astrophysical Journal Letters, 710, L161

de Vaucouleurs, G. 1956, Vistas in Astronomy, 2, 1584

—. 1960, Astrophysical Journal, 131, 585

de Vaucouleurs, G. 1974, in IAU Symposium, Vol. 58, The Formation and Dynamics of Galaxies, ed. J. R. Shakeshaft, 1–52

Deibel, A. T., Valluri, M., & Merritt, D. 2011, Astrophysical Journal, 728, 128

Dine, M., & Fischler, W. 1983, Physics Letters B, 120, 137

Dine, M., Fischler, W., & Srednicki, M. 1981, Physics Letters B, 104, 199

Dodelson, S. 2011, International Journal of Modern Physics D, 20, 2749

Dodelson, S., & Widrow, L. M. 1994, Phys. Rev. Lett., 72, 17

Duffy, L. D., & Sikivie, P. 2008, Physical Review D, 78, 063508

Einstein, A. 1917, Sitzungsberichte der Königlich Preußischen Akademie der Wissenschaften (Berlin), Seite 142-152.

Eisenstein, D. J., Zehavi, I., Hogg, D. W., et al. 2005, Astrophysical Journal, 633, 560

Enander, J., Pargner, A., & Schwetz, T. 2017, ArXiv e-prints, arXiv:1708.04466

Erken, O., Sikivie, P., Tam, H., & Yang, Q. 2012, Physical Review D, 85, 063520

Evrard, A. E. 1988, Monthly Notices of the RAS, 235, 911

Fairbairn, M., Marsh, D. J. E., Quevillon, J., & Rozier, S. 2017, ArXiv e-prints, arXiv:1707.03310

Famaey, B., & McGaugh, S. S. 2012, Living Reviews in Relativity, 15, 10

Fiolhais, C., Nogueira, F., & Marques, M., eds. 2003, Lecture Notes in Physics, Berlin Springer Verlag, Vol. 620, A Primer in Density Functional Theory

Flores, R. A., & Primack, J. R. 1994, Astrophysical Journal, Letters, 427, L1

Freese, K., Lisanti, M., & Savage, C. 2013, Reviews of Modern Physics, 85, 1561

Fry, A. B. 2015, PhD thesis, UW PhD Thesis, 2015

Fry, A. B., Governato, F., Pontzen, A., et al. 2015, Monthly Notices of the RAS, 452, 1468

Garcon, A., Aybas, D., Blanchard, J. W., et al. 2017, ArXiv e-prints, arXiv:1707.05312

Gardner, J. P. 2001, Astrophysical Journal, 557, 616

Gasser, I., Lin, C.-K., , & Markowich, P. A. 2000, Taiwanese Journal of Mathematics, 4, 501

Gates, E. I., Gyuk, G., & Turner, M. S. 1995, Astrophysical Journal, Letters, 449, L123

Gelmini, G., & Gondolo, P. 2001, Physical Review D, 64, 023504

Gilmore, G., Wilkinson, M. I., Wyse, R. F. G., et al. 2007, Astrophysical Journal, 663, 948

Governato, F., Willman, B., Mayer, L., et al. 2007, Monthly Notices of the RAS, 374, 1479

Governato, F., Weisz, D., Pontzen, A., et al. 2015, Monthly Notices of the RAS, 448, 792

Griffin, A., Nikuni, T., & Zaremba, E. 2009, Bose-Condensed Gases at Finite Temperatures

Gross, D. J., Pisarski, R. D., & Yaffe, L. G. 1981, Reviews of Modern Physics, 53, 43

Gupta, R. 1998, ArXiv High Energy Physics - Lattice e-prints, hep-lat/9807028

Guth, A. H., Hertzberg, M. P., & Prescod-Weinstein, C. 2015, Physical Review D, 92, 103513

Hayashi, K., & Chiba, M. 2015, Astrophysical Journal, 810, 22

Herpich, J., Stinson, G. S., Dutton, A. A., et al. 2015, Monthly Notices of the RAS, 448, L99

Hillebrandt, W., & Niemeyer, J. C. 2000, Annual Review of Astron and Astrophys, 38, 191

Holmberg, E. 1961, Astronomical Journal , 66, 620

Huterer, D., & Turner, M. S. 1999, Physical Review D, 60, 081301

Huynh, M., & Lazio, J. 2013, ArXiv e-prints, arXiv:1311.4288

Irastorza, I. G., Avignone, F. T., Caspi, S., et al. 2011, Journal of Cosmology and Astroparticle Physics, 6, 013

Jackson, J. D., & Zia, R. K. P. 1977, Physics Today, 30, 61

Jaeckel, J., & Spannowsky, M. 2015, 753

Jetley, P., Gioachin, F., Mendes, C., Kale, L. V., & Quinn, T. 2008, in 2008 IEEE International Symposium on Parallel and Distributed Processing, 1–12

Jungman, G., Kamionkowski, M., & Griest, K. 1996, Physics Reports, 267, 195

Kafle, P. R., Sharma, S., Lewis, G. F., & Bland-Hawthorn, J. 2012, Astrophysical Journal, 761, 98

Kelley, K., & Quinn, P. J. 2017, Astrophysical Journal, Letters, 845, L4

Kelso, C., Savage, C., Valluri, M., et al. 2016, Journal of Cosmology and Astroparticle Physics, 8, 071

Kim, J. E. 1979, Phys. Rev. Lett., 43, 103

Kim, J. E. 1987, Physics Reports, 150, 1

Kim, J.-h., Abel, T., Agertz, O., et al. 2014, Astrophysical Journal, Supplement, 210, 14

Knollmann, S. R., & Knebe, A. 2009, Astrophysical Journal, Supplement, 182, 608

Kolb, E. W., & Tkachev, I. I. 1993, Physical Review Letters, 71, 3051

Komatsu, E., Smith, K. M., Dunkley, J., et al. 2011, Astrophysical Journal, Supplement, 192, 18

Kopp, J., Machado, P. A. N., Maltoni, M., & Schwetz, T. 2013, Journal of High Energy Physics, 5, 50

Leggett, A. J. 2006, Quantum liquids : Bose condensation and Cooper pairing in condensed-matter systems (Oxford University Press)

Lelli, F., McGaugh, S. S., & Schombert, J. M. 2016, Astronomical Journal , 152, 157

Lentz, E. W., Quinn, T. R., & Rosenberg, L. J. 2016, Astrophysical Journal, 822, 89

Lentz, E. W., Quinn, T. R., Rosenberg, L. J., & Tremmel, M. J. 2017, Astrophysical Journal, 845, 121

Limber, D. N. 1959, Astrophysical Journal, 130, 414

Lin, H.-W. 2011, ArXiv e-prints, arXiv:1106.1608

Ludlow, A. D., Navarro, J. F., Boylan-Kolchin, M., et al. 2013, Monthly Notices of the RAS, 432, 1103

Lyapustin, D. 2015, PhD thesis, UW PhD Thesis, 2015

Madelung, E. 1926, Naturwissenschaften, 14, 1004

Majorovits, B., & Javier Redondo for the MADMAX Working Group. 2016, ArXiv e-prints, arXiv:1611.04549

Marques, M. A. L., & Gross, E. K. U. 2004, Annual Review of Physical Chemistry, 55, 427

Marsh, D. J. E. 2016, Physics Reports, 643, 1

McAllister, B. T., Flower, G., Kruger, J., et al. 2017, ArXiv e-prints, arXiv:1706.00209

McConnachie, A. W. 2012, Astronomical Journal , 144, 4

McGaugh, S. S. 2015, Canadian Journal of Physics, 93, 250

McGaugh, S. S., & de Blok, W. J. G. 1998, Astrophysical Journal, 499, 66

Merritt, D., & Valluri, M. 1999a, Astronomical Journal , 118, 1177

Merritt, D., & Valluri, M. 1999b, in Bulletin of the American Astronomical Society, Vol. 31, American Astronomical Society Meeting Abstracts #194, 893

Mimasu, K., & Sanz, V. 2015, Journal of High Energy Physics, 6, 173

Mitsou, V. A. 2015, in Journal of Physics Conference Series, Vol. 651, Journal of Physics Conference Series, 012023

Montanino, D., Vazza, F., Mirizzi, A., & Viel, M. 2017, Phys. Rev. Lett., 119, 101101

Moore, B. 1994, Nature, 370, 629

Moore, B., Ghigna, S., Governato, F., et al. 1999, Astrophysical Journal, Letters, 524, L19

Moore, B., Governato, F., Quinn, T., Stadel, J., & Lake, G. 1998, Astrophysical Journal, Letters, 499, L5

Morris, D. J., Hobbs, G., Lyne, A. G., et al. 2002, Monthly Notices of the RAS, 335, 275

Navarro, J. F., Eke, V. R., & Frenk, C. S. 1996a, Monthly Notices of the RAS, 283, L72

Navarro, J. F., Frenk, C. S., & White, S. D. M. 1996b, Astrophysical Journal, 462, 563

Navarro, J. F., Ludlow, A., Springel, V., et al. 2010, Monthly Notices of the RAS, 402, 21

Olive, K. A., Particle Data Group, & et al. 2014, Chinese Physics C, 38, 090001

O'Shea, B. W., Bryan, G., Bordner, J., et al. 2004, ArXiv Astrophysics e-prints, astro-ph/0403044

Patrignani, C., & Particle Data Group. 2016, Chinese Physics C, 40, 100001

Peccei, R. D., & Quinn, H. R. 1977, Physical Review Letters, 38, 1440

Peebles, P. J., & Ratra, B. 2003, Reviews of Modern Physics, 75, 559

Peebles, P. J. E. 1969, Astrophysical Journal, 155, 393

Pendlebury, J. M., Afach, S., Ayres, N. J., et al. 2015, Physical Review D, 92, 092003

Perlmutter, S., Aldering, G., Goldhaber, G., et al. 1999, Astrophysical Journal, 517, 565

Petrakou, E. 2017, ArXiv e-prints, arXiv:1702.03664

Pichon, C., Codis, S., Pogosyan, D., et al. 2016, in IAU Symposium, Vol. 308, The Zeldovich Universe: Genesis and Growth of the Cosmic Web, ed. R. van de Weygaert, S. Shandarin, E. Saar, & J. Einasto, 421–432

Planck Collaboration, Ade, P. A. R., Aghanim, N., et al. 2014, Astronomy and Astrophysics, 571, A16

Planck Collaboration, Adam, R., Ade, P. A. R., et al. 2016a, Astronomy and Astrophysics, 594, A1

Planck Collaboration, Ade, P. A. R., Aghanim, N., et al. 2016b, Astronomy and Astrophysics, 594, A13

Polyachenko, V. L. 1981, Soviet Astronomy Letters, 7, 79

Pontzen, A., & Governato, F. 2013, Monthly Notices of the RAS, 430, 121

Pontzen, A., Roškar, R., Stinson, G., & Woods, R. 2013, pynbody: N-Body/SPH analysis for python, Astrophysics Source Code Library, ascl:1305.002

Pontzen, A., e. a. 2017, TANGOS software package, (in preparation)

Preskill, J., Wise, M. B., & Wilczek, F. 1983, Physics Letters B, 120, 127

Quinn, T., & Binney, J. 1992, Monthly Notices of the RAS, 255, 729

Raffelt, G. 1999, Nuclear Physics B Proceedings Supplements, 72, 43

Raffelt, G. G. 1996, Stars as laboratories for fundamental physics : the astrophysics of neutrinos, axions, and other weakly interacting particles

Raffelt, G. G. 2008, Astrophysical Axion Bounds, ed. M. Kuster, G. Raffelt, & B. Beltrán (Berlin, Heidelberg: Springer Berlin Heidelberg), 51–71

Raffelt, G. G., & Dearborn, D. S. P. 1987, Phys. Rev. D, 36, 2211

Redondo, J. 2008, ArXiv e-prints, arXiv:0810.3200

Redondo, J. 2013, Journal of Cosmology and Astroparticle Physics, 2013, 008

Redondo, J., & Ringwald, A. 2011, Contemporary Physics, 52, 211

Reid, M. J., Menten, K. M., Brunthaler, A., et al. 2014, Astrophysical Journal, 783, 130

Riess, A. G., Filippenko, A. V., Challis, P., et al. 1998, Astronomical Journal , 116, 1009

Ringwald, A. 2012, Physics of the Dark Universe, 1, 116 , next Decade in Dark Matter and Dark Energy

Ringwald, A. 2016, in Proceedings of the Neutrino Oscillation Workshop (NOW2016). 4 - 11 September, 2016. Otranto (Lecce, Italy). Online at ¡A href=“http://pos.sissa.it/cgi-bin/reader/conf.cgi?confid=283”¿http://pos.sissa.it/cgi-bin/reader/conf.cgi?confid=283¡/A¿, id.81, 81

Rubin, V. C. 1973, Scientific American, 228, 30

Rubin, V. C., & Ford, Jr., W. K. 1970, Astrophysical Journal, 159, 379

Rubin, V. C., & Ford, Jr., W. K. 1975, in Bulletin of the AAS, Vol. 7, Bulletin of the American Astronomical Society, 253

Rubin, V. C., Ford, Jr., W. K., & Rubin, J. S. 1973, Astrophysical Journal, Letters, 183, L111

Rubin, V. C., Peterson, C. J., & Ford, Jr., W. K. 1980, Astrophysical Journal, 239, 50

Rubin, V. C., Thonnard, N. T., & Ford, Jr., W. K. 1982, Astronomical Journal , 87, 477

Rubin, V. C., Waterman, A. H., & Kenney, J. D. P. 1997, in Bulletin of the American Astronomical Society, Vol. 29, American Astronomical Society Meeting Abstracts, 1379

Ruchti, G. R., Read, J. I., Feltzing, S., et al. 2015, Monthly Notices of the RAS, 450, 2874

Runge, E., & Gross, E. K. U. 1984, Phys. Rev. Lett., 52, 997

Ryden, B. S. 1988, Astrophysical Journal, 329, 589

Ryden, B. S., & Gunn, J. E. 1987, Astrophysical Journal, 318, 15

Sanderson, R. E., & Bertschinger, E. 2010, Astrophysical Journal, 725, 1652

Schaller, M., Frenk, C. S., Fattahi, A., et al. 2016, Monthly Notices of the RAS, 461, L56

Shellard, E. P. S., & Battye, R. A. 1998, in COSMO-97, First International Workshop on Particle Physics and the Early Universe, ed. L. Roszkowski, 233–247

Shifman, M. A., Vainshtein, A. I., & Zakharov, V. I. 1980, Nuclear Physics B, 166, 493

Sikivie, P. 1983, Physical Review Letters, 51, 1415

—. 1999a, Physical Review D, 60, 063501

—. 1999b, Nuclear Physics B Proceedings Supplements, 72, 110

Sikivie, P. 2008, in Lecture Notes in Physics, Berlin Springer Verlag, Vol. 741, Axions, ed. M. Kuster, G. Raffelt, & B. Beltrán, 19

Sikivie, P., & Yang, Q. 2009, Physical Review Letters, 103, 111301

Skordis, C. 2009, Classical and Quantum Gravity, 26, 143001

Sloane, J. D., Buckley, M. R., Brooks, A. M., & Governato, F. 2016, Astrophysical Journal, 831, 93

Springel, V. 2005, Monthly Notices of the RAS, 364, 1105

Srednicki, M. 1985, Nuclear Physics B, 260, 689

Steigman, G. 2007, Annual Review of Nuclear and Particle Science, 57, 463

Stern, I. P., & ADMX, A.-H. C. 2014, in American Institute of Physics Conference Series, Vol. 1604, American Institute of Physics Conference Series, 456–461

Strigari, L. E., Bullock, J. S., Kaplinghat, M., et al. 2006, Astrophysical Journal, 652, 306

Sumiyoshi, K. 2013, in IAU Symposium, Vol. 291, Neutron Stars and Pulsars: Challenges and Opportunities after 80 years, ed. J. van Leeuwen, 67–72

Taylor, J. E., & Navarro, J. F. 2001, Astrophysical Journal, 563, 483

Thompson, T. A. 2008, Astrophysical Journal, 684, 212

Tinyakov, P., Tkachev, I., & Zioutas, K. 2016, Journal of Cosmology and Astroparticle Physics, 1, 035

Tisserand, P., Le Guillou, L., Afonso, C., et al. 2007, Astronomy and Astrophysics, 469, 387

Tremmel, M., Governato, F., Volonteri, M., & Quinn, T. R. 2015a, Monthly Notices of the RAS, 451, 1868

—. 2015b, Monthly Notices of the RAS, 451, 1868

Tremmel, M., Karcher, M., Governato, F., et al. 2017, Monthly Notices of the RAS, 470, 1121

Turner, M. S. 1990, Phys. Rev. D, 42, 3572

Turner, M. S., & Wilczek, F. 1991, Physical Review Letters, 66, 5

Vafa, C., & Witten, E. 1984, Physical Review Letters, 53, 535

Valluri, M., Debattista, V. P., Quinn, T., & Moore, B. 2010, Monthly Notices of the RAS, 403, 525

Valluri, M., Debattista, V. P., Quinn, T. R., Roškar, R., & Wadsley, J. 2012, Monthly Notices of the RAS, 419, 1951

Valluri, M., Debattista, V. P., Stinson, G. S., et al. 2013, Astrophysical Journal, 767, 93

Valluri, M., Loebman, S. R., Bailin, J., et al. 2016, in IAU Symposium, Vol. 317, The General Assembly of Galaxy Halos: Structure, Origin and Evolution, ed. A. Bragaglia, M. Arnaboldi, M. Rejkuba, & D. Romano, 358–359

Valluri, M., & Merritt, D. 2000, Advanced Series in Astrophysics and Cosmology, 10, 229

van den Bosch, F. C. 2002, Monthly Notices of the RAS, 331, 98

Vinyoles, N., Serenelli, A., Villante, F., et al. 2015, 2015

Wald, R. M. 1984, General relativity

Walker, M. G., McGaugh, S. S., Mateo, M., Olszewski, E. W., & Kuzio de Naray, R. 2010, Astrophysical Journal, Letters, 717, L87

Weinberg, S. 1972, Gravitation and Cosmology: Principles and Applications of the General Theory of Relativity, 688

Weinberg, S. 1978, Phys. Rev. Lett., 40, 223

Wigner, E. 1932, Physical Review, 40, 749

Wilczek, F. 1978, Phys. Rev. Lett., 40, 279

Yukalov, V. I. 2011, Physics of Particles and Nuclei, 42, 460

Zachos, C. K., Fairlie, D. B., & Curtright, T. L. 2005, Quantum Mechanics in Phase Space: an Overview with Selected Papers, doi:10.1142/5287

Zapf, V., Jaime, M., & Batista, C. D. 2014, Rev. Mod. Phys., 86, 563

Zaremba, E., Nikuni, T., & Griffin, A. 1999, eprint arXiv:cond-mat/9903029, cond-mat/9903029

Zhitnitsky, A. R. 1980, Sov. J. Nucl. Phys., 31, 260, [Yad. Fiz.31,497(1980)]

Zukin, P., & Bertschinger, E. 2010a, Physical Review D, 82, 104044

—. 2010b, Physical Review D, 82, 104045

Zurek, W. H. 2003, eprint arXiv:quant-ph/0306072, quant-ph/0306072

Zwicky, F. 1937, Astrophysical Journal, 86, 217

—. 1942, Physical Review, 61, 489

—. 1953, Physics Today, 6, 7